



Norwegian University of
Science and Technology

Assessment and Numerical Simulation of the Pendulous Installation Method in Deepwater

**Tharindu Dilshan Madduma
Hewage
Brian Murray**

Marine Technology

Submission date: June 2016

Supervisor: Kjell Larsen, IMT

Norwegian University of Science and Technology
Department of Marine Technology



MASTER THESIS SPRING 2016

for

Stud. tech. Brian James Murray
and
Stud.tech. Tharindu Dilshan Madduma Hewage

Assessment and Numerical Simulation of the Pendulous Installation Method in Deepwater

Olje og gass utbygging på dypt vann - vurdering og simulering av pendelmetoden

Background

Subsea production systems are in most field development scenarios become the most attractive option, both in terms of capital expenditure and technical solution. In order to be able to design, install and operate a subsea oil and gas factory, a cost-effective installation method is crucial. Present capital expenditure of the marine operations for a subsea production system in 300-500m water depth is for some cases in the range 15-30% of the total capital invested. Subsea hardware facilities typically consist of templates, manifolds and x-mas trees as well as lot of in-field flow-lines and pipeline connections (spool pieces).

A key activity to successful subsea installation operations is deep water the planning process. This thesis shall focus on installation activities in 3000m water depth. Lifting of subsea equipment, especially through the wave zone, is a weather critical activity. It is crucial that this part of the operations is planned and understood properly. Numerical simulations are an important part of the decision basis.

This MSc thesis shall build on the work and report made the project work during autumn 2015. Several numerical simulation suites exist. The thesis shall use the tools available in the SIMA/SIMO program suite.

Scope of Work

- 1) Familiarize with the numerical simulation suite SIMA/SIMO and describe the theory that is relevant for a subsea lifting and installation of dual Cap-X subsea equipment for a subsea oil and gas producing factory.
- 2) Establish a numerical simulation model in SIMA for a selected installation set-up and method (vessel and object(s)). Propose parameters that can be detrimental for the design operational limit and establish limits based on simulation results. The variability of the design responses shall be assessed. Relevant sensitivity studies as agreed with supervisor shall be conducted .
- 3) Evaluate some aspects of the planning of the installation operation. The following shall be included : a) safe conditions, b) time consumption and alpha factors, c) required weather windows for typical levels of weather parameters (Hs and Tp).
- 4) Conclusions and recommendations for further work.

General information

The start of the thesis shall be the project work carried out during autumn 2015.

In the project report the candidate shall present hers/his personal contribution to the resolution of problems within the scope of the thesis work.

Theories and conclusions should be based on mathematical derivations and/or logic reasoning identifying the various steps in the deduction.

The candidate should utilise the existing possibilities for obtaining relevant literature.

Thesis format

The thesis should be organised in a rational manner to give a clear exposition of results, assessments, and conclusions. The text should be brief and to the point, with a clear language. Telegraphic language should be avoided.

The report shall contain the following elements: A text defining the scope, preface, list of contents, summary, main body of thesis, conclusions with recommendations for further work, list of symbols and acronyms, references and (optional) appendices. All figures, tables and equations shall be numerated.

The report shall be submitted in two copies (one hard copy and one electronic copy)

- The hard copy shall be signed by the candidate
- The text defining the scope included

Ownership

NTNU has according to the present rules the ownership of the report. Any use of the work has to be approved by NTNU (or external partner when this applies). The department has the right to use the report as if the work was carried out by a NTNU employee, if nothing else has been agreed in advance.

Thesis supervisor:

Prof. II Kjell Larsen (Statoil/NTNU)

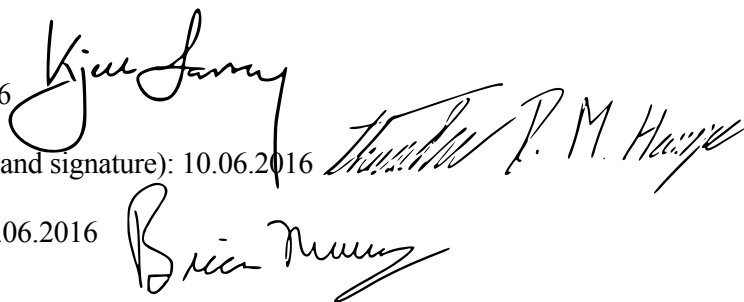
Deadline: June 10th, 2016

Trondheim, June, 2016

Kjell Larsen (date and signature) : 10.06.2016

Tharindu Dilshan Madduma Hewage (date and signature): 10.06.2016

Brian James Murray (date and signature): 10.06.2016



Preface

This master's thesis is the final part of a Master's Degree in Marine Technology with specialization in Marine Subsea Engineering at the Department of Marine Technology (IMT), Norwegian University of Science and Technology (NTNU).

The work was performed during the spring semester of 2016 at NTNU in Trondheim, Norway for IMT at NTNU and Statoil ASA. The workload corresponds to 30 ECTS.

In addition, this master's thesis builds upon the project thesis the authors produced during the fall semester of 2015 with the title "Identification of Areas of Improvement in Deepwater Installation Methods".

Trondheim, June 10, 2016

Brian James Murray

Tharindu Dilshan Madduma Hewage

Acknowledgment

The authors would like to express their sincere gratitude to their supervisor Professor II Kjell Larsen (NTNU and Statoil). His guidance throughout the spring semester of 2016 has been valuable. His knowledge of and enthusiasm for the field of marine operations have been very inspiring.

Furthermore, the authors would like to thank Timothy Edward Kendon (Statoil) for taking time out of his schedule to discuss our thesis with us. The discussions have been extremely beneficial.

The authors have had numerous discussions with Professor Trygve Kristiansen (NTNU), Professor Bjørnar Pettersen (NTNU) and Professor Marilena Greco (NTNU) which have been inspiring and insightful. They have shared their great experience and knowledge in the field of hydrodynamics. For this, the authors are truly grateful.

In addition, the authors would like to thank Associate Professor Erin Bachynski (NTNU) and PhD candidate Xiaopeng Wu (NTNU) for providing truly helpful guidance in the use of the numerical software utilized in this thesis.

B.J.M and T.D.M.H.

Summary

The final frontier of the oil and gas industry is considered by many to be deepwater fields (1500 m - 3000 m). With the recent fall in oil prices, the industry has however seen many deepwater projects postponed as a result of many operators' unwillingness to invest in capital intensive projects. Costs related to the installation of subsea hardware account for up to 30 % of the total capital invested, and significant improvements can therefore be made with respect to this aspect of deepwater developments. Statoil has a goal of being able to install subsea hardware at 3000 m at the same cost as 300 m.

The Pendulous Installation Method is a new state-of-the-art method, until now minimally investigated by the Norwegian oil and gas industry. The method involves allowing relevant subsea hardware to free-fall in a pendulous motion into position above the seabed. Statoil has recently released the Dual Cap-X concept, that likely will be an integral part of future subsea fields. The intention of this thesis is to evaluate the potential of installing the Dual Cap-X at 3000 m water depth using the Pendulous Installation Method.

Numerical simulations in SIMO and Coupled SIMO-RIFLEX were conducted to evaluate the feasibility. The Splash-Zone and Free-Fall phases of the operation were studied in detail. Sensitivity to relevant parameters that may be detrimental with respect to operability were investigated. Design operational limits were determined for relevant phases with respect to relevant acceptance criteria. Operability with respect to weather windows was evaluated based on the determined design limits, and potential improvements discussed.

The findings indicate that the operability and associated cost of the method at 3000 m water depth are comparable to that of traditional subsea installation of a subsea template at 300 m. Potential improvements with respect to operability exist, and should be pursued to optimize the method as well as subsea installation operations in general. If properly executed, it appears that the method has the potential to render deepwater subsea fields feasible.

Sammendrag

Det er forventet at et økende antall av fremtidige undervannsolje- og gassutbyggelser vil foregå på dypt vann (1500 m - 3000 m). Kostnader knyttet til installasjon av undervannsproduksjonsutstyr står for opp til 30 % av den totale kapitalen investert. Betydelige forbedringer må derfor gjøres med hensyn på dette aspektet av dypvannsutbygginger. Statoil har som mål om å muliggjøre installasjon av undervannsproduksjonsutstyr på 3000 m vanndybde like kostnadseffektivt som ved tradisjonelle installasjoner på 300 m vanndybde.

Installasjon ved bruk av pendelmetoden er et relativt nytt konsept i norsk olje- og gassindustri. Metoden innebærer at installasjonsmodulen er festet i et fibertau og får falle nedover i vannsøylen i en pendelbevegelse til den når sluttposisjonen over havbunnen. Statoil har nylig utgitt deres Dual Cap-X konsept, som trolig vil være en integrert del av fremtidige undervannsolje- og gassfelt. Hensikten med denne oppgaven er å vurdere potensialet i å installere Dual Cap-X på 3000 m vanndypde ved bruk av pendelmetoden.

Numeriske simuleringer i SIMO og Coupled SIMO-RIFLEX ble utført for å evaluere gjennomførbareheten av offshoreoperasjonen. Løfting gjennom skvalpesonen og fritt fall er fasene av operasjonen som har blitt studert i detalj. Følsomheten for relevante parametere som kan påvirke operasjonens operabilitet har også blitt undersøkt. Operasjonelle designgrenser for alle relevante faser av operasjonen har blitt utarbeidet basert på de numeriske simuleringene. Videre har operabiliteten med hensyn til vær vinduer blitt vurdert, samt potensielle tiltak for å øke operasjonens operabilitet evaluert.

Resultatene indikerer at installasjonen av Dual Cap-X ved bruk av pendelmetoden på 3000 m vanndybde kan forventes å ha tilnærmet lik operabilitet som det å installere tradisjonelle undervannsbrønrammer ved løfting i 300 m vanndybde. Likevel finnes det potensielle forbedringer for å øke operabiliteten, og disse bør gjennomføres for å optimalisere metoden samt offshoreinstallasjonsoperasjoner generelt. Pendelmetoden utviser svært godt potensial til å realisere kostnadseffektive dypvannsinstallasjoner.

Contents

Preface	i
Acknowledgment	ii
Summary	iii
Sammendrag	iv
1 Introduction	1
1.1 Background	1
1.1.1 Deepwater Installation	1
1.1.2 Statoil Cap-X Solution	3
1.2 Objectives	8
1.3 Limitations	9
1.4 Structure of the Report	9
2 Deepwater Installation Operations	11
2.1 Deepwater Installation Challenges	12
2.1.1 Resonance	13
2.1.2 Self-Weight of Lifting Cable	15
2.1.3 Position Offset	17
2.2 Pendulous Installation Method	20
2.2.1 Installation Procedure	20
2.3 Installation Payload	25
3 Theory	28
3.1 Sea Environment	28

3.1.1	Waves	29
3.1.2	Current	32
3.1.3	Wind	34
3.2	Dynamics of Marine Operations	35
3.2.1	Response Amplitude Operators	35
3.2.2	Vessel Motion	36
3.2.3	Relative Motions between Two Vessels	37
3.2.4	Pendulum Motion	40
3.2.5	Crane Tip Motion	41
3.2.6	Forces	43
3.2.7	Equation of Vertical Motion	50
3.3	Offset in Deepwater Conditions	52
3.3.1	Horizontal Offset	52
3.3.2	Vertical Displacement	54
3.4	Weather Windows	55
3.4.1	Uncertainty in Weather Forecast	56
3.4.2	Hindcast Data	57
3.5	SIMA	60
3.5.1	SIMO	61
3.5.2	Coupled SIMO-RIFLEX	64
4	Methodology	66
4.1	Acceptance Criteria	66
4.1.1	In-Air	66
4.1.2	Splash-Zone	67
4.1.3	Free-Fall Analysis	69
4.2	Numerical Analysis in SIMA	70
4.2.1	Assumptions	70
4.2.2	Environmental Modelling	70
4.2.3	The Installation Vessel	73

4.2.4	SIMO - Splash-Zone Modelling	74
4.2.5	Coupled SIMO/RIFLEX	82
4.2.6	Model Verification	87
4.3	Convergence Test of Wave Seeds for Splash-Zone Analysis	92
5	Results and Discussion	98
5.1	In-Air Phase	98
5.1.1	Pendulous Motion	100
5.1.2	Wind Sensitivity	101
5.1.3	Evaluation of Acceptance Criteria	103
5.2	Splash-Zone Phase	104
5.2.1	Added Mass Sensitivity	104
5.2.2	Depth Dependent Coefficient Sensitivity	107
5.2.3	Drag Sensitivity	115
5.2.4	Wave Heading Sensitivity	119
5.2.5	Current Sensitivity	121
5.2.6	Crane Tip Position Sensitivity	123
5.2.7	Identification of Hydrodynamic Forces	125
5.2.8	Evaluation of Acceptance Criteria	134
5.3	Free-Fall Preparation Phase	145
5.4	Pendulous Free-Fall Phase	148
5.4.1	Current Sensitivity	148
5.4.2	Drag Sensitivity	152
5.4.3	Weight Sensitivity	156
5.4.4	Evaluation of Acceptance Criteria	161
6	Relevance of Findings	164
6.1	Cost Reduction	164
6.2	Planning of Dual Cap-X Installation using PIM	165
6.2.1	Time Schedule	165
6.2.2	Accounting for Uncertainty in Weather Forecast	167

6.2.3	Accounting for Uncertainty in Planned Operation Time	168
6.2.4	Required Weather Window	168
6.2.5	Evaluation of Operability based on Hindcast Data	169
6.3	Improving Operability	170
6.3.1	The Effect of the Reference Time and Operational Criterion	171
6.3.2	Challenging the Safe Condition Criteria	176
6.3.3	Challenging the Contingency Time	178
6.3.4	Challenging the Alfa-Factor	178
6.3.5	Challenging the Design Criteria	179
6.3.6	Implementing Improvements	179
6.4	Comparing Traditional 300 m Installation and 3000 m PIM	182
7	Summary	186
7.1	Summary and Conclusions	186
7.2	Recommendations for Further Work	189
A	Acronyms	191
B	Crane Capacity	193
C	Supporting Free-Fall Results	195
D	Design Criteria	200
D.1	Maximum Lifting Wire Tension	200
D.2	Minimum Lifting Wire Tension	202
D.3	Minimum Sling Tension	203
E	Hydrodynamic Coefficients	205
	Bibliography	208

List of Figures

1.1	Installation costs	2
1.2	Cap-X subsea field layout.	3
1.3	Statoil's Dual Cap-X concept	4
1.4	Conceptual visualization of the installation of Single Cap-X structures illustrating deck space efficiency	5
2.1	Lifting phases	12
2.2	DAF in heave for given values of the damping ratio	14
2.3	Resonance period as function of depth.	15
2.4	Wet lowering capacity of steel wire (ø4")	16
2.5	Degradation of lift capability with depth	16
2.6	Measured current speed (black curve) and direction (red crosses) at 47 m depth at a production block off the coast of Tanzania over a period of 100 days	17
2.7	Horizontal offset.	18
2.8	Horizontal (F_x) and vertical (F_y) forces from ship correction.	19
2.9	Subsea structure displacement.	19
2.10	Pendulous installation connections.	21
2.11	Hydraulic release shackle	22
2.12	Free-fall preparation phase.	23
2.13	Pendulous Free-Fall.	24
2.14	The protection structure of a Single Cap-X concept with some possible outboard connections	26
2.15	Protection cap in open position	27

3.1	Linear and non-linear current profile stretching up to the wave surface	34
3.2	Overview of vessel motions.	37
3.3	Crane lift-off from a separate vessel. The origin of the two coordinate systems are assumed to coincide with the vessels' COGs.	38
3.4	Relative importance of different types of forces on marine structures	43
3.5	Horizontal offset with decomposed forces.	52
3.6	Operation periods.	57
3.7	Storms and calms.	58
4.1	1, 10, 100 and 10000-year extreme contour lines in the $H_s - T_p$ plane	71
4.2	The Scandi Acergy. Courtesy of DOE	74
4.3	Visualization of the SIMO payload and lifting equipment model.	75
4.4	Depth dependency of heave added mass for vertical suction cans	77
4.5	Visualization of the SIMO-RIFLEX payload model. The figure shows the configuration at the start of the drop.	83
4.6	Visualization of the SIMO-RIFLEX vessel model connected to the fiber rope slender system.	85
4.7	Definition of coordinate system.	86
4.8	Payload trajectory.	86
4.9	Time series of the lifting line force in splash-zone for no waves.	88
4.10	Payload trajectory in Y-Z plane.	90
4.11	Top tension, vertical payload velocity and acceleration.	91
4.12	Convergence test of Gumbel parameters for maximum crane wire tension in sea state $H_s=4m$, $T_p=8s$, with 95% confidence interval.	93
4.13	Fitted Gumbel distribution on observed maximum crane wire tension (35 wave seeds) in sea state $H_s=4m$, $T_p=8s$ with lower and upper 95% confidence bounds (vertical lines indicate the 90 th percentiles).	95
4.14	Fitted Gumbel distribution on observed maximum crane wire tension for runs with different numbers of wave seeds. Vertical lines indicate the corresponding 90 th percentiles for each distribution.	96

4.15 Fitted Gumbel distribution on observed minimum crane wire tension (35 wave seeds) in sea state $H_s=4\text{m}$, $T_p=8\text{s}$ with lower and upper 95% confidence bounds (vertical lines indicate the 10 th percentiles as discussed in Section 4.1.2).	97
5.1 Payload motion in head sea conditions.	99
5.2 Payload motion in beam sea conditions.	100
5.3 Resonance period for horizontal pendulum motion.	101
5.4 Wind sensitivity.	102
5.5 Wind force on Dual Cap-X.	103
5.6 Added mass dependency for lifting wire tension.	105
5.7 Relationship between maximum DAF and added mass ratios.	106
5.8 Regimes for relative added mass coefficients.	109
5.9 Change of added mass of suction anchor.	109
5.10 DAF of lifting wire tension against depth of suction anchors.	110
5.11 DAF of lifting wire tension against depth of top of suction anchors.	111
5.12 DLF/DAF for four different impulse forces plotted against the duration of the impulse.	112
5.13 Added mass gradient, $\frac{dA_{33}}{dh}$ plotted against time.	113
5.14 Added mass gradient, $\frac{dA_{33}}{dh}$ plotted against time (scaled).	113
5.15 Relationship between forces and gradient regimes.	115
5.16 Quadratic drag coefficient dependency for lifting wire tension.	117
5.17 Percent change in lifting wire tension for drag ratios.	118
5.18 Vertical resonance periods for increasing depth of Dual Cap-X.	119
5.19 Maximum and minimum DAFs for lifting wire tension from 50 wave seeds for varying wave heading for $H_s=4\text{ m}$, $T_p=8\text{ s}$. The maximum and minimum lifting line tension criteria are included as an upper and a lower horizontal line, respectively.	120
5.20 Current sensitivity.	122
5.21 Lifting wire tension for $H_s=4$, $T_p=8$, wave seed = 1.	124
5.22 90 % fitted EVD	124

5.23 Comparison of the lifting line force for sea state $H_s=4m, T_p=8s$. Depth given from mean surface level. Wave elevation is also included (green line).	126
5.24 Vertical Hydrodynamic Forces and Buoyancy Force on Payload and Wave Elevation - $H_s = 4 m, T_p = 8 s$, wave seed = 9. Depth given from mean surface level.	129
5.25 Vertical hydrodynamic forces and buoyancy force on payload and wave elevation - $H_s = 4 m, T_p = 8 s$, wave seed = 10. Depth given from mean surface level.	130
5.26 Results for a sea state with $H_s = 2m$ and $T_p = 11s$ and wave seed = 9.	133
5.27 Maximum lifting line tension.	136
5.28 Minimum lifting line tension.	137
5.29 Minimum sling tension for a hoisting speed of 0.1 m/s.	138
5.30 Minimum sling tension for a hoisting speed of 0.25 m/s.	138
5.31 Minimum sling tension for a hoisting speed of 0.5 m/s.	139
5.32 Legend for design criterion tables.	139
5.33 Design criteria for a hoisting speed of 0.1 m/s.	140
5.34 Design criteria for a hoisting speed of 0.25 m/s.	140
5.35 Design criteria for a hoisting speed of 0.5 m/s.	140
5.36 Lifting wire tension for hoisting speed 0.25 m/s, $H_s = 4, T_p = 10$, wave seed = 6	142
5.37 Vessel response amplitude operators.	144
5.38 Maximum tension at 50 m depth. The orange line indicates a crane SWL = 1 and the red line SWL = 1.3.	146
5.39 Minimum tension at 50 m depth. The red line indicates the minimum allowable lifting line tension.	147
5.40 Comparison of payload trajectory. Position given in meters in the global coordinate system.	150
5.41 Comparison of top tension.	151
5.42 Comparison of payload velocities.	152
5.43 Comparison of payload trajectory. Position given in meters in the global coordinate system.	154
5.44 Comparison of payload velocities.	155
5.45 Comparison of top tension.	156

5.46 Payload weight sensitivity - Position of payload (given in meters in the global coordinate system).	158
5.47 Payload weight sensitivity - velocities of payload.	159
6.1 Operation window.	171
6.2 Probability of working plotted against T_R for various OP_{WF} given as values of H_s	172
6.3 Probability of working plotted against T_R for various OP_{WF} given as values of H_s	173
6.4 Probability of working plotted against OP_{WF} given as values of H_s for various values of T_R	174
6.5 Probability of working plotted against OP_{WF} given as values of H_s for various values of T_R	175
6.6 Safe state partitioning of operation.	177
B.1 Capacity of Lifting Crane on Skandi Acergy provided by National Oilwell Varco	194
C.1 Payload trajectory.	196
C.2 Top tension.	197
C.3 Payload velocities.	198
C.4 Payload accelerations.	199
D.1 Legend.	200
D.2 Design criteria set by crane capacity for hoisting speed of 0.1 m/s.	200
D.3 Design criteria set by crane capacity for hoisting speed of 0.25 m/s.	201
D.4 Design criteria set by crane capacity for hoisting speed of 0.5 m/s.	201
D.5 Legend.	202
D.6 Design criterias for hoisting speed of 0.1 m/s.	202
D.7 Design criteria for hoisting speed of 0.25 m/s.	202
D.8 Design criteria for hoisting speed of 0.5 m/s.	202
D.9 Legend.	203
D.10 Design criteria for hoisting speed of 0.1 m/s.	203
D.11 Design criteria for hoisting speed of 0.25 m/s.	203
D.12 Design criteria for hoisting speed of 0.5 m/s.	204

E.1	Frame hydrodynamic coefficients.	206
E.2	Fixed body hydrodynamic coefficients.	207
E.3	Quadratic wind coefficients.	207

List of Tables

2.1	Weight and dimensions of the Dual Cap-X structure.	27
3.1	Body types.	61
4.1	Calculated acceptance criteria values for splash-zone analysis of the Dual Cap-X. .	69
4.2	Current data used in model (Statoil, 2010).	73
4.3	Vessel dimensions.	73
4.4	Mass properties of the Dual Cap-X.	75
4.5	Depth dependent hydrodynamic coefficients.	78
4.6	Modelled hydrodynamic properties of the suction can	79
4.7	Quadratic wind coefficients.	80
4.8	HMPE cross sectional data.	83
4.9	Deployment line sectional data.	84
5.1	Added mass ratios.	104
5.2	Quadratic drag coefficient ratios.	116
5.3	Wave headings.	119
5.4	Current velocity regimes.	122
5.5	Crane tip position in η_1 - direction.	123
5.6	Hoisting speeds.	134
5.7	Simulation variables.	135
5.8	Simulation Variables.	146
5.9	Current conditions.	148
5.10	Free-Fall durations for different payload weights (without current).	160

6.1	Time schedule for base case.	166
6.2	Operational limits.	167
6.3	Contingency times.	168
6.4	Probability of working (base case).	170
6.5	Improved probability of working.	180
6.6	Improved probability for independent operations.	181
6.7	Operability of 300 m traditional subsea installation operation for Heidrun data. . .	184
6.8	Comparison of improved PIM in 3000 m with 300 m traditional installation for Heidrun data.	185

Nomenclature

α	Alpha factor
η_1	Surge
η_2	Sway
η_3	Heave
η_5	Pitch
η_6	Yaw
η_r	Roll
η_{ct}	Crane tip vertical motion
ϕ	Velocity potential
ρ	Density of seawater
τ_c	Duration of calm
ζ	Wave elevation
ζ_a	Wave amplitude
A_w	Water plane area
A_{33}	Added mass in heave
B_{33}^1	Linear damping coefficient

B_{33}^2	Quadratic damping coefficient
C_A	Added mass coefficient
C_D	Drag coefficient
C_s	Slamming coefficient
F_B	Buoyancy force
F_c	Steady force due to current
F_D	Viscous drag force
F_I	Inertia force
F_s	Slamming force
F_W	Wave excitation force
F_{line}	Force in lifting wire
g	Gravitational acceleration
H_s	Significant wave height
I_s	Impulse of slamming force
K	Hoisting line stiffness
OP_{LIM}	Design criterion
OP_{WF}	Operational criterion
T_0	Resonance period
T_c	Contingency time
T_p	Peak period
T_R	Reference time

T_w Time waiting

T_{OP} Accumulated operational time

T_{POP} Planned operation time

Chapter 1

Introduction

1.1 Background

1.1.1 Deepwater Installation

The final frontier of the oil and gas industry is considered by many to be deepwater fields (1500 m - 3000 m). With the recent fall in oil prices, the industry has however seen many deepwater projects postponed as a result of many operators' unwillingness to invest in capital intensive projects. It has however been shown that with advances in technology, previously uneconomical projects can be rendered viable. The industry is therefore working towards identifying cost-drivers and developing solutions such that deepwater wells can be exploited. Figure 1.1 illustrates the various costs in a standard offshore development project. Installation costs account for up to 30 %, and significant improvements can therefore be made with respect to this aspect of deepwater developments. Statoil has a goal of being able to install subsea hardware at 3000 m at the same cost as for 300 m.

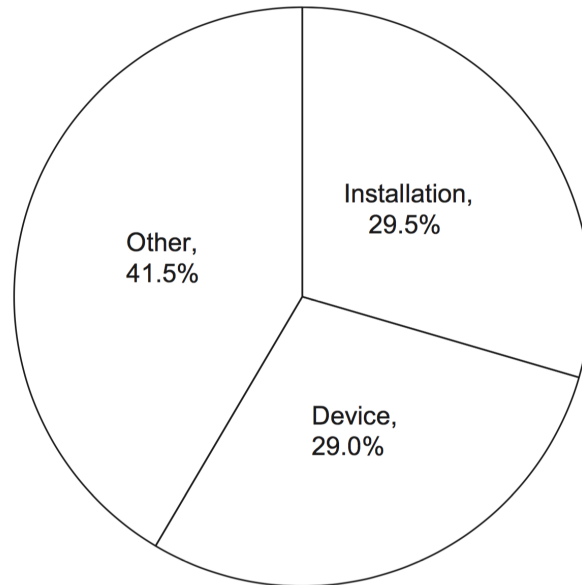


Figure 1.1: Installation costs (Walker et al., 2013).

Deepwater installation operations are associated with a multitude of challenges. As a result, traditional installation methods are often economically infeasible. Installation costs are also often driven by weather sensitivity. Walker et al. (2013) argues that there are three means available for reducing installation costs:

- A reduction in downtime by using vessels capable of installing in more severe weather conditions
- Developing lower cost installation vessels such that downtime has less of a cost implication
- Deriving detailed information of suitable installation weather windows that will be available for a specific site

Pendulous Installation Method

The Pendulous Installation Method is an innovative state-of-the-art deepwater installation method, originally developed by Petrobras in 2003. The motivation for the development of this method

was to avoid many of the challenges associated with deepwater conditions. Smaller vessels, with lower day rates could be utilized in conjunction with fiber rope technology to allow subsea hardware to "free-fall" into position above the seabed. This method is cost-effective, and may have significant potential with respect to realizing Statoil's goal of efficiently installing subsea hardware at 3000 m depth.

1.1.2 Statoil Cap-X Solution

Statoil ASA has recently released their newest concept for subsea developments, the Cap-X solution. The Cap-X is a subsea structure upon which a large variety of subsea hardware can be installed. This can range from standard X-mas trees to manifolds and processing equipment. The concept allows for better market utilization, introduces improved standardization as well as increased transportation efficiency.

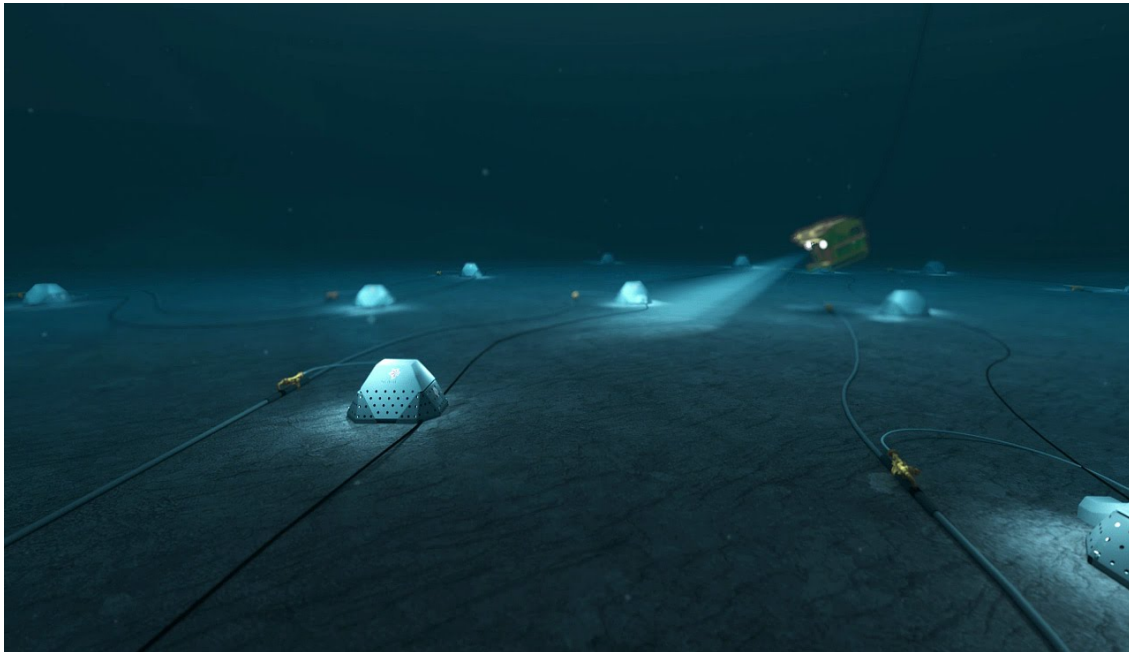


Figure 1.2: Cap-X subsea field layout.

Dual Cap-X

Statoil has developed several Cap-X concepts. One of these concepts is called the Dual Cap-X (see Figure 1.3). The purpose of the concept is to house subsea production hardware such as vertical and horizontal X-mas trees, associated valves, and direct tie-in connections for flowlines. The idea is to allow suppliers to bid for the tendering of different parts of the hardware components housed in the Dual Cap-X. The break-up of deliverables will cut the associated CAPEX through improved market utilisation. At the same time, the Dual Cap-X will also help to standardize the subsea production equipment and introduce greater flexibility to changes.

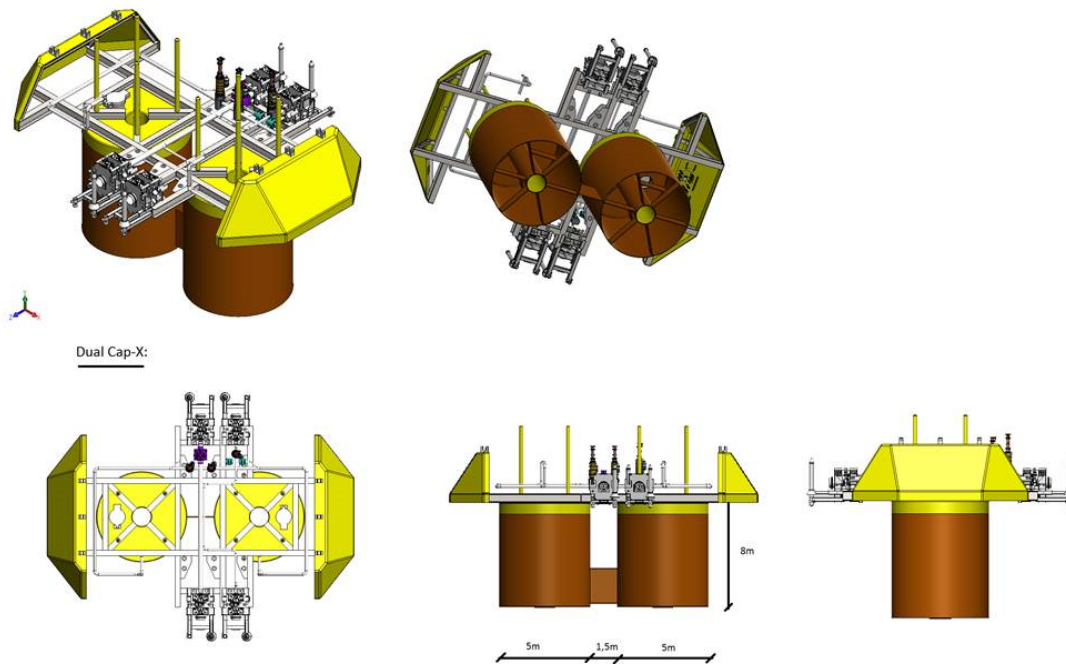


Figure 1.3: Statoil's Dual Cap-X concept (Ellingsen, 2015).

Moreover, installation efficiency is improved since the protection structure can be installed with subsea production equipment in place. As such, the number of surface to seabed trips is reduced. There will also be less seafastening and deck handling required for the Dual Cap-X concept compared to traditional subsea templates with separately installed X-mas trees. The total weight of the structure is also expected to be less than traditional structures and hardware. Due to the compact form of the structure, the crane boom out is also reduced, increasing the available crane capacity. This also means a significant reduction in required deck space (see Figure

1.4).

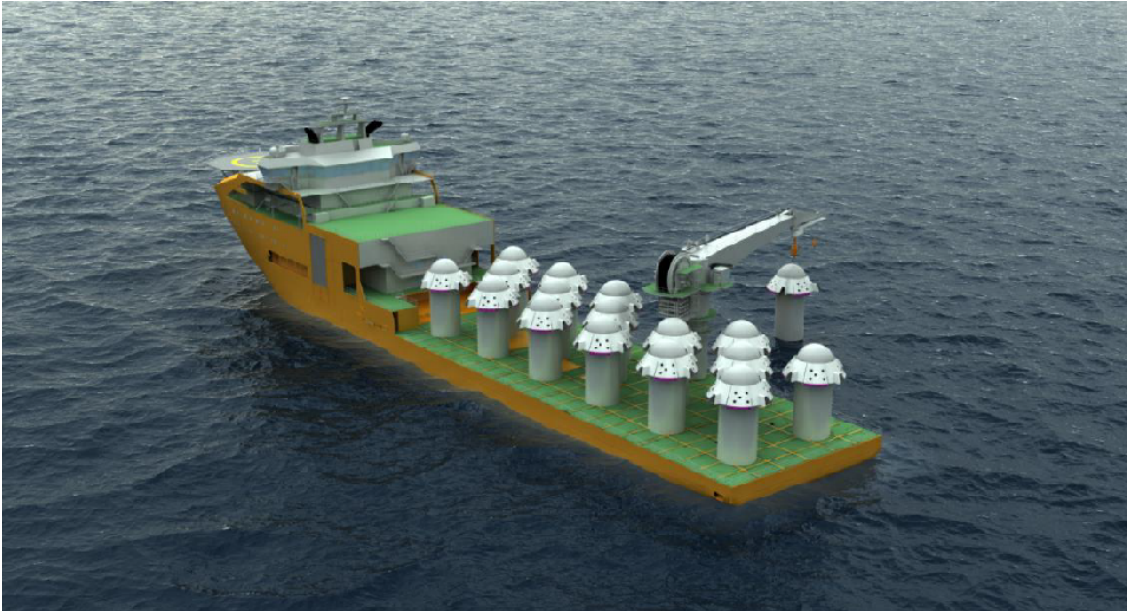


Figure 1.4: Conceptual visualization of the installation of Single Cap-X structures illustrating deck space efficiency (Ellingsen, 2015).

Problem Formulation

The Dual Cap-X will most likely be a key element in future subsea fields. It is therefore of interest to investigate the feasibility of installing such hardware in an efficient and cost-effective manner at 3000 m water depth. The Pendulous Installation Method (PIM) may provide the solution to doing so. The Dual Cap-X concept is still in the design phase, and as such no installation operations have yet been conducted. Due to the complexity of the structure, effectively estimating design limits is difficult. Installation through the splash-zone is often a limiting phase in an installation operation, and the behaviour of the structure through the wave zone must be understood for the integrity of an installation operation to be maintained. The PIM has not yet been utilized on the Norwegian Continental Shelf or by Norwegian companies for installation purposes. As such, there is limited knowledge of the method both with respect to payload behaviour in a state of free-fall, in addition to design limits related to top-tension of the deployment line and required operational time.

Literature Survey

The installation of the Dual Cap-X using PIM incorporates a conventional splash-zone lifting operation with an unconventional free-fall lowering operation. Extensive work has been conducted with respect to splash-zone installation of suction cans, albeit not dual suction cans with a proximity as close as those included in the Dual Cap-X design. Nonetheless, conclusions made based on work for single suction cans can be considered applicable. Work has also been conducted on the PIM free-fall phase, but to a much more limited degree. A sample of the work conducted related to both phases will be presented in this section. A more comprehensive selection of relevant works is presented throughout the remainder of the thesis.

DNV GL (2011b) has published a recommended practice for the modelling and analysis in the planning phase of a marine operation. They have suggested a simplified method for the calculation of the hydrodynamic forces when lowering a payload through the splash zone. The resulting crane wire response obtained using the Simplified Method is generally seen as conservative due to the nature of the simplifying assumptions made. As such, time domain numerical analysis as performed in this thesis may constitute a more accurate method of determining the dynamics in a offshore operation.

Gordon (2013) have performed a direct time domain splash zone analysis in SIMO of a single suction can lowered with its longitudinal axis parallel to the water surface. Sensitivity with respect to the winch wire load has been conducted for various sea states. The importance of the various forces through the splash zone for this particular case have been evaluated, and sensitivity with respect to the characteristic size of the suction cans with respect to the various forces conducted.

Jacobsen and Næss (2014) outlines some lessons learned from traditional subsea installation operations by lifting. Of particular relevance is the investigation of the overboarding and splash-zone lowering of a 400 t template in the Norwegian Sea. Jacobsen and Næss (2014) highlights the importance of controlling the in-air behaviour of the payload. Also, the crane tip motions are important for the dynamic effects in the Splash-Zone phase.

Extensive work has been conducted into determining hydrodynamic coefficients relevant for the modelling of subsea installation operations. The Dual Cap-X is comprised of cylindrical suction anchors and an upper framework section. Søfteland et al. (2014) discusses the selection of hydrodynamic coefficients for framework structures when entering the oscillating sea surface. Øritsland and Lehn (1987), Øritsland (1989) and Sarpkaya (2010) all have done extensive studies on hydrodynamic coefficients for various geometries. Fernandes and Mineiro (2007) also outlines and evaluates methods for relevant coefficients in subsea installation.

Several studies (e.g Plummer et al. (2009) and Ireland (2007)) show that the proximity to the free surface will affect the heave added mass of a body lowered through the splash-zone. Through model testing, Næss et al. (2014) have developed a relationship for the relative vertical heave added mass of a vertical suction can with respect to the distance from the water surface. Based on this relationship, Næss et al. (2014) study the slamming force during the splash-zone lowering of a Integrated Template Structure.

Sarkar and Gudmestad (2010) discusses the use of DNV-RP-H103 with emphasis on the hydrodynamic coefficients and analysis methodology for splash-zone installation operations. Drag coefficients in unsteady flow and the importance of not overestimating drag coefficients with respect to inertia dominated structures is discussed. Added mass coefficients and the effect of perforation and proximity to the free surface are also evaluated. The effect of winch speed and stiffness in the model are evaluated as well.

When lowering the payload through the sea surface and down through the water column, there is a possibility of the occurrence of snap loads due to vessel motion and wave conditions. This is of major concern since the snap load that arises when the cable wire goes from slack to taut can be several times larger than the dynamic tension experienced otherwise. When assessing the deployment of the Dual Cap-X, the occurrence of slack should be investigated. Thurston et al. (2011) presents an efficient method of calculating the probability of cable wire slacking during the lowering of a payload through the splash zone using conservation of momentum.

Limited literature is available on the Pendulous Installation Method. Wang et al. (2013) discuss the installation of a 195 t manifold in 1500 m water depth using the mentioned method. A de-

tailed outline of the necessary procedure is presented. Moreover, Wang et al. (2013) performs a brief investigation into the tension in the deployment line at certain water depths during the free-fall through simulations in SIMO. While Cao et al. (2012) study the behavioural effects of the position of the center of gravity of a 4-slot manifold during the Free-Fall phase. Fernandes and Rodrigues Neves (2007) investigates the coherence between numerical modelling and model testing of the Pendulous Installation Method. The results show that, depending on payload geometry, phenomenas such as fluttering may be of relevance.

Walker et al. (2013) highlights the importance of increasing the operability with respect to weather windows for offshore operations for minimizing cost and better resource usage. With respect to operability studies, extensive research is available on weather window analysis. Chen and Mukerji (2008) and Foo et al. (2014) give insight into important parameters for consideration in weather window analyses.

1.2 Objectives

The overall goal of this thesis is to examine the feasibility of installing the Dual Cap-X in 3000 m water depth using the Pendulous Installation Method. Numerical simulations should be utilized to evaluate design limits relevant for the installation operation. The results should be used to highlight potential improved operability with respect to weather windows. The objectives are:

1. Describe relevant theory for the subsea installation of the Dual Cap-X
2. Establish numerical models in SIMO and Coupled SIMO-RIFLEX of an installation operation of the Dual Cap-X using the Pendulous Installation Method
3. Investigate and evaluate parameters that may be detrimental to the feasibility of the installation operation
4. Establish relevant design operational limits
5. Evaluate the operability of the method with respect to weather windows

6. Investigate potential improvements with respect to the operability of the operation

1.3 Limitations

The evaluation of the installation of the Dual Cap-X using the Pendulous Installation Method focuses solely on the installation phases from surface to seabed. This entails that loading and transportation to site, as well as post installation operations are not considered. The scope is thus limited to lowering of the Dual Cap-X through the splash-zone until in position over the target zone on the seabed. As such, lift-off from deck, positioning and touch-down on seabed phases are not investigated in depth.

The Dual Cap-X is installed without hatches and any additional subsea hardware that may be relevant for integrated installation with the module (e.g X-mas trees). Also, only one type of installation vessel will be considered.

Moreover, the analysis of the Free-Fall phase focus on the global response of the system. As such, detailed local response of the payload during the free-fall is not considered. This limitation is reflected in the simplifications made when modelling in Coupled SIMO-RIFLEX.

Weather window evaluations are based on hindcast data. The investigations are intended solely to gain insight into operational performance of the installation method.

1.4 Structure of the Report

The rest of the thesis is organized as follows. Chapter 2 describes the technical challenges associated with deepwater installation operations. It also describes the procedure involved in the Pendulous Installation Method and introduces the Dual Cap-X solution as the relevant payload for investigation.

Chapter 3 outlines relevant theory related to subsea installation options and weather windows.

Additionally, relevant theory for SIMO and Coupled SIMO-RIFLEX are introduced.

Chapter 4 describes the methodology of the numerical simulations conducted in this thesis. Acceptance criteria relevant to the installation operation is outlined. Relevant modelling to simulate both the Splash-Zone phase and Free-Fall phase of the operation is outlined. Additionally, convergence with respect to wave realizations is tested.

In Chapter 5, the results from the numerical simulation are presented and discussed.

Chapter 6 investigates the relevance of the findings from Chapter 5 with respect to operability.

In Chapter 7, summary and conclusions are given. Recommendations for further work are also presented.

Chapter 2

Deepwater Installation Operations

When constructing a subsea production system, the first stage is the installation of the necessary infrastructure. After being transported out to site, subsea hardware must be lowered into position on the seabed. This is conventionally achieved through a lifting and lowering operation.

Traditional lifting and lowering operations can be considered as five different phases (see Figure 2.1):

1. Lift-Off from deck
2. In-Air
3. Splash-Zone
4. Submerged
5. Landing on seabed

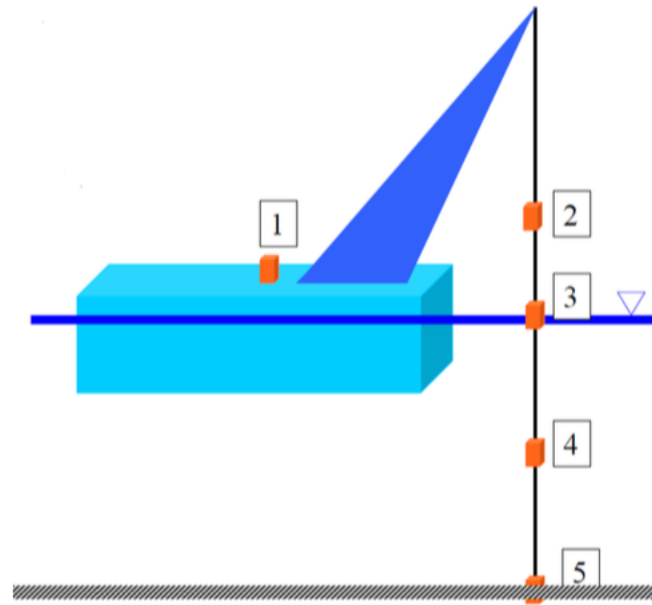


Figure 2.1: Lifting phases (Larsen, 2015).

This is considered a marine operation. DNV GL (2011a) specifies that:

"A marine operation shall be designed to bring an object from one defined safe condition to another", where a "Safe Condition" is defined as a "condition where the object is considered exposed to normal risk (i.e. similar risk as expected during in-place condition) for damage or loss".

Generally, the most effective method to conduct this operation is via the use of a steel lifting wire and guidelines, such that that the hardware is safely and effectively lowered into position. This method is however not as effective in deepwater conditions. This is due to a variety of challenges not as prevalent in shallow water conditions. These challenges limit the feasibility of an installation operation, and alternative methods must be evaluated.

2.1 Deepwater Installation Challenges

Dynamics of marine systems will be elaborated in depth in Section 3.2.7. This section will however introduce certain elements to underline deepwater installation challenges.

2.1.1 Resonance

When lowering a subsea structure into position, it will be subjected to excitation loads due to crane tip motion from the vessel as well as wave induced forces. The response of the payload and lifting system to these excitation loads will determine the dynamic loading of the system. If the dynamic loading exceeds given operational criteria, the installation operation will not be feasible. In lifting operations, the dynamic loading of the lifting wire and crane tip are of interest. Dynamic forces are often expressed using a dynamic amplification factor or DAF. The DAF is defined as

$$DAF = \frac{F_{dynamic}}{F_{static}}$$

A DAF of two will as such be twice the load of the static load due to the weight of the payload and lifting system. It has been shown that if the excitation loads act at frequencies near the natural frequency of the system, the DAF will increase exponentially. This is shown in Figure 2.2, where the frequency ratio $\frac{\omega}{\omega_0}$ is the ratio of the frequency of the excitation over the natural frequency of the lifting system. A value of one corresponds to the natural frequency, also known as the resonance frequency. The degree of damping shown as a ratio against the critical damping value in Figure 2.2 will reduce the effect of resonance to a certain degree. Nonetheless, regions of resonance should be avoided in order to maintain the integrity of the operation.

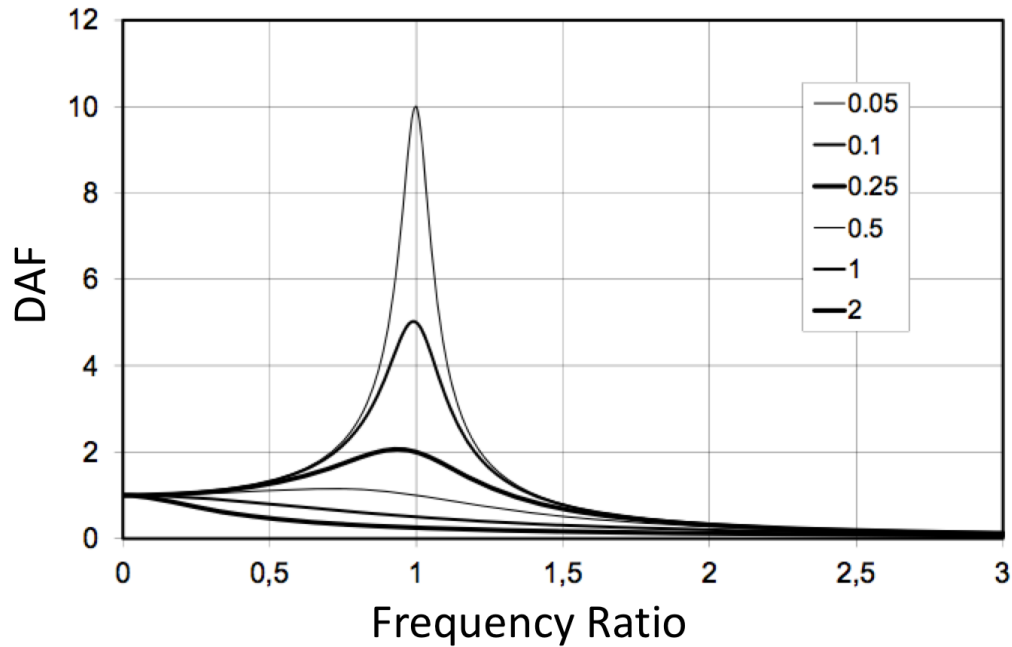


Figure 2.2: DAF in heave for given values of the damping ratio (Larsen, 2012).

The resonance period of a system depends on its stiffness and mass. According to DNV GL (2011b) it is defined for submerged payloads in deepwater operations as:

$$T_0 = 2\pi \sqrt{\frac{M + A_{33} + \frac{1}{3}mL}{K}} \quad (2.1)$$

Where M is the mass of the payload, A_{33} the added mass in heave, m the mass of the cable per unit length, L the length of the cable and K the stiffness of the system. The stiffness is comprised of the crane, wire and sling stiffness and defined as $\frac{1}{K} = \frac{1}{K_{wire}} + \frac{1}{K_{slings}} + \frac{1}{K_{crane}}$. The wire stiffness is given as $\frac{EA}{L}$ where E is the modulus of elasticity and A the cross-sectional area. As the payload is submerged, the length of the wire increases, and the resonance period becomes a function of the length of the wire, simplified as:

$$T_0 = 2\pi \sqrt{\frac{L(M + A_{33} + \frac{1}{3}mL)}{EA}}$$

It is clear that an increase in the length of the wire will result in an increase in the resonance period. This becomes a significant challenge in deepwater operations, as the length will range from 0 m up to 3000 m. Standing et al. (2002) argues that there almost always will be a depth in deepwater lifting operations at which resonance will be excited. Figure 2.3 illustrates the resonance period as a function of depth for an arbitrary system.

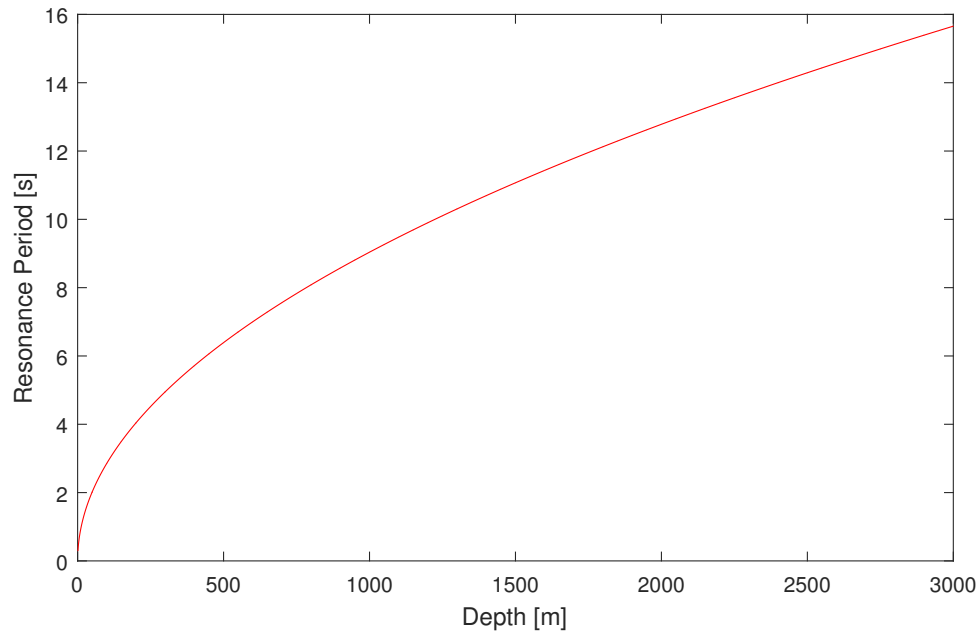


Figure 2.3: Resonance period as function of depth.

In traditional lifting operations, an active heave compensation system can be utilized when crossing zones of resonance. This is however extremely time consuming.

2.1.2 Self-Weight of Lifting Cable

Standard steel wire rope has traditionally been the preferred type of lifting cable for subsea installation in shallow water. However, the use of such cables in deepwater installation operations constitutes a serious challenge. The steel wire rope is a limiting parameter in deepwater due to the self-weight of the cable. As more cable is paid out in a lifting operation, the effective deployment capacity decreases due to the linearly increasing self-weight. Thus, a larger part of

the lifting capacity is used to support the lift cable itself instead of the payload. Ultimately, this means that the maximum design load the lifting system can handle reduces substantially as the operating depth increases. Most steel wire rope lifting systems will have lost around 95 % of the lifting capacity at water depths of 3000 m (Frazer et al., 2005). As seen in figures 2.4 and 2.5, the capacity decreases significantly with depth.

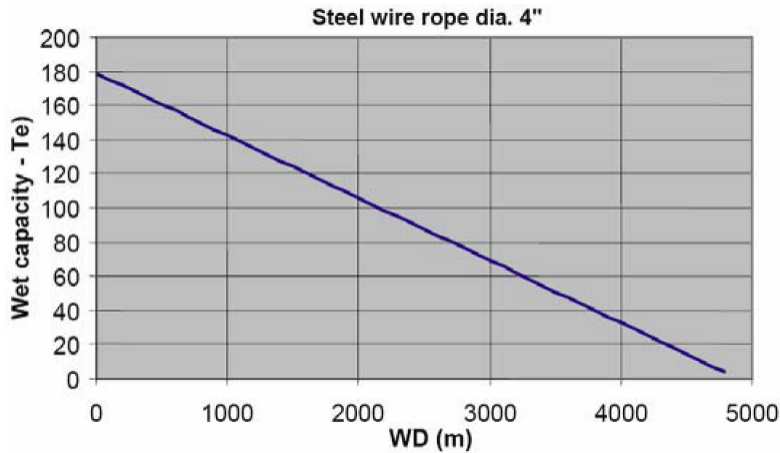


Figure 2.4: Wet lowering capacity of steel wire (ø4") (Wang et al., 2012).

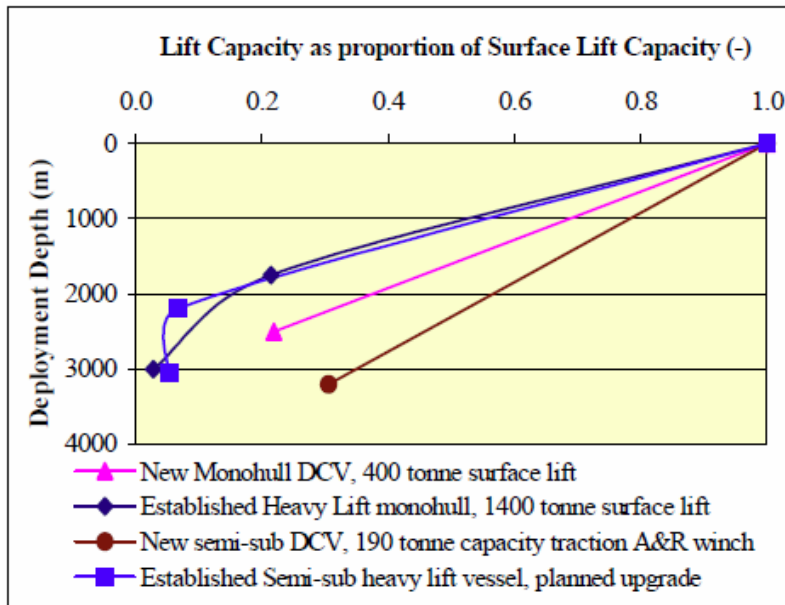


Figure 2.5: Degradation of lift capability with depth (Standing et al., 2002).

2.1.3 Position Offset

Deepwater installation operations are sensitive to ocean currents that vary over the water column, and depending on the drag coefficient, can have significant implications for the positioning of the structure. Many potential deepwater locations are in areas of relatively strong and complex currents (Standing et al., 2002). In the Gulf of Mexico, loop currents due to eddy separation from the Gulf Stream may cause current velocities up to 2 m/s at the free surface that slowly diminish down along the water column (Farrant and Javed, 2001). Figure 2.6 shows current velocities and directions at a production block off the coast of Tanzania. It has been included to illustrate how a ocean current can vary in both velocity and direction at a fixed depth.

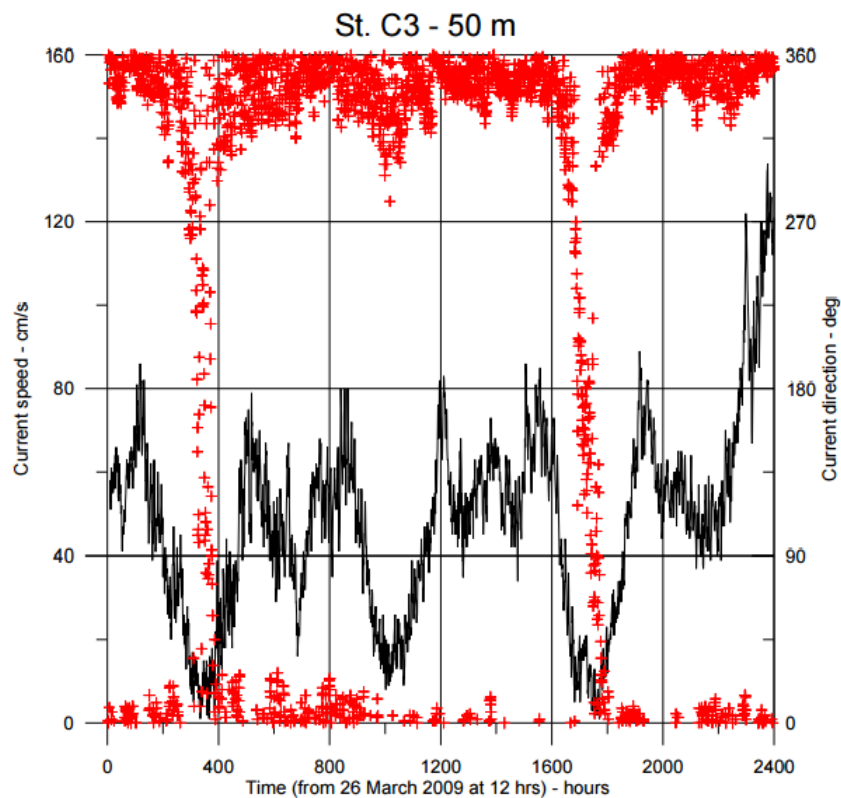


Figure 2.6: Measured current speed (black curve) and direction (red crosses) at 47 m depth at a production block off the coast of Tanzania over a period of 100 days (Statoil, 2010).

These currents can result in significant horizontal offsets of the payload due to the forces acting both on the payload itself and the lifting wire. The effect of ocean currents is illustrated in Figure

2.7, where the current is denoted U .

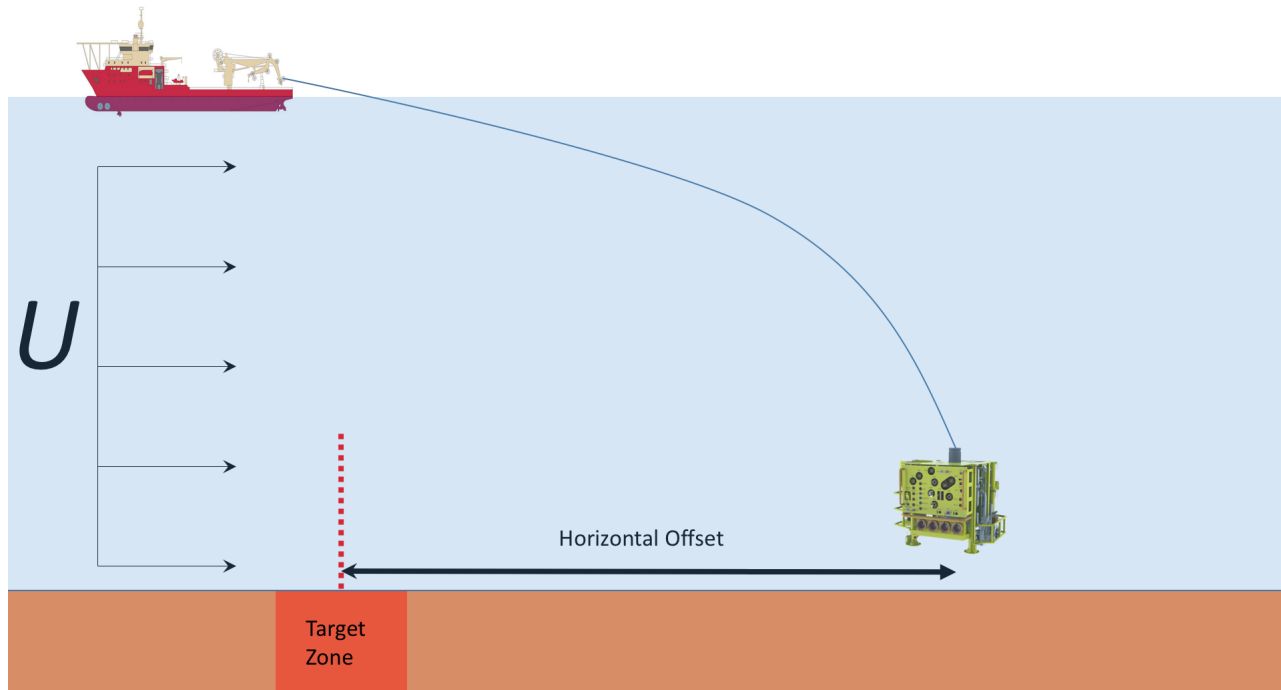


Figure 2.7: Horizontal offset.

Large offsets are commonly remedied by moving the surface vessel, and via the installation cable, the subsea structure. The response time is relatively fast, and the method fairly effective. With a cable length of up to 3000 m in deepwater operations however, this method will not be viable. As can be seen in Figure 2.8, the force acting on the subsea hardware will result in both a horizontal and vertical component. This results in the structure being lifted both vertically and horizontally. The response time will therefore be extremely slow. As you move your vessel forward, the structure will experience a displacement both vertically and horizontally until the vessel has stopped. This process is time consuming, as the length of the cable will result in a low response time. Once the vessel has stopped, the structure will again begin to sink. This process is illustrated in Figure 2.9. Many ship corrections may be necessary to achieve the required accuracy. This is extremely time consuming, and as such economically infeasible.

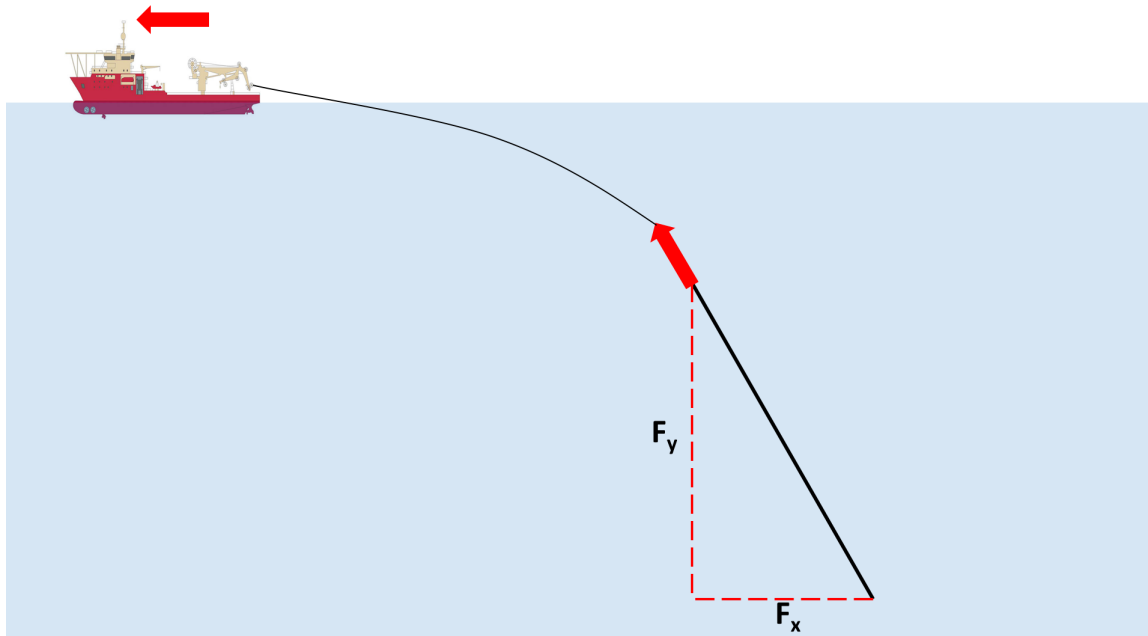


Figure 2.8: Horizontal (F_x) and vertical (F_y) forces from ship correction.

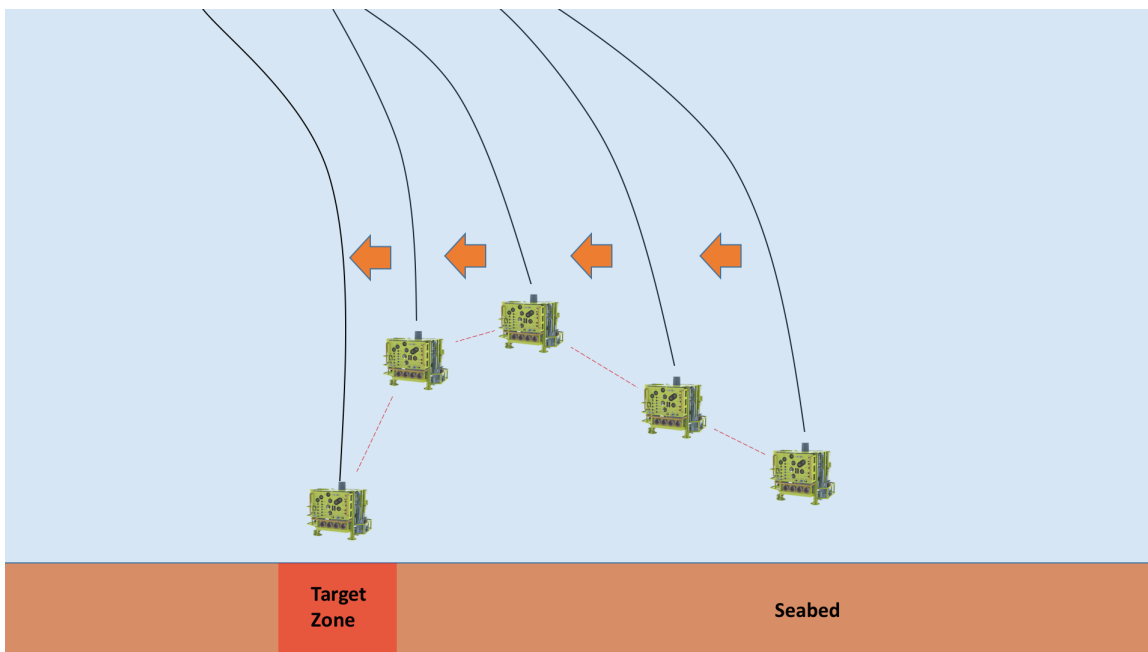


Figure 2.9: Subsea structure displacement.

With an increase in depth, the axial elongation of the lifting wire will result in a vertical offset that will need to be calculated for accurate positioning. As such, deepwater positioning entails more complex positioning considerations than shallow water. The required time dedicated to

accurate positioning can be detrimental to the feasibility of the installation operation.

2.2 Pendulous Installation Method

The Pendulous Installation Method (PIM) is an alternative installation method that attempts to ameliorate many of the challenges associated with deepwater installation operations. The method requires two small installation vessels to launch a subsea module. This reduces costs, as large installation vessels with high day rates are not required. The method in essence involves one vessel launching a subsea module through the splash-zone via traditional lifting methods involving steel wire. An additional vessel will be connected to the module with a synthetic fiber rope such as polyester or High-Modulus Polyethylene (HMPE). This vessel will be positioned at a distance from the first vessel corresponding to the approximate desired depth of the module. The module will then "free-fall" to its desired position above the seabed. Utilizing a deployment line with fixed length, issues related to resonance and dynamic loading during the installation procedure are avoided. Additionally, the use of a synthetic fiber rope with neutral weight in water avoids challenges related to steel wire weight at great depths. The following section will describe in depth the procedure involved in the method.

2.2.1 Installation Procedure

Phase 1 - Splash-Zone Lowering

The first phase of the PIM procedure is the lowering of the relevant structure through the splash-zone. This is done by utilizing a vessel with a crane of sufficient capacity. This vessel should have DP 2 capabilities to ensure the positioning of the vessel (Wang et al., 2013). This vessel will be referred to as Vessel A. The second vessel utilized will be referred to as Vessel B. See Figure 2.12.

Four slings are used to connect the Dual Cap-X to a triplate lifting bracket via shackles of suf-

ficient capacity. This triplate bracket is in turn connected to the bottom of a quadraplate via a conventional shackle connection. Three lines will then be connected to the Dual Cap-X via the quadraplate. See Figure 2.10.

1. Conventional steel wire to Vessel A crane (1)
2. Conventional steel wire to Vessel A winch (2)
3. HMPE rope connected to Vessel B (3)

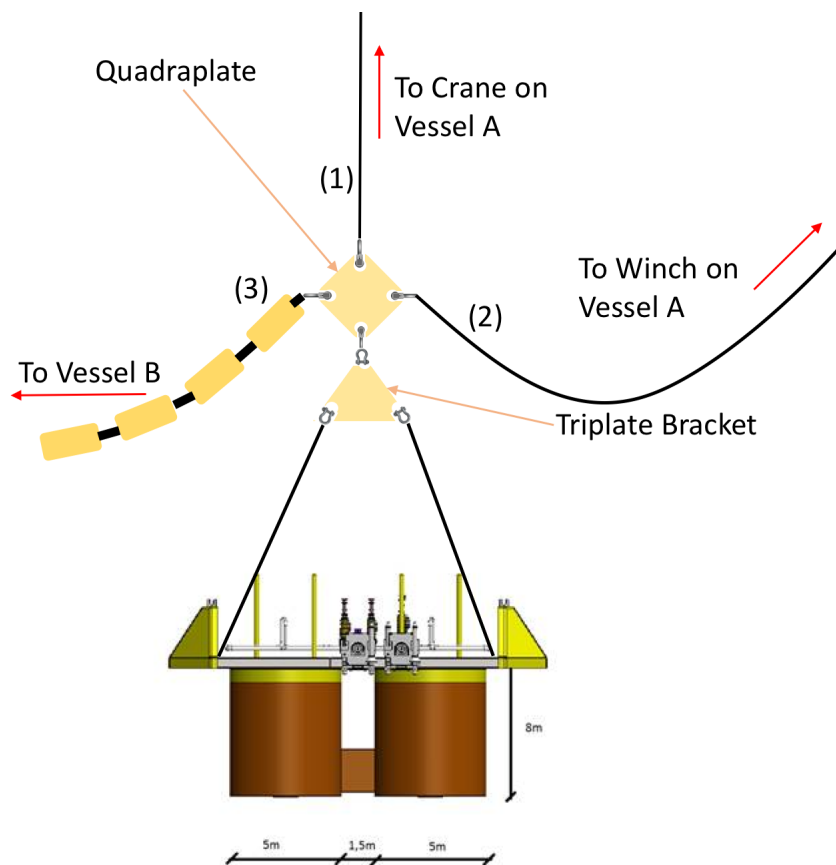


Figure 2.10: Pendulous installation connections.

The steel wire from the crane on Vessel A is connected to the top of the quadraplate via a hydraulic release shackle as shown in Figure 2.11. Upon connecting the crane wire, a conventional steel wire is connected to the right slot of the quadraplate via a hydraulic release shackle. This wire is connected to a winch on Vessel A.

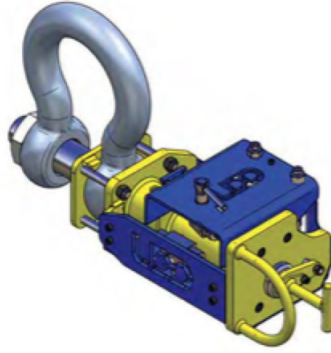


Figure 2.11: Hydraulic release shackle (Wang et al., 2013).

Vessel B will then position itself near to Vessel A such that an HMPE rope can be attached to the Dual Cap-X via the final slot (left side) of the quadraplate. The HMPE rope has buoyancy modules attached to it such that the connection operation will be easier in addition to offsetting part of the weight of the module as well as maintaining a sufficient angle relative to the payload during Free-Fall. Once all the connections have been made, the lifting line (1) will be tensioned as well as the deployment line (3). Vessel B will then proceed to steam away from Vessel A whilst paying out the deployment line until a distance corresponding to 90% desired deployment line length. This length corresponds to the desired depth of the module after pendulating into position without considering elastic elongation of the deployment line. Vessel A will maintain its original position. The Dual Cap-X will then be lifted off the deck and moved overboard via Vessel A's on-board crane. Tugger lines are utilized to avoid pendulum motion in air. The module is then lowered through the splash-zone via the crane's lifting line. If necessary, active heave compensation (AHC) can be utilized to minimize dynamic loading through the splash-zone. The launch line connected to a winch on Vessel A, denoted (2) in Figure 2.10, will be payed out as the module is lowered. Once reaching a depth of 50 m, the launch line (2) will discontinue paying out, whilst the crane continues. This stage in the procedure is visualized in Figure 2.12. In this manner, the load is transferred from the crane to the winch aboard Vessel A. Once 100 % of the load has been transferred to the winch, the crane will pay out its line until it is slack. A Remotely Operated Vehicle (ROV) will then be deployed from Vessel A to activate the hydraulic shackle and disconnect the crane wire.

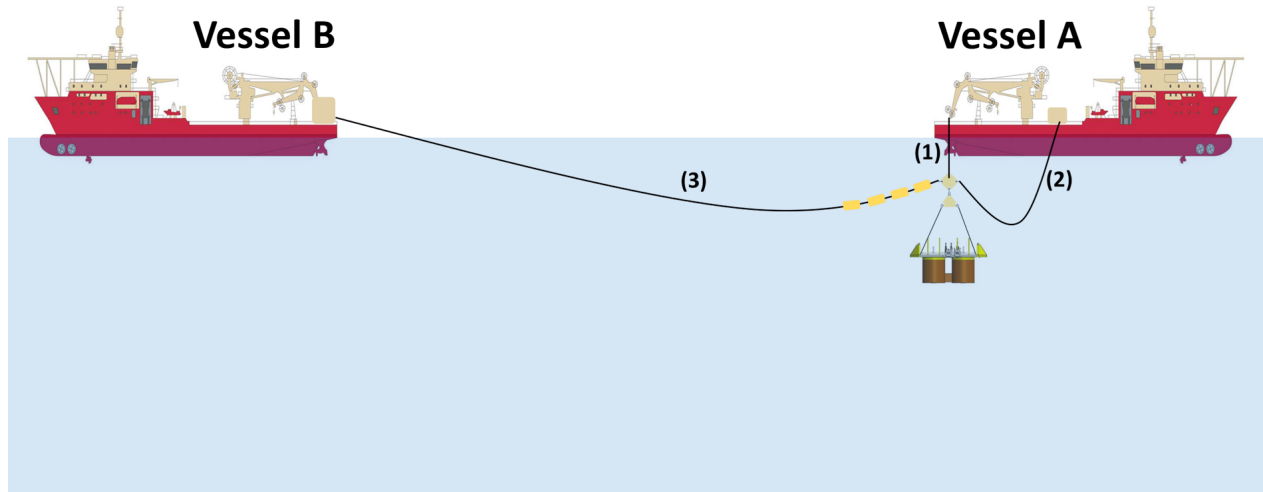


Figure 2.12: Free-fall preparation phase.

Phase 2 - Pendulous Free-Fall

During this stage of the installation procedure, Vessel A and B will maintain their positions, i.e. 90% of the HPME deployment line length. The winch on Vessel A now gradually pays out the launch line (2) such that it is not tensioned and does not hinder the free-fall. The module will move in a pendulous motion until 100% of the load is transferred to the deployment line, see Figure 2.13.

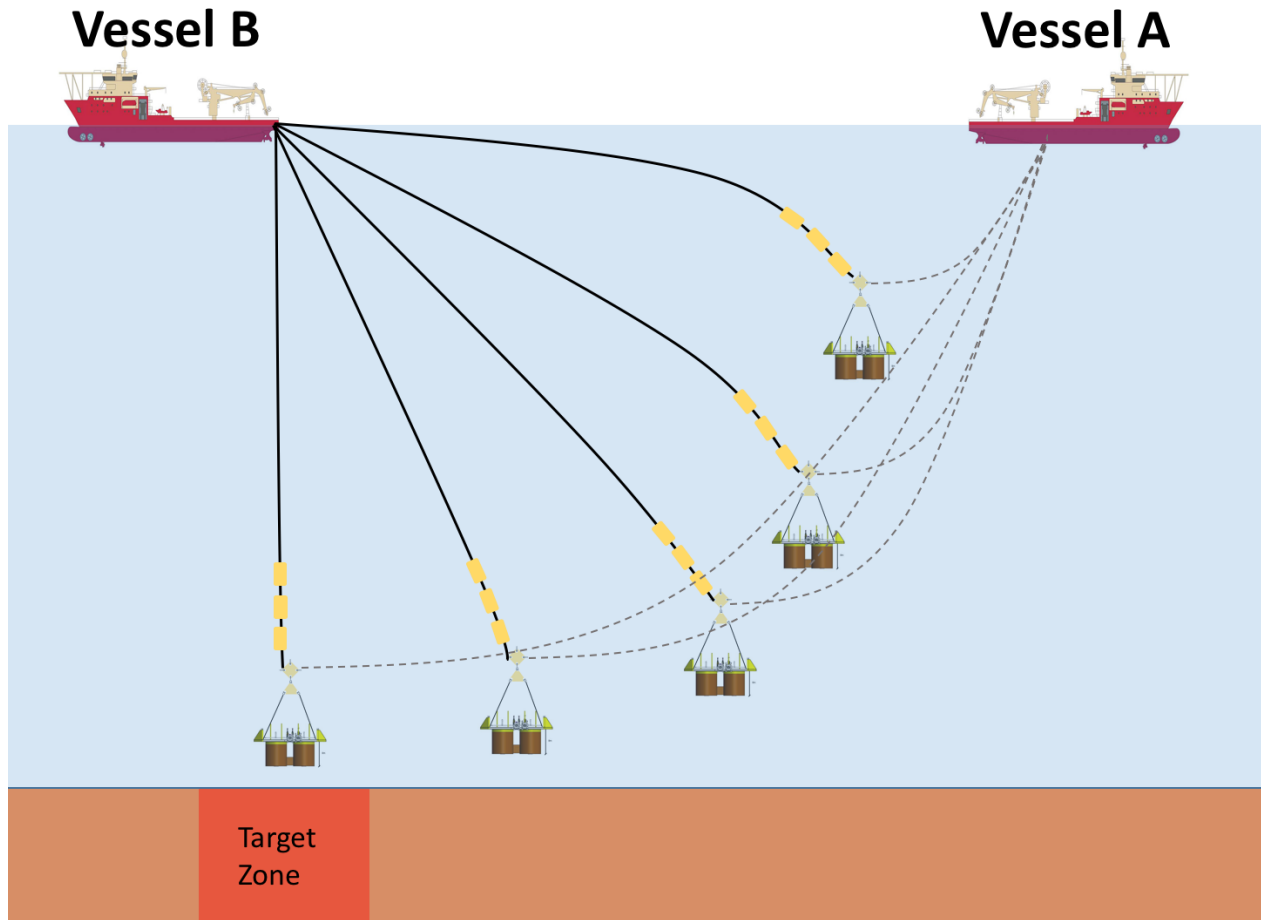


Figure 2.13: Pendulous Free-Fall.

An ROV will be deployed from Vessel B to confirm the position and orientation of the Dual Cap-X using a USBL (Ultra-Short Base Line) system. Once confirmed, Vessel A will move towards Vessel B in order to slacken the line. An ROV will then disconnect the hydraulic shackle connected to the lifting line and the winch will retract it.

The ROV from Vessel B is now utilized to position the Dual CAP-X accurately. Once this is achieved, the HPME rope is payed out until touchdown. If the relative velocity between the module and the touch down point is too high due to vessel motion effects, AHC can be considered for use.

2.3 Installation Payload

The payload of choice for the assessment and analysis conducted in this thesis is presented in this section.

Due to the desire to cut costs through innovative technology, the Dual Cap-X will be evaluated. The Dual Cap-X can be divided into three main parts from a structural point of view. The base of the structure consists of two suction cans connected together with a plate stiffener. The structure can be pre-installed with conductor casings, and as such there will be a casing path tube running from the top of the structure to the bottom on the inside of the suction skirt walls.

The top part of the Dual Cap-X structure consists of the frame bottom which is the base for (see Figure 2.14):

- Standard X-tree envelope
- Standard Tie-in envelope
- Umbilical Termination Assemblies

The frame bottom spans the top area of the two suction cans, with one base frame on each can for the X-mas trees (see Figure 1.3), and envelope the subsea production hardware.

At the top of the bottom protection frame, there are two cap hatches (see Figure 2.15). When closed, these hatches will together with the base protection structure enclose the subsea production hardware. Due to the possibility of large water entrapment and large added mass values, the cap hatches will be installed separately from the rest of the structure.

The CAD drawings of the structure (Statoil, 2016) have been used for payload modelling in SIMO. Table 2.1 summarizes the main dimensions.

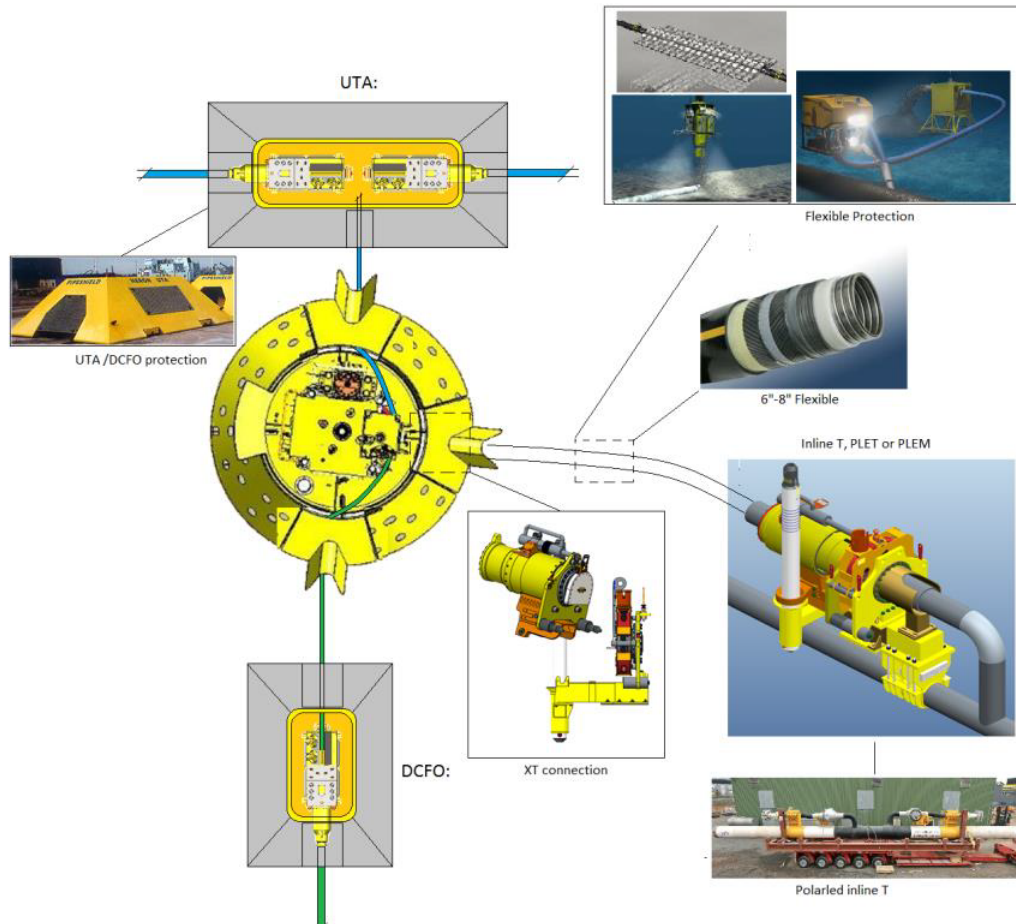


Figure 2.14: The protection structure of a Single Cap-X concept with some possible outboard connections (Ellingsen, 2015).

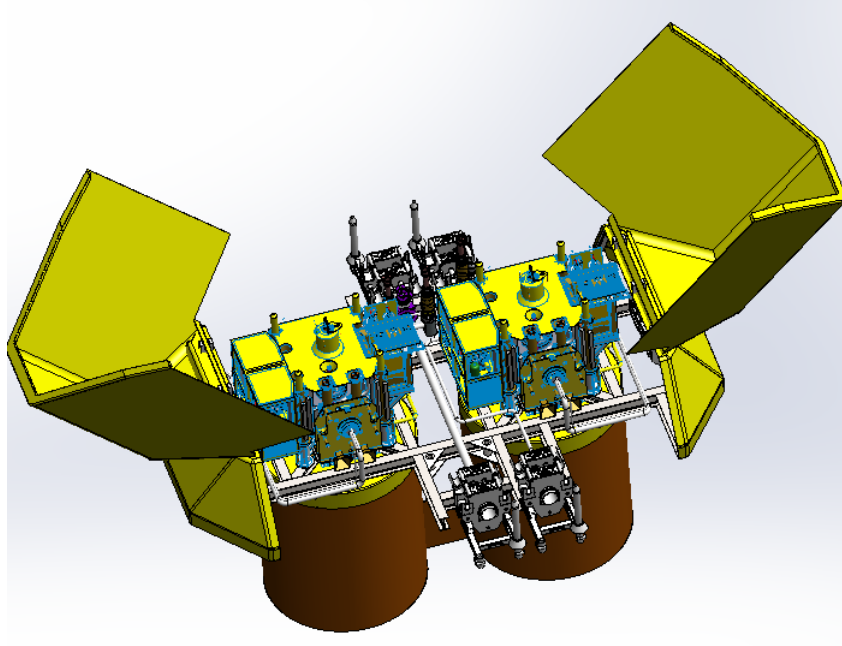


Figure 2.15: Protection cap in open position (Ellingsen, 2015).

Table 2.1: Weight and dimensions of the Dual Cap-X structure.

Description	Value
Total Mass ¹	175 [t]
Suction Can Height	6.04 [m]
Suction Can Diameter	5.00 [m]
Spacing Between Suction Cans ²	6.50 [m]
Bottom Frame Height	2.85 [m]
Bottom Frame Footprint ($L \times B$)	(16.9 \times 10.0) [m]

¹Excluding cap hatches and X-mas trees.

²Distance from centre to centre.

Chapter 3

Theory

3.1 Sea Environment

The installation of subsea equipment will be subject to environmental factors which act as operational boundaries. The environmental factors give rise to forces that affect motions of the installation vessel(s) and the deployed payload. The environmental factors relevant for deep-water installation operations are mainly:

- Waves
- Current
- Wind

These factors are discussed and the underlying theory of the phenomena presented in this section.

3.1.1 Waves

Linear Wave Potential Theory

In this thesis, the analysis is based on first order waves. The first order waves are based on linear wave potential theory. The basic assumptions are (Faltinsen, 1990) :

- The sea water is incompressible
- The sea water is inviscid
- The fluid motion is irrotational

The assumptions make it possible to express the velocity vector of the fluid at any given time and space by a scalar variable, ϕ , which is called the velocity potential. This relationship is expressed in Equation (3.1).

$$\mathbf{V} = \nabla\phi = \mathbf{i}\frac{\partial\phi}{\partial x} + \mathbf{j}\frac{\partial\phi}{\partial y} + \mathbf{k}\frac{\partial\phi}{\partial z} \quad (3.1)$$

where

\mathbf{V} =Fluid velocity vector

ϕ =Velocity potential

\mathbf{i} =Unit vector along x-axis

\mathbf{j} =Unit vector along y-axis

\mathbf{k} =Unit vector along z-axis

The advantage of using the velocity potential is that the governing Laplace equation can be expressed in a Cartesian coordinate system fixed in space.

Sarpkaya (2010) shows how the Laplace governing equation follows from the basic assumptions. Equation (3.2) express the governing equation.

$$\frac{\partial^2 \phi}{\partial x^2} + \frac{\partial^2 \phi}{\partial y^2} + \frac{\partial^2 \phi}{\partial z^2} = 0 \quad (3.2)$$

Finding pressure and velocity can now be found by solving for the velocity potential, ϕ . This means that only one scalar function is needed. Without the introduction of ϕ , one would have to solve one vectorial and one scalar equation. To solve the Laplace governing equation for ϕ , relevant boundary conditions have to be applied. Faltinsen (1990) have presented both the dynamic free-surface boundary condition and the sea bottom impermeability condition, which are used to derive the velocity potential for linear propagating waves. The dynamic free-surface boundary condition assumes that both fluid velocity and acceleration are constant from the mean surface to the free surface. The mathematical derivation of the velocity potential for linear propagating waves can be found in Newman and Landweber (1978).

The resulting velocity potential for directional short-crested waves can be expressed as (3.3) (SIMO Project Team, 2015).

$$\phi = \frac{\zeta_a g}{\omega} \frac{\cosh k(z+d)}{\cosh kd} \cos(\omega t - x \cos \beta - k y \sin \beta + \epsilon) \quad (3.3)$$

where

ζ_a =Wave amplitude

g =Gravitational acceleration

$k = \frac{\omega^2}{g}$ =Wave number

d =Water depth

β =Wave propagation direction

ϵ =Wave component phase angle

If the water depth is assumed to be infinite, i.e $d \rightarrow \infty$, ϕ can be expressed as in (3.4).

$$\phi = \frac{\zeta a g}{\omega} e^{kz} \cos(\omega t - x \cos \beta - ky \sin \beta + \epsilon) \quad (3.4)$$

The fluid pressure, p , is found by using Bernoulli's equation as in (3.5) (Faltinsen, 1990).

$$p + \rho g z + \rho \frac{\partial \phi}{\partial t} + \frac{\rho}{2} \mathbf{V} \cdot \mathbf{V} = C \quad (3.5)$$

where

C =Arbitrary function of time

ρ =Density of seawater

Wave Spectrum

The principles of linear theory is applied to obtain statistical estimates of an irregular short term sea state and construct a wave spectrum. A wave spectrum describes the energy distribution in a sea state and contains statistical information about the particular sea state. Faltinsen (1990, p.23) shows how the wave spectrum for a fully developed sea state is connected to the amplitudes of the wave components in an irregular sea. The significant wave height, H_s , and the spectral peak period, T_p , are common variables in most wave spectrum.

According to Faltinsen (1990), the JONSWAP (Joint North Sea Wave Project) wave spectrum is commonly used for wave generation with limited fetch. DNV GL (2011b) recommends the use of JONSWAP for wind sea conditions during the most severe sea states. The JONSWAP spectrum, S_{JP} , is included in SIMO/RIFLEX and is formulated in (3.6) (SIMO Project Team, 2015). The expression for α allows a parametrization of the spectrum in terms of H_s and T_p . According to DNV GL (2011b), the JONSWAP spectrum is a reasonable interpretation for the interval $3.6 < T_p / \sqrt{H_s} < 5$.

$$S_{JP}(\omega) = \frac{\alpha g^2}{\omega^5} \exp(-\beta(\frac{\omega_p}{\omega})^4) \gamma^{\exp(\frac{(\omega/\omega_p-1)^2}{2\sigma^2})}$$

$$\alpha = 5.061 \frac{H_s^2}{T_p^4} (1 - 0.287 \ln \gamma)$$
(3.6)

where:

α =Spectral parameter

ω_p =Peak frequency

γ =Non-dimensional peak shape parameter

β =Form parameter, default value $\beta=1.25$

σ =Spectral width parameter with default values:

$\sigma_a=0.07$ for $\omega < \omega_p$

$\sigma_a=0.09$ for $\omega > \omega_p$

3.1.2 Current

The current is an important environmental factor to consider for marine operations, especially for installation operations in deep waters. Currents can cause drag and lift forces on submerged bodies.

The depth dependent current velocity, $U(z)$, is divided into several components. The first component is the current contribution generated by local wind, denoted U_w . The second component, U_t , is due to the tidal effects. The tidal current will arise in the close proximity of the highest or lowest astronomical tide. Even though tidal current is generally weak in deep waters (DNV GL, 2010), the effects should not be neglected during deep water installation operations. Moreover, U_m is the current component caused by ocean circulation. U_d is current caused by changes in density along the water column, while U_s is the component generated by Stokes drift phenomena. U_{set-up} is due set-up and storm surges. The breakdown of the current velocity into

its components is summarized in Equation (3.7).

$$U(z) = U_w + U_t + U_d + U_{set-up} \quad (3.7)$$

Current velocity will vary over the water depth and on the phenomena and oceanographic effects described over. Since specific current conditions will vary from area to area and season to season, local statistical current data should be used when investigating the conditions at a specific area of interest. SIMO has the option to include a user-specified current condition. This is accomplished by defining the speed and direction at different water levels and utilizing linear interpolation between these reference points.

It is important to account for the variation in the current profile due to surface elevation and depression caused by wave presence in order to more accurately capture the current conditions at site. DNV GL (2010) recommends stretching and compressing the current profile in vertical direction in order to follow the wave surface. Linear stretching of the current profile will generally give acceptable estimates of the hydrodynamic loads and is defined as (DNV GL, 2010):

$$z_s = (d + \eta)(1 + z/d) - d; \quad -d \leq z_s \leq \eta \quad (3.8)$$

where

z_s =Stretched vertical coordinate

η =Water surface elevation

d =Still water depth

If the current speed is relatively high at the water surface and there is a large vertical velocity gradient to the water depths below, non-linear stretching should be implemented. The non-linear stretching is expressed as (DNV GL, 2010):

$$z_s = z + \eta \frac{\sinh(k_{nl}(z + d))}{\sinh(k_{nl}d)} \quad -d \leq z_s \leq \eta \quad (3.9)$$

where

k_{nl} =Non-linear wave number

The principles of linear and non-linear stretching of the current profile are illustrated in Figure 3.1. Current profile stretching as recommended by DNV GL (2010) is included in SIMA.

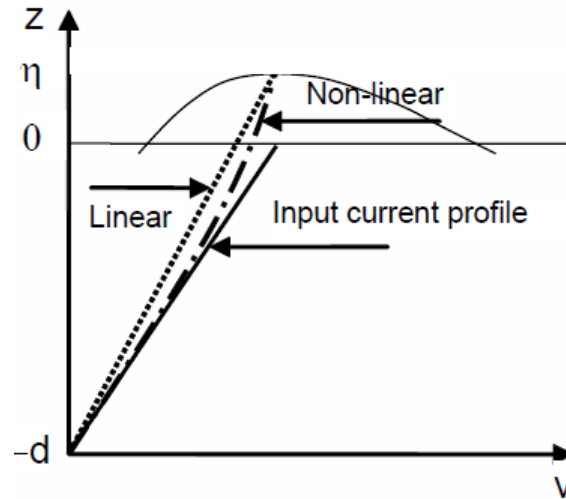


Figure 3.1: Linear and non-linear current profile stretching up to the wave surface (DNV GL, 2010).

3.1.3 Wind

Depending on geographic location and season, wind is an important factor to consider when planning and executing a offshore marine operation. The following is based on SIMO Project Team (2015).

The wind field is assumed to be parallel to the horizontal plane (2-D). The wind velocity consist of a varying and constant component. The varying component is called wind gust. For this thesis, the ISO 19901-1 wind spectrum is relevant for the wind gust. The general wind profile used for the mentioned wind spectrum can be expressed as:

$$\bar{u}(z) = \bar{u}_r \frac{z}{z_r}^\alpha \quad (3.10)$$

where

z =height above the water surface

z_r =reference height, which is taken as 10 m

\bar{u}_r =average wind velocity at height z_r

α =height coefficient, which is taken as 0.11

The ISO 19901-1 wind spectrum for the design wind speed over an time period of $t \leq t_0 = 3600$ s can be expressed as in (3.11).

$$u(z, t) = U(z) \left[1 - 0.41 I_u(z) * \ln\left(\frac{t}{t_0}\right) \right] \quad (3.11)$$

where

$U(z)$ =1 hour mean wind speed

$I_u(z)$ =turbulence intensity factor

For further reading, the reader is referred to SIMO Project Team (2015).

3.2 Dynamics of Marine Operations

3.2.1 Response Amplitude Operators

In the field of sea keeping the Response Amplitude Operator (RAO), denoted $|H(\omega)|$, is commonly used to express the ratio between the response amplitude of a given parameter such as motion to the wave amplitude, i.e $|H(\omega)| = \eta_a / \zeta_a$. The RAO should also include the phase lag related to the response, and is then also called transfer function in some literature. The RAO assumes the linear equation of motion, and is used to utilize the frequency spectrum of a sea state in order to output a spectrum of motion.

3.2.2 Vessel Motion

A ship will have a certain response to its environment. The coupled vessel motions set limitations on marine operations and are immensely important to consider when determining a deepwater installation method. Vessel motion is important throughout all phases of a marine operation: from steaming into position to final touchdown of the load on the seabed. Installation of subsea equipment relies on relatively calm motions of the installation vessel in order to execute the operation in a safe and accurate manner. Another important aspect of better vessel motion control is associated with an increased operability. Having a thorough understanding of vessel motions and exploiting this knowledge is crucial in order to minimize the operational time.

Environmental factors that will effect the physical behaviour of an installation vessel include:

- Wind
- Waves
- Current

The most significant factor for the vessel motion is the sea-state, which describes the wave height and period for the site. Vessel motions can be separated into six degrees of freedom (see Figure 3.2):

- Surge, η_1
- Sway, η_2
- Heave, η_3
- Roll, η_4
- Pitch, η_5
- Yaw, η_6

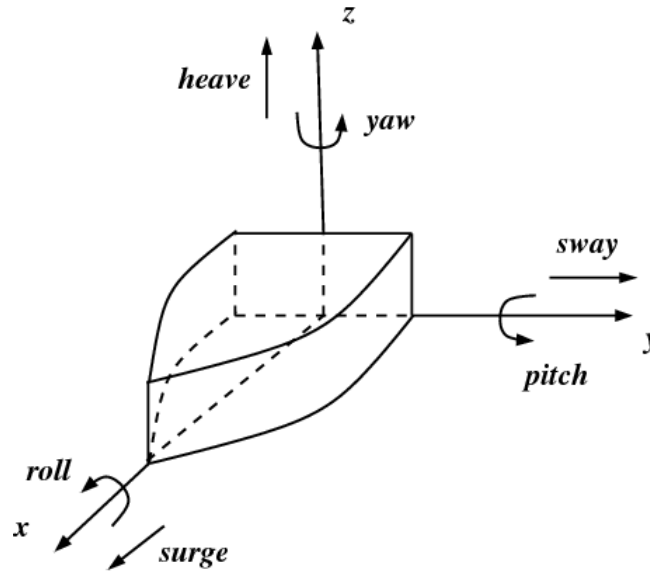


Figure 3.2: Overview of vessel motions.

Using the definitions of translation and rotation motions listed above, Equation 3.12 from Faltinsen (1990) gives the position, s , at any point on the vessel.

$$s = (\eta_1 + z\eta_5 - y\eta_6)i + (\eta_2 - z\eta_4 + x\eta_6)j + (\eta_3 + y\eta_4 - x\eta_5)k \quad (3.12)$$

where

i =Unit vector along X-axis

j =Unit vector along Y-axis

k =Unit vector along Z-axis

3.2.3 Relative Motions between Two Vessels

The vessel motion has a significant impact on the lift-off phase, especially when the payload is lifted off a separate barge by a crane on the lifting vessel. Vessel motion due to wave, current and wind loads will cause a relative motion between the crane tip and the deck of the barge. If the relative motion is sufficiently large, it may cause uncontrollable motion of the payload during lift-off. The consequence of this can be payload impact with personnel and/or damage to asset

and/or re-hit of the object.

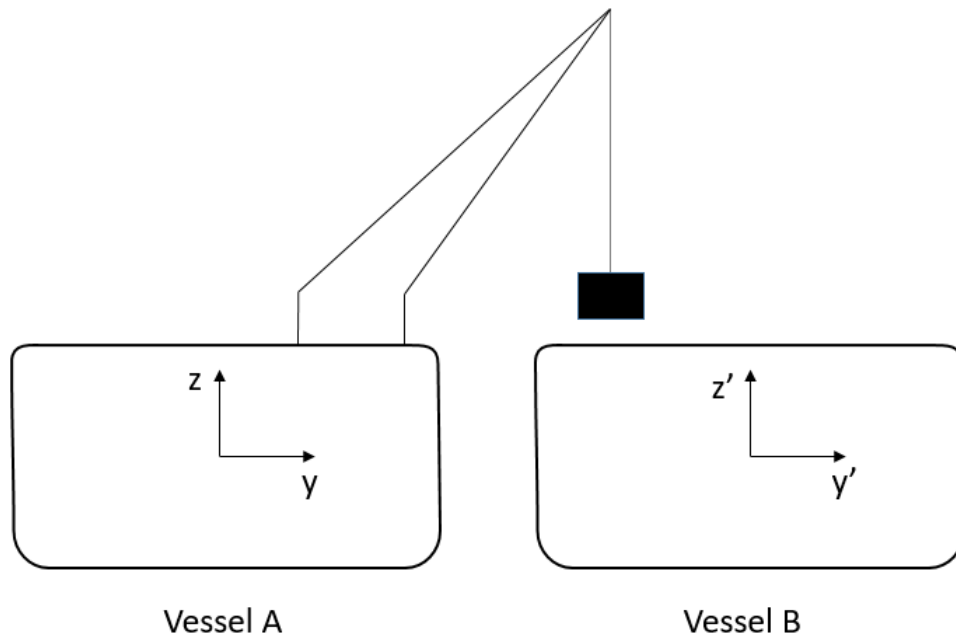


Figure 3.3: Crane lift-off from a separate vessel. The origin of the two coordinate systems are assumed to coincide with the vessels' COGs.

Due to the importance of especially cable wire tension during the Lift-Off and the Splash-Zone phase of an installation, vertical motions of the ship are of great interest.

Assuming the situation presented in Figure 3.3, the relative motion between Vessel A and Vessel B at the position of the payload hanging from the crane can be found. The vertical motion of a point due to heave, roll and pitch, s_3 , can be found by using the vertical component of Equation (3.12), i.e:

$$s_3 = \eta_3 + y\eta_4 - x\eta_5 \quad (3.13)$$

Furthermore, a harmonic short crested wave which propagates along a line with an angle θ with the positive X-axis is introduced. The wave elevation in the (x,y,z) coordinate system can then be expressed as (Myrhaug et al., 2014):

$$\zeta(x, y, t) = \zeta_a \sin(\omega t - kx \cos \theta - ky \sin \theta) \quad (3.14)$$

The next step is to find the relationship between the wave elevation expressed in the (x,y,z) and the (x',y',z') coordinate system. This can be done by expressing the wave elevation at the centre of Vessel B in two ways:

$$\zeta(x, y, t) = \zeta_a \sin(\omega t - kx_a \cos \theta - ky_a \sin \theta) \quad (3.15)$$

where

x_a =Distance from origin in (x,y,z) coordinate system to COG of Vessel B along X-axis

y_a =Distance from origin in (x,y,z) coordinate system to COG of Vessel B along Y-axis

and

$$\zeta(x', y', t') = \zeta_a \sin(\omega t') \quad (3.16)$$

By comparing (3.15) and (3.16), the following relationship is found:

$$\omega t' = \zeta_a \sin(\omega t - kx_a \cos \theta - ky_a \sin \theta) \quad (3.17)$$

It should be noted that $t' - t$ expresses the time it takes for a wave crest to propagate from the origin in Vessel B's to the origin in Vessel A's coordinate system.

The rigid vessel motions are then expressed by using RAOs:

$$\begin{aligned} \eta_i^{VesselA} &= |H(\omega)|_i^{VesselA} \sin(\omega t) && \text{for } i = 3, 4, 5 \\ \eta_i^{VesselB} &= |H(\omega)|_i^{VesselB} \sin(\omega t - x_a k \cos \theta - ky_a \sin \theta) && \text{for } i = 3, 4, 5 \end{aligned} \quad (3.18)$$

where

η_i =Translation or rotation in the degree of freedom i

$|H(\omega)|_i$ =RAO in the degree of freedom i for specific vessel

Finally, the relative motion at the position of the payload is equal to the vertical motion of the crane tip minus the vertical motion of the deck of Vessel B. This is expressed in (3.19), where the rigid motions of the vessels are as defined in (3.18).

$$s_3 = (\eta_3^{VesselA} + y_{\text{crane tip}}\eta_4^{VesselA} - z_{\text{crane tip}}\eta_5^{VesselA}) - (\eta_3^{VesselB} + y_{\text{crane tip}}\eta_4^{VesselB} - z_{\text{crane tip}}\eta_5^{VesselB}) \quad (3.19)$$

Depending on the vessel RAOs, the relative motion of the payload may be significant. By inspection of (3.19) it can be observed that similar RAOs between the two vessels is favourable in order to restrict the relative motion of the payload. Furthermore, the phase lag between the responses of the two vessels is also important to consider. The importance of the phase lag on the relative motion of the payload will vary depending on the direction of the incoming waves. In head sea, the incoming waves will reach both vessels at almost the same time. In beam sea however, the phase lag can be of greater significance. The pendulum motion of the crane wire and payload is not considered in the simple derivation performed in this subsection. It is discussed in Section 3.2.4

3.2.4 Pendulum Motion

Horizontal pendulum motion should be accounted for when planning a lifting operation due to the risks of personnel injury and equipment damage associated with an uncontrollable load hanging from a crane. The horizontal motion η_1 of the object can be determined by solving Equation 3.20.

$$M\ddot{\eta}_1 + 2C_u U \dot{\eta}_1 + \frac{T}{L}\eta_1 = \frac{T}{L}\eta_{1,CT} + C_u U^2 \quad (3.20)$$

Where M is the mass of the payload, C_u is the wind force coefficient, U is the wind speed, T is the tension in the lifting wire, $\eta_{1,CT}$ is the horizontal motion of the crane tip and L the distance from the crane tip to the payload. The resonance period, T_c , of the pendulum motion depends on the length of the crane wire, and is expressed in (3.21).

$$T_c = 2\pi\sqrt{\frac{l}{g}} \quad (3.21)$$

where

l = Length of cable wire [m]

g = Acceleration of gravity [$\frac{m}{s^2}$]

For the sake of illustration, it is reasonable to consider a cable wire length of $l = 20m$ during lift-off since the Dual Cap-X height is approximately 11 m (see Table 2.1). Taking $g = 9.81m/s^2$, (3.21) gives $T_c = 8.9s$. This eigenperiod is in close proximity to the wave periods commonly experienced in areas such as the North Sea. As such, the crane tip motion may excite the pendulum motion of the crane wire.

One can see from Equation 3.20 that damping is provided by the wind force. The wind force will therefore be of importance when resonance periods are experienced.

3.2.5 Crane Tip Motion

A light lift is defined as a lift in which the weight of the lifted object is less than 1-2 % of the displacement of the crane vessel (DNV GL, 2011b). The total mass of the Dual Cap-X is 175 t as outlined in Section 1.1.2. As such, one can conclude that the lifting operation will be considered a light lift.

In the case of a light lift, the motion characteristics of the crane tip are not affected by the lifted object. The crane tip motion is then solely dependent upon vessel motion. The translational motions of the crane tip in surge (x_{ct}), sway (y_{ct}) and heave (z_{ct}) can therefore be determined from the RAOs of the vessel. These are typically defined for the center of gravity of the vessel,

and the translated values for the crane tip will need to be determined.

Vertical translation is of greatest interest in a subsea installation operation. The crane tip vertical motion is expressed in Equation (3.22) (DNV GL, 2011b).

$$\eta_{ct} = \sqrt{\eta_3^2 + (b \cdot \sin \eta_4)^2 + (l \cdot \sin \eta_5)^2} \quad (3.22)$$

where

η_{ct} = Characteristic single amplitude of vertical crane tip motion [m]

η_3 = Characteristic single amplitude heave motion of vessel [m]

η_4 = Characteristic single amplitude roll angle of vessel [deg]

η_5 = Characteristic single amplitude pitch angle of vessel [deg]

b = Horizontal distance from the vessel's center line to the crane tip [m]

l = Horizontal distance from midship to the crane tip [m]

The vertical velocity of the crane tip can be expressed through equation (3.23) (DNV GL, 2011b).

$$v_{ct} = \sqrt{\left(\frac{\eta_3}{T_3}\right)^2 + \left(\frac{b \cdot \sin \eta_4}{T_4}\right)^2 + \left(\frac{l \cdot \sin \eta_5}{T_5}\right)^2} \quad (3.23)$$

where

v_{ct} = Characteristic single amplitude of vertical crane tip motion [m/s]

T_3 = Heave natural period [s]

T_4 = Roll natural period [s]

T_5 = Pitch natural period [s]

3.2.6 Forces

Based on the characteristic dimensions of the Dual Cap-X and the wave heights and wave lengths common at the Heidrun field, the payload can be considered as a small volume structure. As such, the payload's capability of generating waves is less prominent (see Figure 3.4). For small-volume bodies the wave field is generally unaffected by the structure's presence. Moreover, the long-wave approximation is applicable. Using the long wave-approximation, it is assumed that the wave induced loads on the structure are mainly connected to the acceleration (therefore the term "mass forces" in Figure 3.4) of the incident waves, and that diffraction effects are small.

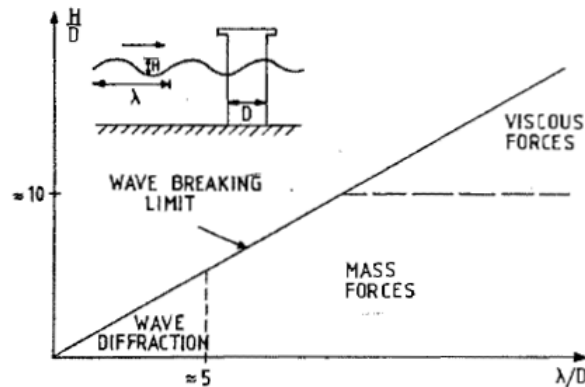


Figure 3.4: Relative importance of different types of forces on marine structures (Faltinsen, 1990).

DNV GL (2011b) have listed the following forces to be of importance in such cases:

- Weight of Payload
- Buoyancy Force
- Steady force due to current
- Inertia Force
- Wave Excitation Force
- Viscous Drag Force

- Slamming Force

These forces are of special significance during the Splash-Zone phase, as noted by DNV GL (2011b). During the free-fall pendulous phase, it is most likely that the most important forces are the drag and inertia forces. All of these forces that will arise during the installation of the Dual Cap-X by the PIM are presented in this section, and is based on DNV GL (2011b).

Weight of Payload

The weight of the relevant subsea structure is the primary source of tension in the wire. The force acting on the wire due to the weight of the structure in air, W_0 , is then defined by equation (3.24).

$$W_0 = Mg \tag{3.24}$$

where

M =Mass of the payload [kg]

g =Acceleration of gravity [$\frac{m}{s^2}$]

Buoyancy Force

As the payload is lowered through the splash-zone, the buoyancy force will come into play. The time dependent buoyancy force, $F_B(t)$ corresponds to the the weight of the instantaneous displaced water as given in (3.25) (DNV GL, 2011b).

$$F_B(t) = \rho g V(t) \tag{3.25}$$

where

ρ =Mass density of water

$V(t)$ =Time dependent displaced volume of water

The buoyancy force acts in the opposite direction of the weight of the payload.

Steady Force due to Current

When the payload is lowered through the splash-zone, steady forces from the prevailing current conditions act upon the load. The steady current force is opposed by the horizontal component of the lifting wire force and will vary with the current at depth z_0 of the object can be expressed as a drag force:

$$F_c(z_0) = 0.5\rho C_{DSi} A_{pi} U_c(z_0) \quad (3.26)$$

where

C_{DSi} =Steady state drag coefficient in the current direction i

A_{pi} =Projected area in direction i

$U_c(z_0)$ =Current velocity at depth z_0 of object

Inertia Force

The inertia forces due to a moving object in pure translation in direction i ($i=1,2,3$) can be found via utilization of equation (3.27).

$$F_{I,i} = -(M\delta_{i,j} + A_{ij})\ddot{\eta}_j \quad (3.27)$$

where

M =Structural mass

A_{ij} =Added mass in direction i due to acceleration in direction j

$\ddot{\eta}_j$ =Acceleration of object in direction j ($1 = x, 2 = y, 3 = z$)

$$\begin{aligned}\delta_{i,j} &= 1 \text{ if } i=j \\ &= 0 \text{ if } i \neq j\end{aligned}$$

Generally, the added mass is expressed by using an added mass coefficient. The added mass will vary with factors such as distance from free surface, frequency of oscillation, and size of open hatches in the payload and it is therefore challenging to accurately define during the splash-zone lifting phase.

Wave Excitation Forces

The wave excitation forces and moments are the loads on the payload when it is restrained from any motion response and is subjected to incident waves. Since it is assumed that the payload to be small compared to the wavelength of the incident wave (long-wave approximation), the wave excitation force in direction i , F_{Wi} , is defined by equation (3.28) when the payload is fully submerged.

$$F_{Wi} = \rho V (\delta_{ij} + C_A^{ij}) \dot{v}_j + F_{Di} \quad (3.28)$$

where

V = Submerged volume of object (taken to still water level $z=0$)

C_A^{ij} = Added mass coefficient in direction i due to acceleration in direction j [kg]

\dot{v}_j = Water particle acceleration in direction i

F_{Di} = Viscous drag excitation force

$\delta_{i,j} = 1$ if $i = j$

$= 0$ if $i \neq j$

The first term in (3.28) contains the Froude-Krylov ($\rho V \dot{v}_j$) and diffraction ($C_A^{ij} \dot{v}_j$) forces ex-

pressed in the long-wave approximation form. The diffraction force is included to account for the impermeability of the payload.

During the period in which the structure is only partially submerged, the force in direction i is defined by equation (3.29).

$$F_{Wi} = \rho g A_w \zeta(t) \delta_{i3} + \rho V (\delta_{ij} + C_A^{ij}) \dot{v}_j + F_{Di} \quad (3.29)$$

where

A_w =Water plane area

$\zeta(t)$ =Wave surface elevation

$\delta_{i3} = 1$ if $i = 3$

$= 0$ if $i = 1$ or $i = 2$

Slamming Force

When the payload is lifted down through the splash-zone, impulse loads with high pressure peaks can arise due to the interaction between the payload structure and the water (Faltinsen, 1990). This phenomena is called slamming, and is an important aspect of marine operations. The slamming force, $F_s(t)$, during water entry in a wave environment can be expressed in terms of a dimensionless slamming coefficient as expressed in Equation (3.30).

$$F_s(t) = \frac{1}{2} \rho C_s A_p (\dot{\zeta} - \dot{\eta})^2 \quad (3.30)$$

where

C_s =Slamming coefficient

A_p =Horizontal projected area of object

$\dot{\zeta}$ =Vertical velocity of sea surface

$\dot{\eta}$ =Vertical velocity of payload

By inspection of (3.30), it is clear that the slamming force is proportional to the square of the relative vertical motion between the payload and the sea surface. The slamming coefficient, C_s , is expressed in (3.31).

$$C_s = \frac{2}{\rho A_p} \frac{dA_{33}^{\infty}}{dh} \quad (3.31)$$

dA_{33}^{∞}/dh is the rate of change of the high-frequency limit of the added mass in heave with submergence relative to the surface elevation h . The use of A_{33}^{∞} is a simplification that is reasonable for high frequency phenomena. The simplification is reasonable since the gravity acceleration, g , is considered to be much smaller than the acceleration of the fluid when the payload enters the water (DNV GL, 2011b).

Viscous Drag Force

In oscillatory flow, the viscous drag force on the payload can be expressed by utilizing the drag component in Morison's equation. The force arises due to resistance of the flow along the submerged body. The expression for the force is:

$$F_{di} = \frac{1}{2} \rho C_D A_p |V_r| V_{ri} \quad (3.32)$$

where

F_{di} =Viscous drag force in direction i

C_D =Dimensionless drag coefficient in oscillatory flow

A_p =Projected area normal to motion or flow direction

v_r =Relative velocity

v_{ri} =Relative velocity component in direction i

As stated in DNV GL (2011b), F_{di} can be considered a damping force or an excitation force con-

tingent on the magnitude and direction of the relative motion part in (3.32). In other words, depending on the phase angle between the payload motion and the fluid motion, the viscous drag force may act as a damping or excitation force.

When calculating the damping force in vertical direction, Equation (3.33) may be utilized.

$$F_{D3} = B_1(\dot{\zeta} - \dot{\eta}_3) + B_2(\dot{\zeta} - \dot{\eta}_3)|\dot{\eta}_3 - \dot{\zeta}| \quad (3.33)$$

where

B_1 =Linear damping term

B_2 =Quadratic damping term

The first term of (3.33) represents the linear damping which is associated with skin friction, while the second term is the quadratic damping which is associated with form drag. Due to the oscillatory motions of the payload in the splash-zone, the results presented by Øritsland and Lehn (1987) is of particular interest. According to Øritsland and Lehn (1987) the damping coefficients depend on the Keulegan-Carpenter (KC) number. DNV GL (2011b) recommends to limit the use of Equation (3.33) to $KC < 10$. In this interval of KC numbers, Øritsland and Lehn (1987) argue that the damping coefficients can be considered to be less dependent on the KC number.

By expressing the drag as in Equation 3.33, amplitude dependency is avoided. Øritsland (1989) provides expressions for the linear and quadratic terms, B_1 and B_2 , respectively:

$$B_1 = \frac{2\rho A_p D}{3\pi^2 \sqrt{D/2g}} b_1 \quad (3.34)$$

$$B_2 = 0.5\rho A_p b_2$$

where

b_1 =Linear damping coefficient

b_2 =Quadratic damping coefficient

A_p =Projected area in the velocity direction

D =Characteristic body length

Using b_1 and b_2 , the quadratic drag coefficient, C_d , in Morison's equation can be expressed as:

$$C_d = \frac{b_1}{KC\omega'} + b_2 \quad (3.35)$$

$$\omega' = \omega \frac{D}{2g}$$

where

$KC = \pi H/D$ =Keulegan Carpenter number

ω' =Non-dimensional oscillation frequency

D =Characteristic length in flow direction

3.2.7 Equation of Vertical Motion

By combining the forces mentioned in Section 3.2.6, one can express the dynamic equation of vertical motion when an object is being lifted through the wave zone. The vertical motion of the payload as a function of time, denoted $\eta(t)$ is expressed in Equation (3.36) (DNV GL, 2011b):

$$(M + A_{33})\ddot{\eta} = B_{33}^1(v_3 - \dot{\eta}) + B_{33}^2(v_3 - \dot{\eta})|(v_3 - \dot{\eta})|$$

$$+ (\rho V + A_{33})\dot{v}_3 + \frac{dA_{33}^\infty}{dh}(\dot{\zeta} - \dot{\eta})^2 + \rho gV(t) - Mg + F_{line}(t) \quad (3.36)$$

where

B_{33}^1 = Linear damping coefficient [kg/s]

B_{33}^2 = Quadratic damping coefficient [kg/m]

v_3 = Water particle velocity [m/s]

\dot{v}_3 = Water particle acceleration [m/s^2]

$F_{line}(t)$ = Force in lifting line [N]

η = Vertical motion

This equation is valid for small bodies, i.e. bodies that have dimensions much smaller than the wavelengths they are subjected to. The force in the lifting line can be expressed through Equation (3.37).

$$F_{line}(t) = Mg - \rho gV(t) + K(z_{ct} - \eta) \quad (3.37)$$

where

K = Hoisting line stiffness [N/m]

z_{ct} = Motion of crane tip [m]

Combining equations (3.36) and (3.37) yields Equation (3.38).

$$\begin{aligned} (M + A_{33})\ddot{\eta} = & B_{33}^1(v_3 - \dot{\eta}) + B_{33}^2(v_3 - \dot{\eta})|(v_3 - \dot{\eta})| \\ & + (\rho V + A_{33})\dot{v}_3 + \frac{dA_{33}^\infty}{dh}(\dot{\zeta} - \dot{\eta})^2 + K(z_{ct} - \eta) \end{aligned} \quad (3.38)$$

This equation can then be solved for η seeing as all other values are known. The tension in the lifting wire can then be expressed as:

$$\begin{aligned} F_{line}(t) = & (M + A_{33})\dot{\eta} - B_{33}^1(v_3 - \dot{\eta}) - B_{33}^2(v_3 - \dot{\eta})|(v_3 - \dot{\eta})| \\ & - (\rho V + A_{33})\dot{v}_3 - \frac{dA_{33}^\infty}{dh}(\dot{\zeta} - \dot{\eta})^2 - \rho gV(t) + Mg \end{aligned} \quad (3.39)$$

Variations in the lifting wire force are a direct result of dynamic loading on the body. It has been shown that these forces are dependent on the acceleration, velocity and translation. The vertical motion of the payload will be a summation of the wave induced motion, the lowering velocity as well as the crane tip motions outlined in Section 3.2.5. In order to understand the forces involved, one should have a thorough understanding of the parameters involved in the

dynamic equation.

3.3 Offset in Deepwater Conditions

3.3.1 Horizontal Offset

DNV GL (2011b) outlines a simplified method to estimate horizontal offset during deepwater installation. The following is taken from DNV GL (2011b):

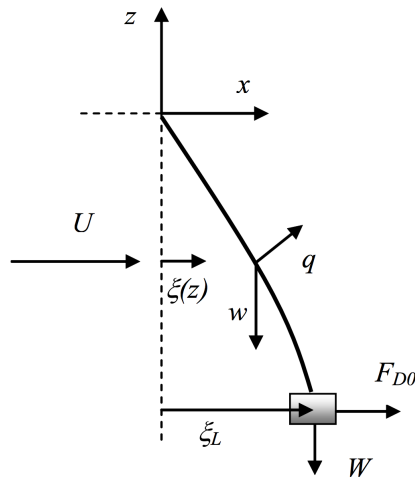


Figure 3.5: Horizontal offset with decomposed forces. (DNV GL, 2011b)

For an axially stiff cable with negligible bending stiffness, the offset of a vertical cable with a heavy weight W at the end of the cable in an arbitrary current with unidirectional (in X-direction) velocity profile $U_c(z)$ is given by Equation (3.40) from DNV GL (2011b).

$$\xi(z) = \int_z^0 \left[\frac{F_{D0} + \frac{1}{2} \rho \int_{-L}^{z_1} C_{Dn} D_c [U_c(z_2)]^2 dz_2}{W + w(z_1 + L)} \right] dz_1 \quad (3.40)$$

where

$$F_{D0} = \frac{1}{2} \rho C_{Dx} A_x [U_c(-L)]^2 \quad (3.41)$$

is the hydrodynamic drag force on the lifted object.

For a uniform current and cable properties D_c, C_n , the horizontal offset can be derived by:

$$\xi(z) = L \left(\frac{q}{w} \kappa - \lambda \right) \ln \left[\frac{\kappa + \frac{z}{L} + 1}{\kappa + 1} \right] - \frac{qL}{w} z [m] \quad (3.42)$$

$$\xi_L = L \left(\frac{q}{w} \kappa - \lambda \right) \ln \left[\frac{\kappa}{\kappa + 1} \right] + \frac{qL}{w} [m] \quad (3.43)$$

$$\kappa = \frac{W}{wL} \quad (3.44)$$

$$\lambda = \frac{F_{D0}}{wL} \quad (3.45)$$

$$q = \frac{1}{2} \rho C_{Dn} D_c U_c^2 [N/m] \quad (3.46)$$

where

$\xi(z)$ = Horizontal offset at vertical position z [m]

ξ_L = Horizontal offset at end of cable [m]

L = Un-stretched length of cable [m]

C_{Dn} = Drag coefficient for normal flow past cable

C_{Dx} = Drag coefficient for horizontal flow past lifted object

D_c = Cable diameter

A_x = X-projected area of lifted object [m^2]

$U_c(z)$ = Current velocity at depth z [m/s]

ρ = Density of water [kg/m^3]

W = Weight of lifted object

w = Fully submerged weight per unit length of cable [N/m]

q = Hydrodynamic drag force per unit length of cable

z_1, z_2 = Integration variables

3.3.2 Vertical Displacement

The distance to the seabed is an important aspect to consider when installing subsea hardware, and as such the vertical displacement of the lifting line is of interest for investigation. The longer the line, the greater the vertical displacement. The difference Δz with respect to the real vertical position of the lower end of the lifting cable compared to the unstretched condition can be found through two contributions according to DNV GL (2011b):

$$\Delta z = \Delta z_G + \Delta z_E \quad (3.47)$$

where

Δz_G = Vertical geometric displacement due to curvature of the cable

Δz_E = Vertical elastic displacement due to cable stretch

The geometric contribution is due to current effects, and will result in an increase of clearance from the seabed, whilst the elastic contribution contributes towards a decrease due to axial elongation.

$$\frac{\delta z_G}{L} = \frac{q}{w} \left(\frac{q}{w} \kappa - \lambda \right) \left(\ln \left[\frac{\kappa}{\kappa + 1} \right] + \frac{1}{2} \left(\frac{1 - \frac{\lambda w}{\kappa q}}{1 + \kappa} \right) \right) + \frac{1}{2} \left(\frac{q}{w} \right)^2 \quad (3.48)$$

$$\frac{\Delta z_E}{L} = -\frac{1}{EA} \left(W + \frac{1}{2} (wL - q\zeta_L) \right) \quad (3.49)$$

where

E = Young's modulus

A = Cross sectional area

With a varying current, this can be difficult and a finite element investigation should be conducted to acquire accurate results for 3D simulations.

3.4 Weather Windows

Marine operations are generally separated into two categories:

1. Weather restricted
2. Weather unrestricted

Operations with a planned operational period T_{POP} below 72 hours are generally considered to be weather restricted. Operations with a duration over 72 hours must be able to be carried out in any weather condition that is experienced during a season, and are as such considered weather unrestricted. The statistical extremes at the specific location and season should be considered

when determining the environmental conditions in this case (DNV GL, 2011a). Subsea lifting operations are generally considered to be weather restricted.

In the case of weather restricted operations, a design criterion OP_{LIM} will be set with respect to the environmental conditions. Significant wave height H_s is commonly used, but wind and current effects can also be of significance depending on the operation. A marine operation must be conducted in periods during which the environmental conditions are below the operational criteria (see Section 3.4.1). Such periods are called weather windows and can be defined as:

"[...] the time span over which the stringent, multi-parametric conditions required by weather-sensitive marine operations [...] are met". (Foo et al., 2014).

Both the environmental conditions as well as the period during which the environmental conditions are of an acceptable level are important. Weather forecasts are therefore essential in planning weather restricted marine operations.

3.4.1 Uncertainty in Weather Forecast

Another important aspect of determining the required weather window is the alpha factor, α . The purpose of the α factor is to capture the uncertainty in monitoring and forecasting the weather conditions. The α factor is tabulated in DNV GL (2011a) for H_s , and Design Wind Speed, V_d . In addition, α is a function of T_{POP} . An increase in T_{POP} will cause a decrease in α and thus stricter operational criteria, OP_{WF} , for the planned operation. This can be seen in Equation (3.50).

$$OP_{WF} = \alpha OP_{LIM} \quad (3.50)$$

Figure 3.6 illustrates the required weather window and how the weather forecast influences the operation time.

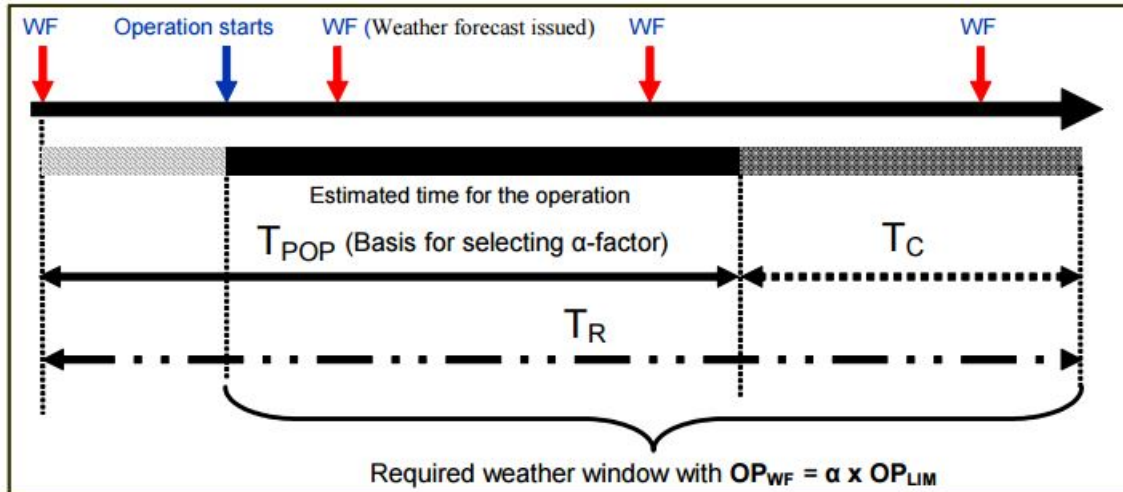


Figure 3.6: Operation periods. (DNV GL, 2011a)

T_R is the operational reference period, and T_C is the contingency time. T_C takes into account uncertainty in T_{POP} allowing for contingency situations in which additional time is required. T_C should generally not be less than 6 hours. The reference time $T_R = T_{POP} + T_C$. (DNV GL, 2011a)

3.4.2 Hindcast Data

For weather restricted operations, it can be very useful to know the probability of having a sufficient weather window, as well as the expected waiting time for the operation. Time waiting, T_w , is the length of the period from the point being investigated until the first point after which a sufficient weather window is present. Decisions for an operation are normally made based on weather forecasts, but statistical hindcast weather data can also be quite useful in planning budgets, schedules and contingencies for operations (Chen and Mukerji, 2008).

Once the operational criterion has been determined, the probability of having such a condition is important to find. Many regions have data sets related to environmental conditions over a number of years. These provide a sufficient population with which statistical analyses can be conducted. One can define periods as both calm and storm, where calm refers to periods during which the environmental conditions are below the specified limit, and storms when they are above. This is depicted in Figure 3.7 where significant wave height is plotted as a function of

time. Linear interpolation between measurements is used. The relevant weather windows correspond to calm periods. The average duration of calms can be calculated based on hindcast data, and will give an indication of the duration of a weather window for a specific operating criteria or limit. If one considers significant wave height as the operating criteria, one can find the cumulative probability of a specific significant wave height H_s , denoted $P(H_s)$. H'_s is here used to denote the operating limit, OP_{WF} .

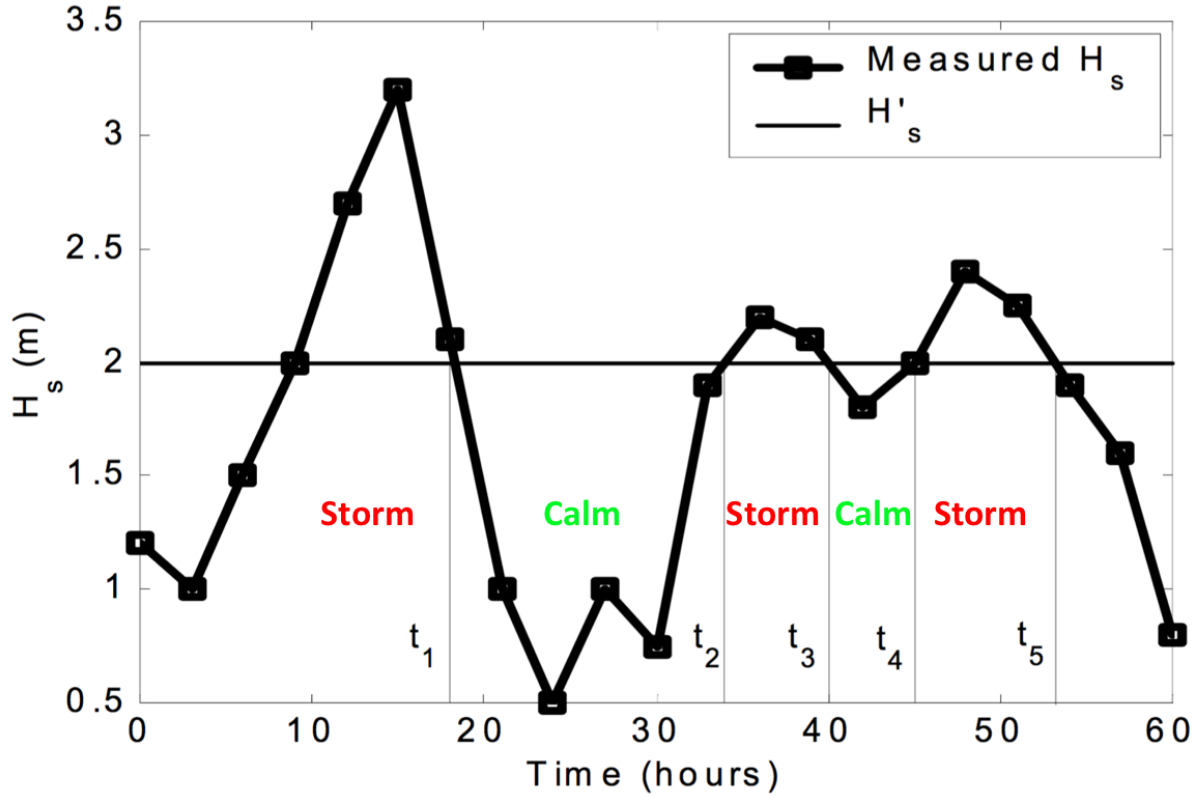


Figure 3.7: Storms and calms. (Nielsen, 2007)

The following is largely based on Larsen (2015). One can express the average duration of calms, $\bar{\tau}_c$, as:

$$\bar{\tau}_c = P(H'_s) \frac{T_{tot}}{N_c} \quad (3.51)$$

Here T_{tot} is the total duration of the time series considered, N_c is the total number of calm periods, i.e. number of times during which the significant wave height encountered, H_s , is less

than the limiting value H'_s .

It has been found that if one plots the average duration of calms $\bar{\tau}_c$ against the cumulative probability of significant wave heights $P(H_s)$, the relationship fits well to a two parameter Weibull distribution. The relationship can be expressed through Equation (3.52).

$$\bar{\tau}_c = A[-\ln(P(H_s))]^{-\frac{1}{B}} \quad (3.52)$$

These values of A and B vary for the specific region. For the North Sea, $A = 20$ and $B = 1.3$. A weather window however relies on two conditions:

1. Operating limit
2. Sufficient duration

As such the probability of having a weather window, later also referred to as the probability of working, will depend on two factors and can be expressed as:

$$P((H_s \leq OP_{WF}) \cap (\tau_c \geq T_R)) \quad (3.53)$$

Where τ_c is the duration of the the calm period and OP_{WF} the operational criteria. This can be rewritten as:

$$\sum_{H_s=0}^{H_s=OP_{WF}} P((\tau_c \geq T_R)|(H_s)) * P(H_s) \quad (3.54)$$

It has been found that the cumulative probability of the duration of a calm period can be expressed as a two parameter Weibull distribution as shown in Equation (3.55).

$$P(\tau_c \geq t) = e^{-\left(\frac{t}{t_c}\right)^\beta} \quad (3.55)$$

$P(\tau_c \geq t)$ is the probability that the duration of a calm period is greater than t . The values of t_c and β are unknown, and must be found. β can be determined from empirical data and varies with H_s . It is also dependent upon the season and location. Utilizing Equation (3.52), t_c can be determined based on the the following relationship (3.56):

$$\bar{\tau}_c(h) = t_c * \Gamma(1 + \frac{1}{\beta}) = A[-\ln(P(H_s))]^{\frac{1}{\beta}} \quad (3.56)$$

Solving this equation for t_c , one can plot the cumulative probability of length of calms expressed in Equation (3.55).

Now that both $P(\tau_c \geq t)$ for a given H_s and $P(H_s)$ are known, the probability of being able to perform an operation can be determined.

The accumulated available operational time can be found as:

$$T_{OP} = T_{TOT}P((H_s \leq OP_{WF}) \cap (\tau_c \geq T_R)) \quad (3.57)$$

3.5 SIMA

SIMA is a simulation workbench for marine applications that enables modelling and analysis within the field of marine technology. The SIMA simulation workbench includes a user-friendly interface and 3D graphics that allow the user to visualize and verify their model. Within SIMA, computer simulation programs can be run dependent on the simulations requirements. In this thesis, SIMO and coupled SIMO-RIFLEX were utilized. SIMA enables the user to introduce batches in which relevant parameters can be set as variables and altered. The results can then be run through a built in post-processor, and output files created for further processing if necessary.

3.5.1 SIMO

SIMO, or Simulation of Marine Operations is a computer program that solves the equations of motion in the time domain. This function allows for relevant motions and forces to be evaluated against acceptance criteria for an operation.

Modelling

SIMO applies various force and motion models based on the body type utilized. SIMO allows four different body types to be defined (SIMO Project Team, 2015). These are presented in Table 3.1.

Table 3.1: Body types.

Type 1	Large Volume	6 DOF	Time domain simulation
Type 2	Large Volume	6 DOF	Separation of motions in frequency domain HF motions and time domain LF motions
Type 3	Small Volume	3 DOF	Position dependent hydrodynamic coefficients are allowed
Type 4	Large Volume	6 DOF	Time domain simulation and fixed or prescribed body position

Distributed Elements

If a body is modelled as Type 1, distributed elements can be utilized to represent sections of the body. These can be either:

- Slender Elements
- Fixed Body Elements

Slender elements are long extended elements, whilst fixed body elements are concentrated elements at a fixed point. Distributed elements utilize small-body theory to calculate forces. The

forces acting on all the distributed elements are then transferred to the main body. Slender elements are divided into a predefined number of strips of equal length. Forces are calculated for each strip.

An entire body can be modelled using distributed elements. A structural mass must nonetheless be applied to the main body. This however can be defined as zero, and the structural mass attributed to the distributed elements. In this manner the moment of inertia will automatically be calculated. Alternatively, the distributed elements can be modelled without any mass, with the structural mass and relevant moments of inertia defined for the main body.

Small-body theory is utilized to calculate forces for distributed elements. External loads on an element strip consist of three contributions:

- Buoyancy forces, F_B
- Wave forces, F_W
- Slamming forces, F_S

The resulting force on a distributed element is the summation of the contribution on each strip.

Wave forces are calculated according to Morison's formula (SIMO Project Team, 2015):

$$F_w = (\rho V + A_i) \dot{v}_{r,i} + B_2 v_{r,i} |v_{r,i}| + B_1 v_{r,i} \quad (3.58)$$

where

A_i = Added mass in direction i [kg]

$v_{r,i}$ = Relative velocity between body and water particles in direction i [m/s]

\dot{v}_i = Wave particle acceleration in direction i [m/s]

and the final two terms are the quadratic drag term and the linear drag term. In addition to Morison's formulation, slamming forces are included in the hydrodynamic force calculations. The following formulation is adopted by SIMO:

$$F_s = \frac{\delta A_i}{\delta h} \frac{\delta h}{\delta t} v_{r,i} \quad (3.59)$$

Where h is the distance between instantaneous surface elevation and element origin in global Z-direction. (SIMO Project Team, 2015).

Coordinate Systems

SIMO utilizes orthogonal and right handed coordinate systems. Three coordinate systems are defined:

- X_G - Global coordinate system
- X_B - Local body coordinate system
- X_S - Local strip coordinate system

The global coordinate system is earth-fixed, and is used to define the position of all bodies in the model. The X-Y plane coincides with the free surface in calm water. The Z-axis points vertically upwards. Propagation of environmental parameters are defined based on this coordinate system. The position of a body defines the origin for X_B . One can then place distributed elements defined within X_B . This position again defines the origin for X_S .

Environment

During a dynamic simulation, wind, waves and current can be simulated. Wind can be modelled based on a chosen wind spectrum, and forces on relevant bodies calculated. Waves are simulated based on linear potential theory as discussed in Section 3.1.1. Regular and irregular waves can be modelled. For irregular waves, a number of wave spectra are available. Current velocity can be also be described explicitly or by the DnV profile.

Calculation Methods

The calculation of wave responses for various time steps can be performed in SIMO by the summation of harmonic components in the time domain. This entails a summation of sine or cosine series. Calculations are made for the instantaneous locations of all bodies or distributed elements. This method yields the most accurate wave kinematics and loads for all bodies (SIMO Project Team, 2015). This process is however quite time consuming. An alternative method is using Fast Fourier Transform (FFT) pre-generation of time series. This method however does not take into account variation in body depth. As such, a body will experience the same wave forces at all depths, and therefore not yield an accurate representation of reality. FFT generation is therefore not a viable option for subsea lifting operations.

SIMO conducts motion calculation via three numerical integration methods (SIMO Project Team, 2015):

1. Modified Euler Method
2. 3rd order Runge-Kutta-like Method
3. Newmark - β Predictor-Corrector Method

The user specifies which method is to be utilized in SIMA.

3.5.2 Coupled SIMO-RIFLEX

MARINTEK's Coupled SIMO-RIFLEX is used for the numerical analysis of the Free-Fall phase. The Coupled SIMO-RIFLEX software package combines the hydrodynamic calculation abilities of SIMO with RIFLEX's structural analysis of slender structures. The deployment line is in this case regarded as the slender structure. The use of Coupled SIMO-RIFLEX is required to capture the global response of the payload during the Free-Fall phase. The motions of the vessel and the dynamic forces in the deployment line are calculated simultaneously in time domain to output the global response of the payload.

Since SIMO is discussed earlier, this section is dedicated to present the RIFLEX software package. RIFLEX calculates the structural response of slender structures based on non-linear Finite Element (FE) formulation. This analysis only considers the total global motion response of the payload during the Free-Fall phase. The deployment line is the only component that will be evaluated based on an FE formulation. As such, a detailed theoretical description of the FE method will not be presented.

Lines can be modelled as beam elements with negligible horizontal stiffness. Nodes are attached at each end of the beam elements, and supernodes at the beginning and end of defined lines. For a more detailed description of the theory governing the RIFLEX model formulations, the reader is referred to MARINTEK (2011).

Chapter 4

Methodology

4.1 Acceptance Criteria

In a subsea installation operation, it is essential to determine operational limits such that the integrity of the operation is maintained. Such operational limits are normally outlined by a limiting sea state. Any sea state that excites loads over a given acceptance criteria are unacceptable. The following sections outline the acceptance criteria for the In-Air, Splash-Zone and Free-Fall phases of the Pendulous Installation Method.

4.1.1 In-Air

During the In-Air phase, criteria related to the motion of the Dual Cap-X will need to be evaluated. Motion that can result in damage to assets and injury to personnel must be avoided. This will vary significantly between different operations, and acceptance criteria will need to be evaluated on a case to case basis. In general, motion that does not result in injury to personnel or the payload hitting the vessel during lowering will govern the acceptance criteria. This will be a subjective evaluation, and conservative assumptions should be made to ensure the integrity of the operation.

4.1.2 Splash-Zone

For a subsea lifting operation, acceptance criteria are outlined in DNV GL (2014). The following forces will be evaluated:

- Lifting wire tension
- Tension in slings

Due to the significant added mass when the payload is lowered through the splash-zone as well as the effect of vessel motion and other hydrodynamic forces, the dynamic lifting line load may potentially considerably exceed the static load. Water particle kinematics is also generally large in the splash-zone contributing to significant dynamic loading.

To preserve the structural integrity of the hoisting system and the safety of the operation, a maximum allowable load in the lifting wire should be implemented. This can be taken as the crane capacity at the radius of deployment. The crane winch may have a lower capacity, but it is not taken into account in this analysis. The crane capacity is based on a Safe Working Load (SWL), which includes a DAF. In the case of subsea lifting, DNV GL (2014) recommends $DAF = 1.3$. As such crane manufacturers often incorporate this value into the SWL for offshore operations. This is the case for the crane investigated in this thesis. The actual crane capacity can therefore be found by multiplying the DAF utilized with the given SWL as seen in Equation (4.1). These values are readily available by the crane manufacturer. It should be noted that the DAF referred to in Equation (4.1) is not the actual DAF experienced by the crane during the lifting operation.

$$\text{Crane Capacity} = \text{SWL} * \text{DAF} \quad (4.1)$$

As such DNV GL (2014) states that the maximum allowable lifting line tension must not exceed the crane capacity. This value provides the upper bound for the allowable lifting line tension. This is expressed in Equation (4.2):

$$T_{LW} < \text{Crane Capacity} \quad (4.2)$$

where T_{LW} is the lifting wire tension.

In order to avoid slack in lifting line and slings, DNV GL (2014) recommends that the following criteria are adhered to:

$$T_{LW} > 0.1 * T_{static}$$

$$T_{sling} > 0$$

Where T_{static} is the static weight of the payload in air and T_{sling} is the tension in any sling utilized. These values represent the minimum or lower bound of the tension allowed in the lifting system.

It should be noted that in some cases the dynamic re-tensioning of the lifting line after slack condition may still be within the maximum acceptable lifting line tension. Considering the uncertainties associated to snap loading of the lifting line, a detailed analysis of this phenomena is not considered in this thesis. Instead, it is assumed that the design criterion is limited by the occurrence of slack in the line.

DNV GL (2014) cites that the probability of exceeding the calculated extreme characteristic load in the operation period must not exceed 10 %. An appropriate distribution should be utilized, and the tail of the distribution checked. For this thesis a Gumbel distribution is utilized to fit the extreme values. In the case of maximum values, the 90th percentile is investigated, and for minimum values, the 10th percentile. In this manner one can identify the 10 % most extreme values dependent on whether the extreme is defined as minimum or maximum.

Table 4.1 gives the calculated values used as acceptance criteria in this thesis for the splash-zone analysis of the Dual Cap-X. The crane capacity is based on the capacity diagram found in Appendix B for the model conditions.

Table 4.1: Calculated acceptance criteria values for splash-zone analysis of the Dual Cap-X.

SWL [kN]	Maximum Allowable Lifting Line Tension [kN]	Minimum Allowable Lifting Line Tension [kN]	Minimum Allowable Tension in Slings [kN]
2940	3820	164	> 0

In summary, the objective of determining the lifting line tension is essential for the success of the operation. Furthermore, the load characteristics have a significant impact on the decision making in the planning phase in terms of vessel, lifting gear and rigging selection, and determining the accessible sea states (Ireland, 2007).

4.1.3 Free-Fall Analysis

The nature of the dynamic forces and the local behaviour of the payload during the Free-Fall phase are highly complex. The complex dynamic picture may introduce effects such as fluttering as discussed by Fernandes (2010) and twisting of the payload which may cause difficulties in controlling the pendulum fall through the water column. From an operational perspective, investigating the global response is most relevant.

This thesis studies the parameters that influence the operability during the Free-Fall phase. These parameters are identified mainly as:

- Duration of the Free-Fall phase (from drop til the payload is at a rest over the target zone)
- Top tension (at the connection point between deployment line and vessel)

The acceptance criteria related to the top tension should ensure that the integrity of the winch and deployment line are maintained. This means that the tension should not exceed the maximum capacity of either.

Since operational limits of the pendulum free-fall phase are to be investigated, it is not necessary to set intrinsic acceptance criteria related to the duration of the Free-Fall phase. As such, the

investigation of this parameter will be in more relative terms.

4.2 Numerical Analysis in SIMA

4.2.1 Assumptions

The numerical simulations were conducted under the following assumptions.

- The Dual Cap-X is installed without hatches or relevant subsea hardware (e.g. X-mas trees)
- Air cushioning effects in the suction cans are minimal
- Slings are assumed to be dimensioned to handle the relevant loading
- The winch on Vessel A pays out the line attached to the payload at a rate such that it has no significant effect on the global response during the free-fall phase. The weight of the line is assumed to be supported by Vessel A
- The lifting crane is assumed to be rigid

4.2.2 Environmental Modelling

Waves

The modelling of waves was conducted based on the environmental conditions present at the Heidrun field. Significant wave heights and peak periods within the 1 year extreme contour line shown in Figure 4.1 are relevant for investigation.

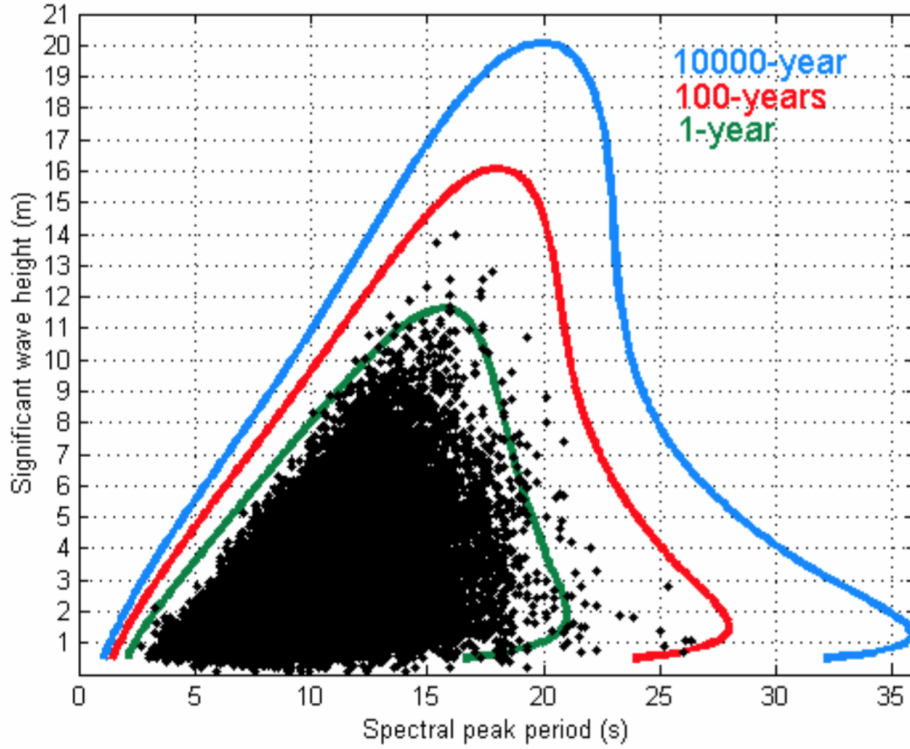


Figure 4.1: 1, 10, 100 and 10000-year extreme contour lines in the $H_s - T_p$ plane (Statoil, 2004).

Waves were modelled using a 2-parameter JONSWAP spectrum. The non-dimensional peak shape parameter γ is calculated based on the H_s and T_p input. For values between $3.6 < \frac{T_p}{\sqrt{H_s}} < 5$, γ is calculated as:

$$\gamma = \exp\left[3.484\left(1 - 0.1975\delta\frac{T_p^4}{H_s^2}\right)\right]$$

where

$$\delta = 0.036 - 0.0056\frac{T_p}{\sqrt{H_s}}$$

as outlined in SIMO Project Team (2015) and conforms to the recommendations by DNV GL (2011b). SIMO Project Team (2015) outlines that for values in which $\frac{T_p}{\sqrt{H_s}} \leq 3.6$, $\gamma = 5$ is implemented while for $\frac{T_p}{\sqrt{H_s}} \geq 5$, $\gamma = 1$ is implemented. Values far outside the ideal region for the JONSWAP spectrum can alternatively be more accurately modelled with a Torsethaugen spectrum. This was assumed unnecessary for the cases evaluated in this thesis based on the values

in the one year contour for Heidrun. The H_s and T_p values used are specified for each analysis.

Wind

Wind was modelled using an ISO19901-1 (NPD) wind spectrum. The direction and average velocity are taken as input. Using the NPD spectrum, the wind velocity may be simulated in the time domain by use of a state space model.

Current

The current used in this thesis is based on the conditions at an undisclosed production block outside the coast of Tanzania owned by Statoil. The following is based on the Metocean Design Basis for this area (Statoil, 2010).

The dominant current in this area is the East African Coastal Current, and the current conditions can be considered to be relatively significant. Statoil has performed current measurements at site using Acoustic Current Doppler Profilers. Based on hindcast data, statistical information on the current conditions has been developed.

In this thesis, the current data used by Statoil in their analysis of the block has been chosen. As such, the current data used in this thesis is presented in Table 4.2. The data is based on measurements from the period March 2009 to April 2010. Since the water depth at the site outside the coast of Tanzania is around 2000 m, the current value at the bottom was "moved" to a water depth of 3000 m (which is used in this thesis). In this way, similar bottom conditions were achieved. It should also be mentioned that SIMO uses linear interpolation between each given value. The current data given here is primarily used in the Free-Fall phase, and both maximum and mean current speeds are used. The current directions are specified for each application.

Table 4.2: Current data used in model (Statoil, 2010).

Depth below MSL [m]	Maximum Current Speed [m/s]	Mean Current Speed [m/s]
0	1.38	0.7
47	1.35	0.56
108	1.33	0.47
147	0.85	0.38
207	0.82	0.30
307	0.79	0.25
508	0.63	0.21
748	0.52	0.17
1008	0.52	0.14
1410	0.34	0.10
2982	0.26	0.06

4.2.3 The Installation Vessel

The installation vessel utilized in the numerical analysis conducted in this thesis is the construction support vessel Skandi Acergy. The model is used in both the splash-zone analysis and the pendulum free-fall analysis.

Vessel dimensions are given in Table 4.3. The RAOs of the Scandi Acergy for all degrees of freedom and different wave directions were provided by Statoil, and implemented into SIMO and Coupled SIMO-RIFLEX.

Table 4.3: Vessel dimensions.

LPP [m]	LOA [m]	Breadth [m]	Draught [m]
137.7	156.9	27	6.4



Figure 4.2: The Scandi Acergy. Courtesy of DOF.

4.2.4 SIMO - Splash-Zone Modelling

As mentioned before, a real challenge is to determine accurate added mass and drag coefficients for complex structures as the Dual Cap-X. Normally, model testing should be performed in order to achieve more accurate estimates. However, due to natural limitations of the scope of this thesis, coefficients based on historic test data and analytical approaches have been utilized. For example, the added mass of the Dual Cap-X is found by dividing the payload into smaller components with more regular and well-known geometries. The total added mass is then found by summing the contributions from each component.

Figure 4.3 shows the final Dual Cap-X model and the lifting equipment as modelled in SIMO. The Dual Cap-X is modelled as a Body Type 1 with 6 DOF (see Table 3.1). This was done in order to be able to model the suction cans and the frame as a fixed body element and slender elements, respectively. As such, even though the whole body is defined as a large body, the suction cans and the frame are treated as small bodies in SIMO. Furthermore, the two suction cans of the Dual Cap-X is for simplicity modelled as one suction can. Thus, the single suction can in the model represents the hydrodynamic properties of two suction cans. Even though some interaction effects will be lost in SIMO, hydrodynamic coefficients for twin cylinders are implemented in order to account for some of the effect of having two suction cans. This is discussed in Section 4.2.4.

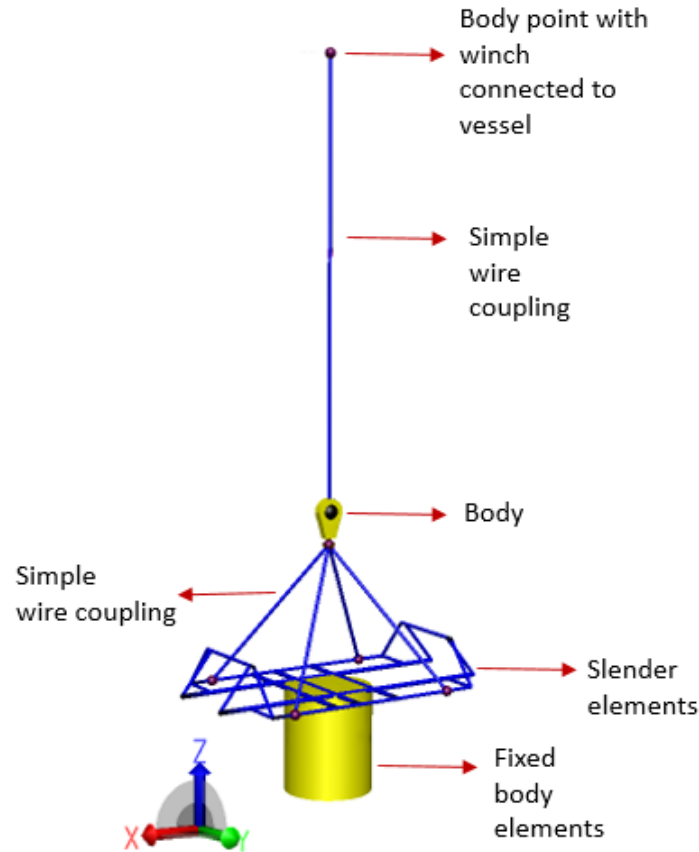


Figure 4.3: Visualization of the SIMO payload and lifting equipment model.

Table 4.4 lists the mass properties of the payload. The moments of inertia are given with respect to the local body coordinate system.

Table 4.4: Mass properties of the Dual Cap-X.

Mass [kg]	I_{xx} [kgm^2]	I_{yx} [kgm^2]	I_{yy} [kgm^2]	I_{zx} [kgm^2]	I_{zy} [kgm^2]	I_{zz} [kgm^2]
1.6751×10^5	1.4341×10^{18}	3.9265×10^{16}	2.6545×10^{18}	-7.9935×10^{15}	-4.4518×10^{16}	2.8451×10^{18}

Simulations were conducted using Runge-Kutta integration and cosine wave method.

The following subsections describe how each part of the model is built, and how their hydrodynamic properties are estimated.

Suction Can Modelling

The Dual Cap-X is made up of two suction cans which are connected by a stiffener plane. Although there most probably will be interaction effects due to the close proximity of these to suction cans to each other, it is very difficult to accurately describe these phenomena and correctly include them when estimating the hydrodynamic coefficients.

The added mass coefficient in heave in infinite fluid for a flat plate disk is given in Table D-2 in Appendix D in DNV GL (2010). This represents the top plate of the suction. In addition, DNV GL (2011b) requires that the water inside the suction can should also be included in the added mass. The uncoupled added mass coefficients in surge and sway are found by using the added mass coefficients in infinite fluid for the twin circular cylinders presented in Øritsland (1989, p.7.5) to better capture the interaction effects between the two cylinders.

The added mass is influenced by the free surface, and will depend on the submergence depth. Both Næss et al. (2014) and Plummer et al. (2009) argue that the heave added mass of a single suction can is practically negligible from when the bottom of the suction can penetrates the surface up to the point of time when the top is about to penetrate the surface. The added mass coefficient is therefore defined from when the top of the suction cans penetrate the surface in this analysis. Næss et al. (2014) have provided a graph based on model tests that can be utilized to determine the the submergence depth dependency of the heave added mass of a vertical suction can (see Figure 4.4). This relationship has been implemented into SIMO, and provides the basis for the calculation of the slamming forces. The depth dependent coefficients are applied to the total added mass for both suction cans. The depth dependency of the surge and sway added mass coefficients is assumed minimal, and has not been implemented into SIMO.

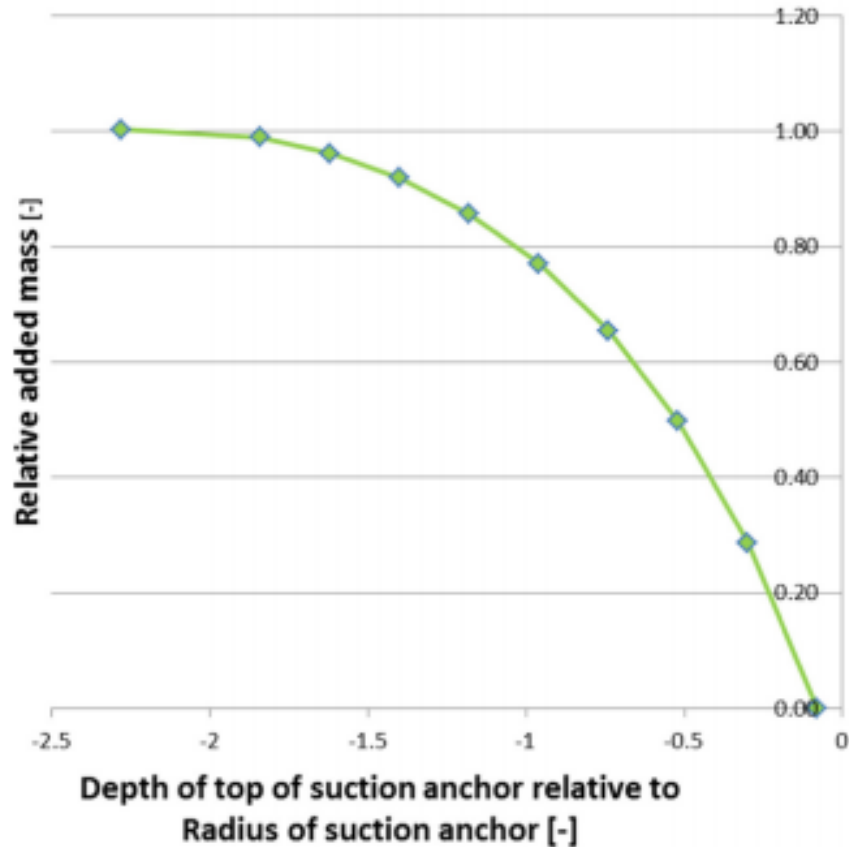


Figure 4.4: Depth dependency of heave added mass for vertical suction cans (Næss et al., 2014).

Table 4.5 shows the depth dependent relative hydrodynamic coefficients implemented into SIMO. The vertical position is defined as the position of the top of the suction can in relation to the water surface. SIMO automatically performs a linear interpolation between each step. It was important to implement sufficient number of steps in order to better capture the depth dependency of the vertical added mass suggested by Næss et al. (2014). It can be observed that the large increase in added mass at the beginning is captured by having larger space between the first couple of steps, compared to the end.

Table 4.5: Depth dependent hydrodynamic coefficients.

Vertical Position [m]	$RC2_x$ [-]	$RC2_y$ [-]	$RC2_z$ [-]	RA_x [-]	RA_y [-]	RA_z [-]
6.035	0	0	0	0	0	0
0	1	1	1	1	1	0
-0.197	1	1	1	1	1	0
-0.75	1	1	1	1	1	0.3
-1.35	1	1	1	1	1	0.5
-1.87	1	1	1	1	1	0.666
-2.45	1	1	1	1	1	0.775
-3.0	1	1	1	1	1	0.86
-3.38	1	1	1	1	1	0.916
-4.1	1	1	1	1	1	0.97
-4.67	1	1	1	1	1	0.989
-5.77	1	1	1	1	1	1

The drag coefficient in heave for the suction cans is based on the tabulated value of a simple circular cylinder with axis parallel to flow given in Table B-2 in Appendix B in DNV GL (2011b). For a height/diameter ratio of $L/D=1.2$, the drag coefficient in steady flow is approximately $C_{ds}=0.90$ for Reynolds numbers $Re > 10^3$. The drag coefficient is corrected to capture that the suction cans differs from the cylinders by having open bottoms. A closed vertical cylinder lifted through the splash-zone will have a flow stagnation point at bottom of the body. While a cylinder with an open bottom will have inflow into the body and the stagnation point will thus occur on the backside of the cylinder top. The extra flow distance inside the body will therefore cause a larger pressure at the stagnation point, than in the case of a closed cylinder. This means that it is expected that the drag coefficient in heave for the can is higher than for a closed cylinder. As a rough approximation, it is therefore increased approximately 20% (based on comparisons of a hemisphere and a open cup given in Øritsland (1989, p.4.3)) to $C_{ds}=1.08$. The two cylinders are placed in tandem along the X-axis. Due to the close proximity of the suction cans, interaction between the suction cans will arise. The drag coefficients in the X-direction (one placed behind

the other) and in Y-direction (both parallel to each other) can be approximated by using the hydrodynamic data given for circular cylinders in twin arrangements in Blevins (1984, p.7.6).

It should be pointed out that the drag coefficients found are for steady flow, due to the lack of available experimental results on drag coefficients for oscillatory flow for more complex geometries. As pointed out by Øritsland and Lehn (1987), C_{dd} varies with KC number and is often 2-3 times larger than C_{ds} . As a result, using C_{ds} values in the splash-zone is expected to overestimate resonant motions of the system when the drag force acts as a damping force (DNV GL, 2011b). However, due to the small eigenperiod in heave for the suction can, resonance in heave is unlikely to occur in the splash-zone. As such, the use of C_{ds} in heave is seemingly reasonable. A sensitivity study of the drag coefficients is performed in Section 5.4.2.

Table 4.6 shows the fully submerged quadratic drag and added mass along each local axis (see Figure 4.3 for axis reference), based on the discussion on estimating hydrodynamic properties of the suction cans presented above. Since the payload has been modelled with only one suction can for simplicity, these values actually represent the hydrodynamic properties of two suction cans as in the original concept.

Table 4.6: Modelled hydrodynamic properties of the suction can

Quadratic Drag [Ns^2/m^2]			Added Mass [kg]		
C_{2_x}	C_{2_y}	C_{2_z}	A_x	A_y	A_z
9019.0	29462	20536	2.6107×10^5	2.7514×10^5	3.0795×10^5

Quadratic wind coefficients are modelled using the same drag formulations as for the hydrodynamic coefficients. The values presented in Table 4.7 were implemented in the model. Symmetry about the X-axis was defined. Values are defined with respect to the local body coordinate system.

Table 4.7: Quadratic wind coefficients.

Quadratic Wind Coefficients [Ns^2/m^2]

Direction [°]	$C2_x$	$C2_y$	$C2_z$
0	10.8	0	0
45	5.4	17.6	0
90	0	35.2	0
135	5.4	17.6	0
180	10.8	0	0

Frame Modelling

The upper frame of the Dual Cap-X was modelled using slender elements. The model was simplified based on CAD drawings supplied by Statoil (Statoil, 2016). The main dimensions were retained as well as the general layout the structure, but detailed elements were omitted. It was assumed that the general behaviour of the model would be maintained despite the alterations. The position of each slender element was calculated relative to the center of gravity and the resultant model can be seen in Figure 4.3.

Each element was then given attributes that matched those of the Dual Cap-X. The frame itself is comprised of multiple I-beams of various profiles. Data relevant to these is taken from European standard I sections. The cross sectional area of the I-beams was used as the cross-sectional area of the slender elements to accurately model the buoyancy forces associated with them. Mass was however neglected as it was included in the total body mass, and would as such be redundant. The hydrodynamic coefficients for each slender element were calculated based on tabular values found in Øritsland (1989, p. 3.17). Added mass and quadratic damping terms in heave, surge and sway were calculated based on the dimensions of the I-beam profiles in the relevant directions. These values were defined for a local slender element coordinate system. As such, values in surge were assumed to be negligible due the cross-sectional area of the elements, and therefore set to zero. Relevant calculations can be found in Appendix D.3.

Lifting Equipment Modelling

The crane, winch, lifting line, hook and slings are the components of the lifting system included in the SIMO model. The winch is attributed to a body point connected to the vessel representing the crane tip. Winch properties include speed, acceleration and maximum wire length at the drum. It is also possible to assign different time intervals with specific winching speeds. The winching speed was set to 0.5 m/s in the base case and for all sensitive studies. Moreover, the crane tip is located midships and approximately 40 m over the vessel deck. The lifting line between the crane tip body point and the body point on the hook (see Figure 4.3), is modelled as a simple wire coupling. The lifting line is a steel wire with cross sectional stiffness $EA=965$ MN (Wang et al., 2013). Furthermore, the model also includes four equal slings. They are modelled as simple wire couplings and have the same wire characteristics as the lifting line in order to simplify the model. The hook is modelled as a small-volume body (Body Type 3) without hydrodynamic properties, since its presence will have negligible impact on the dynamics in the lifting line compared to the payload.

The crane is assumed as rigid compared to the lifting line, and as such constitutes a simplification of the lifting system. This assumption may introduce some deviation in the lifting line tensions in the numerical time domain analysis compared to reality, especially when the lifting line length is short (such as at the start of the Splash-Zone phase). However, since the natural frequency in heave of a typical offshore lifting system is very low compared to common wave periods, the effect of neglecting crane stiffness is assumed to be reasonable (even when taking into account that the crane stiffness may change the natural frequency of the lifting system).

Vessel Modelling

The installation vessel used in this thesis is the Skandi Acergy and is presented in Section 4.2.3. For the Splash-Zone phase, the vessel is modelled as a large volume body with the following properties provided by Statoil:

- Structural Mass

- Linear Damping
- Hydrostatic stiffness for coupled motions
- Vessel RAOs

Build-Up Period

In order to reduce the influence of transients, the waves and the motions of the vessel is allowed a build-up period of 100 s. In this way, the transients related to the development of the sea state from still to a fully developed state are minimized on the subsequent splash-zone lowering.

4.2.5 Coupled SIMO/RIFLEX

The final stage of the installation of the Dual Cap-X at 3000 m water depth is the Free-Fall phase. The behaviour of the the payload and deployment line during this phase is highly complex, and accurate modelling is difficult. In order to most accurately model this phase, Coupled SIMO-RIFLEX was utilized. This allowed for the Dual Cap-X to maintain a high degree of accuracy with respect to hydrodynamic coefficients and general dynamic behaviour whilst introducing finite element modelling of the deployment line. In this manner, the free-fall stage should be relatively accurate when studying the global response. Nonetheless, the model is still too crude to gain a full representation of the detailed local behaviour in free-fall.

The model was designed to illustrate the effect of allowing the Dual Cap-X to free-fall from a water depth of 50 meters down to 3000 m. It was determined that the line should be 2900 m long to allow for elastic elongation of the fibre rope. The Dual Cap-X was connected to the slender system using a supernode at the payload connection point. Modelling of the slings was not possible in Coupled SIMO-RIFLEX. In order to capture the effect of the slings the payload was modelled at a distance corresponding to the vertical distance between the crane tip and payload. This can be seen in Figure 4.5. The center of gravity was also offset to the correct position.

Dual Cap-X

The Dual Cap-X (frame and suction cans) model is imported from the splash-zone analysis. The modelling of the payload is described in Section 4.2.4.

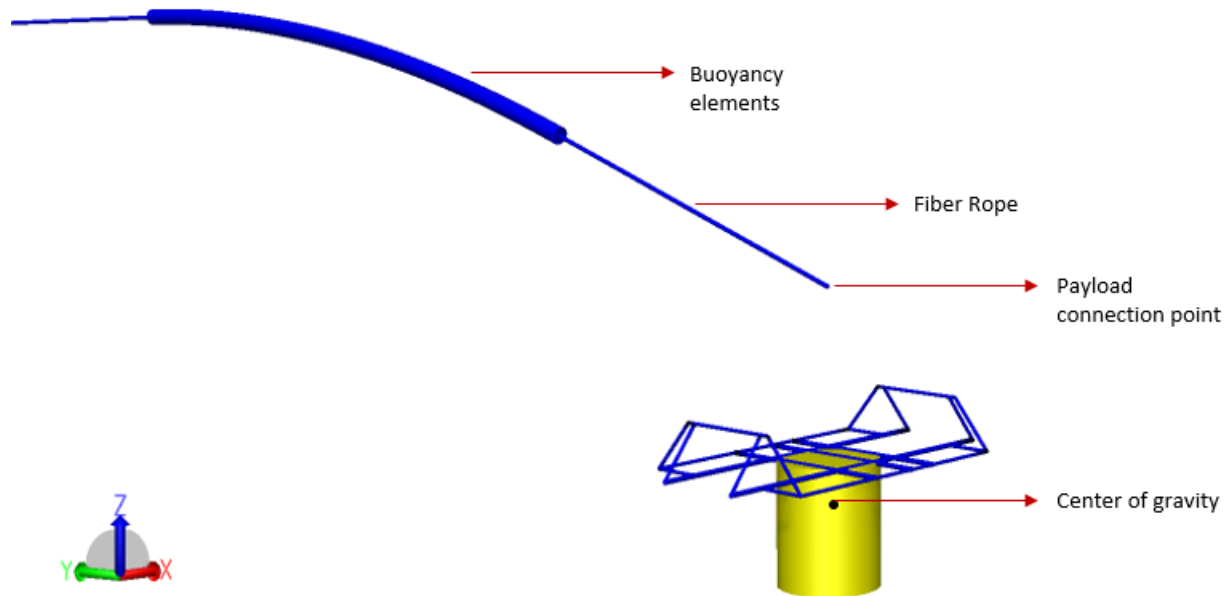


Figure 4.5: Visualization of the SIMO-RIFLEX payload model. The figure shows the configuration at the start of the drop.

Slender System

The fibre rope deployment line was modelled using slender elements in RIFLEX. In order to maintain bending stiffness in the model, beam elements were utilized to model the fibre rope deployment line. The basis of the slender system in RIFLEX is the cross section that can be attributed to a given line in the model. The cross section for the HMPE deployment line was given the following characteristics based on given values for HMPE rope.

Table 4.8: HMPE cross sectional data.

Diameter [mm]	Axial Stiffness [MN]	Bending Stiffness [Nm^2]
150	250	155

This cross section was then attributed to a line type. The line type divides the line into a desired number of sections. Each section can then be given section specific attributes such as length, number of elements as well as additional components on the line. It was determined that in order to effectively model the HMPE deployment line it should be divided into three sections. In this way the buoyancy elements on the deployment line as outlined in Section 2.2 could effectively be implemented. As seen in Table 4.9, an external wrapping is given to section 2 of the deployment line model. The external wrapping is defined per meter, and can be given buoyancy characteristics as a volume per unit length. It can also be modelled to act only along a certain percentage of each element within the section. In this manner one can create separate buoyancy elements at a given distance from each other instead of one continuous element for the entire section. The buoyancy or external wrapping elements can be seen in Figure 4.5.

Table 4.9: Deployment line sectional data.

	Section 1	Section 2	Section 3
Length	2840 m	40 m	20 m
Components	None	External Wrapping	None

The HMPE deployment line is defined between two supernodes, one at the payload connection point located 50 m below the mean sea level, and the other at the location of the vessel.

Vessel Modelling

The vessel utilized in the free-fall model is the same as that for the splash-zone and is discussed in Section 4.2.3. In SIMO-RIFLEX however, the vessel is not modelled as a body, but as a support vessel. This implies that only the RAOs for the vessel will be utilized in the model, and the structural mass attributes will not be implemented. As such, the movement of the vessel as a result of environmental effects will transfer to the supernode it is connected to. The kinetics of this vessel connection point will then provide the basis for excitation of the deployment line and payload due to vessel excitation.

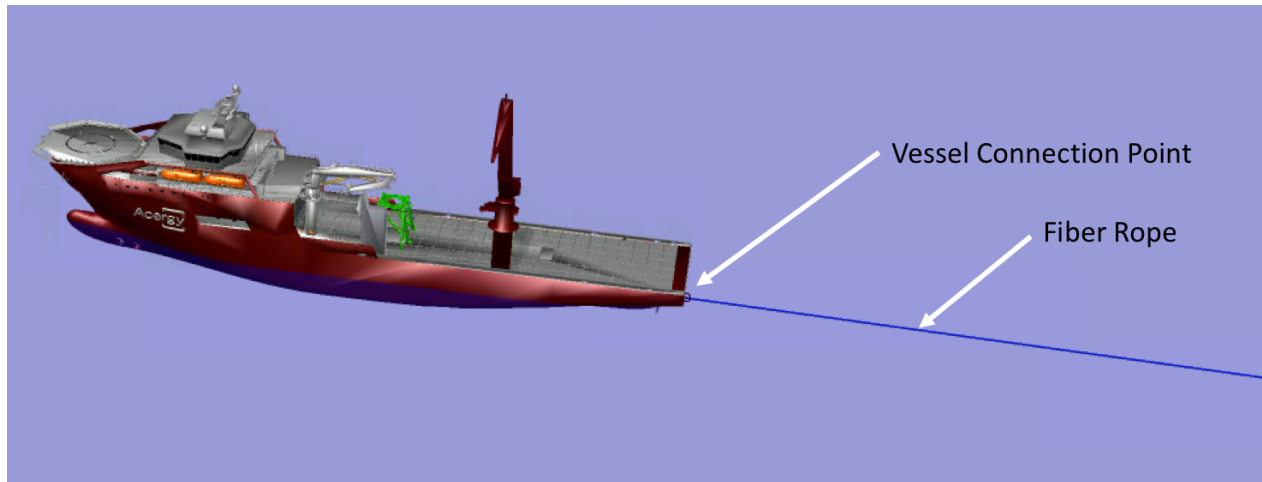


Figure 4.6: Visualization of the SIMO-RIFLEX vessel model connected to the fiber rope slender system.

Boundary Conditions

In order to facilitate the free-fall motion of the pendulous phase, a boundary condition change was utilized. Initially, the payload connection point (supernode) was fixed in all degrees of freedom. This allowed for the static analysis to reach equilibrium. After 150 seconds, the boundary conditions are altered such that all degrees of freedom for the supernode are free. When this occurs, the payload begins to drop. 150 seconds was chosen such that transient effects are eliminated. The supernode connected to the vessel was fixed to the vessel (see Figure 4.6), but rotational degrees of freedom were set free.

Payload Trajectory

Figure 4.7 shows how the free-fall model is set up in terms of the global coordinate system. The main pendulous motion occurs in the Y-Z plane (note that the payload is also free to translate in X-direction).

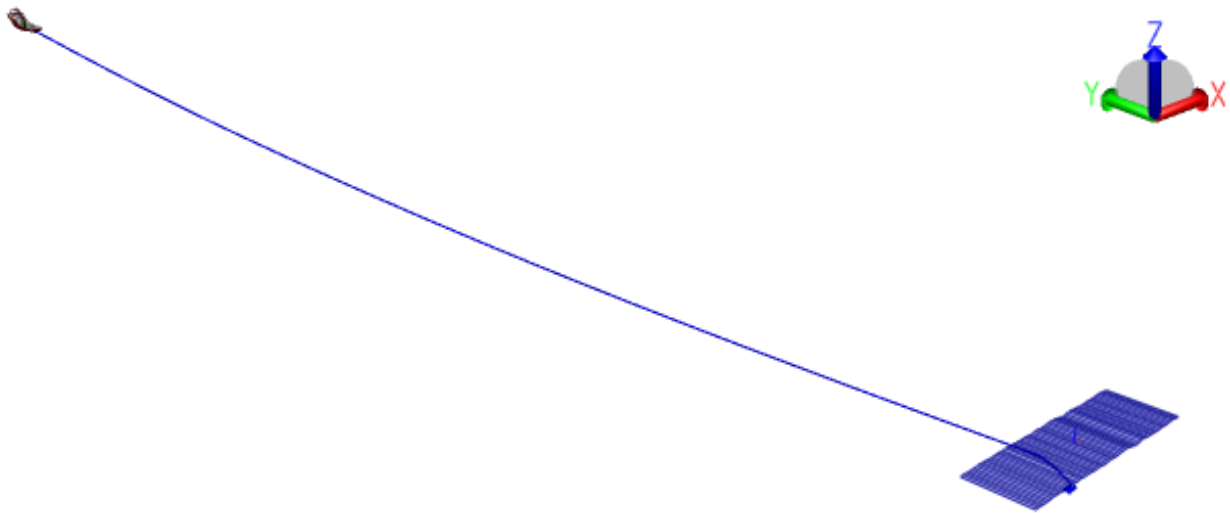


Figure 4.7: Definition of coordinate system.

Figure 4.8 shows the payload trajectory in terms of the global coordinates.

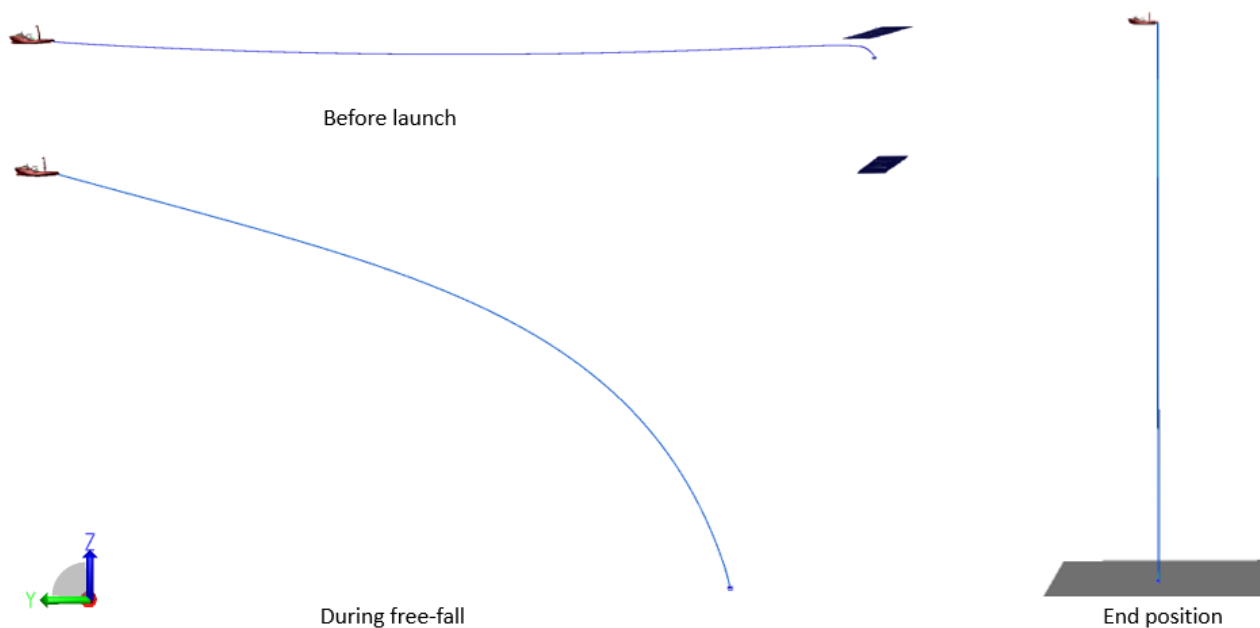


Figure 4.8: Payload trajectory.

This means that translation in Y-direction is defined as the horizontal direction towards the connection point at the vessel in global coordinates, while translation in negative Z-direction is towards the sea bed. The vessel is offset from the global origin in Y-direction. As such the connection point between vessel and deployment line is located at $Y=2900$ m. Taking the length

of the deployment line, and the location of the center of gravity of the payload into account, the final position of the payload after the pendulous free-fall should be $X=0$ m, $Y=2900$ m, $Z=-2910$ m (excluding axial elongation of the deployment line) in global coordinates.

4.2.6 Model Verification

Splash-Zone Model

In order to reveal any potential faults in the SIMO model such as wrong input of hydrodynamic coefficients or incorrect structural modelling of the payload, the lifting line tension in still water has been investigated. The purpose is to check whether the results capture the expected dynamic picture.

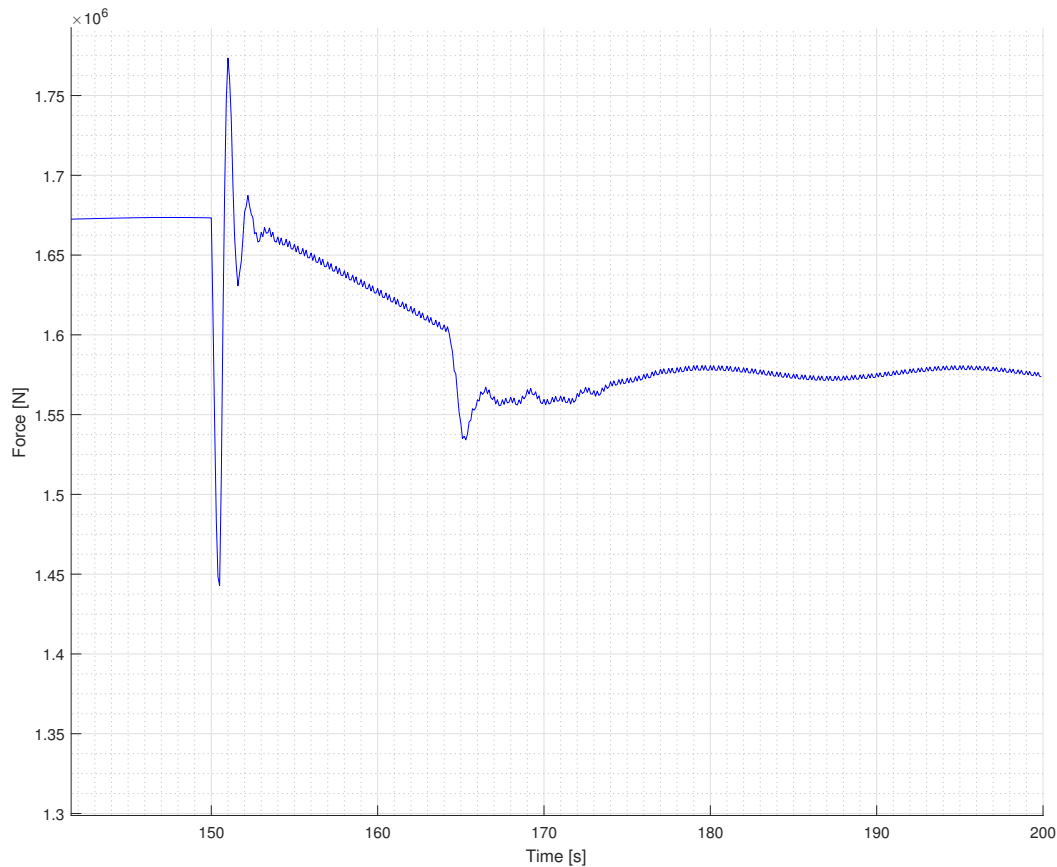


Figure 4.9: Time series of the lifting line force in splash-zone for no waves.

Figure 4.9 presents the lifting line tension for the verification study. The start tension in the lifting wire before winch start is around 1.7 MN, which constitutes the weight of the payload. The winch is started at 150 s at a speed of 0.5 m/s with the top of the suction can around 6.8 m over the water surface. As the winch is started, a relative large drop in the lifting tension with subsequent tensioning can be observed. This is due to inertia force, $(M + A_{33})\ddot{\eta}$, in air (negligible vertical added mass) caused by the winch's acceleration at start. The bottom of the payload penetrates the water surface at around 152 s, and as expected the results shows an linear reduction in the lifting line tension due to the increasing buoyancy force and vertical drag force. After around 165 s, the top of the suction can is just below the water surface. At this point, a simple calculation of the quadratic drag term and the buoyancy term in (3.39) gives a force of around 7.1 kN working upwards on the payload. The tension in the lifting line at this point of

time seems correspond well with this calculated value. Subsequently, a slamming force occurs which can be seen as a drop in the tension in the lifting line. The slamming force in the figure corresponds with the input of the depth dependent relative vertical added mass input in SIMO. After the slamming force, the dynamics in the lifting force are as expected very small.

Summing up, it may be concluded that the results suggests good coherence with the expected dynamic picture, and that the model is acceptable for use in further analysis. A break-down of the contributions from the hydrodynamic forces on the lifting line tension is presented in Section 5.2.7. These forces are then used to reconstruct the lifting line tension. Subsequently, these values are compared with the total lifting line tension obtained from SIMO, and as such also serves as a type of verification of the model.

Free-Fall Model

Similar to Section 4.2.6, this section presents a verification study of the Free-Model in Coupled SIMO-RIFLEX with the purpose to uncover potential faults in the modelling. The numerical time domain analysis used in this verification study is performed with no current and irregular head waves from a JONSWAP spectrum with $H_s=4$ m and $T_p=8$ s. The payload is launched after 150 s.

Figure 4.10 presents the payload trajectory during the pendulous free-fall in the Y-Z plane. The positions are given in the coordinate system defined in Section 4.2.5. As expected, the results indicate the payload moves more quickly through the payload trajectory at the start, compared to when it approaches the bottom point of the trajectory. This is due to the weight of the payload causes a larger moment about the pivot point when it is closer to the horizontal line, compared to later in the trajectory. The duration of the free-fall is around 45 min.

As stated in Section 4.2.5, the final position of the payload should be $X=0$ m, $Y=2900$ m, $Z=-2910$ m. The Z-position given here does not account for axial elongation of the deployment line. By performing a rough calculation using the axial stiffness of the deployment line and the payload weight, a reasonable axial elongation for a 2900 m deployment line is expected to be around 10

m. By inspection of the final Z-positions, this axial elongation seems to correlate well with the results. The small oscillations in the vertical position at the end of the free-fall seems to be a result of vessel motion caused by the surface waves.

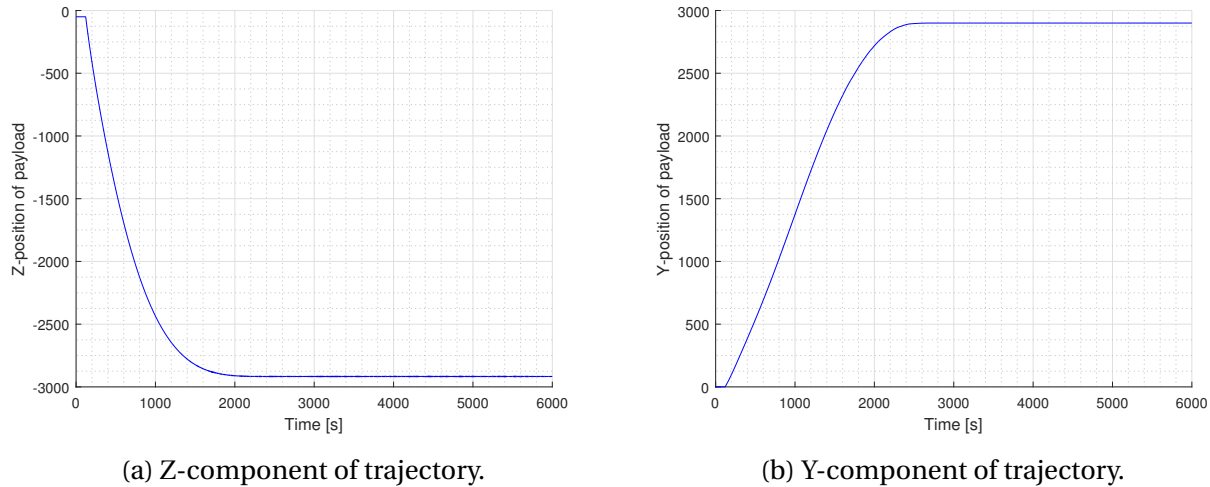


Figure 4.10: Payload trajectory in Y-Z plane.

Figure 4.11a shows the top tension during the free-fall. The top tension is here defined as the axial force in the line element connected to the vessel. The results shows that there is an gradual increase in the top tension as the payload moves through the pendulum trajectory. The trend seems to correlate well with the time series of the position of the payload, as the top tension increases as more and more of the payload weight is supported by the tension in the top line element. As the payload reaches the end position, the top tension seems to oscillate about a mean tension around 1.3 MN. This force matches well with the weight of the payload when taking into account the buoyancy force caused by the buoyancy elements attached to the deployment line.

Figure 4.11b shows the time series of the vertical velocity of the payload, while Figure 4.11c shows the vertical acceleration. As the payload is launched, there is an spike in the vertical acceleration downward. Subsequently, it exercises oscillatory behaviour about zero acceleration, which is mainly caused by vessel motions. Comparing the vertical acceleration and vertical velocity with the top tension, it can be understood that drag forces are the most dominating hydrodynamic forces during the free-fall with respect to the top tension. As the payload reaches the end position, both inertia forces and drag forces are important. These forces are mainly

caused by wave excited vessel motions. When the payload is at the end position, the assumption of a rigid crane is more acceptable than at lower water depths, since the deployment line constitutes the main source of vertical elasticity in the system at large wire lengths. This is also pointed out by Sarkar and Gudmestad (2010). However, the relatively high oscillatory behaviour of the top tension present when the payload has reached the final position may indicate that the deployment line is modelled with a relatively high axial stiffness.

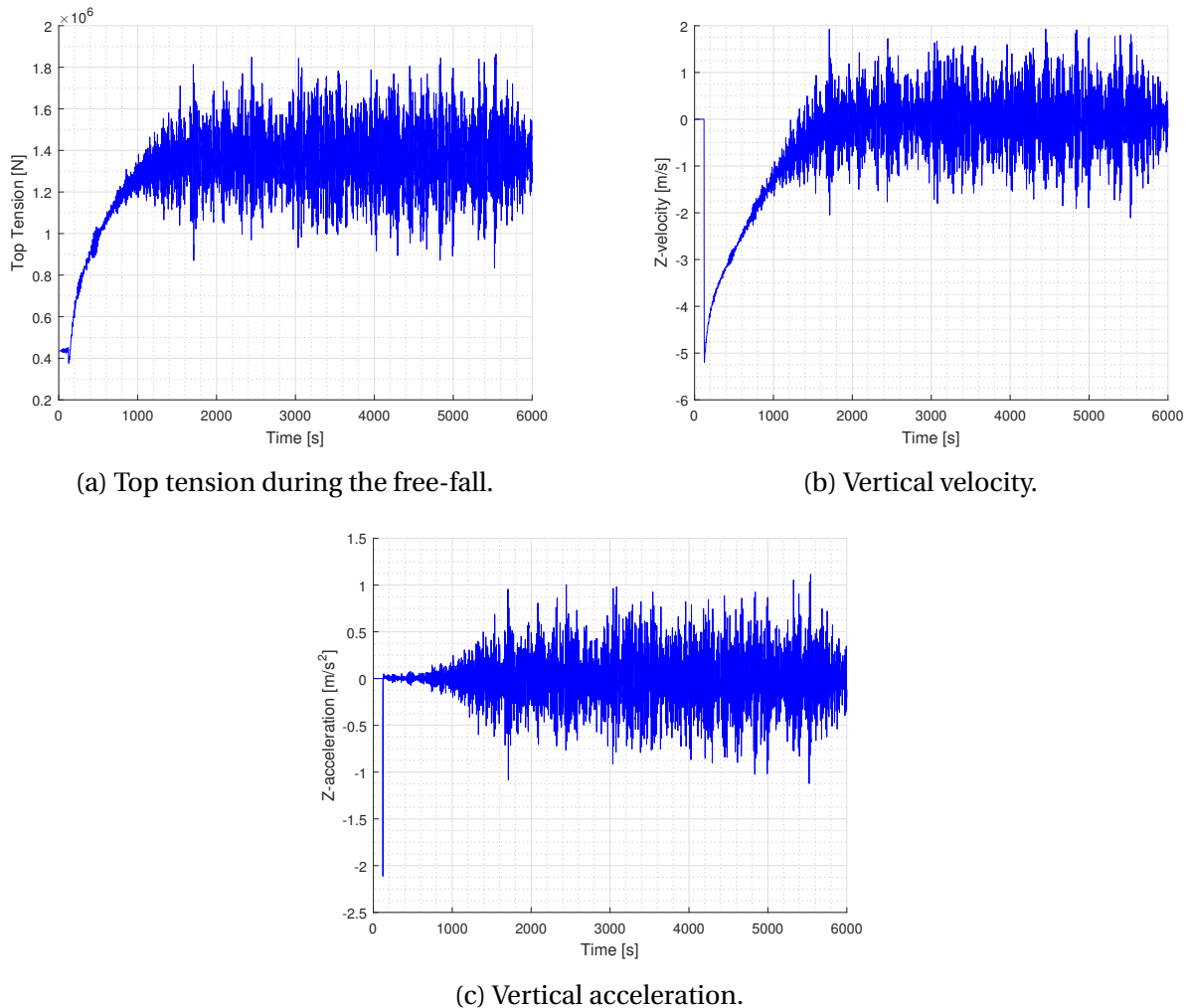


Figure 4.11: Top tension, vertical payload velocity and acceleration.

Based on the results presented in this section, it can be concluded that the Coupled SIMO-RIFLEX model used for the free-fall analysis seems to show good coherence with the expected dynamics. As such, the model is acceptable for use in further analysis.

4.3 Convergence Test of Wave Seeds for Splash-Zone Analysis

The effect of varying the wave seed for a specific sea state with the same operational start, is to simulate the random selection of start time within the sea state. Having many different wave seeds for a specific sea state therefore gives a larger statistical sample of data to determine the hydrodynamic lifting properties in the sea state. This means that there should be sufficient realizations for each sea state when performing dynamic analysis in SIMO to achieve a more accurate picture of the response of lifting system. Failure to include enough realizations may result in large uncertainty in results. However, simulation time is greatly increased by increasing the number of wave seeds. Thus, a convergence test of wave seeds should be performed in order to reach an acceptable compromise between result accuracy and simulation time.

A fitted Gumbel distribution was used as an extreme value distribution when determining the 90th percentile of the maximum crane wire tension. Equation 4.3 express the Gumbel distribution probability function $f_X(x)$.

$$f_X(x) = \frac{1}{\beta} e^{-(z+e^{-z})} \quad (4.3)$$

$$z = \frac{x - \mu}{\beta}$$

where

β =Scale parameter

μ =Location parameter

The location parameter determines the location of the peak in the fitted Gumbel distribution, and as such express the mode of the data set. The larger magnitude of the scale parameter, the more the probability density function (PDF) is stretched.

The parameters for the fitted Gumbel distribution of the maximum crane wire tension for 10, 20, 35, 50 and 100 different wave seeds are presented in Figure 4.12. The 95% confidence interval for the estimated parameter values are also included.

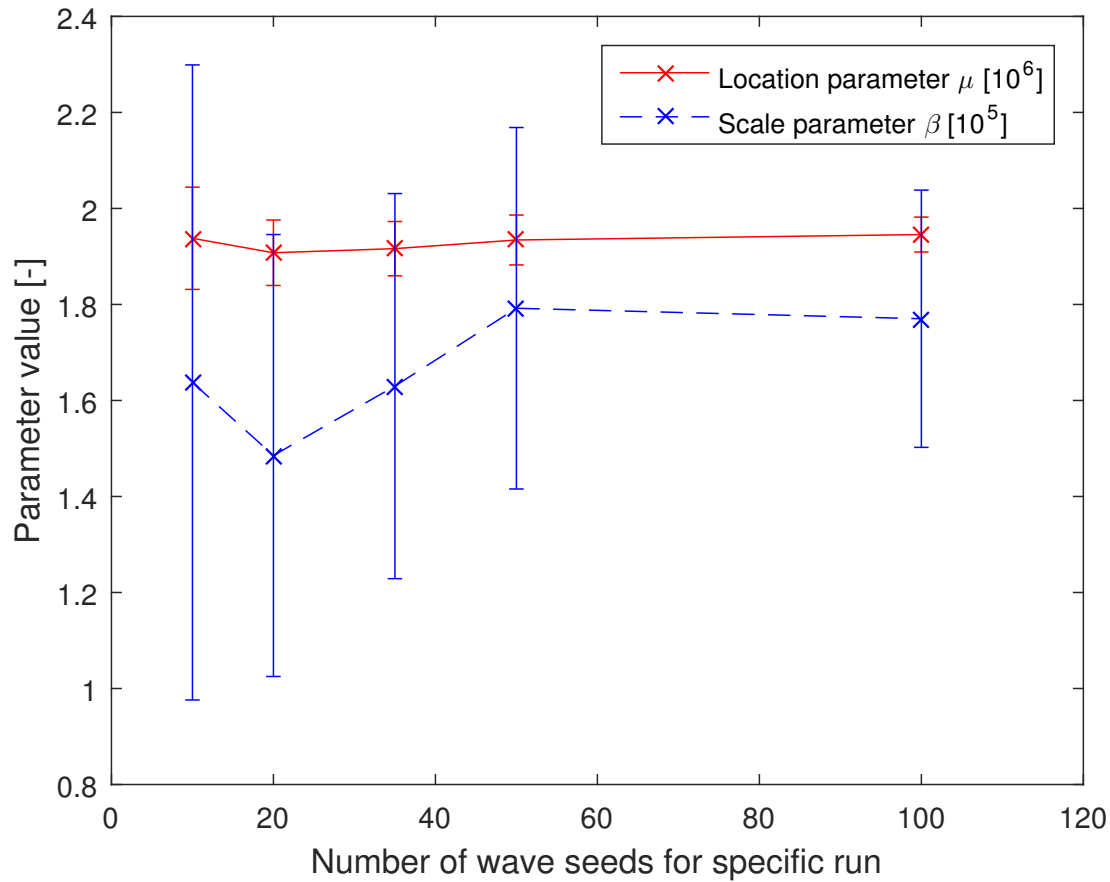


Figure 4.12: Convergence test of Gumbel parameters for maximum crane wire tension in sea state $H_s=4\text{m}$, $T_p=8\text{s}$, with 95% confidence interval.

Figure 4.12 suggests that both parameters start to approach convergence for over 50 wave seeds, although runs for more than 100 wave seeds ideally should have been performed in order to see clearer signs of convergence. The change in the parameter value with increasing number of wave seeds is more profound for β , than for μ . This means that the overall trend seems to be that by increasing the number of wave seeds and at the same time obtaining a larger data sample, the probability density function becomes more stretched. The peak location, however, does not move significantly with varying wave seeds.

Moreover, the 95% confidence interval for μ is significantly lower for each variation of wave seeds. On the other hand, the 95% confidence interval is considerably large for β . For example, 10 wave seeds gives an 95% confidence interval of almost 40% of the data value. An interesting

observation is that the 95% confidence interval is still relatively large for the scale parameter at 100 wave seeds. As expected, the confidence interval decreases with increasing wave seed due to a larger sample of data. The uncertainty in estimating the parameters also introduces an uncertainty in determining the 90th percentile for the maximum crane wire tension, since the Gumbel distribution changes with the parameters.

Figure 4.13 shows the uncertainty introduced by the 95% confidence interval bounds of the estimated parameter values for the case with 35 wave seeds. The upper confidence bound is here defined as the Gumbel distribution obtained from the upper bound of the 95% confidence interval of both μ and β , and opposite for the lower bound. As such, these bounds illustrate the most "extreme" cases of uncertainty. As seen in the figure, the uncertainty of the 90th percentile of the maximum lifting wire tension introduced by the parameters is around 8%. This result highlights the importance of minimizing the uncertainty when estimating the 90th percentiles. The figure also brings up the question of using the mode of the fitted Gumbel distribution instead of the 90th percentiles, since the location parameter has a lower 95% confidence interval. The mode may therefore have less uncertainty compared to the 90th percentiles. However, choosing the 90th percentiles will be more conservative. The results also suggests that if higher estimation accuracy is achieved, there would be more room to challenge existing requirements in the operational planning of the installation of the Dual Cap-X.

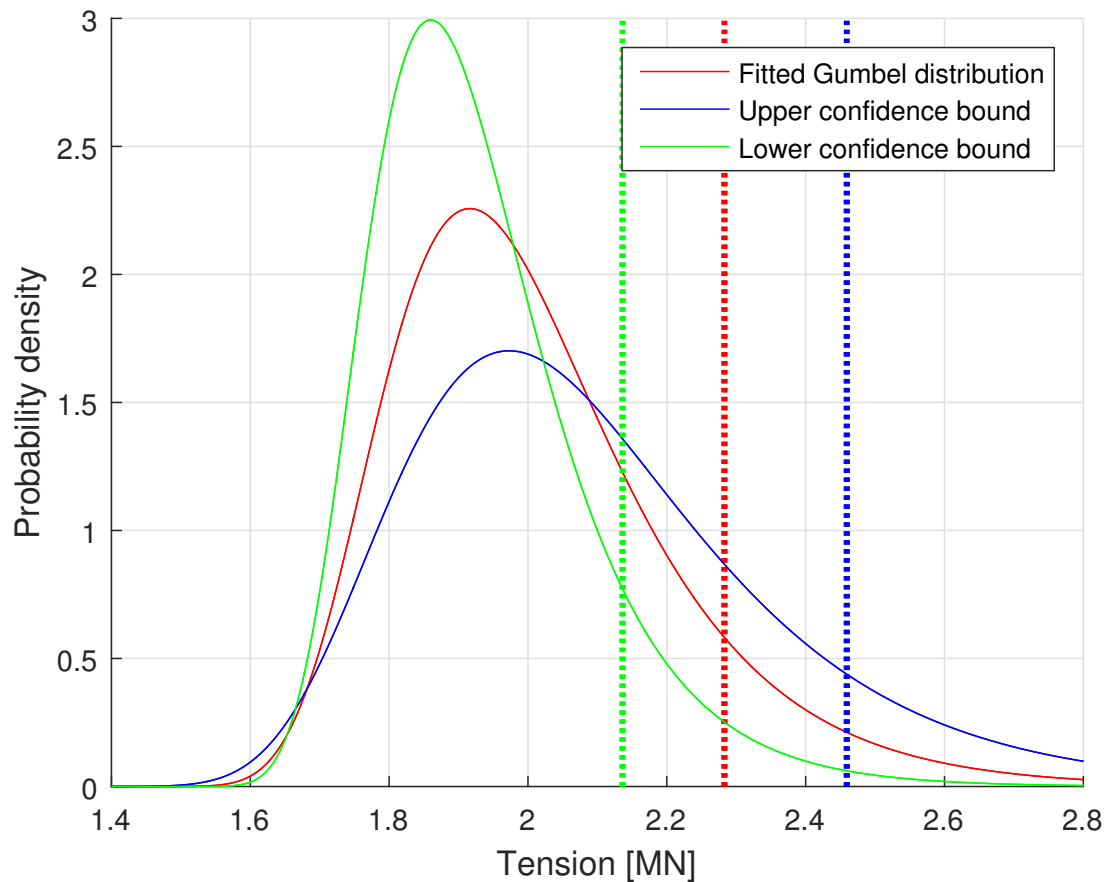


Figure 4.13: Fitted Gumbel distribution on observed maximum crane wire tension (35 wave seeds) in sea state $H_s=4\text{m}$, $T_p=8\text{s}$ with lower and upper 95% confidence bounds (vertical lines indicate the 90th percentiles).

Figure 4.14 shows how the variation of β and μ affects the corresponding Gumbel distribution and the 90th percentile. As discussed, the scale parameter increases with increasing number of wave seeds. This results in a more stretched distribution and a lower peak, which also means that the 90th percentile mark moves to the right towards larger maximum tensions. The fact that μ does not change much with increasing numbers of wave seeds is also evident, as the peak location (mode) does not move much between the distributions. The convergence of the Gumbel distribution parameters observed in Figure 4.12, is also evident as 50 and 100 wave seeds yield similar distributions. These results show that there is a larger uncertainty introduced in a single run due to Gumbel distribution parameter estimation (Figure 4.13), than between the "base cases" of different wave seeds (Figure 4.12). These results indicate that the selection of a

sufficient number of wave seeds when determining the 90th percentile should be dedicated attention. The result of choosing an insufficient number of wave seeds could potentially challenge the integrity of the lifting system. It should also be noted that choosing enough wave seeds will affect the process of determining suitable weather windows for the Dual Cap-X.

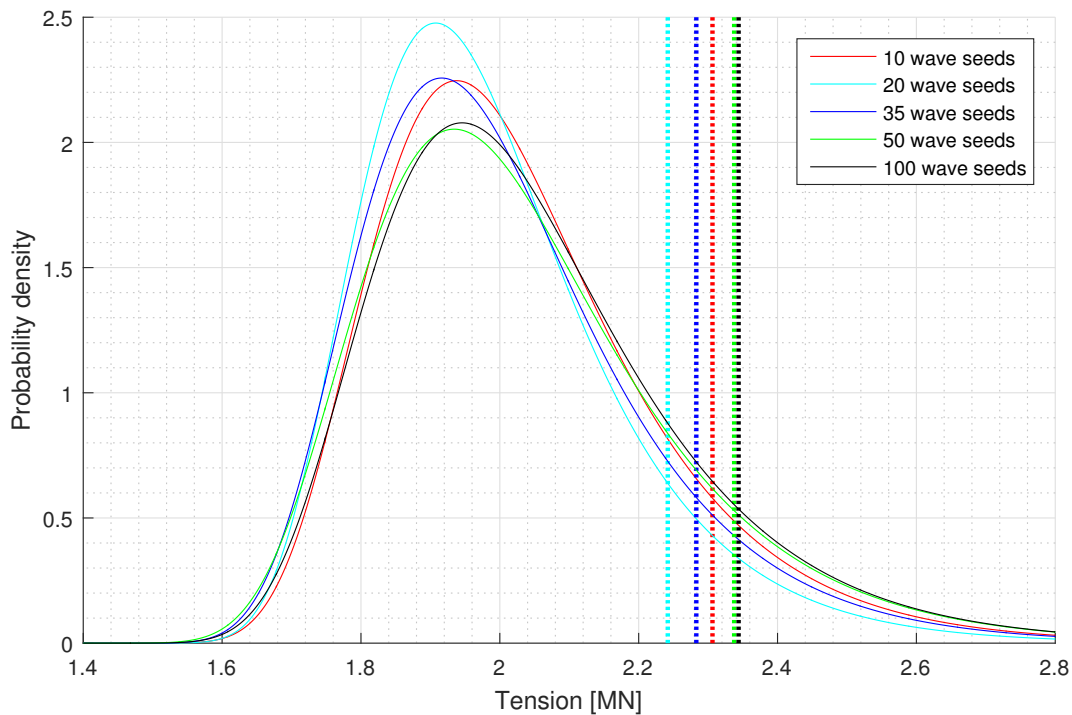


Figure 4.14: Fitted Gumbel distribution on observed maximum crane wire tension for runs with different numbers of wave seeds. Vertical lines indicate the corresponding 90th percentiles for each distribution.

Another point to be noted is that the static weight of the Dual Cap-X is considerably large, and thus the uncertainty in estimating dynamic forces that contribute to the lifting line tension will amount to a smaller percentage of the total lifting line tension compared to a payload with a small weight. Therefore, special attention to uncertainty in statistical estimation for payloads with small weights and large dynamic forces should be applied.

The results above are valid for the maximum lifting line tension. It is of interest to check whether the same trend is present when estimating other parameters associated with the lowering of the Dual Cap-X through the splash-zone. Figure 4.15 illustrates the same as Figure 4.13, only for the

minimum lifting line tensions. The reader should be aware that the upper and lower confidence bounds illustrated in the figure is calculated in the same way as previously. Namely, the upper confidence bound is based on the upper bound of the 95% confidence interval for both μ and β of the fitted Gumbel distribution of the minimum lifting line tensions for 35 wave seeds. The opposite was done for the lower confidence bound. The figure suggests that the uncertainty associated with the estimation of the distribution parameters has a smaller impact when determining the minimum lifting line tensions compared to the maximum lifting line tensions for this case.

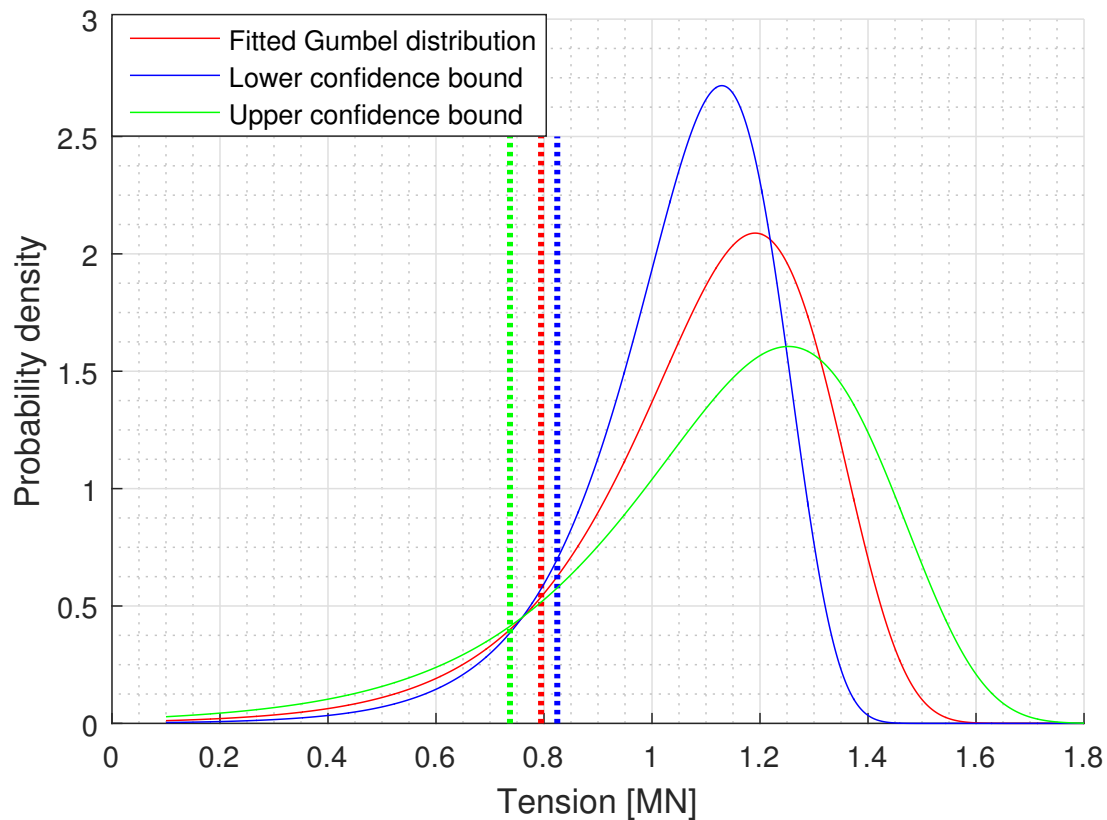


Figure 4.15: Fitted Gumbel distribution on observed minimum crane wire tension (35 wave seeds) in sea state $H_s=4\text{m}$, $T_p=8\text{s}$ with lower and upper 95% confidence bounds (vertical lines indicate the 10th percentiles as discussed in Section 4.1.2).

For the simulations performed in this thesis, 35 wave seeds have been generally used if not stated otherwise. Although this is not optimal, this had to be done due to limitations in the computational power available.

Chapter 5

Results and Discussion

5.1 In-Air Phase

During the In-Air phase of a subsea installation operation, the movement of the payload is of extreme importance. If the motion is too large it can result in injury to personnel as well as damage to assets. A common challenge in this phase relates to the excitation of pendulous motion. This can be a result of the orientation of the vessel relative to the heading of the incoming waves, as well as excitation of pendulous resonance. As a result, an investigation into the motion of the payload should be investigated for various environmental conditions. To achieve this, both head and beam sea conditions were modelled. A head sea should result in maximizing translations in the η_1 direction, referred to in this section as X-direction, and beam sea maximize translation in the η_2 direction, referred to in this section as the Y-direction.

SIMO was utilized to model such sea conditions, and the translations of the Dual Cap-X and vessel were extracted. Based on these one can determine the motion of the payload relative to the vessel. Figure 5.1a illustrates movement in the X-direction and Figure 5.1b the movement in the Y-direction for various peak periods and significant wave heights for the case of head sea. All simulations were run for wave seed = 1.

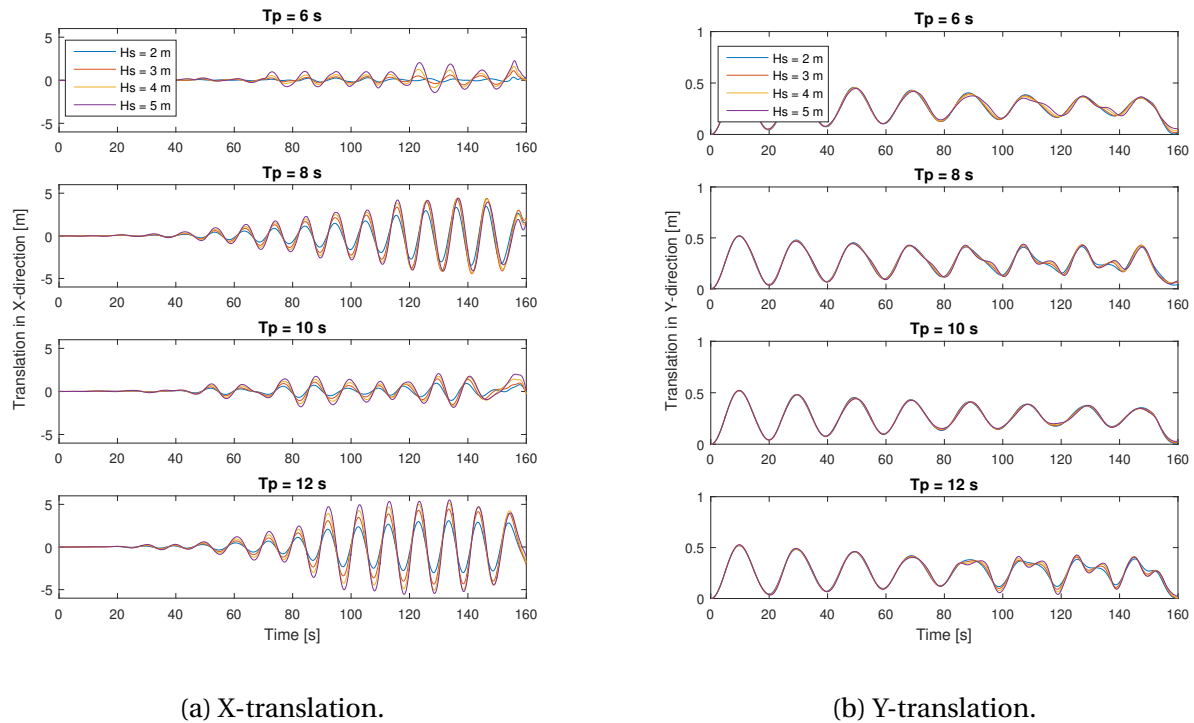


Figure 5.1: Payload motion in head sea conditions.

As expected, the motion in the X-direction is much greater than that it in the Y-direction in head sea waves. Translations of up to 5 meters are experienced in the X-direction, and limited to below 1 meter in the Y-direction. This is most likely due to the high degree of pitch motion inducing oscillations in the X-direction.

Figures 5.2a and 5.2a illustrate beam sea conditions.

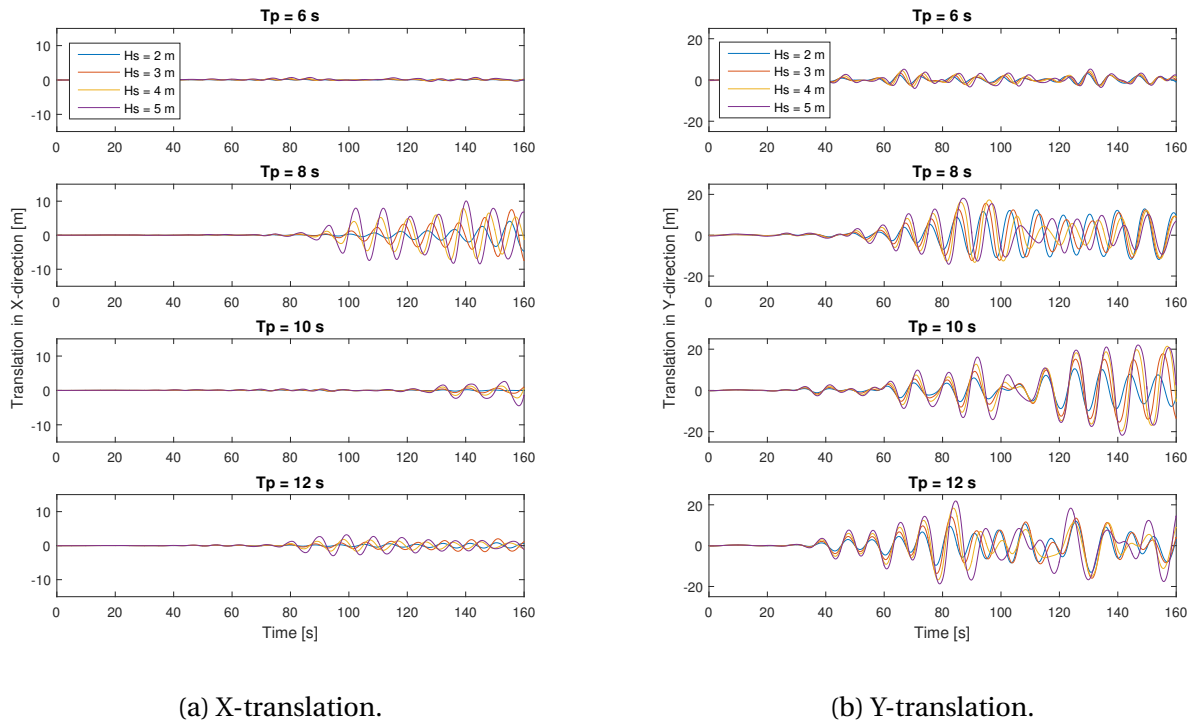


Figure 5.2: Payload motion in beam sea conditions.

Beam sea conditions result in much greater oscillations than head sea. This corresponds well with the results outlined in Section 5.2.4 where the sensitivity of wave heading is investigated for the Splash-Zone phase. Figure 5.2b indicates oscillations of up to 20 meter amplitude for certain peak periods. Oscillations in the X-direction also reach up to 10 meters for $T_p = 8$ s in beam sea. This indicates a circular motion of the payload that is excited by the environmental conditions. This was confirmed by examination of the SIMA visualization file.

5.1.1 Pendulous Motion

In general, a trend in all cases is found in which an increase in significant wave height results in greater translation, but significant motions are not experienced for all peak periods. The dominant variable appears therefore to be the peak period.

As discussed at the end of Section 3.2.4, pendulous motion can be a significant issue in lifting

operations. In addition, if the resonance frequency is excited, large oscillations will result. Equation 3.21 gives the resonance period for a given wire length. Figure 5.3 illustrates the change in the pendulum resonance period for the lifting system.

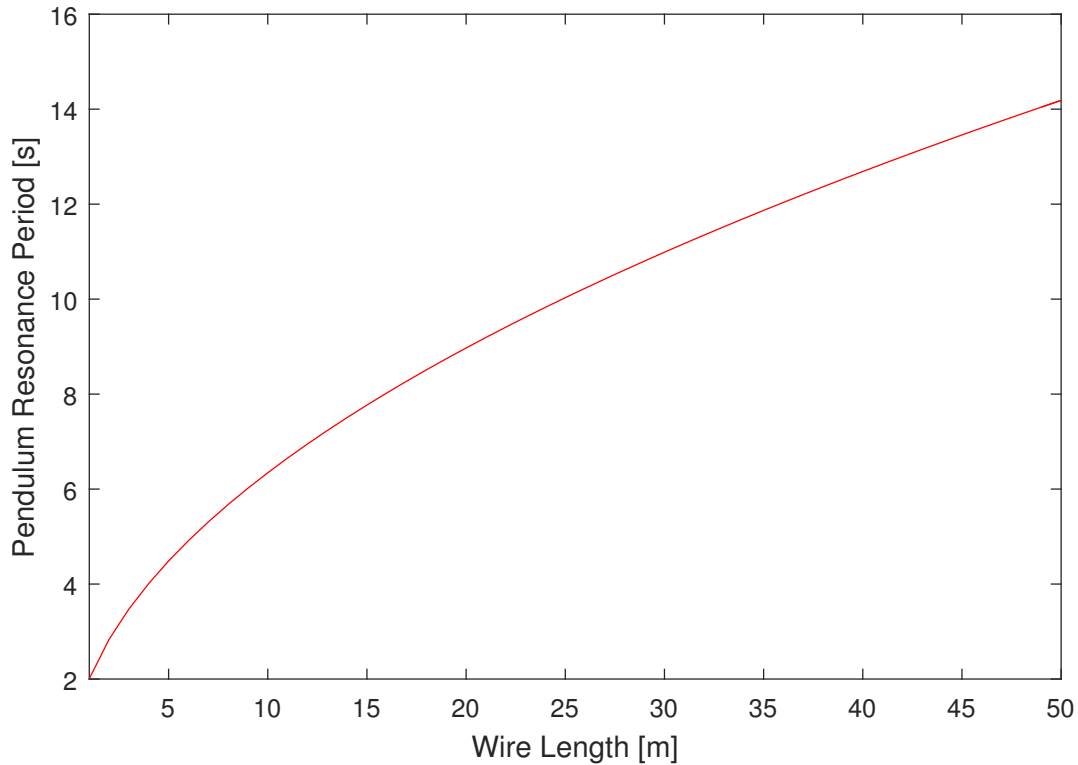


Figure 5.3: Resonance period for horizontal pendulum motion.

One can clearly see that with a low period, resonance motion is not excited by the wave environment. Between 8 and 12 seconds however the Dual Cap-X experiences significant oscillations. This appears to be related to the relevant wire lengths involved in the operation. Due to the excitation of resonance, it is of interest to investigate the effect wind speed will have on damping the motions of the Dual Cap-X as outlined in Section 3.2.4.

5.1.2 Wind Sensitivity

By increasing the wind speed, the damping force in Equation 3.20 will increase, and should result in a decrease of horizontal motion. Figure 5.4 illustrates the effect wind speed had on the

horizontal motion of the Dual Cap-X for beam sea conditions and a peak period of 8 seconds. The wind was modelled in the same direction as the waves, as this will provide the greatest damping force.

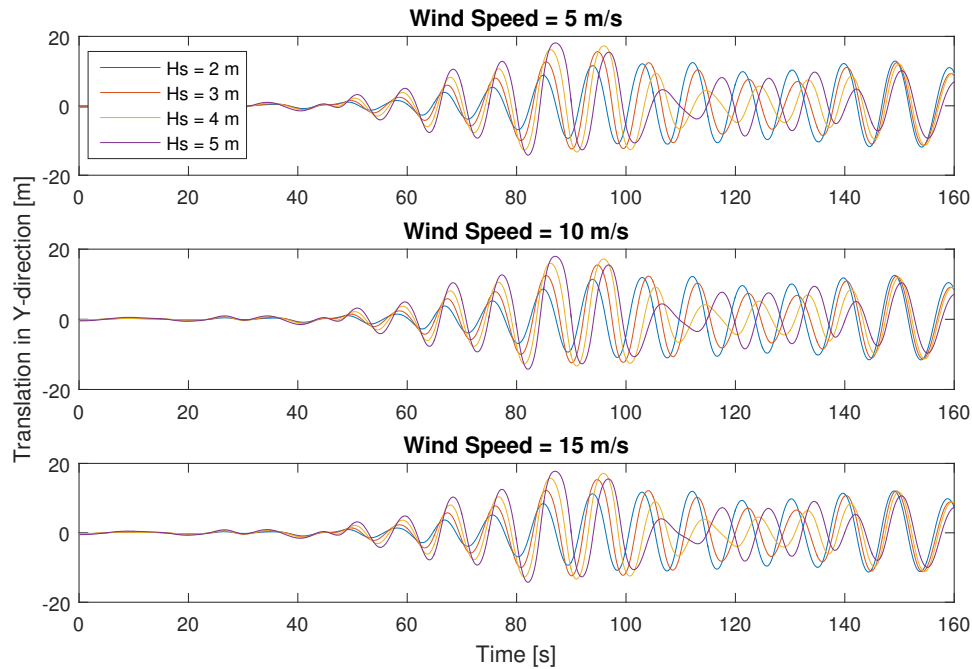


Figure 5.4: Wind sensitivity.

It is clear from Figure 5.4 that increasing the wind speed has virtually no impact on the total translation of the Dual Cap-X for the relevant conditions. This trend repeated itself for head sea conditions as well. It was therefore concluded that wind has minimal effect on the damping of horizontal motion during the In-Air phase. Figure 5.5 illustrates the total wind force acting on the Dual Cap-X in the Y-direction. The forces are in the order of $10^4 N$. One can easily decompose the horizontal and vertical components of the static weight of the module for a given offset, and compare the horizontal component with the wind force. Rough hand calculations show that at an offset of 5 m the horizontal weight component is approximately $3.5 * 10^5 N$. An increase in offset will give rise to an even higher value. Wind forces are therefore of an insignificant magnitude to provide sufficient damping for the Dual Cap-X. This conclusion was found to be valid for both beam sea and head sea conditions.

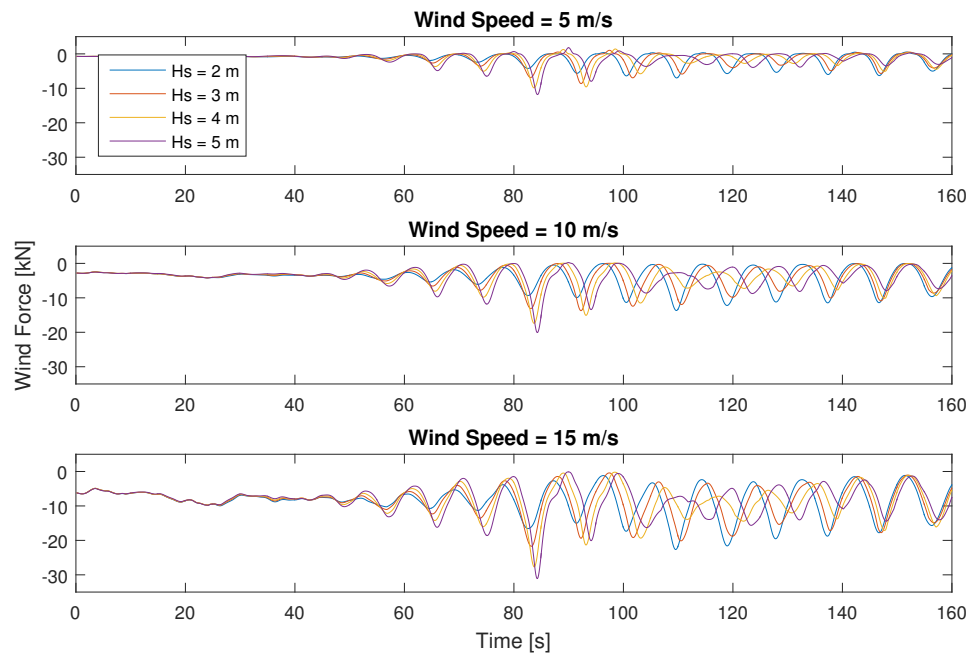


Figure 5.5: Wind force on Dual Cap-X.

5.1.3 Evaluation of Acceptance Criteria

It is evident that uncontrolled pendulum motion of the Dual Cap-X can result due to environmental effects related to the sea state. The degree to which this effect is excited depends on the wave direction and peak period. The results clearly show that the motion will in certain cases be of an unacceptable magnitude. The heading of the ship relative to the incoming waves can be controlled to a certain degree to minimize this effect. The wave periods in the irregular sea are however beyond control. Wind provides insufficient damping of the system and the use of tugger lines to minimize the motion of the Dual Cap-X during the Lift-Off phase will be necessary.

5.2 Splash-Zone Phase

5.2.1 Added Mass Sensitivity

Added mass is decisive for calculating the hydrodynamic forces acting on the Dual Cap-X model. The inertia, wave excitation and slamming forces are functions of the added mass as outlined in equations 3.27, 3.28 and 3.30. SIMO incorporates the added mass values into the model through element specific values. The sensitivity of these values must be investigated in order to assure the validity of the model.

Given that vertical motions will be decisive for the operation limits, only added mass in heave, A_{33} , was investigated. Ratios relative to a base case value of A_{33} , i.e. the calculated value, were utilized. A ratio of one will as such represent the base case, and a ratio of two, twice the value utilized. The only element investigated was the fixed body element representing the combined suction anchors. This was determined to be the most efficient method of investigating the added mass dependency of the model, as the forces on the suction anchors will dominate the model. The ratios listed in Table 5.1 were investigated. All simulations were conducted in the same environment, such that the only variable would be the added mass in heave.

Table 5.1: Added mass ratios.

0.25	0.5	0.75	1	1.25	1.5	1.75	2
------	-----	------	---	------	-----	------	---

The results shown in Figure 5.6 visualize the dependency of the total lifting wire force on various values of A_{33} for the following sea state:

$$H_s = 4m$$

$$T_p = 8s$$

$$\text{Wave Seed} = 1$$

The DAF is given for the lifting wire tension.

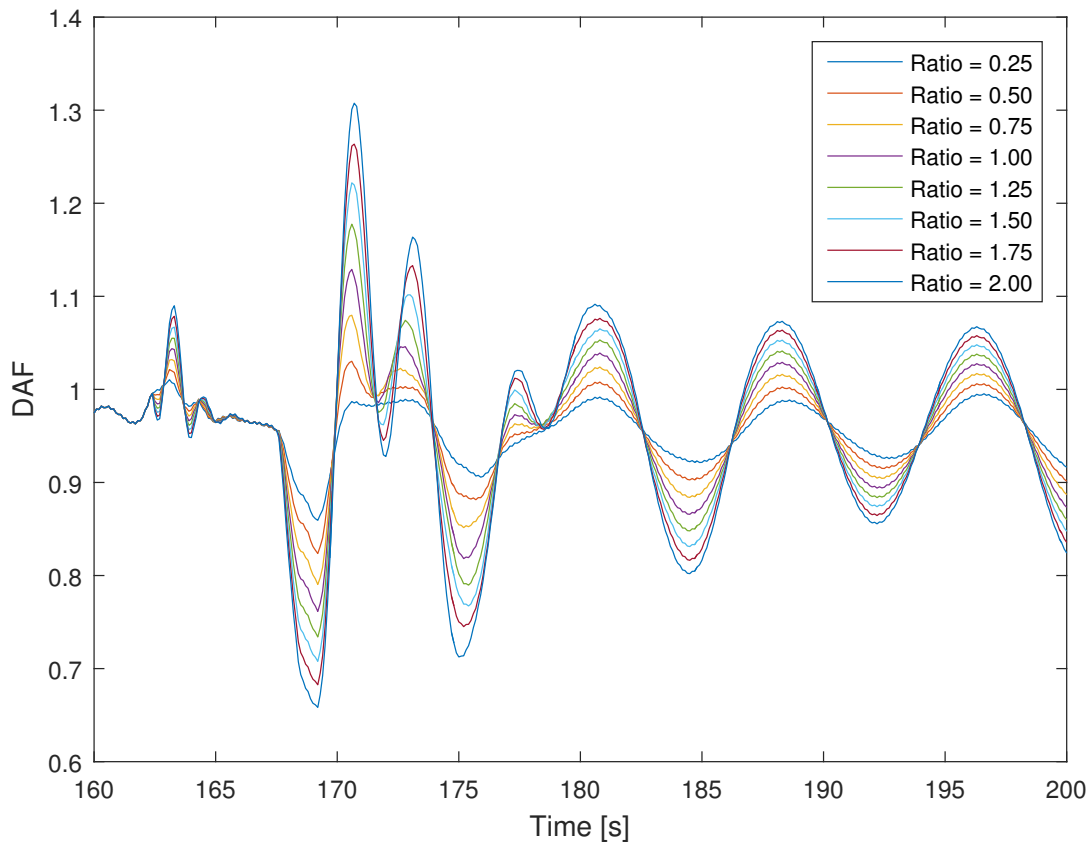


Figure 5.6: Added mass dependency for lifting wire tension.

Figure 5.6 clearly shows a trend in which an increase in added mass results in an increase in the lifting wire tension. The Dual Cap-X is fully submerged between 160 and 165 seconds, reflected by the abrupt difference in DAF values. The Splash-Zone phase yields the highest DAF values, where an added mass ratio of 2.00 reaches a DAF of 1.3. The maximum values for each added mass ratio are presented in Figure 5.7.

After approximately 180 seconds, one sees a periodic trend take over. The period appears to match the peak period of 8 seconds, and is therefore most likely due to the change in crane tip acceleration and the associated inertia forces. The inertia forces are a function of both mass and added mass in heave, and as such will increase for a higher added mass ratio. In addition, part of the wave excitation force is also a function of added mass.

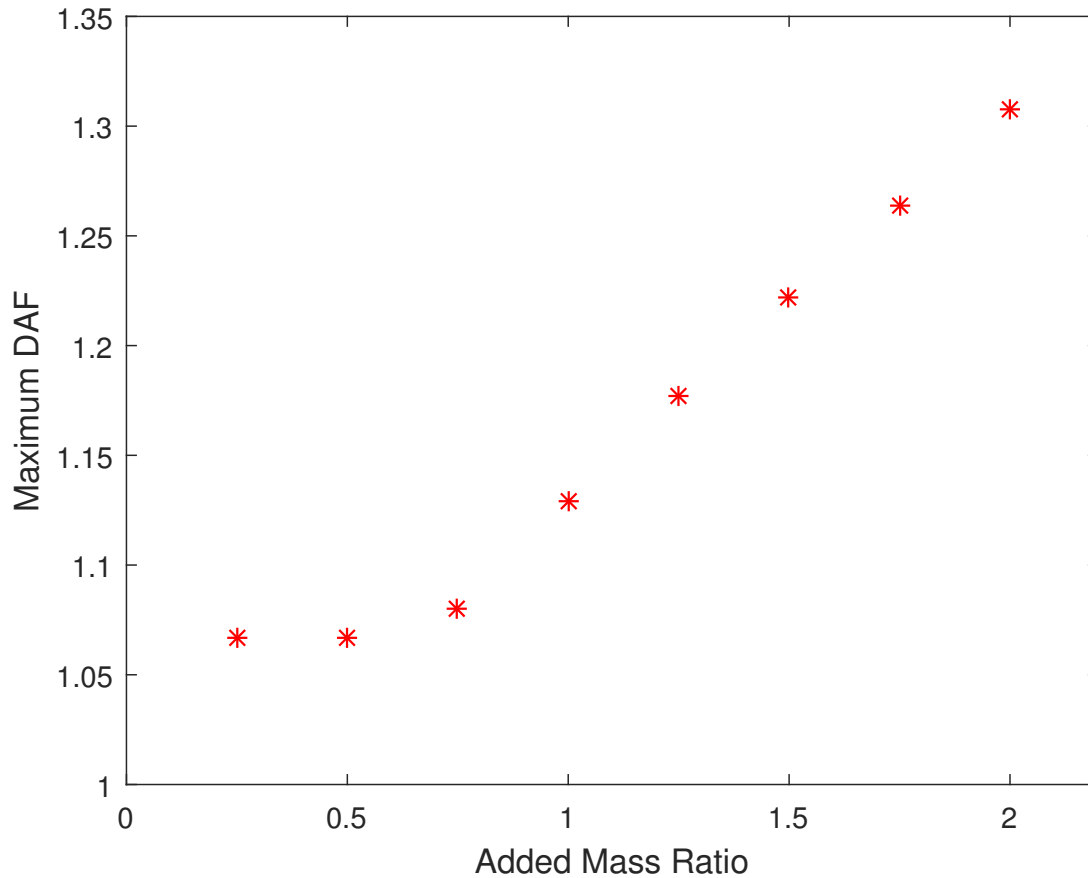


Figure 5.7: Relationship between maximum DAF and added mass ratios.

Figure 5.7 indicates there is an almost linear relationship between an increase in added mass and the dynamic amplification factor for the lifting wire tension. The results show that accurate modelling of added mass in heave is highly important for the lifting wire tension. The assumption that the model is mass force dominated as outlined in Section 3.2.6 is also confirmed based on the high level of dependency of the added mass term.

Despite the sensitivity of the model to the added mass value, it was determined that the calculated value should be utilized. This is due to the conservative nature of the calculations conducted, and the inherent overestimation associated.

5.2.2 Depth Dependent Coefficient Sensitivity

As mentioned in Section 4.2.4, depth dependent coefficients provide the basis for the slamming force in the SIMO model. The inserted values generate the gradient $\frac{\delta A_{33}}{\delta dh}$. Accurately modelling this gradient is important to attain accurate results. The values utilized in the SIMO model were adopted from Næss et al. (2014) as discussed in Section 4.2.4. It is therefore of interest to investigate the sensitivity of the depth dependent coefficients, as the gradient will have an effect on the final results.

Slamming

To understand the implications of altering the depth dependent coefficients, one must have a thorough understanding of the slamming force implemented in SIMO. Newton's second law of motion states that force is equal to the rate of change of momentum with respect to time.

$$F = \frac{d(mv)}{dt}$$

Differentiating, the equation yields

$$F = \underbrace{\frac{dm}{dt} v}_{\text{Slamming}} + m \underbrace{\frac{dv}{dt}}_{\text{Inertia}} \quad (5.1)$$

Generally, one assumes that the mass remains constant and as such $\frac{dm}{dt}$ is equal to zero yielding the classic $F = ma$. This however is not the case when crossing the splash-zone. Added mass is introduced into the system, at a rate in the vertical direction that can be expressed as $\frac{dA_{33}}{dt}$. The term $\frac{dm}{dt} v$ as shown in 5.1 is the slamming force due to the change in mass of the system. The slamming force F_s can be expressed as:

$$F_s = \frac{dA_{33}}{dt} v$$

The change in added mass with time is difficult to express and can be rewritten to be expressed as the change with respect to depth, h .

$$\frac{dA_{33}}{dt} = \frac{dA_{33}}{dh} \frac{dh}{dt}$$

Given that velocity, v acts in the vertical direction is equal to $\frac{dh}{dt}$ and the slamming force can now be expressed as:

$$F_s = \frac{dA_{33}}{dh} v^2$$

Slamming is as such the change in momentum of the system due to an increase in mass. SIMO implements this through the gradient $\frac{dA_{33}}{dh}$ defined by the depth dependent coefficients.

Sensitivity

In order to investigate the degree to which the total tension in the lifting wire was affected by the relative added mass coefficient at various depths, a number of regimes designed to capture a higher gradient were evaluated. These regimes are presented in Figure 5.8.

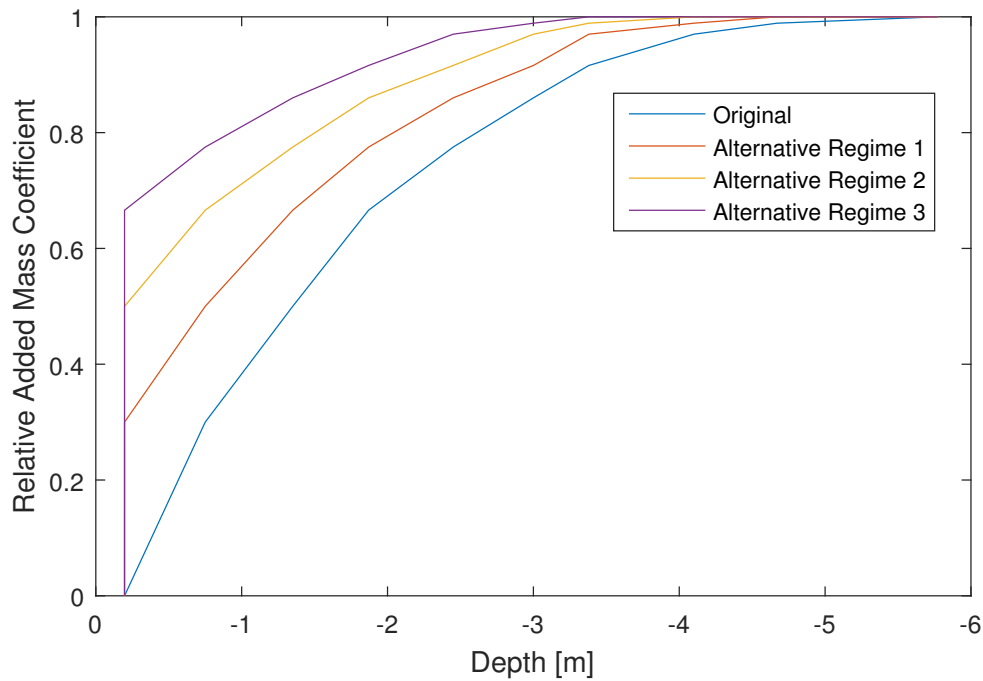


Figure 5.8: Regimes for relative added mass coefficients.

The original regime is the regime as presented in Næss et al. (2014). Næss et al. (2014) argue that the added mass of a suction anchor will increase from virtually zero, to the fully submerged value over a short vertical distance. This indicates the instantaneous increase once the anchor has become fully submerged may be quite high, i.e. a high gradient.

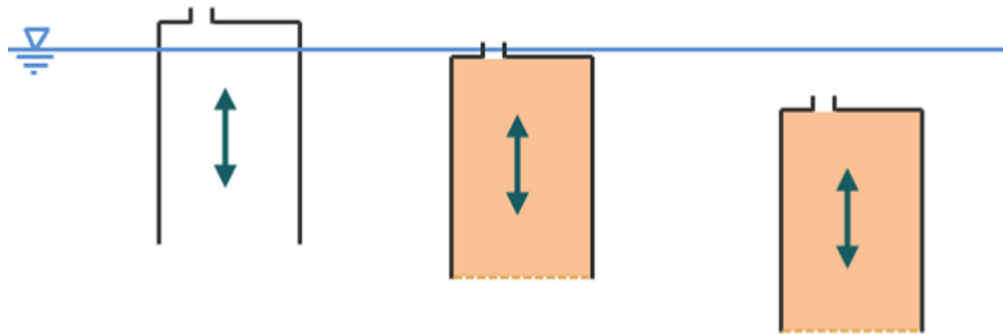


Figure 5.9: Change of added mass of suction anchor (Næss et al., 2014).

This indicates a depth dependent added mass regime driven by a large δA_{33} and a low δh in the first moments after submergence. This yields a high gradient. If this aspect of the change in

added mass is underestimated, it may have an effect on the total lifting line force. As such, regimes 1-3 introduce a higher gradient immediately after submergence. An instantaneous jump to a higher relative added mass coefficient is introduced, and the remainder of the regime outlined by Næss et al. (2014) is maintained. The results of running these regimes are presented in Figure 5.10.

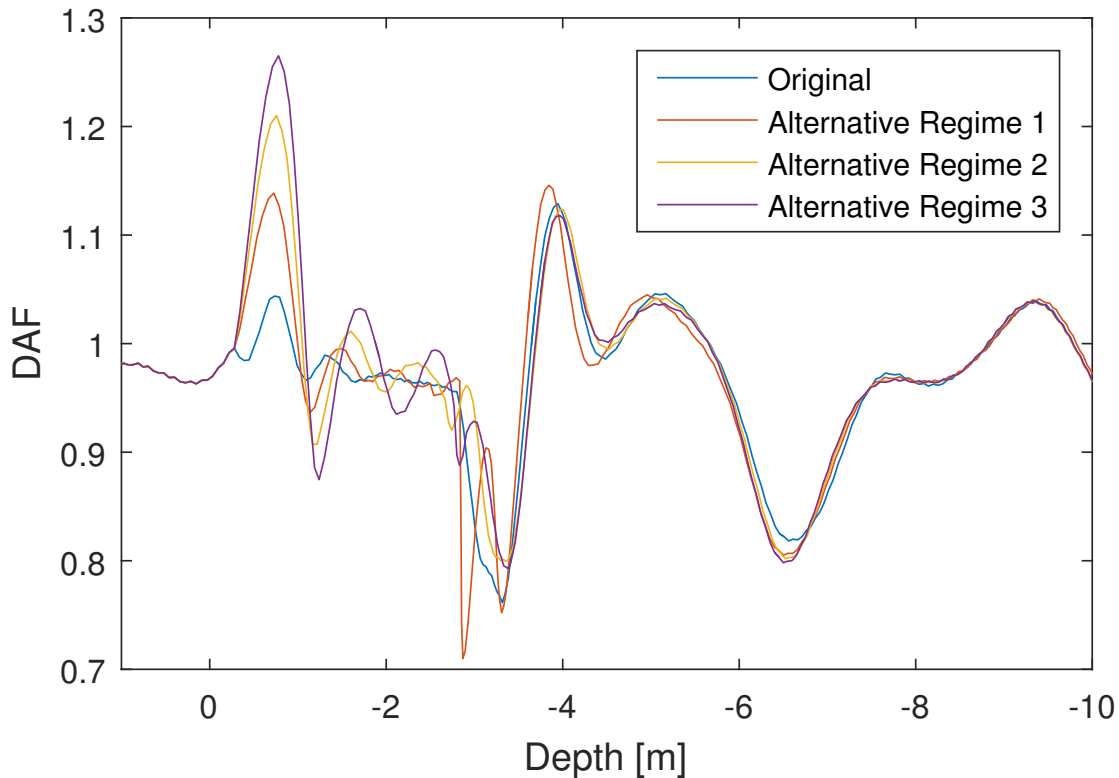


Figure 5.10: DAF of lifting wire tension against depth of suction anchors.

At first glance, the results appear to confirm the belief that an increased gradient in the first moments of submergence will result in higher slamming loads. The DAF increases significantly with an increasing gradient, as seen by the peaks just after submergence. These peaks however can not be a result of slamming forces. Slamming acts in the positive Z-direction, and will therefore contribute to lower tension in the wire. The results indicate the opposite. Higher tension in the lifting wire is experienced for higher added mass gradients. Similar results were found for other wave realizations as well. These results were unexpected, and further investigation into the dynamic forces was therefore required.

Simulations were run in an environment without waves. This removed all wave induced forces, and allows the effect of the added mass regime to be evaluated in an isolated state. A lowering speed of 0.5 m/s was utilized, as well as the same added mass regimes outlined in Figure 5.8. Figure 5.11 illustrates the results obtained for the four added mass regimes.

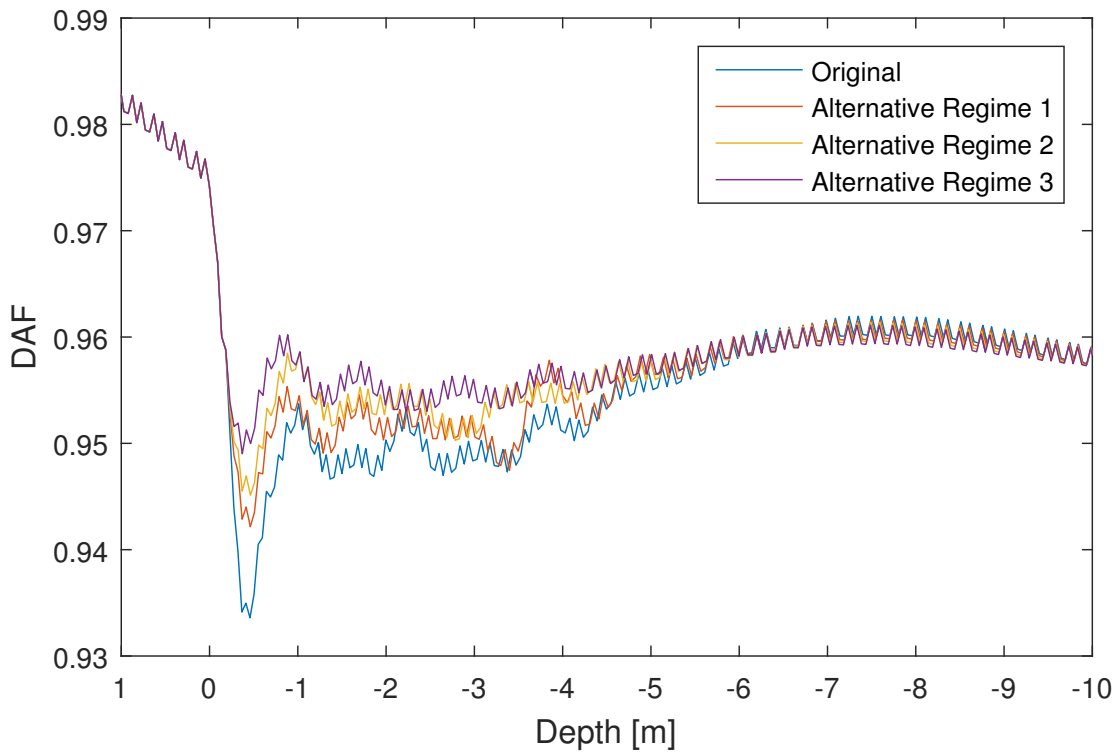


Figure 5.11: DAF of lifting wire tension against depth of top of suction anchors.

The results clearly show that the original regime yields the highest slamming force. The trend is in fact opposite to that which was expected. The slamming force decreases with regimes that increase the gradient.

For a system, the change in momentum will govern its behaviour and will therefore be most important for the global response. Forces acting on the Dual Cap-X during the splash-zone will have varying durations. The duration which they act will yield the change in momentum, and is quantified as the impulse, I . It can be quantified as :

$$I = \int_{t_1}^{t_2} F(t) dt$$

The time increment during which a force acts is therefore very important. It is shown in Larsen (2012) that for short impulses, the dynamic load factor increases proportionally with the duration of the impulse. A short impulse in this case is defined as $t_1 < 0.2T_0$ where t_1 is the duration of the impulse and T_0 is the eigenfrequency of the system. This is visualized in Figure 5.12. The figure clearly shows that for short durations, the relationship between the DLF or DAF is almost linear.

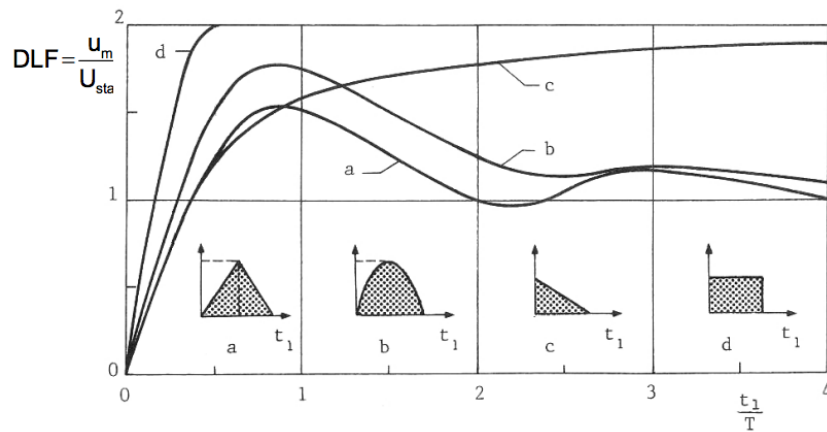


Figure 5.12: DLF/DAF for four different impulse forces plotted against the duration of the impulse (Larsen, 2012).

Faltinsen (1990) argues that the most important parameter for global response of a structure when lowering through the splash-zone for short time intervals is the impulse. As discussed, slamming is quantified as the change in momentum due to the change in added mass. The gradient $\frac{dA_{33}}{dh}$ utilized in the SIMO model was calculated and plotted against time. The results are shown in Figure 5.13

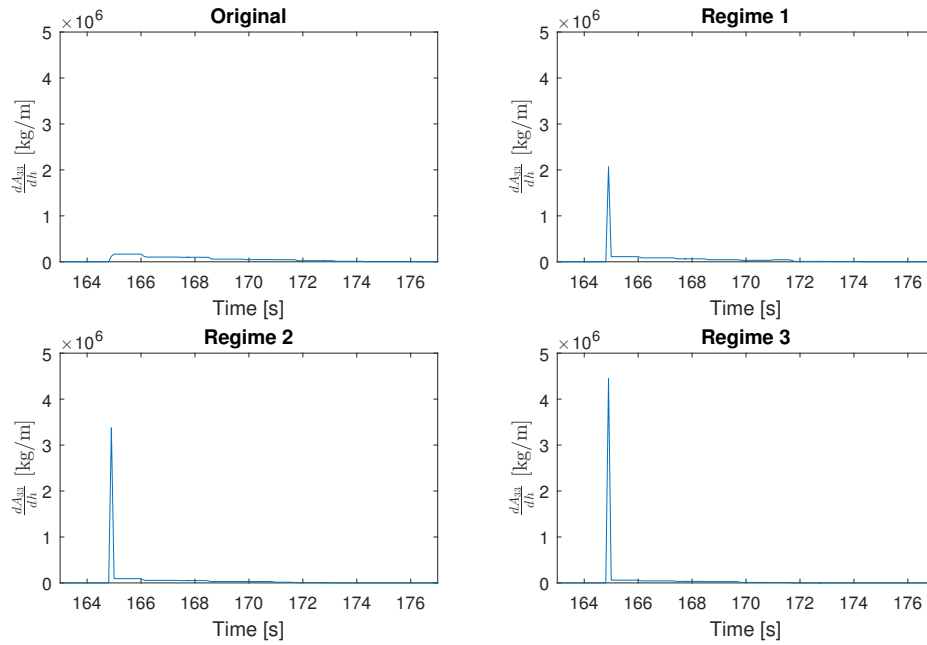


Figure 5.13: Added mass gradient, $\frac{dA_{33}}{dh}$ plotted against time.

Figure 5.13 clearly shows the peaks in the gradients for each regime. However, if one maintains the same scale on the X-axis and decrease the scale of the Y-axis, Figure 5.14 is obtained.

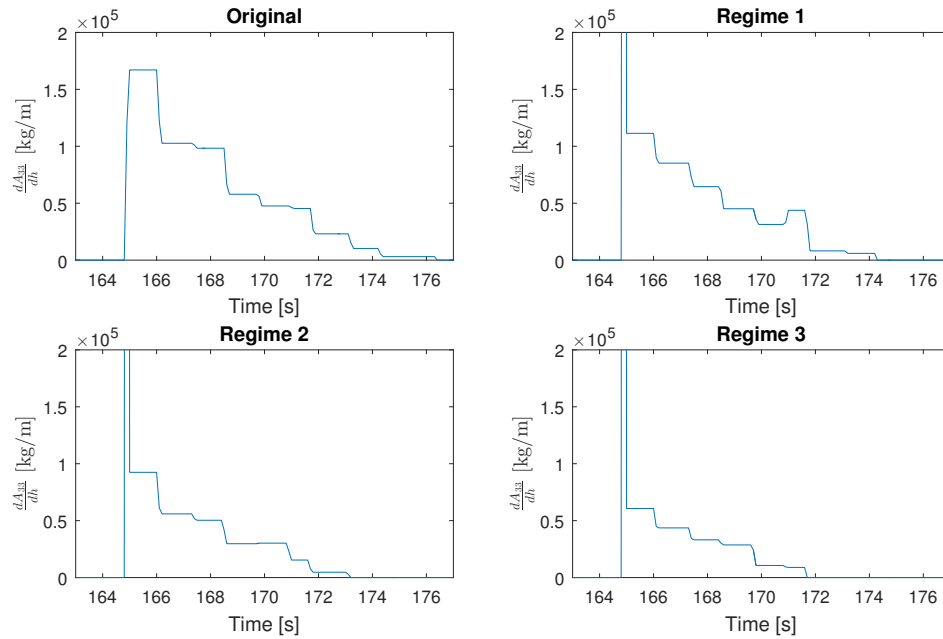


Figure 5.14: Added mass gradient, $\frac{dA_{33}}{dh}$ plotted against time (scaled).

Figure 5.14 is more valuable in terms of understanding the slamming forces acting on the Dual Cap-X. It is evident that the time period during which the first peak acts is extremely small. As such, one can conclude that the impulse of the slamming force given as:

$$I_s = \int_{t_1}^{t_2} \frac{dA_{33}}{dh} v^2 dt$$

will be quite small. As discussed by Larsen (2012), the duration of the impulse is so short that the resultant dynamic load factor will be limited. The dominant effect will be the duration of the remainder of the slamming force that results from the added mass gradient.

The decreased duration of the force as well as the decreasing value of gradient after the first peak from the original regime to regime 3 will therefore result in a decrease in the dynamic forces shown in Figure 5.11. It can therefore be concluded the slamming force is less sensitive to high gradients of short duration than lower gradients of longer durations.

Nonetheless, Figure 5.10 indicates an increase of the dynamic response for regimes that incorporate a larger instantaneous added mass gradient. Such an increase has now been shown to result in lower slamming forces. However, inertia and wave excitation forces as defined in Section 3, depend on the magnitude of the added mass in heave, not the gradient. An increase in the magnitude of A_{33} will result in an increase in force. The relationship between the forces and the added mass coefficient regimes is illustrated in Figure 5.15.

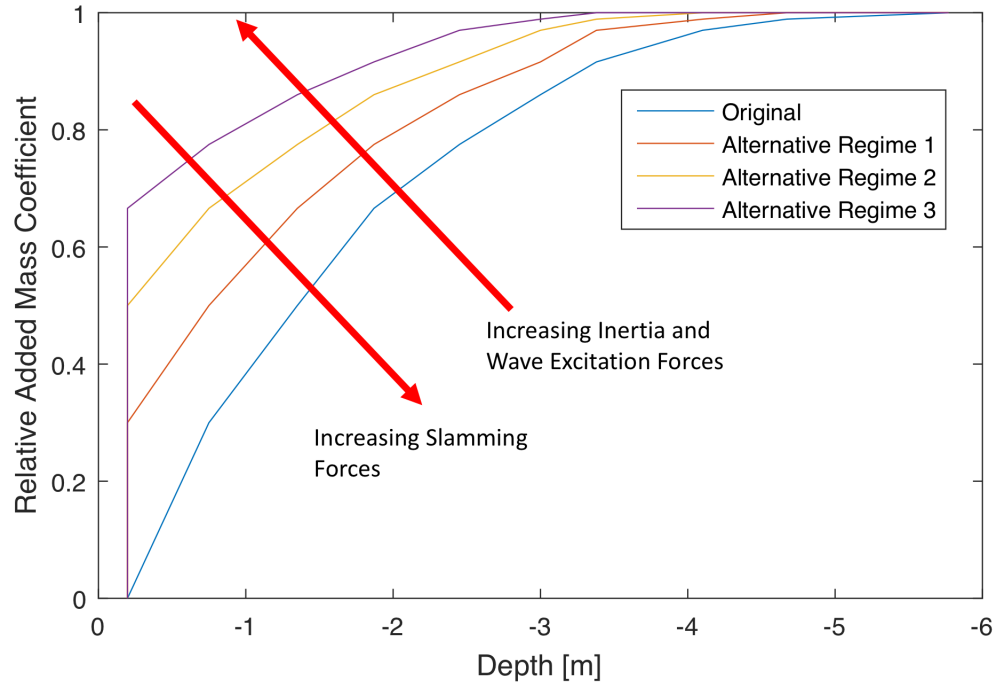


Figure 5.15: Relationship between forces and gradient regimes.

The results found in Figure 5.10 may now be evaluated with this in mind. As the regime moves from the original to regime 3, the inertia and wave excitation forces increase in magnitude for the same time step. These forces contribute to an increase in the lifting line tension (downward). At the same time the magnitude of the slamming force decreases. The slamming force contributes towards slack (upwards). As such, when moving from the original regime to regime 3, the force in the lifting line will increase due to higher inertia and wave excitation forces in conjunction with lower slamming forces.

5.2.3 Drag Sensitivity

Drag in the SIMO Dual Cap-X model was modelled as quadratic drag. In this section the sensitivity to the drag coefficients is checked. As mentioned in Section 5.2.1, the vertical motions will be decisive for the operational limits and as such only the quadratic drag term in heave, B_{33} will be investigated. Similarly to Section 5.2.1, the drag term for the fixed body element representing both suction anchors will be evaluated due to its dominating nature in the model. Ratios rela-

tive to a base case value of B_{33} , i.e. the calculated value, were utilized. A ratio of one will as such represent the base case, and a ratio of two, twice the value utilized. The ratios listed in table 5.2 were investigated. All simulations were conducted in the same environment, such that the only variable would be the added mass in heave.

Table 5.2: Quadratic drag coefficient ratios.

0.25	0.5	0.75	1	1.25	1.5	1.75	2
------	-----	------	---	------	-----	------	---

The results shown in Figure 5.16 visualize the dependency of the DAF for the lifting wire force on various values of B_{33} for the following sea state:

$$H_s = 4 \text{ m}$$

$$T_p = 8 \text{ s}$$

$$\text{Wave Seed} = 1$$

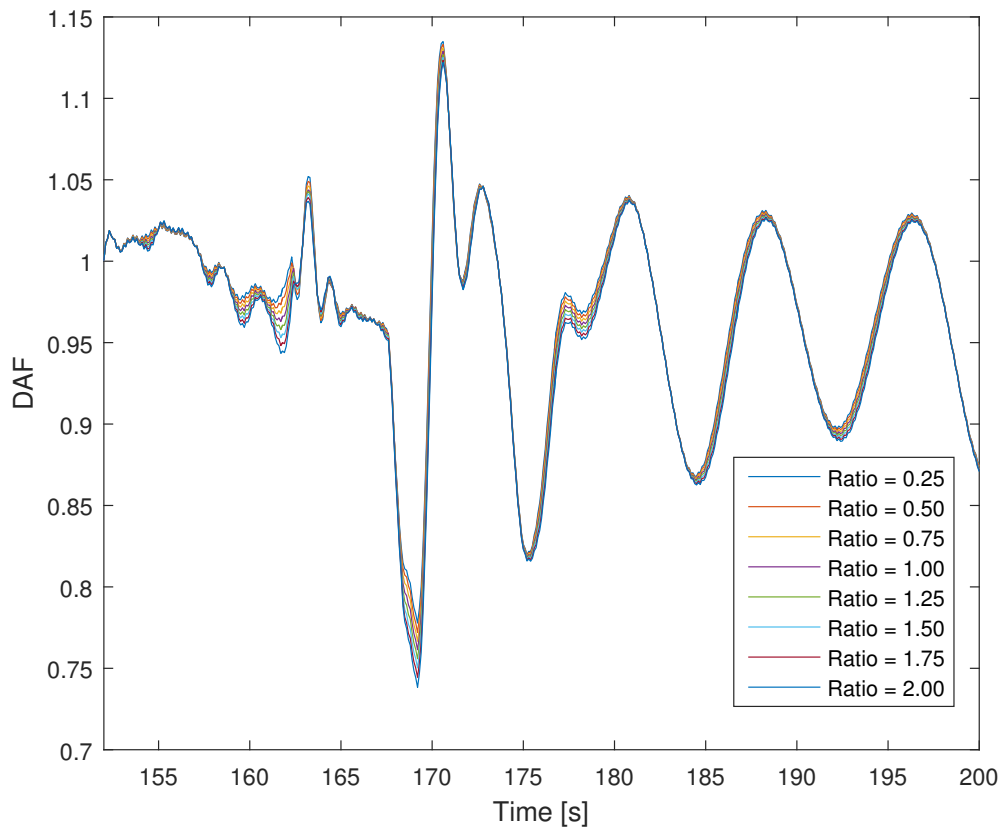


Figure 5.16: Quadratic drag coefficient dependency for lifting wire tension.

Figure 5.16 indicates that the model has a low degree of dependency on the quadratic drag coefficient. In Figure 5.17 the change in lifting wire tension for various ratios is visualized in percent change. Doubling the drag coefficient does not even result in a 1 % change in tension. As such one can conclude that drag will have minimal effect of the SIMO Dual Cap-X model through the splash-zone.

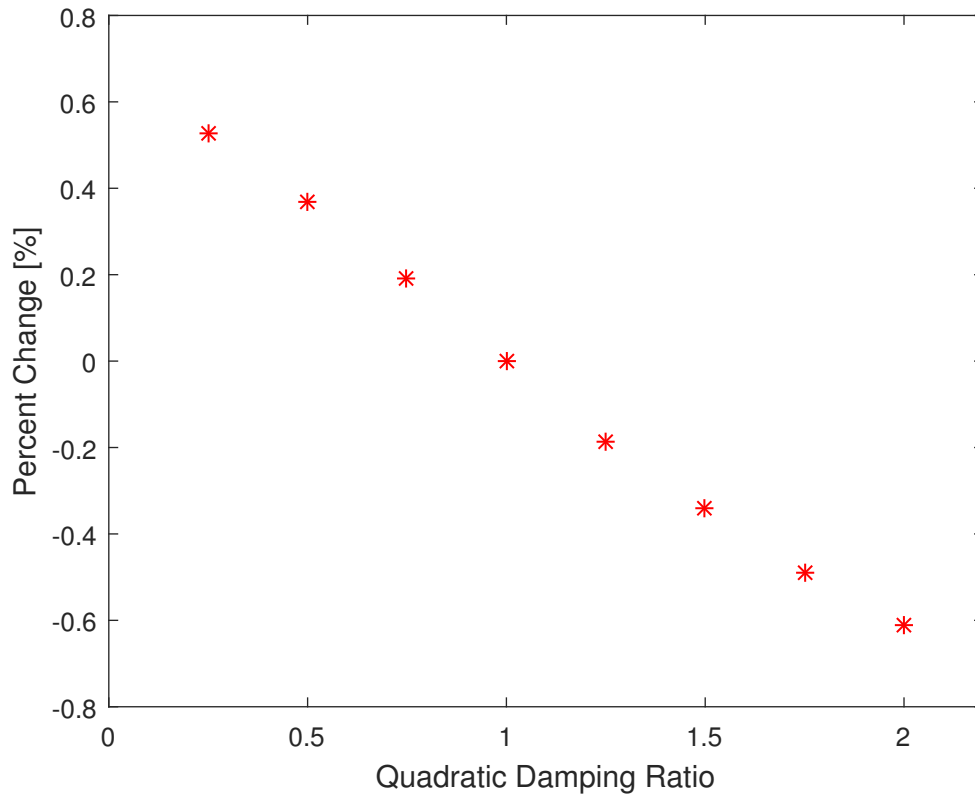


Figure 5.17: Percent change in lifting wire tension for drag ratios.

Despite the low sensitivity of the model to drag through the splash-zone, drag as a damping force will remain important in regions of resonance. As such the resonance period of the system needs to be investigated in order to check if damping is of little importance in our model. Figure 5.18 illustrates the change in vertical resonance period of the system for an increasing depth of the Dual Cap-X. The stiffness of the system as previously discussed is assumed to not include crane stiffness. It is clear that during the first phase of installation, there will be no issues with wave excited resonance, as the resonance period is so low. As such, it can be concluded that damping is relatively unimportant in the SIMO model.

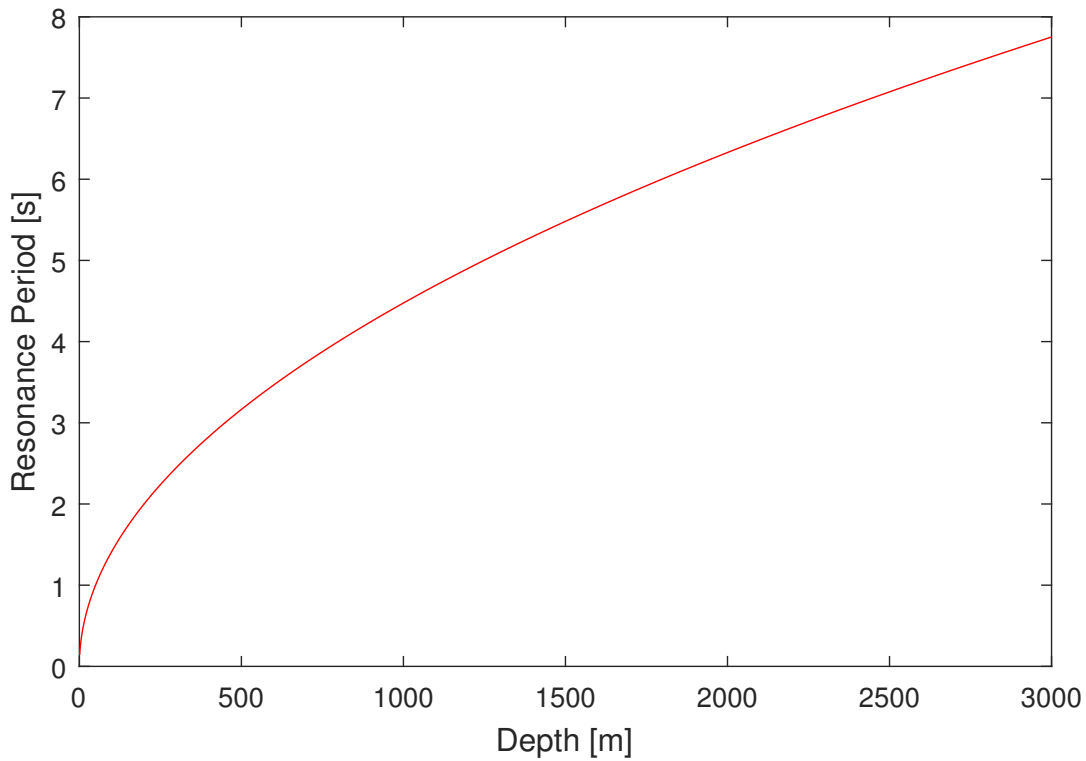


Figure 5.18: Vertical resonance periods for increasing depth of Dual Cap-X.

5.2.4 Wave Heading Sensitivity

A sensitivity study to understand how the wave heading affects the tension in the lifting wire is performed. The analysis consists of 5 different wave headings for a sea state of $H_s=4\text{m}$ and $T_p=8\text{s}$ with 50 realizations for each wave heading case. Table 5.3 presents the wave headings tested. It should be noted that wave heading 0° is defined as waves propagating from the stern of the ship towards the bow. Wave heading 90° represents beam sea with waves incoming from the opposite ship side of the payload deployment.

Table 5.3: Wave headings.

180°	165°	135°	90°	0°
------	------	------	-----	----

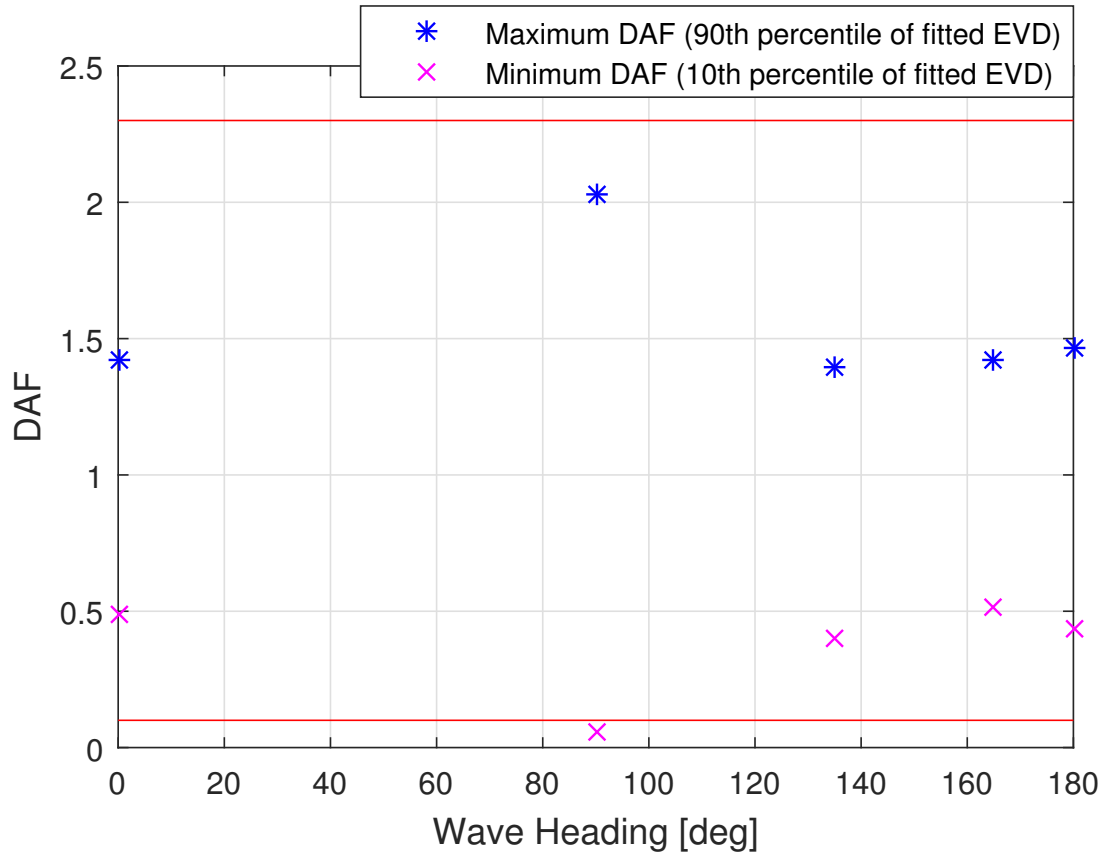


Figure 5.19: Maximum and minimum DAFs for lifting wire tension from 50 wave seeds for varying wave heading for $H_s=4$ m, $T_p=8$ s. The maximum and minimum lifting line tension criteria are included as an upper and a lower horizontal line, respectively.

Figure 5.19 shows both the maximum and minimum DAF in the lifting wire experienced during each wave heading. The maximum and minimum values are found by using the 90th and 10th percentiles from a fitted Gumbel distribution, respectively, as stated in Section 4.1.

The general observation is that beam waves are the most critical in terms of both maximum allowable crane wire tension and the slack criterion. Beam waves have a significant larger relative effect on the lifting wire tension compared to the other wave headings. Waves propagating from stern towards bow are marginally less critical than waves propagating from bow towards stern for both maximum and minimum lifting wire tensions, and they have similar effect as the quartering waves.

Furthermore, none of the observed percentiles exceed the maximum allowable lifting line tension. However, the results suggest that beam waves will introduce slack in the lifting line for

the specific sea state. As such, beam waves during splash-zone lowering should be of particular concern.

The reason for the significant difference in the lifting line tension for beam waves compared to the other wave headings, is the increased movement of the crane tip with incident beam waves on the vessel. As discussed in Section 3.2.5, the lowering of the Dual Cap-X is considered a light lift, thus the motion characteristics of the crane tip is assumed to be solely depend on vessel motion. As shown in Equation 3.22, vessel movement in heave, roll and pitch influence the crane tip vertical motion. In this case, vessel movement in roll is probably most significant due to a combination of beam waves and a crane position close to midships. Inspection of the vessel motions also confirms significantly larger movement in roll in beam waves compared to the other wave directions. With larger vertical crane tip motions, and thus larger vertical payload motions, the dynamics of the hydrodynamic forces on the payload will be larger and more profound.

A plausible explanation of the source of the small minimum lifting line tension in beam waves could be that the profound roll motions of the ship translates into a larger vertical velocity of the payload. Depending on the phase angle, the velocity of the payload could be directed downwards as it goes through the splash-zone. This would result in a larger slamming force compared to the cases with smaller vessel motion in roll, which again contributes to slack in the lifting line.

5.2.5 Current Sensitivity

Current can provide damping as well as act as an excitation force for the installation of the Dual Cap-X through the splash-zone. It is therefore of interest to examine the effect of various current speeds on the total lifting line tension. Based on values established in Statoil (2004), the current velocity regimes found in Table 5.4 were established, in which Regime 1 corresponds to a value in the order of a 100-year return period. This was chosen simply as the largest value to conduct sensitivity.

Table 5.4: Current velocity regimes.

	Surface Velocity [m/s]	50 m Velocity [m/s]	150 m Velocity [m/s]
Regime 1	1.00	0.50	0.25
Regime 2	0.50	0.25	0.10
Regime 3	0.25	0.10	0.05

Simulations in SIMO were conducted with $H_s = 4$ m, $T_p = 8$ s and a wave seed of 1. Current was modelled from a direction of 0° . The results of introducing the three regimes outlined in Table 5.4 are illustrated in Figure 5.20.

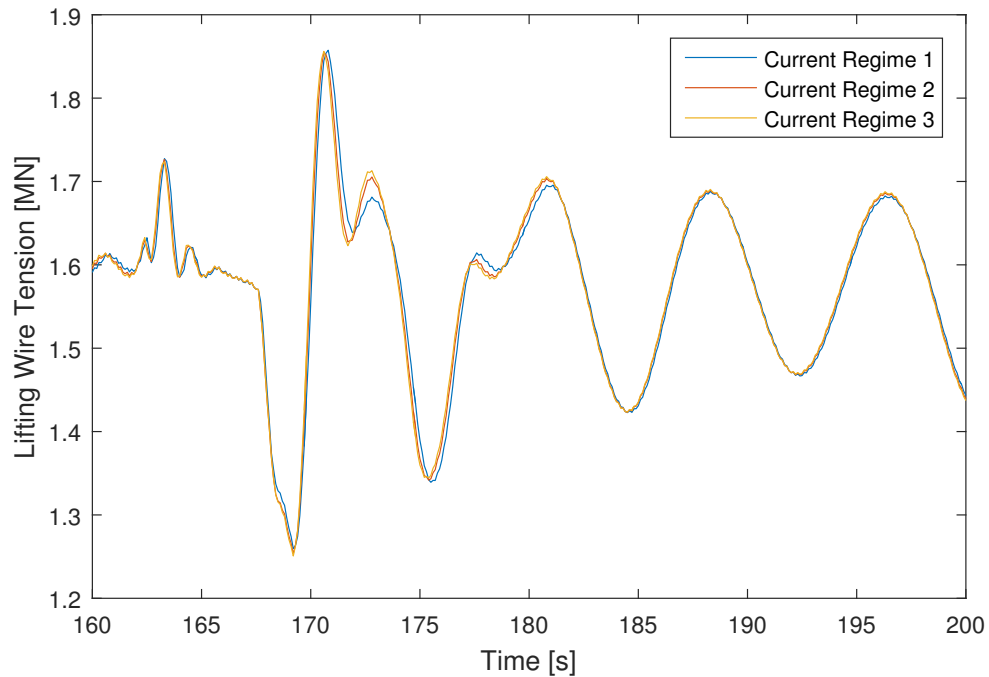


Figure 5.20: Current sensitivity.

It appears that current has little or no effect on the total wire tension. This is most likely due to the magnitude of the weight and hydrodynamic forces acting on the Dual Cap-X.

5.2.6 Crane Tip Position Sensitivity

As outlined in Section 3.2.5, crane tip motions depend on the position of the crane tip relative to the center of gravity of the vessel. For vertical motions, it is dependent on η_3 , η_4 and η_5 of the vessel. Typically the distance in the horizontal, η_2 direction remains approximately the same, as it minimizes the radius of the crane whilst maintaining a safe distance from the deck to avoid collisions between the payload and the ship. As such, the major variable is the crane position along the ship in the η_1 direction. An investigation into the sensitivity of this position was conducted in SIMO, where various crane positions were evaluated. An $H_s = 4\text{ m}$, $T_p = 8$ and wave seed of 1 were used for a heading of 15 degrees. The crane tip positions investigated are presented in Table 5.5. It should be noted that values are given as the distance from the center of gravity of the vessel in the η_1 direction where η_1 is defined positive towards the bow.

Table 5.5: Crane tip position in η_1 - direction.

Crane Tip Position [m]
10
0
- 10
- 20
- 30
- 40

Figure 5.21 illustrates the total lifting wire tension for varying crane tip positions. The results suggests that the position has a significant effect on the total force experienced by the lifting wire. 35 wave realizations were run, and the results analyzed in an attempt to determine a trend between crane tip position and the total lifting line force. This trend however was difficult to identify, as the variability between results was quite large. Figure 5.22 illustrates the 90th percentile values from Gumbel fitted distribution for maximum values of the lifting wire force as well as the minimum values corresponding to a 10th percentile. EVD indicates the Gumbel extreme value distribution

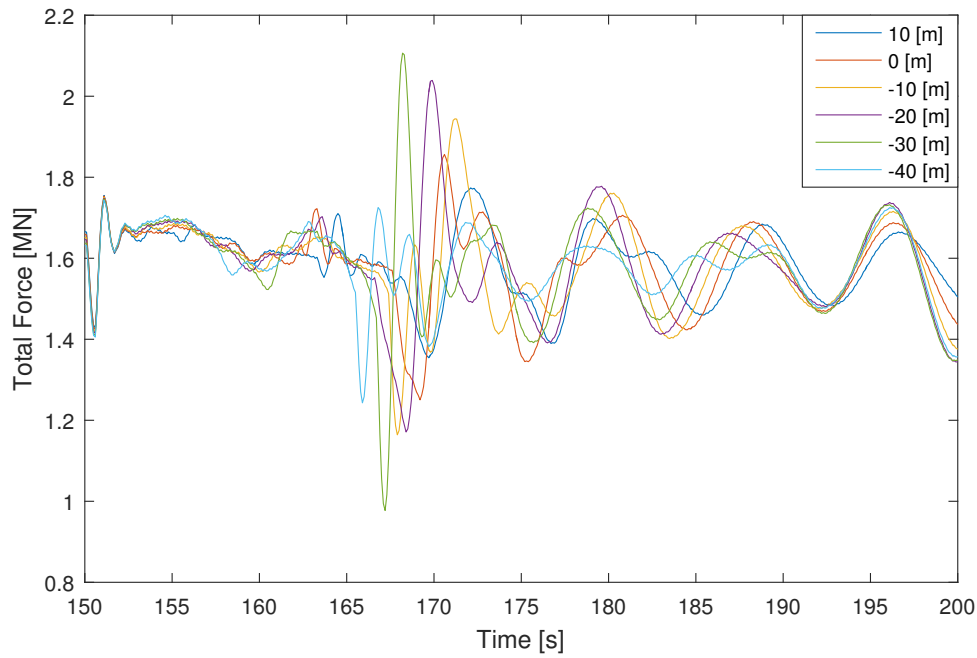


Figure 5.21: Lifting wire tension for $H_s = 4$, $T_p = 8$, wave seed = 1.

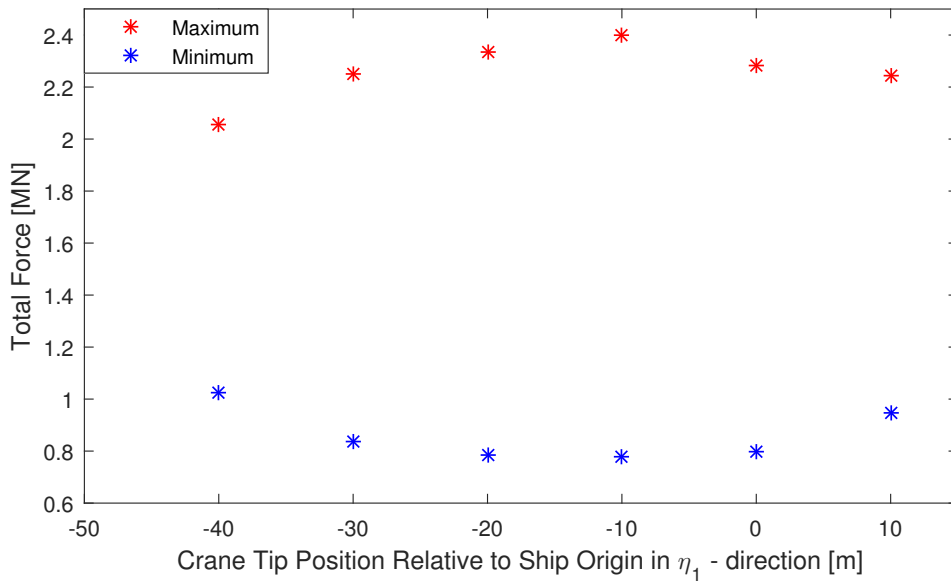


Figure 5.22: 90 % fitted EVD

It is difficult to determine whether or not a trend is evident from Figure 5.22. It appears that the largest value occurs at a crane tip position of -10 m from the origin, and decreases in both directions. One would however expect an increase in both direction from the origin due to increased

crane tip motions from the pitch motions of the vessel. This however does not appear to be the case. Based on the general variability of the results, it appears that the position of the crane depends highly on the particular wave environment as the module enters the splash-zone. As such it is difficult to recommend an optimal position, as this will vary significantly from operation to operation.

5.2.7 Identification of Hydrodynamic Forces

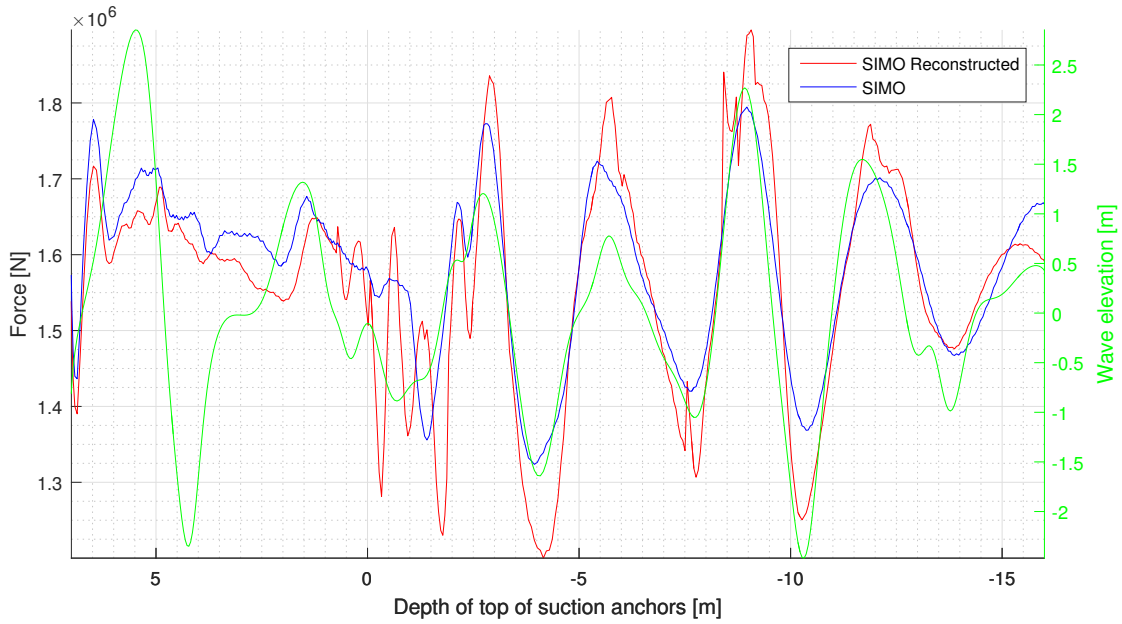
In order to fully understand the dynamics of the lifting of the Dual Cap-X through the splash-zone, one will have to understand which hydrodynamic forces have largest impact on the integrity of the operation, and which dynamic phenomena that dominate in this phase. These issues are discussed in this section.

Since SIMO does not provide a way of separating the hydrodynamic forces acting on the lifting system, reconstruction of each type of hydrodynamic force is performed manually in the post-processing by utilizing Equation (3.39). By using the output translations, velocities and accelerations from SIMO for a specific run, each hydrodynamic force is determined.

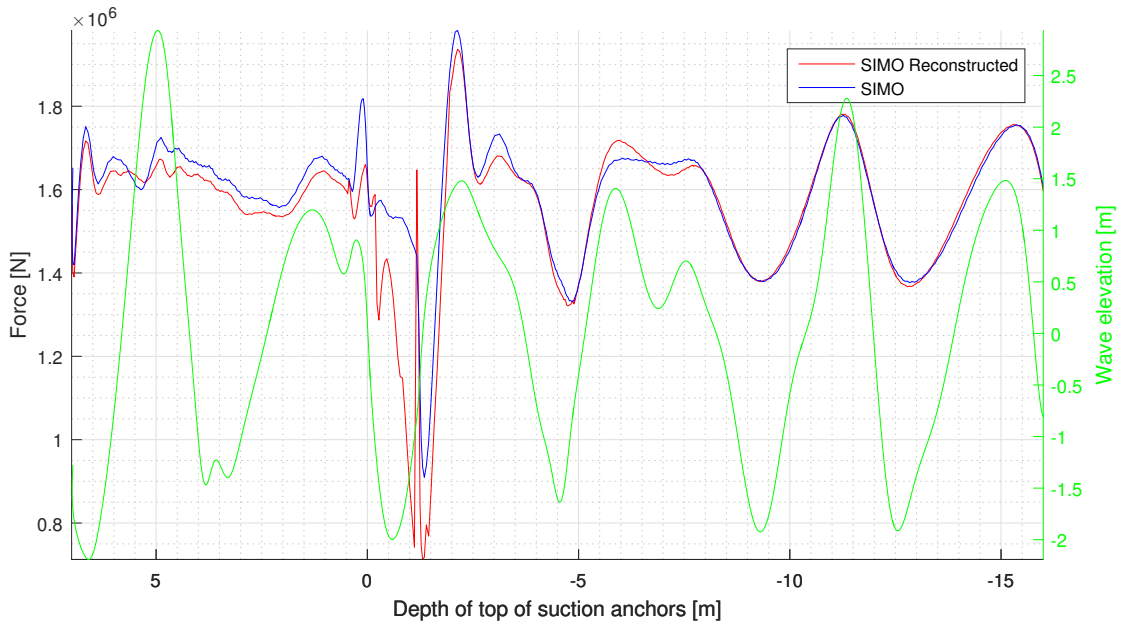
Reconstruction of the Lifting Line Force

By summing the calculated values of each hydrodynamic force and the buoyancy force using Equation (3.39), the force in the lifting line can be reconstructed, and then compared to the lifting line force obtained directly as an output from SIMO.

Figures 5.23a and 5.23b show the lifting line force obtained directly from SIMO ("SIMO") and the reconstructed lifting line force ("SIMO Reconstructed") for the same sea state, but for two different wave realizations. The results indicate that the general trend of the reconstructed lifting line force shows good coherence with the direct output from SIMO. However, it seems that the reconstructed values overestimate the dynamic forces compared to the direct output from SIMO. The general tendency is that the largest discrepancies occur when the payload passes the free surface, and when its fully submerged but in close proximity to the free surface.



(a) Wave seed = 9.



(b) Wave seed = 10.

Figure 5.23: Comparison of the lifting line force for sea state $H_s=4\text{m}, T_p=8\text{s}$. Depth given from mean surface level. Wave elevation is also included (green line).

A plausible explanation to the deviation between "SIMO" and "SIMO Reconstructed" could be the fact that SIMO does not include the water exit force, which normally would be included

by replacing the slamming force in Equation 3.39 by a specific water exit term. Instead, SIMO simply omits the slamming term $\frac{dA_{33}^{\infty}}{dh}(\dot{\zeta} + \dot{\eta})^2$ in Equation 3.39 during the water exit phase. To simplify the calculation of "SIMO Reconstructed", the slamming term is always included, even when the submergence depth from the free surface decreases due to change in the wave elevation. As such, it should be noted that neither "SIMO" nor "SIMO Reconstructed" capture the full dynamic picture during water exit. Figures 5.23a and 5.23b have a distinct difference in that wave seed 9 has a higher degree of oscillatory behaviour in "SIMO Reconstructed" than is present in wave seed 10. This is evident just after submergence. This may be a result of the difference in wave elevation at this specific time since the X-axis in the figures is defined with its origin as the mean sea level. This supports the theory that the discrepancy between "SIMO" and "SIMO Reconstructed" is due to the omission of the slamming term during water exit.

Another possible explanation to the difference in "SIMO" and "SIMO Reconstruction" could be related to how "SIMO" defines the slope of $\frac{dA_{33}^{\infty}}{dh}$. Due to the way the relative vertical added mass is defined for increasing water depths in SIMO, there will be certain discontinuities in the slope of $\frac{dA_{33}^{\infty}}{dh}$. SIMO may be able to filter out the effects of the discontinuities. This was not taken into account in the calculation of "SIMO Reconstructed".

Dominating Forces

Figures 5.24 and 5.25 present both the hydrodynamic forces and the buoyancy force for the same sea state, but with two different wave realizations. These are the results used to reconstruct the lifting line force in Figures 5.23a and 5.23b. The instantaneous wave elevation is also included in 5.25 and 5.24.

Positive force direction is defined upwards. For clarity, the Froude-Krylov (FK) and diffraction (related to water particle acceleration) forces presented in the figures should be understood as part of the wave excitation force given in Section 3.2.6. Since the the FK and diffraction forces are presented together in the results, it should be pointed out that the FK forces are expected to be more dominant relatively to the diffraction forces. This is due to the payload being considered as a small-body structure (as discussed in 3.2.6). However, these forces are presented together

in the following discussion. The inertia force is $F_{I,i} = -(M\delta_{i,j} + A_{ij})\ddot{\eta}_j$ as presented in 3.2.6. The definitions of the other hydrodynamic forces referenced to in the figures, are found in Section 3.2.6.

The general trend in 5.24 and 5.25 is that immediately after the two suction cans of the Dual Cap-X are submerged, there is an abrupt slamming load which dominates the dynamic picture at this specific time. After the slamming load, the dominating hydrodynamic forces are the FK and diffraction forces (wave excitation), which continue to dominate as the payload is submerged further down the water column. In both figures, a large spike in the inertia force can be observed around the time both suction cans are fully submerged. For wave seed 10 this inertia force acts downward, and therefore contributes to the tension in the lifting line. For wave seed 9, this inertia force acts in the opposite direction, and therefore contributes to slack the lifting line. The effect of these inertia load spikes on the lifting line tension can be observed in "SIMO Reconstructed" in figures 5.23a and 5.23b, and seem to contribute to the discrepancy between "SIMO" and "SIMO Reconstructed". Inspection of the payload acceleration at the time of the inertia load spikes, confirms that there is a large jump in the magnitude of the acceleration. A possible explanation to this spike in the inertia load may be that SIMO calculates the lifting line tension by using Equation (3.37), where vertical payload translation η_3 is used. However, when the inertia force was calculated and used with the other forces to obtain "SIMO Reconstructed", the vertical acceleration $\ddot{\eta}_3$ was used. It is expected that the $\ddot{\eta}_3$ signal output contains a larger degree of noise than η_3 , and as such explain the peak in the calculated value of inertia force and also the discrepancy between "SIMO" and "SIMO Reconstructed".

For wave seed 10, Figure 5.25 shows that the slamming force is the most dominating hydrodynamic force in the splash-zone, and that it contributes to slack in the lifting line. At the time of submergence of the top of both suction cans, the figure shows two occurrences of slamming. This is due to the change in the wave elevation causing the distance from the top of suction cans to the free surface to increase, and then decrease, before finally increasing again (note that the X-axis in the figure uses the mean sea level as reference). It is the second peak of the slamming load that causes the most extreme minimum tension in the total lifting line wire seen in Figure 5.23b. The subsequent tensioning of the lifting line in 5.23b is caused by a combination of

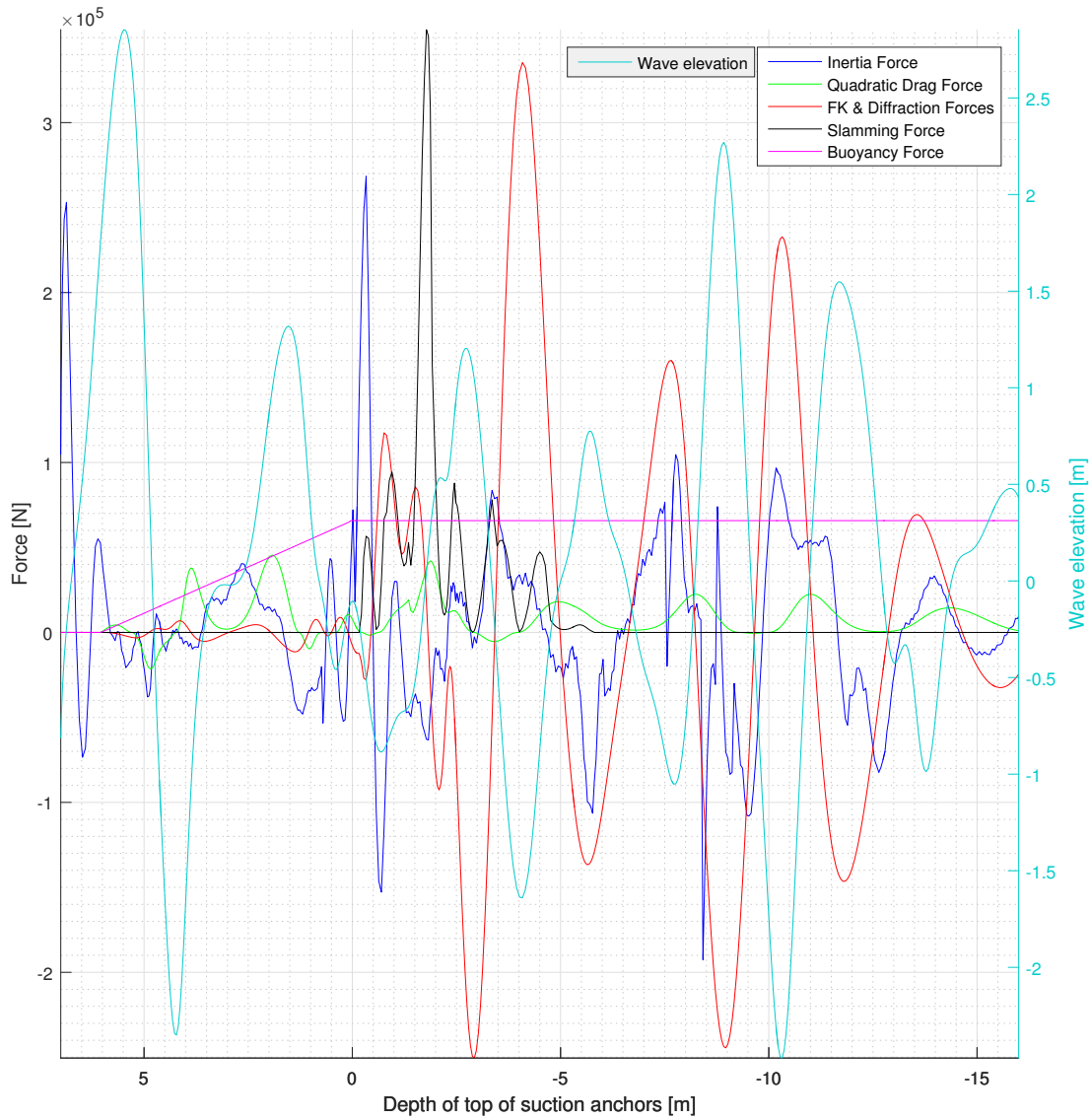


Figure 5.24: Vertical Hydrodynamic Forces and Buoyancy Force on Payload and Wave Elevation - $H_s = 4$ m, $T_p = 8$ s, wave seed = 9. Depth given from mean surface level.

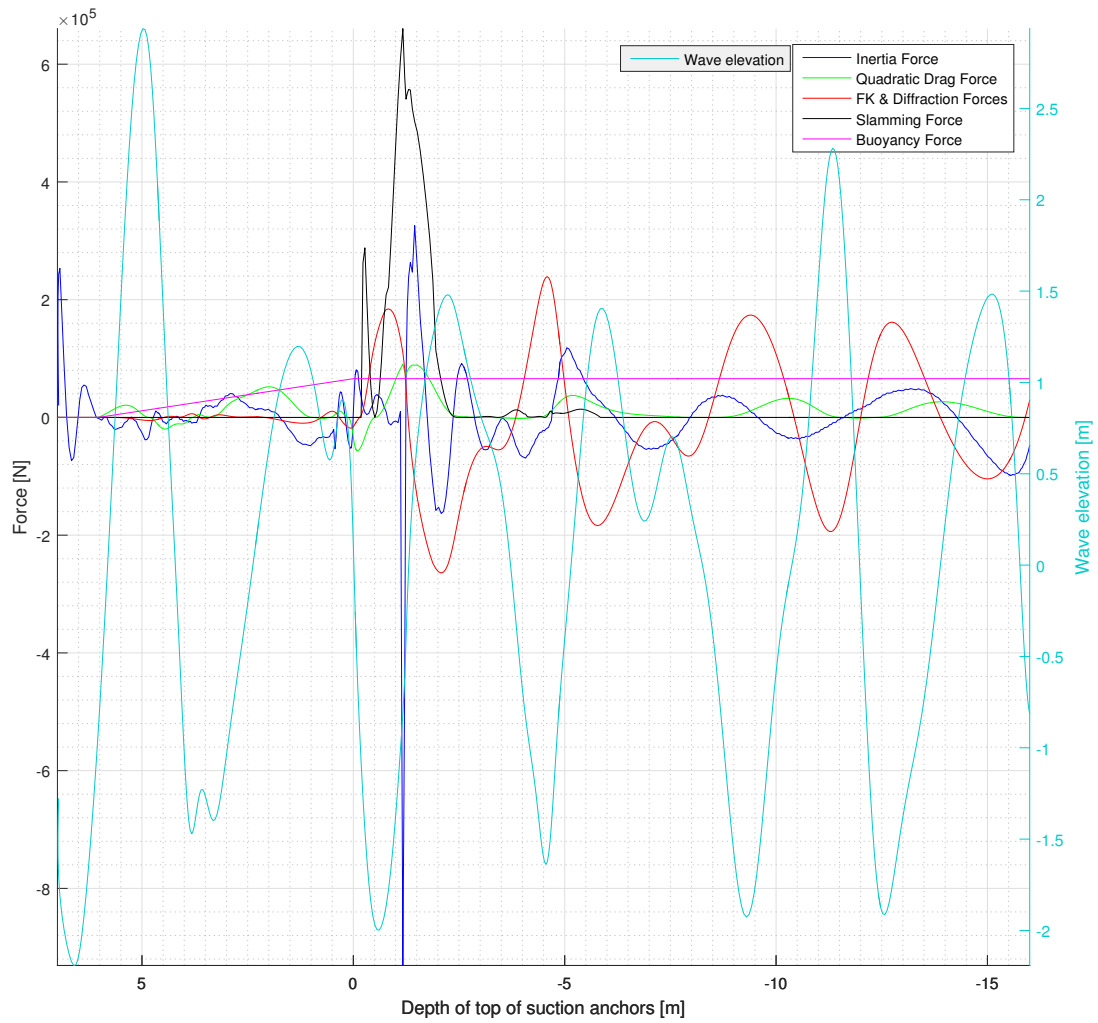


Figure 5.25: Vertical hydrodynamic forces and buoyancy force on payload and wave elevation - $H_s = 4$ m, $T_p = 8$ s, wave seed = 10. Depth given from mean surface level.

inertia and wave excitation (FK and diffraction) forces. This constitutes the most extreme maximum tension in the total lifting line. After this, the FK and diffraction forces give the largest contribution to the dynamic forces in the lifting line.

The results presented in Figure 5.24 are somewhat surprising, and indicate that even though the slamming force can be considerable, it does not always dominate the hydrodynamic picture alone. It can be observed that as the top of the two suction anchors are submerged to a water depth of 1.5 m, a large slamming peak load acting against the downward velocity of the Dual Cap-X arises. As seen in Equation (3.39), this force will contribute to slack in the crane wire tension. By inspection of Figure 5.23a, it can be seen that the effect of this slamming does not cause the most extreme dynamic forces in the lifting wire. On the contrary, the most extreme dynamic forces in the lifting line seems to be caused by the wave excitation forces.

The fact that the FK and diffraction forces are of such dominating magnitude in the splash-zone, suggests that attention to accurately capturing the added mass of the structure is of immense importance in installation planning. Since the vertical Z-component of the water particle acceleration is 90° out of phase with the wave elevation, the FK and diffraction forces both contribute to tensioning and slack in the crane wire, depending on the direction of the acceleration. For the case presented in Figure 5.24, it is clear that the maximum force amplitude peak contributing to slack is considerable. It should also be noted that there also are two large peaks (at around -2.6 m and -8.6 m) in the opposite direction in the time series that act downward and as such contribute to tension in the lifting wire. A tendency in the industry is to put a lot of effort into determining the slamming coefficient in splash-zone analyses. Even though slamming is important, 5.24 suggests that emphasis on accurately capturing added mass of the payload is essential and should not be neglected since FK and diffraction forces can be of high importance in the splash-zone. This is especially true since the vertical added mass of the Dual Cap-X is very large compared to the structural mass.

The spike in the inertia force at the very start is due the abrupt start of the winch (from 0 to $0.5 \frac{m}{s}$). As such, this causes a large downward acceleration of the payload.

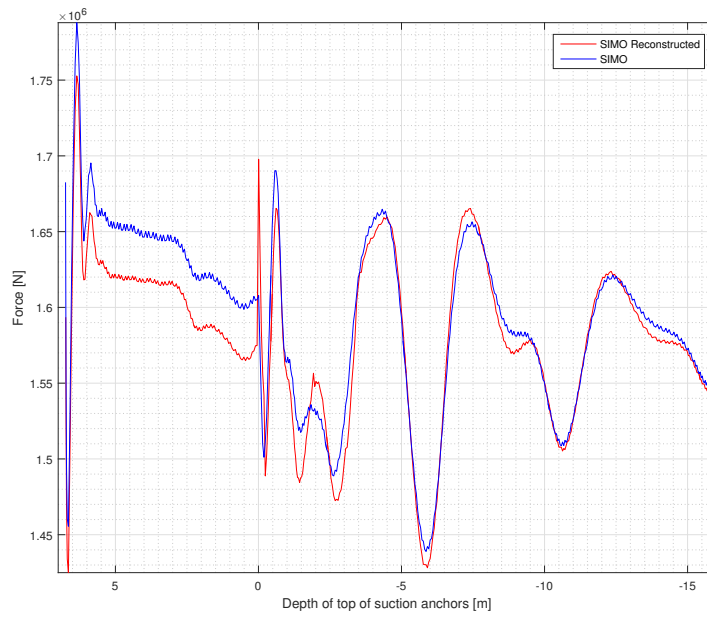
The quadratic drag force is directed opposite to the relative velocity between the water particle

and payload velocity in heave. As such it will contribute to both slack and tension the crane wire. The amplitude of the quadratic drag does not change much as the payload is submerged through the splash-zone. When the payload is fully submerged, a more or less stable cyclic quadratic drag loading arises. It is quite clear from these two wave realizations that the quadratic drag force has a negligible impact on the crane wire tension through the splash-zone lifting phase. This also confirms the findings from Section 5.2.3.

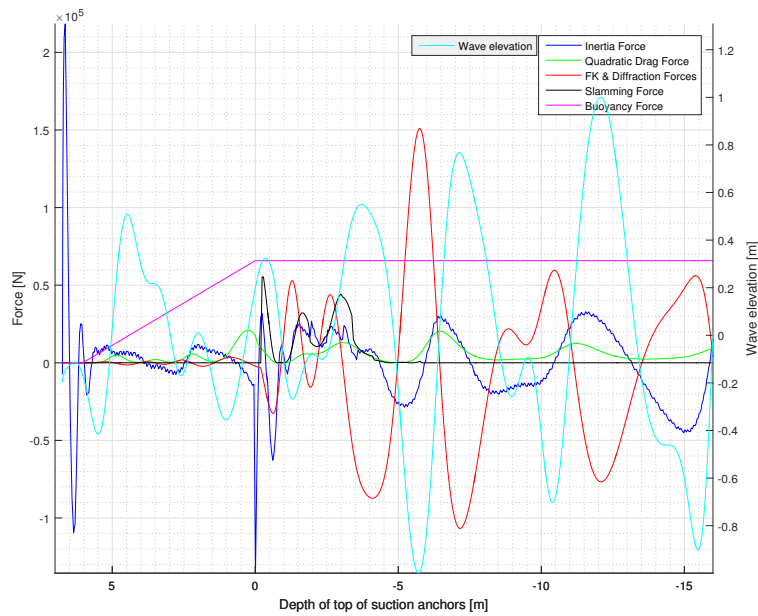
The buoyancy force is not directly considered a hydrodynamic force, but is nevertheless included in the discussion. As seen in figures 5.25 and 5.24, the buoyancy force increases linearly with submergence depth of the two suction cans, and reaches a maximum as they are fully submerged. The buoyancy force due to the frame of the Dual Cap-X is neglected in "SIMO Reconstructed" due to the small enclosed volume of this part of the structure. The buoyancy force is directed upwards, and will therefore contribute towards reducing the lifting line tension. The buoyancy force is as expected not a dominating force in the lowering of the Dual Cap-X through the splash-zone, due to the small enclosed volume of the payload. Nevertheless, it is interesting to see that the buoyancy force affects the force in the lifting line more than the vertical quadratic drag force.

Dominating Forces in Milder Sea Conditions

The results presented in the previous subsections, apply to a sea state with $H_s = 4m$ and $T_p = 8s$. In this subsection, the dominating hydrodynamic forces in milder sea conditions are presented in order to investigate whether the same trend is present. Figures 5.26a and 5.26b show the total lifting line force and the vertical hydrodynamic forces on the payload, respectively, for a sea state with $H_s = 2m$ and $T_p = 11s$ for a single wave realization. Note that some discrepancy between "SIMO" and "SIMO Reconstructed" can be seen in Figure 5.26a around the mean sea level, although the general trend seems to be the same. It should be understood that the possible explanations to the discrepancy provided for the results in the sea state with $H_s = 4m$ and $T_p = 8s$, also apply for this case. Especially the inertia load spike visible at 0 m should be considered a result of signal noise associated with $\ddot{\eta}_3$.



(a) Comparison of the lifting line force. Depth given from mean surface level.



(b) Hydrodynamic forces and buoyancy force on payload. Wave elevation is also included. Depth given from mean surface level.

Figure 5.26: Results for a sea state with $H_s = 2m$ and $T_p = 11s$ and wave seed = 9.

First of all, the results for this specific wave realization show overall smaller magnitudes of the

hydrodynamic forces in the lifting line compared to the results from the rougher sea state. Secondly, the FK and diffraction forces seem to be more dominating than the slamming force with respect to the extreme values of the total lifting line force. The relative importance of the buoyancy force is also more profound due to the overall smaller hydrodynamic forces. As the top of the payload passes a water depth of 8-9 m (from mean sea level), the inertia forces appear to partially cancel out the effect of the FK and diffraction forces. In general, it seems that the relative difference in magnitude between inertia forces and FK and diffraction forces is smaller compared to rougher sea. This is due to smaller fluid particle kinematics in milder sea states.

5.2.8 Evaluation of Acceptance Criteria

In order to determine the operational limits of the Splash-Zone phase of the PIM, various combinations of hoisting speeds, H_s and T_p were investigated. 35 different wave seeds were evaluated to provide a sufficient population for statistical analysis. An increased number of wave seeds would be optimal, but due to restrictions related to available computational power was not feasible. For each simulation, the maximum and minimum values were extracted with respect to relevant parameters. A population comprised of the relevant values for all 35 seeds in a given combination of H_s and T_p were then fitted to a Gumbel distribution as outlined in Section 4.3. The relevant variables implemented in the analysis are shown in Tables 5.6 and 5.7. Relevant combinations were run based on the one year contour for the Heidrun metocean data outlined in Section 4.2.2. The simulations were separated into cases for different hoisting speeds. Each case therefore required 1225 simulations. In total 3665 simulations were conducted to provide the results presented in this section. No wind or current were introduced in the simulations. The wave heading was set to 15° .

Table 5.6: Hoisting speeds.

Hoisting Speed [m/s]		
0.1	0.25	0.5

Table 5.7: Simulation variables.

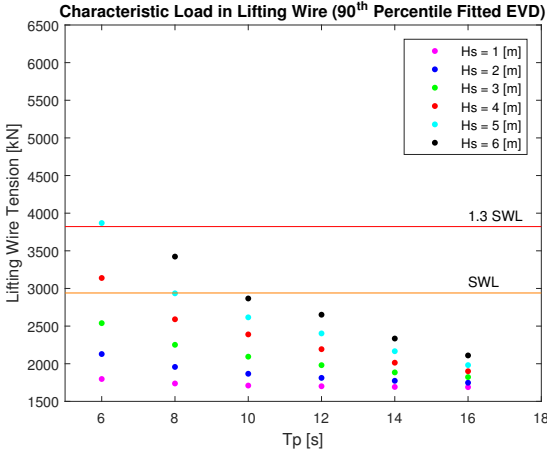
H_s [m]	T_p [s]
1	6
2	8
3	10
4	12
5	14
6	16

The following parameters were evaluated with respect to the acceptance criteria outlined in Section 4.1:

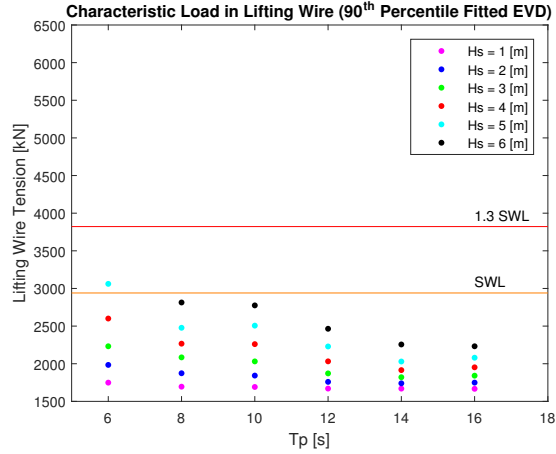
- Maximum lifting line tension
- Minimum lifting line tension
- Minimum sling tension

Maximum Lifting Line Tension

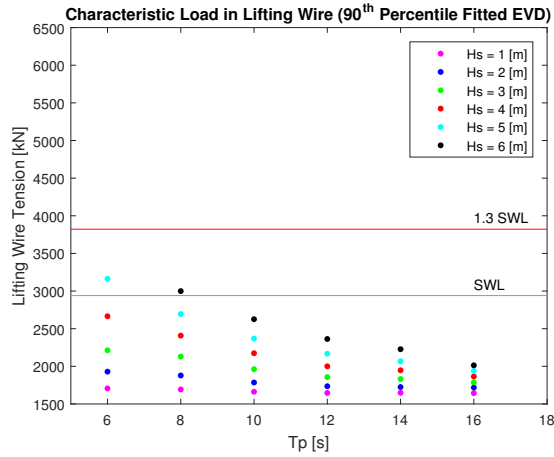
The results shown in Figure 5.27 illustrate the maximum tension in the lifting line. Each point represents the 90th percentile of a fitted Gumbel distribution for the maximum values from each wave seed. The orange line indicates the safe working load (SWL) of the crane, and the red line the maximum allowable lifting line tension (1.3 SWL) as outlined in Section 4.1.



(a) Hoisting speed = 0.1 m/s.



(b) Hoisting speed = 0.25 m/s.

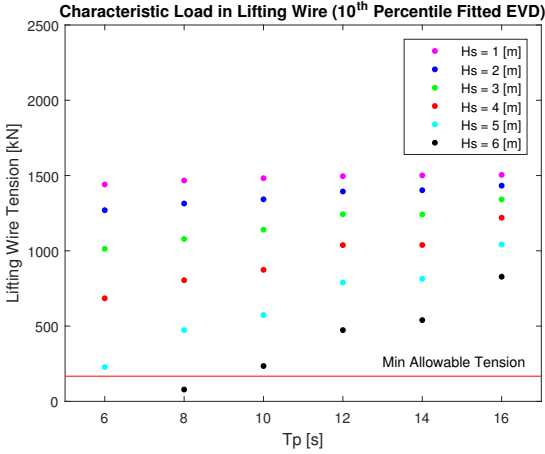


(c) Hoisting speed = 0.5 m/s.

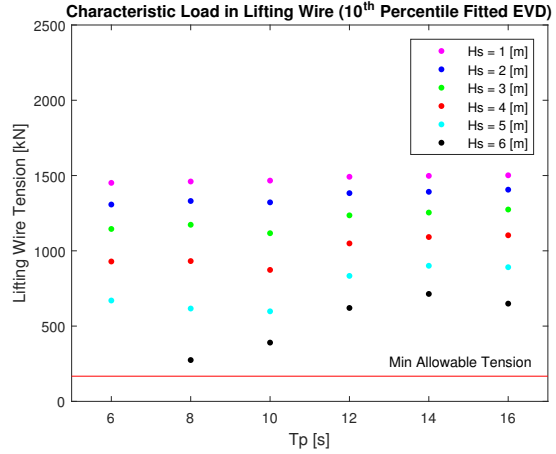
Figure 5.27: Maximum lifting line tension.

Minimum Lifting Line Tension

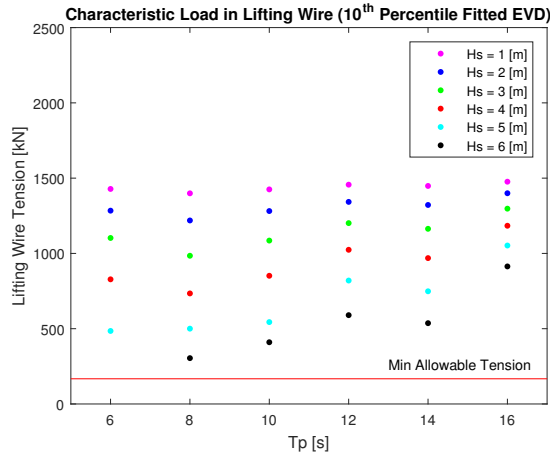
Figure 5.28 illustrates the minimum tension in the lifting line. Each point represents the 10th percentile of a fitted Gumbel distribution for the minimum values from each wave seed. The red line indicates the minimum allowable lifting line tension as outlined in Section 4.1.



(a) Hoisting speed = 0.1 m/s.



(b) Hoisting speed = 0.25 m/s.



(c) Hoisting speed = 0.5 m/s.

Figure 5.28: Minimum lifting line tension.

Minimum Sling Tension

Figures 5.29, 5.30 and 5.31 illustrate the minimum tension in each sling. Each point represents the 10th percentile of a fitted Gumbel distribution for the minimum values from each wave seed. The red line indicates a value of 0 N, as the acceptance criteria outlined in Section 4.1 require only that slings never experience slack conditions.

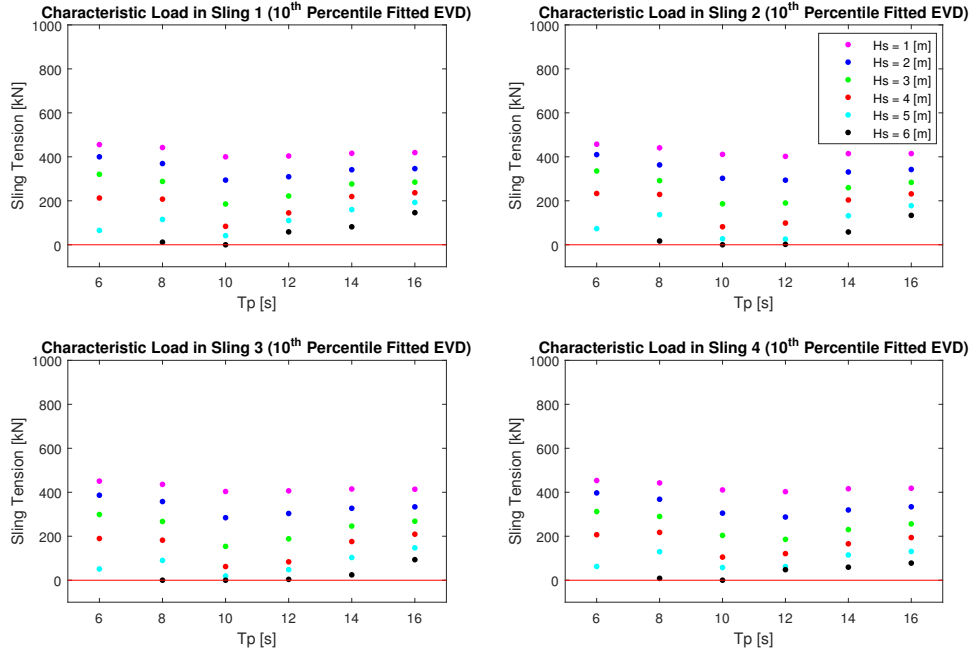


Figure 5.29: Minimum sling tension for a hoisting speed of 0.1 m/s.

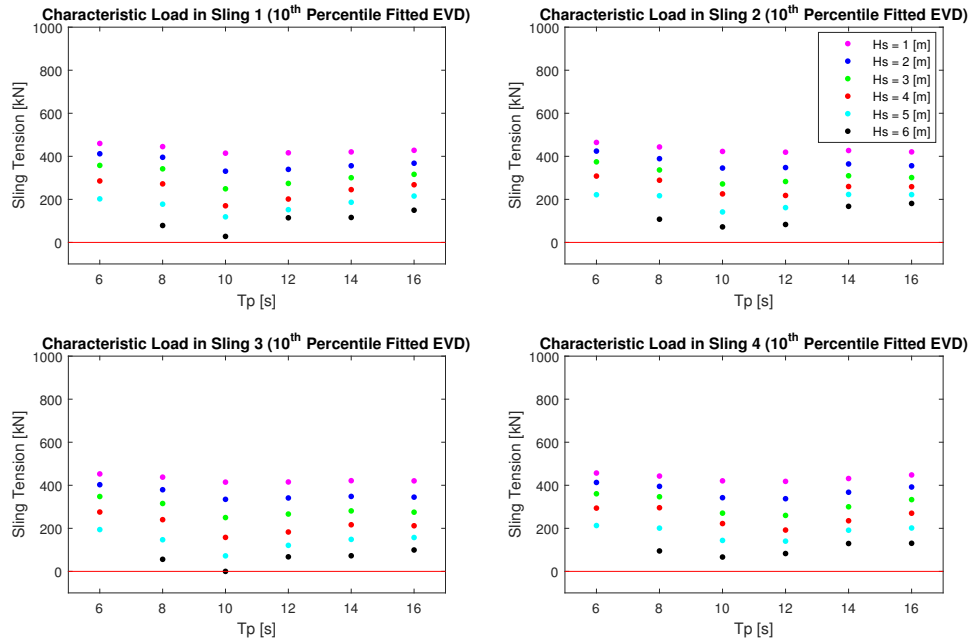


Figure 5.30: Minimum sling tension for a hoisting speed of 0.25 m/s.

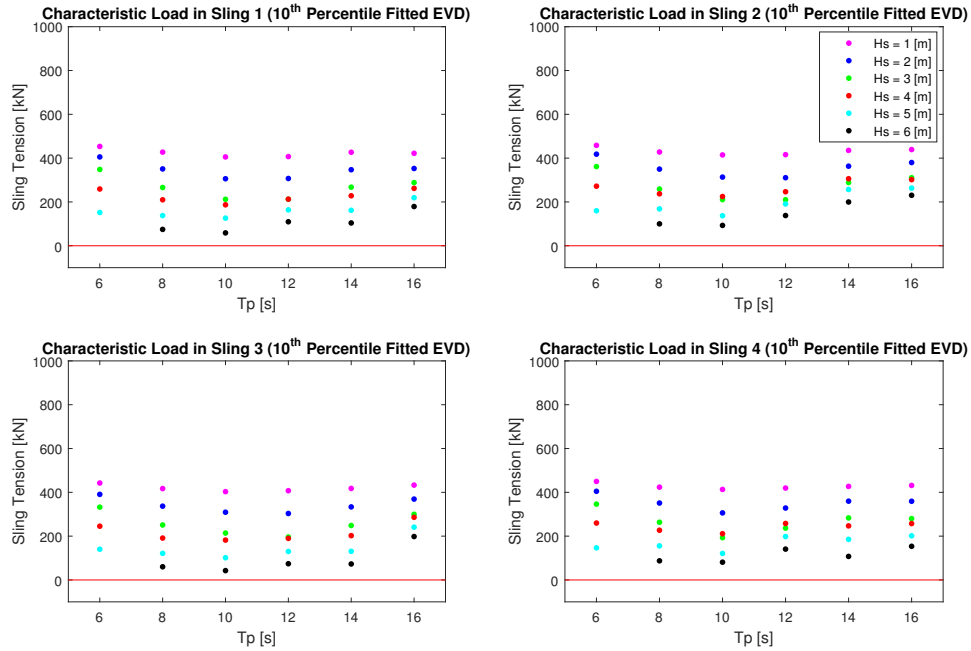


Figure 5.31: Minimum sling tension for a hoisting speed of 0.5 m/s.

Design Criteria

Based on the results found, design criteria with respect to the criteria outlined in 4.1 could be determined. The resultant limits are presented for each hoisting speeds in figures 5.33, 5.34 and 5.35. The design criteria are determined based on all acceptance criteria outlined. Acceptance criteria specific design criteria can be found in Appendix D.

	Within acceptance criteria
	Bordering acceptance criteria
	Above SWL of crane but below maximum allowable tension
	Outside acceptance criteria

Figure 5.32: Legend for design criterion tables.

Hs/Tp	6	8	10	12	14	16
1						
2						
3						
4						
5						
6	NA					

Figure 5.33: Design criteria for a hoisting speed of 0.1 m/s.

Hs/Tp	6	8	10	12	14	16
1						
2						
3						
4						
5						
6	NA					

Figure 5.34: Design criteria for a hoisting speed of 0.25 m/s.

Hs/Tp	6	8	10	12	14	16
1						
2						
3						
4						
5						
6	NA					

Figure 5.35: Design criteria for a hoisting speed of 0.5 m/s.

Discussion

Looking at the design criteria in Section 5.2.8, clear trends can be seen. The design criterion decreases for:

- Increasing H_s
- Decreasing T_p
- Decreasing hoisting speed

It should be noted that a decrease in the design criterion entails a more limiting state. One clearly sees from Appendix D, that these limits are not solely determined by any one of the acceptance criteria, but a combination. A speed of 0.1 m/s undeniably yields the lowest limits, and the limits increase with the hoisting speed. This is most likely due to the fact that the Dual Cap-X is subjected to forces in the wave zone for a longer period of time. As such, the probability of encountering a wave that excites forces that result in a breach of the acceptance criteria increases. Due to the fact that slamming is proportional to the squared relative velocity of the payload, one would expect higher slamming loads, and resultant lower operational limits for higher hoisting speeds. This effect however seems to be minimal compared to the dominating effect of increased exposure to splash-zone effects. It is also evident that breaches of maximum allowable tension often coincide with a breach of the minimum allowable tension or a slack sling condition. This may indicate the occurrence of snap loads.

The trends aforementioned are less apparent between speeds of 0.25 m/s and 0.5 m/s. Certain discrepancies were noticed such as lower values for the maximum lifting line tension for a T_p of 8 for a hoisting speed of 0.25 m/s than experienced for a speed of 0.5 m/s as seen in Figure 5.27. Both Figure 5.27a and 5.27c, indicate a clear trend, where an increase in H_s and a decrease in T_p yield higher tension. 5.27b also displays such a trend, but values of $T_p = 8$ s do not match. They are in fact lower than the corresponding values for the higher hoisting speed of 0.5 m/s. Values for $T_p = 6$ s are also lower than their corresponding values for 0.5 m/s. An attempt was

made to investigate the source of these findings, as the trends seen for a hoisting speed of 0.25 m/s generally do not match those found for 0.1 m/s and 0.5 m/s.

As outlined in Section 5.1, pendulous motion in air can be significant for certain wave periods. As the wave heading was set to 15° , contributions from the effects found for head and beam sea wave conditions investigated in Section 5.1 will affect the system. As such significant in-air oscillations may occur. Figure 5.36 shows the lifting line tension for a hoisting speed of 0.25 m/s, $H_s = 4$ m, $T_p = 10$ s and wave seed = 6. The oscillatory behaviour of the Dual Cap-X while in-air has significant effects on the lifting line tension. This is due to the excitation of pendulous motion as outlined in Section 5.1.

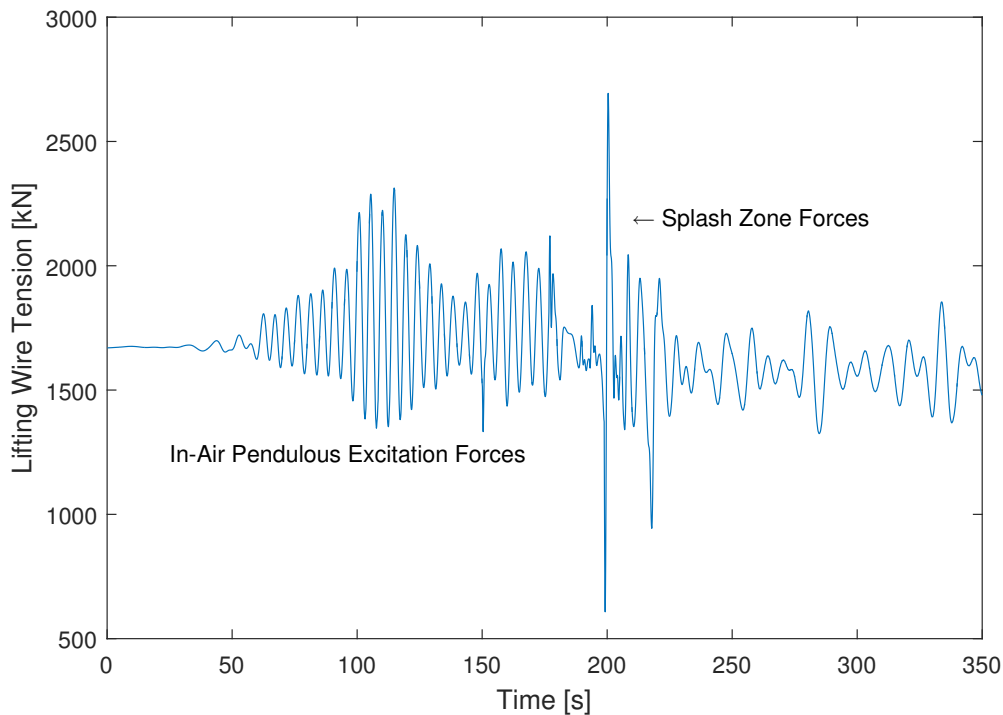


Figure 5.36: Lifting wire tension for hoisting speed 0.25 m/s, $H_s = 4$, $T_p = 10$, wave seed = 6

These effects can be significant and in certain cases would provide the largest forces experienced. In order to minimize the effect of the pendulous motion on the results, the results were filtered to only include values once the bottom of the Dual Cap-X began to enter the water, and the motion was damped out to a certain degree. In most cases the splash-zone forces were di-

mentioning, but for lower significant wave heights, this filtering provided greater accuracy with respect to operational limits due to splash-zone effects.

Tugger lines will be essential to avoid pendulous motion during the lowering of the Dual Cap-X. Pendulous motion would then be minimized, and the only significant forces would be experienced through the splash-zone. As such, the validity of the results using filtering was assumed. Nonetheless, the residual motion of the Dual Cap-X in the splash-zone will have an effect on the results as it is not instantaneously damped out. This will have an adverse effect on the accuracy of the results, and depend highly on the specific wave realization with respect to behaviour. This may be the origin of the anomalies found for the hoisting speed of 0.25 m/s. Improved results could be yielded from running a higher number of wave seeds. This was attempted, but was found to be unachievable due to constraints related to available computational power.

The degree to which crane tip excitation affects the results is also of interest. Figure 5.37 illustrates the RAOs of the vessel for the heading utilized in the analyses. Naturally, an increase in H_s results in an increase in the response of the vessel, but the RAOs also give an indication as to which periods will yield the highest motion response. For vertical crane tip motion, one can translate the RAOs via the equations outlined in Section 3.2.5. The heave, roll and pitch of the vessel will therefore be of importance. Figure 5.37a shows the RAO for the heave of the ship, indicating the largest values for periods over 25 seconds, with a local peak around 7 seconds, but of minimal significance. Figure 5.37b illustrates the RAO of the roll of the vessel, with a peak around 14-15 seconds. Figure 5.37c illustrates the pitch of the vessel, with a peak around a period of 10-11 seconds. Based solely on crane tip motions, one would therefore expect the largest forces to be experienced for peak periods over 10 seconds. This is however not the case. These values in fact yield the lowest lifting line tensions encountered.

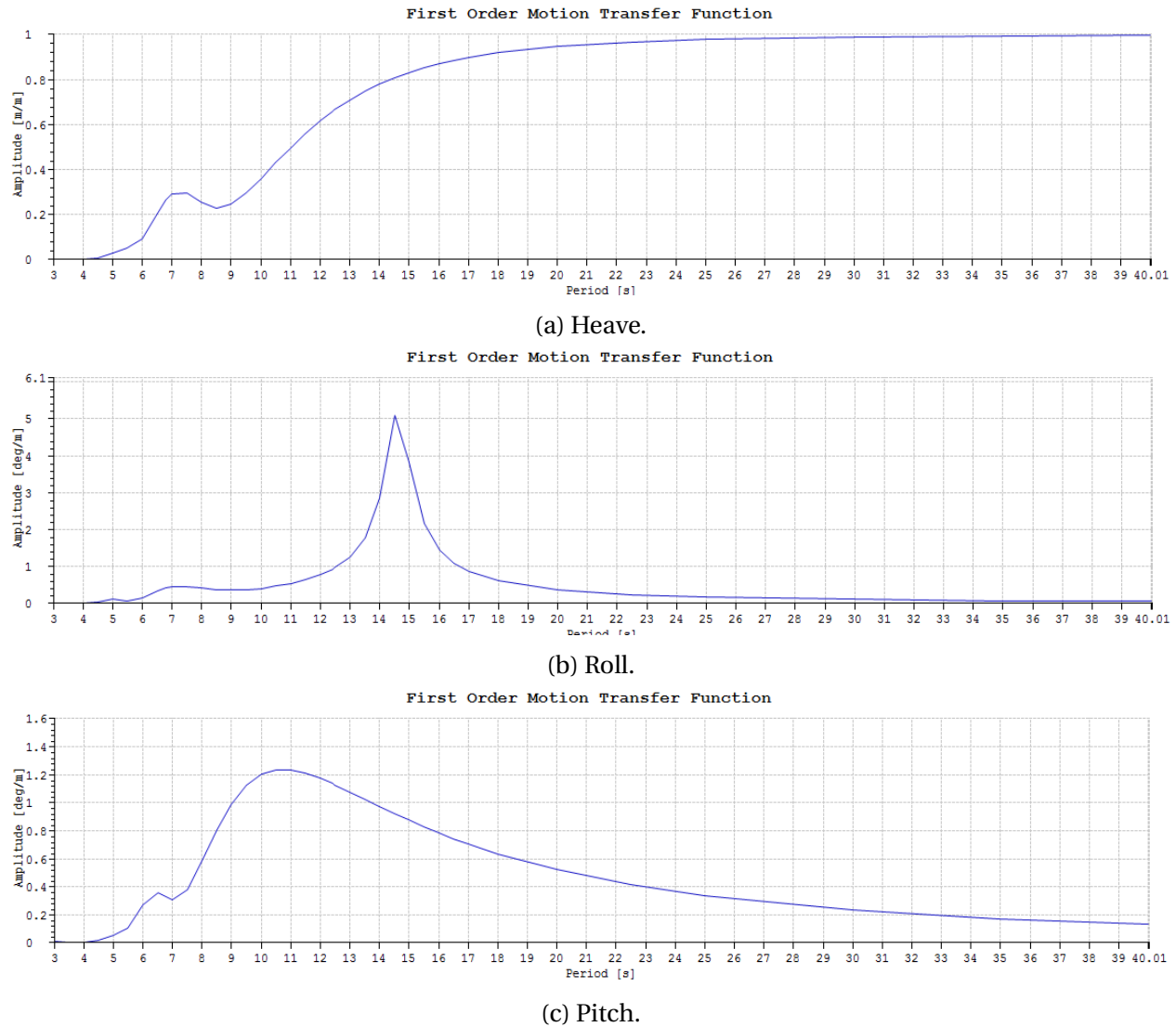


Figure 5.37: Vessel response amplitude operators.

The force in the lifting wire is outlined in Equation (3.37) and defined to depend on the crane tip motions through the $K(z_{ct} - \eta)$ term. In this case, the short length of the wire will cause the system to be stiffness dominated. In such a system, the loading frequency is much lower than the eigenfrequency. The loading frequency will therefore be experienced as slowly varying such that the system behaves in an almost static, or quasi-static manner (Larsen, 2012). The forces acting at a given time step will act in an almost static manner, where the wave excitation forces will dominate the loading.

The trend in lower periods exciting higher forces is likely due to a variety of phenomena. As the peak period decreases, a larger number of waves will pass the Dual Cap-X. This will also increase the probability of a larger wave interacting with the body. As such, the importance of wave excitation forces will most likely increase for lower periods. Additionally, the FK and diffraction forces in the wave excitation term are a function of the wave particle acceleration. The wave particle acceleration is proportional to the square of the circular frequency $\omega^2 = (\frac{2\pi}{T})^2$ where T is the wave period. As such, as the wave period decreases, the wave particle acceleration will increase, giving rise to an increase in the wave excitation forces. The sensitivity analyses conducted found these forces to be dominating in the model as well. This is most likely a significant factor in the trends found. The Dual Cap-X will also experience increased variations in vertical position relative to the free surface when multiple waves interact with it through the splash-zone. This will introduce slamming forces at multiple time instances, and the probability of slack conditions increases.

It is worthy of noting that there are very few conditions that excite slack in slings. This is most likely due to the magnitude of the weight of the Dual Cap-X relative to its size. Its large weight will act towards maintaining tension in the lifting line and slings, whilst the splash-zone forces will contribute to slack conditions. As previously seen, the dynamic forces are generally quite small relative to the weight of the Dual Cap-X. This is due to the small size and associated surface area that forces will act upon. Slack conditions will therefore generally be unlikely.

5.3 Free-Fall Preparation Phase

Between the Splash-Zone and Free-Fall phases in the Pendulous Installation Method, the Dual Cap-X will be suspended at a depth of 50 m such that the hand-off from the lifting line to the HMPE deployment line can be facilitated. It is therefore of interest to investigate the operational limits for this phase of the operation.

Simulations in SIMO were conducted using the same model as for the Splash-Zone phase. The initial position of the payload was set to a depth of 50 m, and the winch function removed. An

irregular sea state was applied to the model without current or wind effects. It was assumed that this phase would have a low degree of sensitivity to the wave realization, and as such only 10 wave realizations were run for each combination of H_s and T_p . The following values of H_s and T_p were investigated:

Table 5.8: Simulation Variables.

H_s [m]	T_p [s]
3	6
4	8
5	10
6	12
7	14
8	

The results for the maximum lifting line tension are displayed in Figure 5.38 and the minimum lifting line tension in Figure 5.39

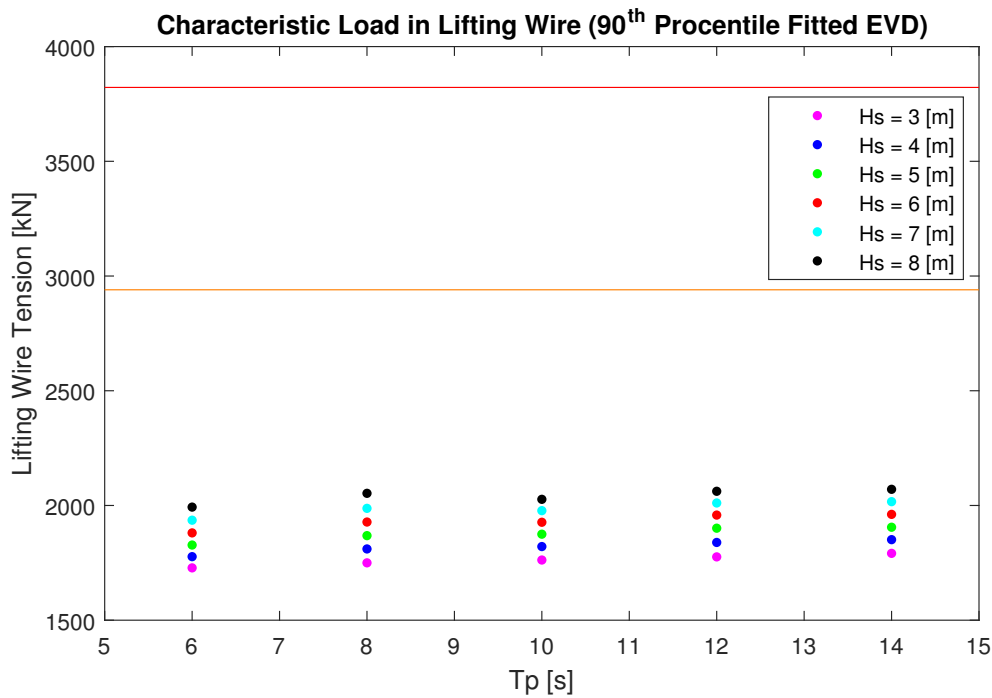


Figure 5.38: Maximum tension at 50 m depth. The orange line indicates a crane SWL = 1 and the red line SWL = 1.3.

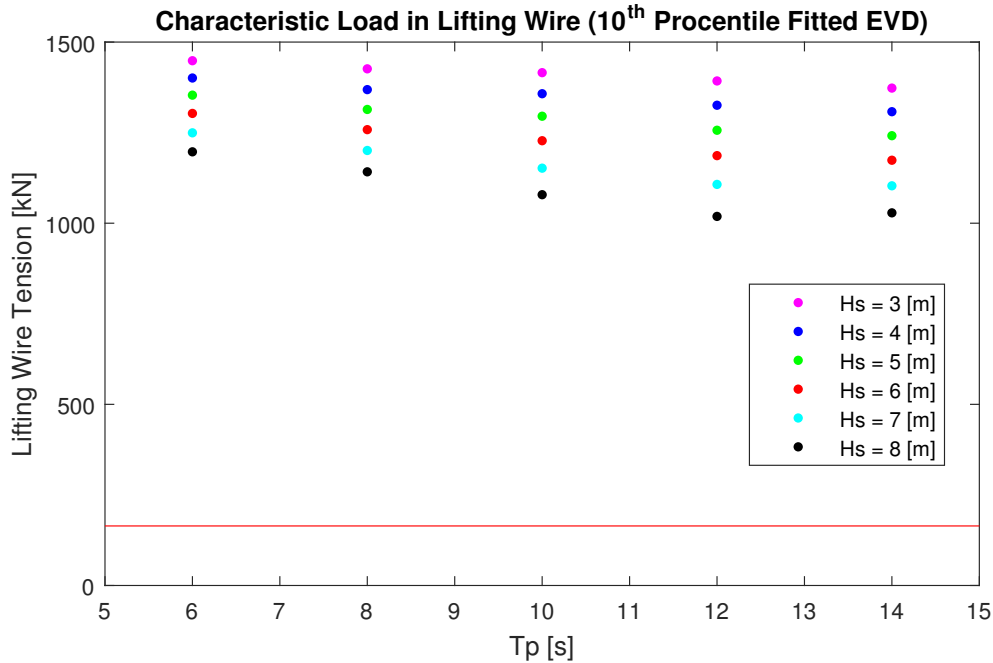


Figure 5.39: Minimum tension at 50 m depth. The red line indicates the minimum allowable lifting line tension.

Discussion

It is clear that the operational limits are not even close to being breached for the sea states investigated. One may assume that the design criteria may be over $H_s = 10$ m with respect to wave height. This is however not deemed relevant for investigation as values above 8 m are not feasible from an operational standpoint due to factors other than the lifting line tension.

The hand-off operation involved in this phase of the PIM requires ROV intervention, and limitations will therefore be applied to this operation as well. These may be limiting for this phase of the operation. The ROV operation is however not within the scope of this thesis and is as such not investigated. It can however be assumed that safety related to personnel on deck and general behaviour of the vessel at significant wave heights over 8 m will not be sufficiently maintained. In summary, this phase is minimally sensitive to sea state variation with respect to the operational criteria established.

5.4 Pendulous Free-Fall Phase

5.4.1 Current Sensitivity

In deepwater conditions, there often are significant currents. It is therefore of interest to investigate the effect of current conditions on the global response of the Dual Cap-X in the Free-Fall phase. In this section, results from different current conditions are presented and discussed. Table 5.9 lists the conditions tested.

Table 5.9: Current conditions.

Current Speed	Current Direction [deg]
Maximum current	270
Maximum current	0
Mean current	270
Mean current	0

The terms "Maximum current" and "Mean current" are as defined in Section 4.2.2. The current directions are as defined in SIMO's global coordinate system. This means that a current direction of 270° corresponds to current along the negative Y-axis, while 0° is along the positive X-axis (see Section 4.2.5 for definition of the coordinate system). Moreover, irregular waves with $H_s=4$ m and $T_p=8$ s are also included for all current conditions. The direction of the waves are set to match the direction of the current for each condition. The payload is launched into free-fall at 150 s.

Figure 5.40 shows a time series of the payload trajectory for all current conditions. The results indicate that the duration of the Free-Fall phase is highly influenced by the current conditions used in this study. The duration for almost all conditions is found by inspection to be around 45 min. For the case with maximum current along the negative Y-axis, the duration is increased to around 1 hour. This is mainly due to a slower change in Y-position (Figure 5.40b) since the current velocity directly opposes the payloads pendulous motion in Y-direction. It is also inter-

esting to note that current normal to the plane of the main pendulous motion (Y-Z plane) also can cause significant increase in the free-fall duration (Figure 5.40c). This is due to a large payload offset in the direction of the current (X-direction). Maximum current in this direction gives a duration of around 1 hour as well. Independent of direction, the mean current conditions provide minimal change in the duration compared to no current. As such, the higher the speed of the current profile along the tested directions, the longer the Free-Fall phase takes.

Figure 5.40 also shows that the maximum current profile causes a large offset in X-direction and Z-direction of the payload for current direction 270° and 0° , respectively, when it has come to rest. This highlights the need for re-positioning of the vessel to counter the offsets. As such, the current profile should be taken into account during operation planning in order to avoid re-positioning of the vessel after the payload has been launched, and thus reducing operation time.

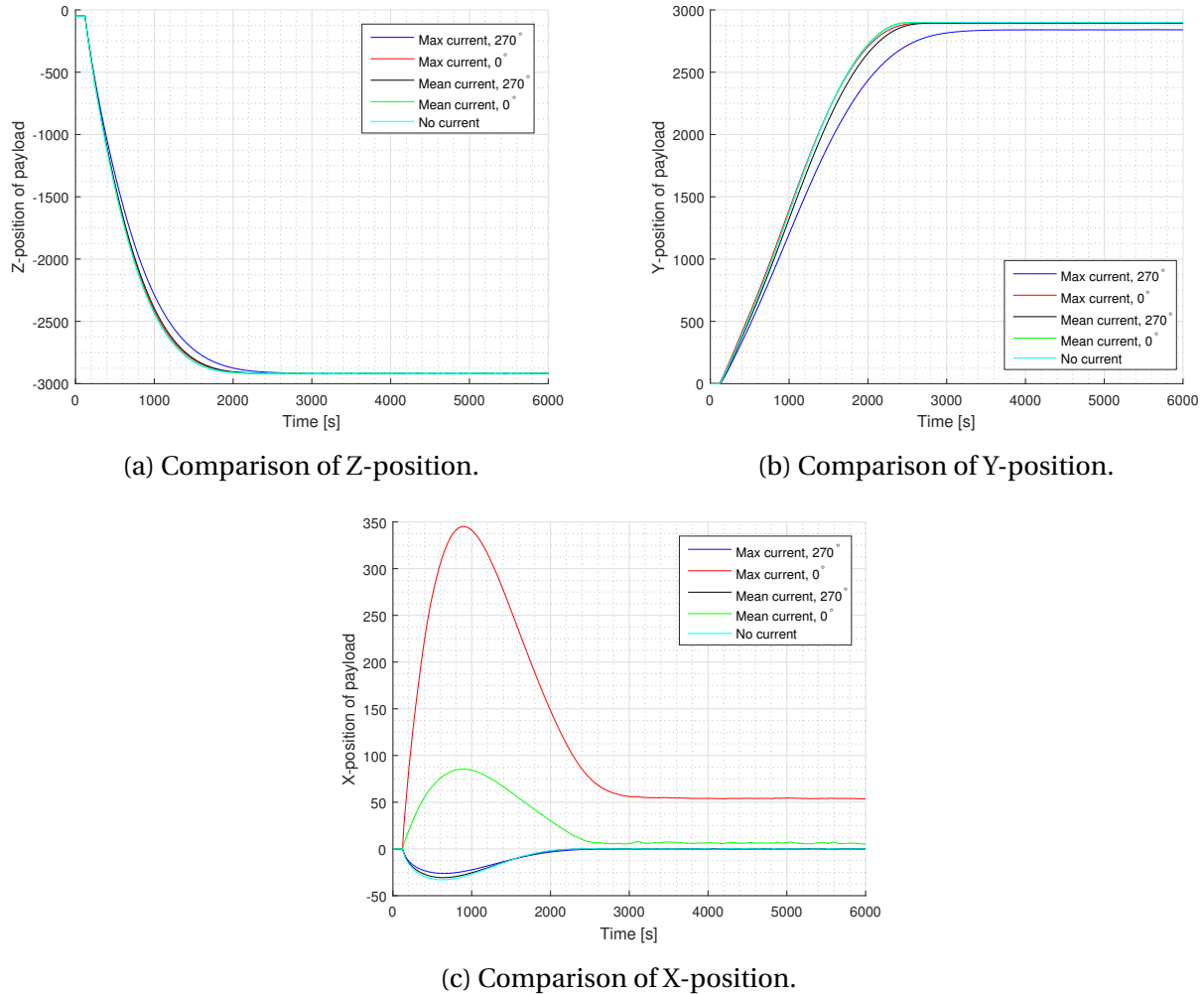


Figure 5.40: Comparison of payload trajectory. Position given in meters in the global coordinate system.

Figure 5.41 shows the top tension during the Free-Fall phase for all cases. The results indicate that the magnitude of the tension is dominated by the payload weight, and therefore the maximum tensions are around the same values for all conditions. However, when there is no current, the top tension when the payload has reached the bottom of the pendulum trajectory seems to exercise a larger degree of oscillatory behaviour. A plausible explanation could be that the drag forces on the payload due to the current opposes the vertical movement of the payload caused by vessel motion, and as such reduces the oscillatory behaviour of the top tension. Figure 5.42a seems to support this, as there is a high degree of oscillatory behaviour of the vertical velocity when there is no current, compared to the other conditions. Even though the top tension

for each case is acceptable with respect to the maximum capacity of the deployment system, excessive cyclic top tension can be a problem with respect to fatigue.

The clear spike in top tension at the start of the time series for the case with maximum current in direction 0° is most likely a result of the current induced drag forces which act on the payload while it is fixed in all directions before launch. The same spike, albeit smaller in magnitude, can also be observed for the case with mean current in the same direction.

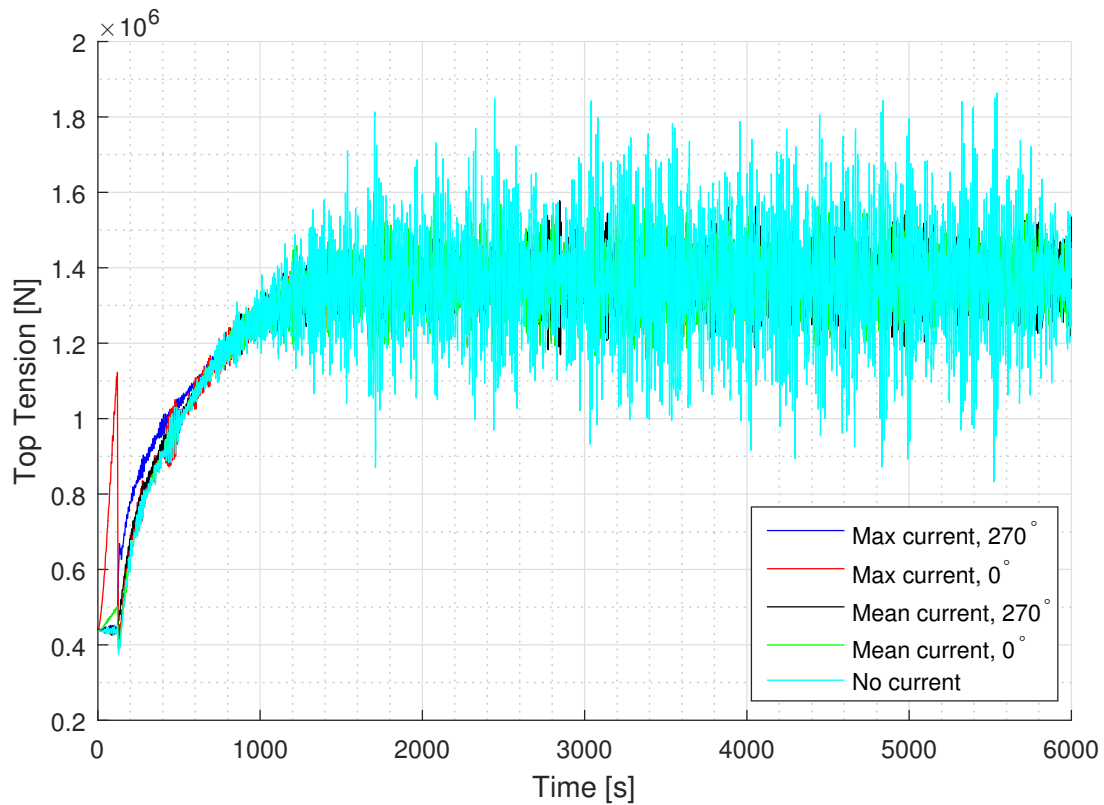


Figure 5.41: Comparison of top tension.

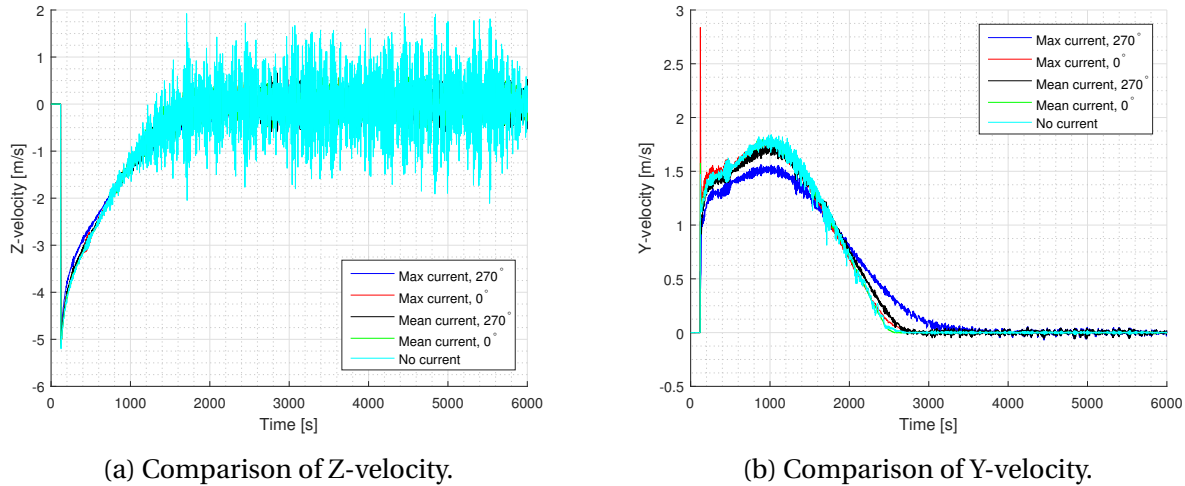


Figure 5.42: Comparison of payload velocities.

5.4.2 Drag Sensitivity

The dominating hydrodynamic force during the free-fall is the drag force. As discussed in Section 4.2.4, the quadratic drag coefficients used in the modelling of the Dual Cap-X are based on tabulated steady flow drag coefficients. Contrary to the Splash-Zone phase, the flow conditions during the Free-Fall phase can be considered as steady. As such, the modelled quadratic drag coefficients should be reasonable for the Free-Fall phase.

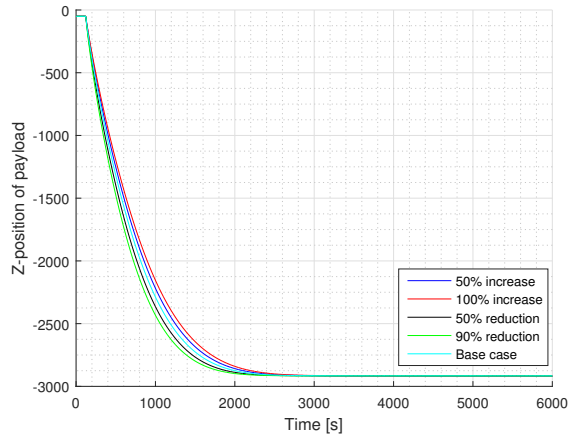
As discussed, accurate modelling of the hydrodynamic properties is essential. This is especially true for the drag coefficients of the Free-Fall model, due to the dominant nature of the drag forces. Moreover, it is of interest to identify the effect of drag forces when the Dual Cap-X is in a pendulous free-fall. This section investigates the influence of the drag coefficients on the global response of the Dual Cap-X in the Free-Fall phase. The following cases were run for this study:

- Drag coefficients increased by 50 %
- Drag coefficients increased by 100 %
- Drag coefficients decreased by 50 %
- Drag coefficients decreased by 90 %

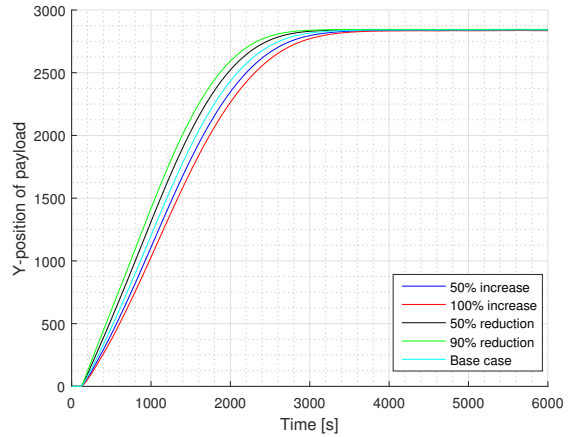
For each case, the quadratic drag coefficient along all three translational degrees of freedom were changed by the same percentage. Furthermore, each case is run with the current profile "Maximum current" (see Section 5.4.1) in a direction of 270° . As such, the current profile is modelled opposite to the direction of the Y-component of the payload velocity in the pendulum trajectory. The "Base case" is defined as the case with the quadratic drag coefficients as presented in Table 4.6 in Section 4.2.4. Irregular head waves with $H_s = 4$ m and $T_p = 8$ s are also included.

Figure 5.43 compares the payload trajectory for each case. As indicated in Figure 5.43a, the vertical component of the trajectory seems to be minimally affected by the change in drag coefficients. Figure 5.43c shows that the time the payload uses to reach the wanted position in X-direction, also seems to be minimally affected by the change in drag coefficients. However, it is clear that the magnitude of the offset in X-direction during the free-fall increases with increasing drag forces. The offset is for all cases largest when the payload is in the upper part of the water column, as the current speed is larger here.

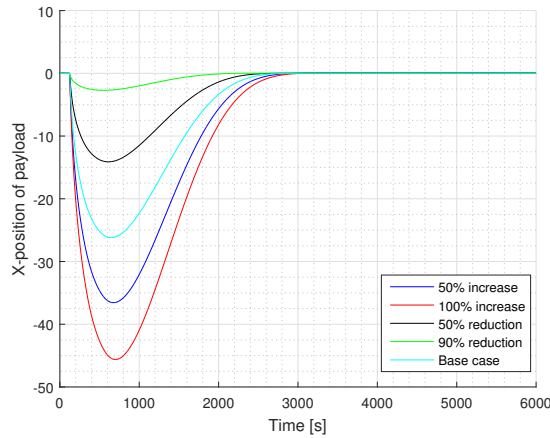
Comparing the three time series in Figure 5.43 it is clear that it is the Y-position of the payload that determines the total free-fall duration in these cases. As expected, the larger the hydrodynamic drag coefficients are, the longer time the payload uses to reach the final position. However, the results suggest that the change in duration is relatively small compared to the degree of change in the drag coefficients. For example, Figure 5.43b shows that the duration of the Free-Fall phase is around 65 minutes when the quadratic drag coefficients are increased by 100 %. This constitutes only a 5 min increase in duration compared to the base case. The difference in duration between the case with 90 % reduction and the case with 100 % increase is around 15 minutes. This may indicate that the drag acting on the deployment line governs the drag in the system.



(a) Comparison of Z-position.



(b) Comparison of Y-position.



(c) Comparison of X-position.

Figure 5.43: Comparison of payload trajectory. Position given in meters in the global coordinate system.

Figure 5.44 shows the Y- and Z-velocity components of the payload. These results clearly support that it is the Y-position of the payload that determines the end time of the free-fall in these cases. The Z-velocities differ relatively little from case to case. The largest differences between each case is in the Y-velocity.

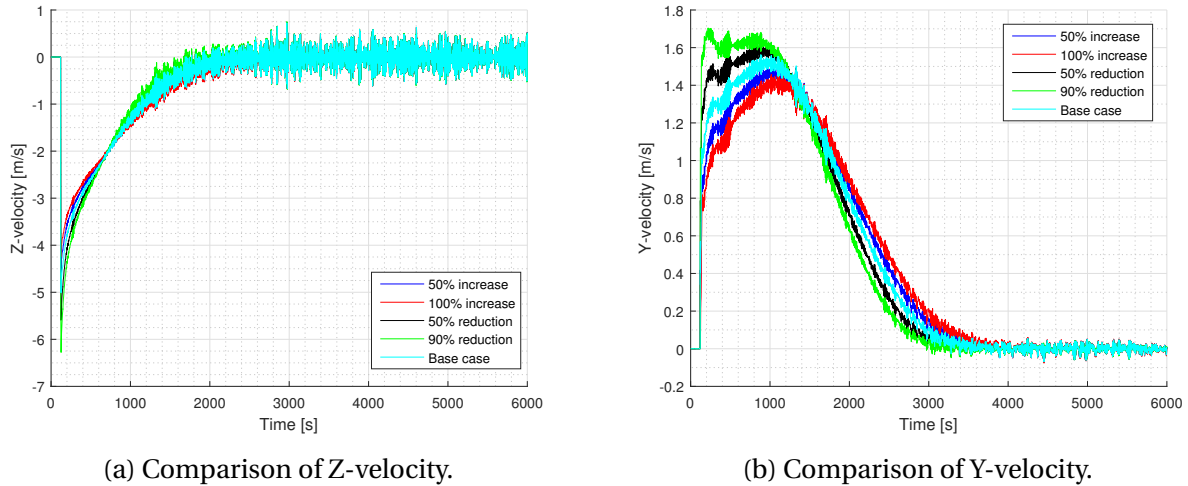


Figure 5.44: Comparison of payload velocities.

Figure 5.45 compares the time series of the top tension for all cases. The general trend is that the top tension during the free-fall reduces as the drag coefficients are increased. With increasing drag forces on the structure, which are in the opposite direction of the payload velocity, the drag force contributes towards slack in deployment line and thus the top tension will be reduced. Furthermore, the overall tensions can be considered to be acceptable with respect to the maximum capacity of the deployment system for all cases.

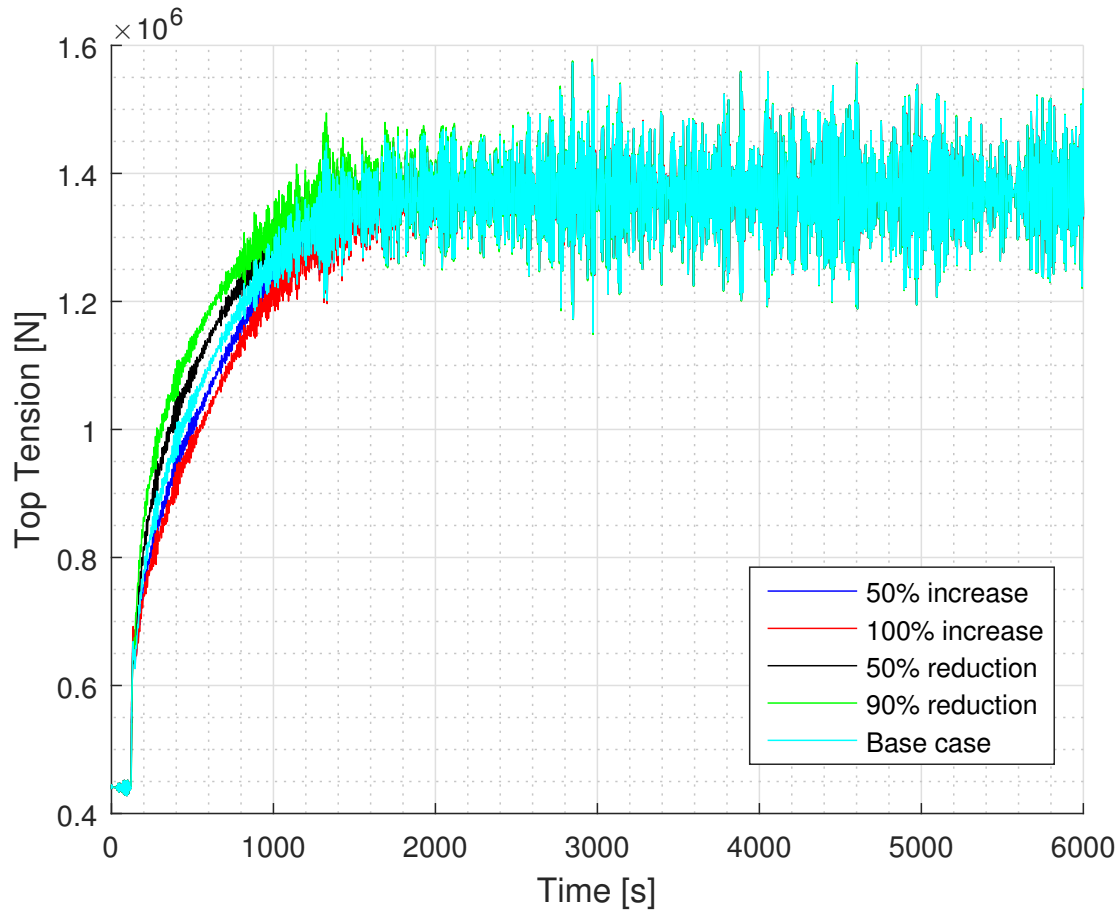


Figure 5.45: Comparison of top tension.

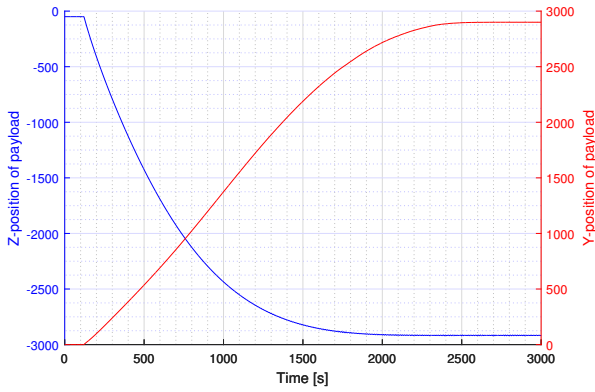
5.4.3 Weight Sensitivity

In this subsection a sensitivity study on the payload weight is presented. The purpose is to investigate the influence of the payload weight on the duration of the free-fall. The numerical time domain analysis is performed for the following cases:

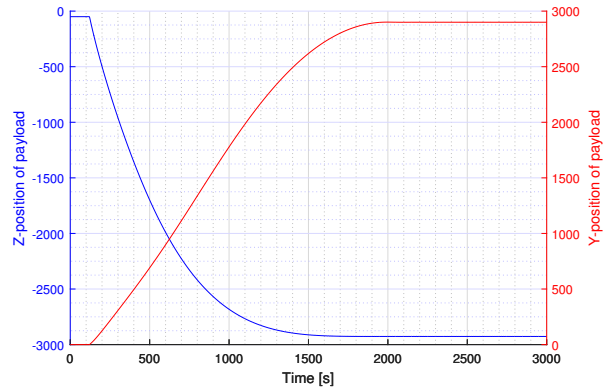
- Reduction of payload weight by 50 %
- Reduction of payload weight by 70 %
- Increase of payload weight by 50 %
- Increase of payload weight by 100 %

As a simplification, other hydrodynamic and structural parameters, such as moment of inertia and drag coefficients, are held constant. The tests are run without current in order to better isolate the effect of the weight change on the free-fall duration. In order to better investigate the effect of the crane tip motions on the payload during the free-fall, irregular waves were included ($H_s=4$ m, $T_p=8$ s).

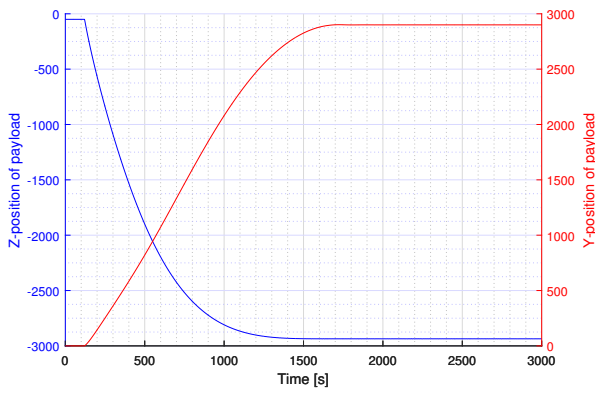
Figure 5.46 and 5.47 present the results obtained from the weight sensitivity. The position of the payload during the free-fall is given in the Y-Z plane (see Section 4.2.5 for definition of the coordinate system) against time. The payload is launched into the pendulous free-fall after 150 s.



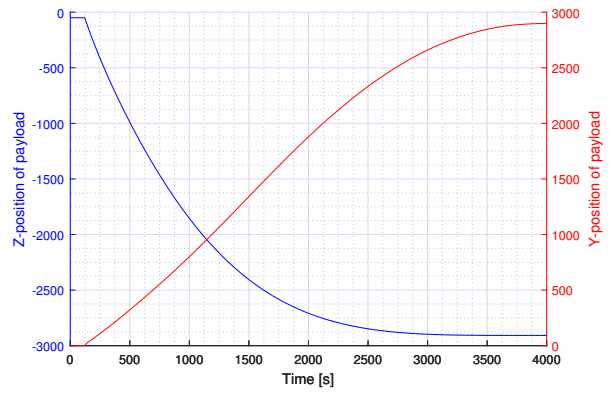
(a) Original weight.



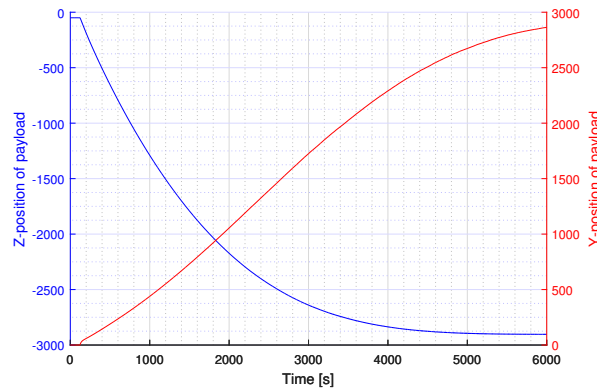
(b) 50 % weight increase.



(c) 100 % weight increase.

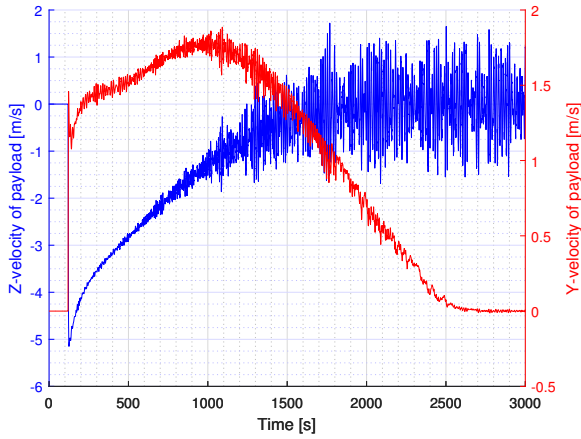


(d) 50 % weight reduction.

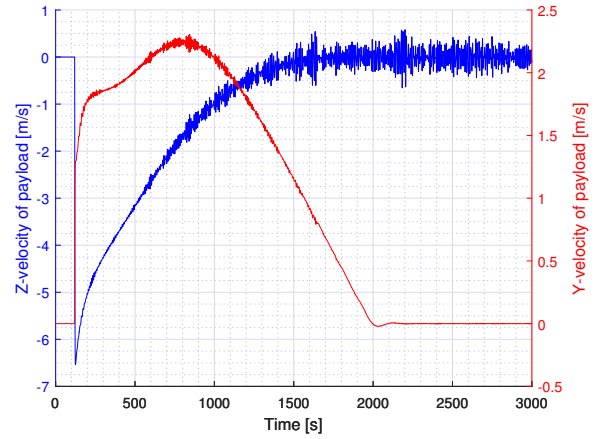


(e) 70 % weight reduction.

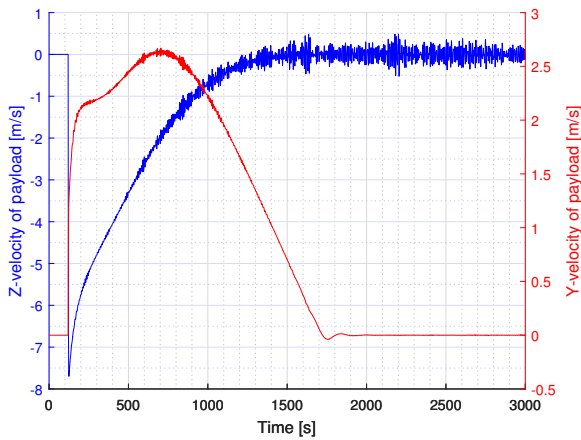
Figure 5.46: Payload weight sensitivity - Position of payload (given in meters in the global coordinate system).



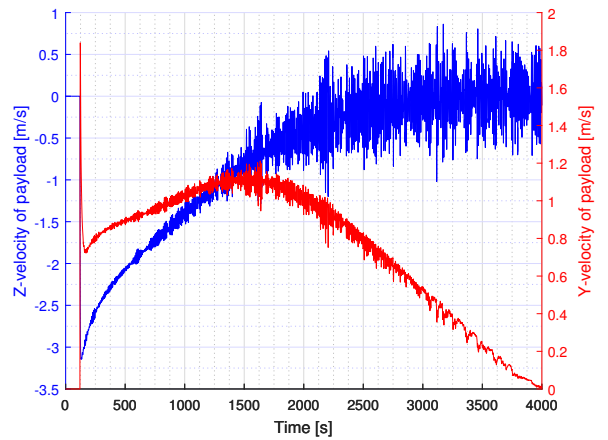
(a) Original weight.



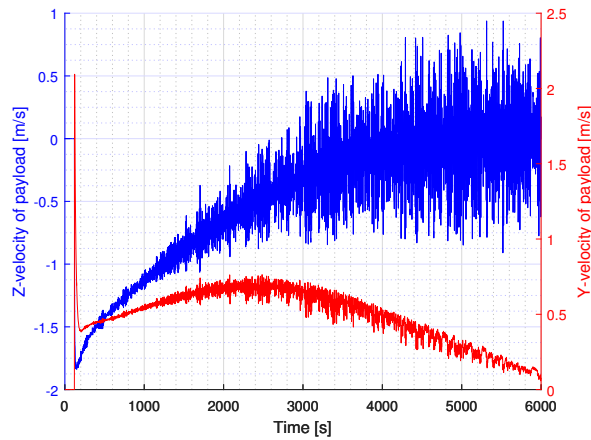
(b) 50 % weight increase.



(c) 100 % weight increase.



(d) 50 % weight reduction.



(e) 70 % weight reduction.

Figure 5.47: Payload weight sensitivity - velocities of payload.

The results presented in Figure 5.46 clearly show that the duration of the free-fall reduces when

the weight of the payload is increased, and opposite when the weight is reduced. It could be argued that the simulation length for the 70 % weight reduction case (Figure 5.46e) could have been somewhat longer in order to clearly see that the payload is at rest. However, the present results gives an good indication of the duration. The results are summarized in Table 5.10.

Table 5.10: Free-Fall durations for different payload weights (without current).

Weight Case	Free-Fall Duration [min]	Change in duration from original case [%]
Original weight	45	0
50 % weight increase	35	-22
100 % weight increase	27	-40
50 % weight decrease	67	+48
70 % weight decrease	100	+120

The Z-position is reached faster than the Y-position for all cases, and as such the duration of the free-fall is governed by the time it takes to reach final Y-position. This is due to the fact that the payload moves more slowly when it approaches vertical in its trajectory. This can also be seen from the Z-position line as its steeper at the start of the free-fall then towards the end.

Figure 5.47 shows a large velocity spike in both Y- and Z-directions immediately after the payload is dropped for all cases. As expected, the Z-velocity decreases faster in the start of the pendulous motion. After the drop, the largest Y-velocity occurs when the payload is at the lower part of the pendulous trajectory since it moves in a more horizontal manner during this time. When the weight is decreased, this Y-velocity is smaller than the Y-velocity at drop. When the weight is increased, this velocity is the global maximum. In general, the velocities in both Y- and Z-direction are overall higher when the payload weight is increased. For example, the Z-velocity at the time of drop for the original case is around 5 m/s (downwards), while for the 100 % weight increase case the same velocity is increased by almost 60 %.

Furthermore, Figure 5.47 shows that the vertical movement when the payload has reached its final position is larger for smaller payload weights. These movements are likely caused by crane

tip motions due to incoming surface waves.

These results indicate that it may be beneficial to add weights to the Dual Cap-X in order to reduce the duration of the free-fall phase. The weights should be included in such a manner that the drag coefficients are not increased. However, one should be aware of the increased payload velocities which may cause instability of the payload during the free-fall. Also, a larger payload weight will also give larger top tension.

5.4.4 Evaluation of Acceptance Criteria

The investigative studies performed for the Free-Fall phase indicate that the magnitude of the current along the negative Y-axis has a large impact on the free-fall duration. The effect of increasing the current speed has a more dominant effect on the free-fall duration compared to changing the quadratic drag coefficients of the payload. This is most likely due to the fact that the quadratic drag force is proportional to the square of the relative velocity between the payload and the fluid particles. As such, an increase in the current speed results in a quadratic increase in the drag force, while an increase in the quadratic drag coefficients results in a linear increase.

These results also indicate that high current speeds in the direction opposite to the horizontal component of the main pendulous trajectory result in the the longest free-fall durations. As such they are one of the most limiting factors with respect to installation time. Minimizing the drag forces acting on the payload during the free-fall is necessary in order to reduce the duration. It should also be noted that adding clump weights can help to reduce the free-fall duration as indicated in the weight sensitivity studies.

Moreover, the top tension is dominated by the weight of the Dual Cap-X. When the payload has reached its final position in the free-fall phase, inertia and drag forces on the payload caused by vessel motions are particularly relevant. These forces cause the top tension to exercise a highly oscillatory behaviour. The acceptance criteria will depend on the capacity of the winch attached to the deployment line. Nonetheless, the results indicate that the maximum top tensions are

well within acceptable ranges with respect to both the maximum capacity and SWL of the crane for the relevant wave conditions. The results also indicate that increased drag forces on the payload when at its final position help to reduce the magnitude of the top tension oscillations.

The results also show that there seems to be no issue with slack in the deployment line. However, slack conditions have not been investigated for the lifting slings due to limitations in the model. As the payload moves through the trajectory, it is probable that some slings may experience higher tensions than others due to payload translation and rotation. This should be investigated in a more detailed study.

The vertical movement of the payload when it is at the end of the pendulous trajectory indicates that seabed landing will require additional measures to increase payload control. Active Heave Compensation (AHC) will most likely be necessary due to the magnitude of the vertical velocity of the payload in order to safely land the Dual Cap-X on the seabed. ROV guidance will also be necessary to overcome the horizontal offset and facilitate accurate positioning. As outlined in Section 1.3, sea bed landing is not investigated in detail in this thesis.

In terms of design criteria, the effect of the current conditions on the free-fall duration seems to be the dominant factor. With increasing current speeds, the duration of the free-fall increases. The duration of the free-fall phase is however not limited to any value. Its minimization is however highly desirable. In terms of top tension, there is no clear limit with respect to maximum tension for realistic sea states. It should however be understood that incident waves impacting on the vessel can cause potentially large oscillations in the top tension when the payload is held for longer periods of time at the end position for extreme sea states. However, when the payload is at this stage it should be regarded as part of the lowering sub-operation, and as such, other factors such as safety of personnel and vessel station-keeping for deepwater lowering will become the limiting factors. H_s and T_p will therefore most likely not be limiting for the Free-Fall phase in realistic conditions.

By inspection of the trajectory results, it seems that the payload exercises relatively stable motion behaviour during the free-fall. However, since the model may not be suitable for detailed local response investigation of the payload motion this should be looked into closer. As men-

tioned before, this thesis only investigates the global response during the free-fall.

Appendix C presents the results of the analysis for the case with the condition "Maximum current" along the negative Y-axis (head current). The duration of the free-fall is 1 hour for this case. As such, this case represents conservative current conditions, and is used in further discussions in Chapter 6.

Chapter 6

Relevance of Findings

The feasibility of developing deepwater fields relies on the development of innovative solutions. The motivation is to push the limits of installation operations such that the profit margins are maintained going from 300 m to 3000 m. The development of the Dual Cap-X in conjunction with the Pendulous Installation Method may be the solution. This chapter will investigate the potential based on findings from the time domain analyses through estimating weather windows for the operation. Investigation into relevant cost saving measures for the installation operation will then be conducted.

6.1 Cost Reduction

The main cost drivers in an installation operation are:

- Vessel day rate
- Operation time
- Time waiting on weather

Conventional deepwater installation methods entail the use of Heavy Lift Vessels with astro-

nomical day rates due to challenges addressed in Section 2.1. The operation time for traditional lifting operations are also high. The installation in 2014 of the 280 t Tyrihans template at 300 m lasted 5.5 hours (from lift-off to touchdown) (Næss, 2014). One can then contemplate the time consumption of an operation at 3000 m water depth using similar methods. Subsea installation operations are weather sensitive operations, and will be limited by environmental conditions. These limitations will dictate when an operation can be conducted, and the operation often must wait for extended periods of time for acceptable weather conditions. Robust installation methods are therefore favorable.

6.2 Planning of Dual Cap-X Installation using PIM

In this section, weather windows for the installation of the Dual Cap-X are estimated based on the results of the analyses and hindcast weather data from the Heidrun field on the Norwegian continental shelf. The data was collected over a time period of 50 years and provided by Statoil.

6.2.1 Time Schedule

In order to effectively identify potential cost saving measures, a break down of the installation operation is necessary. Table 6.1 provides an overview of the various sub-operations involved in the installation. The planned operation times and design criteria are based on the numerical analyses when applicable and assumptions based on common practice. The sub-operations are based on the procedure outlined in Section 2.2. The design criterion, OP_{LIM} , are given in terms of significant wave height.

Table 6.1: Time schedule for base case.

Sub-Operation	T_{pop} [h]	Design Criterion [m]0	Reason for criterion
1: Connecting deployment line from Vessel B	0.5	2.0	Safety of personnel and feasibility of operation
2: Steaming 2900 m and positioning (Vessel B)	2	4.0	Navigation
3: Cutting sea fastening, lift-off and over-boarding	0.5	4.0	Safety of personnel
4: Lowering through splash-zone to a depth of 50 m	0.5	3.8	Maximum lifting line tension (SWL of crane)
5: Connect winch from Vessel A and disconnect lifting line (ROV operation)	1	4.5	Feasibility of ROV operation
6: Pendulous free-fall	1	No limitations in realistic conditions	
7: Positioning of payload (ROV operation)	1	No limitations in realistic conditions	
8: Lowering and landing on seabed	1	No limitations in realistic conditions	
	7.5		

Sub-Operation 1 was determined to take approximately 0.5 hours and has a design criterion of 2 due to risk related to safety of personnel.

Sub-Operation 2 takes 2 hours based on the assumption of a maximum winch speed of 0.5 m/s when paying out the deployment line. The design criterion was based on assumptions related to navigation capabilities of the vessel.

T_{pop} for Sub-Operation 3 is based on experience from the Tyrihans template installation. The criterion was set based on risk related to safety of personnel on deck.

Time consumption and design criteria for Sub-Operations 4-6 are based on results from the

numerical analyses. It should be noted that dynamic loading on the payload in sub-operation 5 has no limitations in realistic conditions as shown in Section 5.3. However, criteria were set with respect to the ROV operation necessary to facilitate the operation.

Sub-Operations 7-8 have not been studied in detail as they are not within the scope of this thesis. Time constraints were therefore based on general assumptions. The general limiting factors for the design criteria relate to current velocity near the seabed.

6.2.2 Accounting for Uncertainty in Weather Forecast

Marine operations currently rely on accurate weather forecasts to determine whether or not an operation is feasible. As discussed in Section 3.4, uncertainty in weather forecasts is accounted for via the α factor. As seen in Equation 3.50, the α factor determines the operational limit OP_{WF} that the operation must adhere to. The following will be based on α factor recommendations from DNV GL (2011a). DNV GL (2011a) requires that subsea installation operations have a weather forecast level of B. Level B forecasts apply to environmental sensitive operations of significant importance with regard to value and consequences. Based on the T_{pop} for each sub-operation, the corresponding α factor is found. Subsequently, OP_{WF} is found by using Equation (3.50). Table 6.2 gives an overview of the installation schedule when considering weather forecast uncertainty.

Table 6.2: Operational limits.

	Sub-Op. 1	Sub-Op. 2	Sub-Op. 3	Sub-Op. 4	Sub-Op. 5
OP_{lim} [m]	2.0	4.0	4.0	3.8	4.5
Duration [h]	0.5	2	0.5	0.5	1
T_{pop} [h]	0.5	2.5	3	3.5	1
α [-]	0.800	0.830	0.83	0.827	0.833
OP_{WF} [m]	1.6	3.3	3.3	3.1	3.7

Op_{WF} is the operational limit that will need to be adhered to during the installation operation.

Sub-Operations 6-8 are not considered due to the fact that they are minimally sensitive to environmental conditions and assumed to not have limitations in realistic conditions. They are therefore not given an α factor or presented in Table 6.2.

6.2.3 Accounting for Uncertainty in Planned Operation Time

DNV GL (2011a) states that general uncertainty in the T_{POP} should be accounted for through a contingency time. Contingency times take into account contingency situations that require additional time to complete the operation. Generally, the contingency time T_c is not acceptable if less than 6 hours (DNV GL, 2011a). If the uncertainty in T_{POP} is not assessed in detail, it should be given the same value as T_{POP} . As such, the reference time will then be twice the planned operation time. As there is little experience with PIM, the contingency time will be treated as such.

Table 6.3: Contingency times.

Sub-Op.:	1	2	3	4	5	6	7	8
T_c [h]:	0.5	2.0	0.5	0.5	1.0	1.0	1.0	1.0

6.2.4 Required Weather Window

Based on the values determined for T_{POP} , T_c and OP_{WF} , the requirements for the installation operation are:

- $T_R = 15$ h
- $OP_{WF} = 1.6$ m

Since a real weather forecast is not used in this hypothetical case, the smallest OP_{WF} has been used as the operational limit for the entire T_R . This is however not realistic seeing as if a real weather forecast had been issued one would evaluate the OP_{WF} for each sub-operation against

the forecasted H_s . As such, if the forecast indicates a H_s smaller than the OP_{WF} for each sub-operation, the operation could still be carried out. Thus, requiring that the forecasted H_s is smaller than the smallest OP_{WF} for the whole reference period based on hindcast data constitutes a much more conservative approach. It is nonetheless utilized to illustrate the effect of having an operational limit of such low magnitude for the reference period established.

6.2.5 Evaluation of Operability based on Hindcast Data

Section 3.4 gives an overview of how hindcast data can be utilized to estimate the level of operability for given values of OP_{WF} and T_R . Historical data for the Heidrun field was investigated for this operation due to the challenging wave conditions on the Norwegian continental shelf. It was assumed that operations would not be feasible during the winter months. As such, the following investigation was limited to the months from March to November. For each month, the probability of being able to conduct an operation with a $H_s \leq OP_{WF}$ and $\tau_c > T_R$ was calculated as outlined in Section 3.4. The accumulated available operational time was also evaluated. The results for $OP_{WF} = 1.6$ m and $T_R = 15$ h are presented in Table 6.4. The monthly operability can be understood as the probability of being able to work given a random time point in the specified month. The greater the operability the less the time waiting on weather will be.

The results in Table 6.4 indicate that the installation of the Dual Cap-X using the PIM has highest operability during the summer season. Based on the monthly operabilities, the yearly operability for this operation is around 15 % including the non-operable months December to February.

Table 6.4: Probability of working (base case).

	Available Operational Time [h]	Monthly Operability [%]
March	27	4
April	82	11
May	208	28
June	257	36
July	327	44
August	281	38
September	98	14
October	40	5
November	21	3

At this point, it is of interest to investigate whether the results can be improved in some manner. As such, this case is considered as the base case for which the succeeding discussion in this chapter will be based on.

6.3 Improving Operability

It should be understood that the estimation of the operability of an subject strict regulations. Therefore, improving the operability will require a thorough understanding of the factors influencing the weather window. Moreover, the traditional mindset behind operational planning must be challenged.

In this section, factors influencing the operability, and measures for improving the weather window for the installation of the Dual Cap-X using PIM are discussed.

6.3.1 The Effect of the Reference Time and Operational Criterion

The values set for T_R and OP_{WF} will dictate the probability of being able to work. Figure 6.1 illustrates the relationship between the two with respect to the window in which an installation operation is feasible.

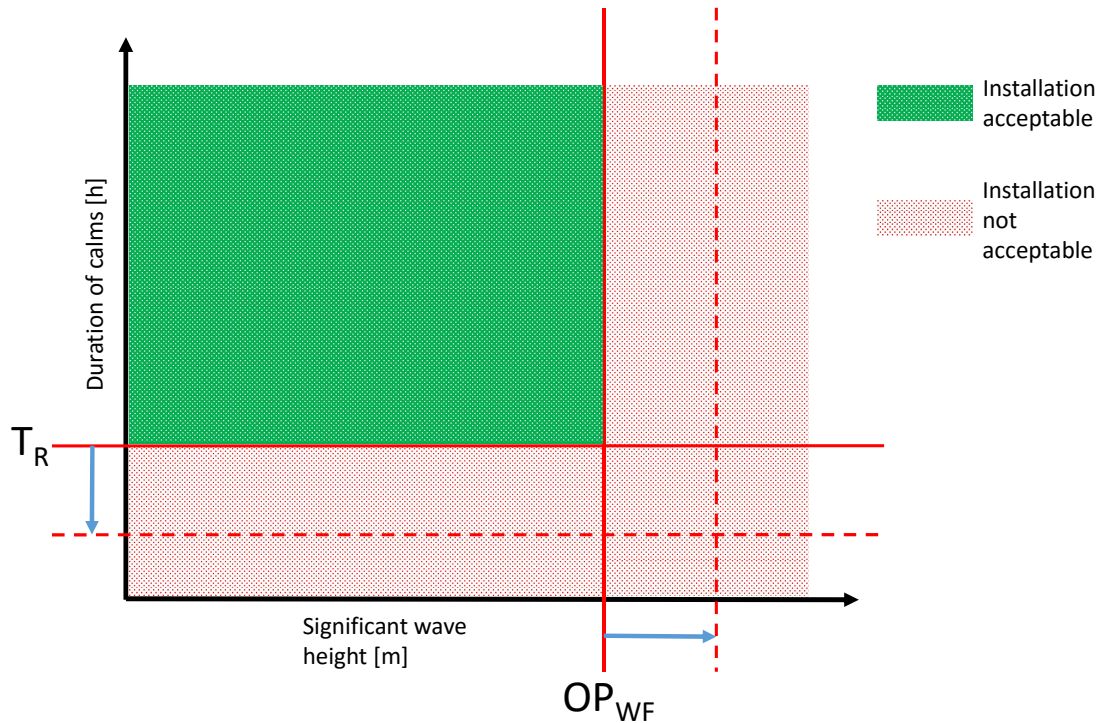
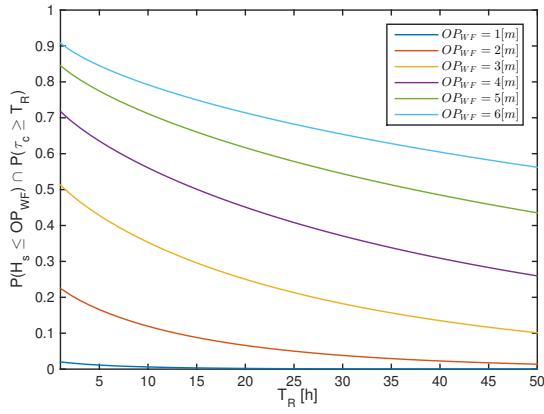
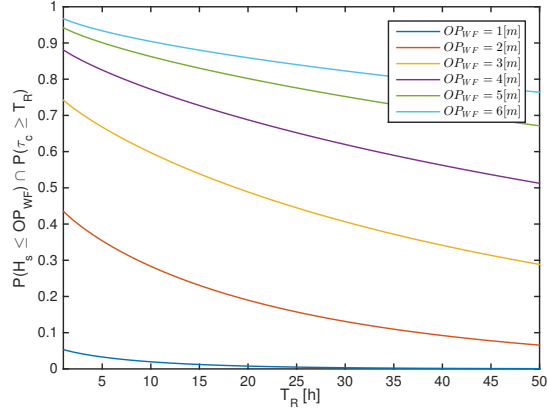


Figure 6.1: Operation window.

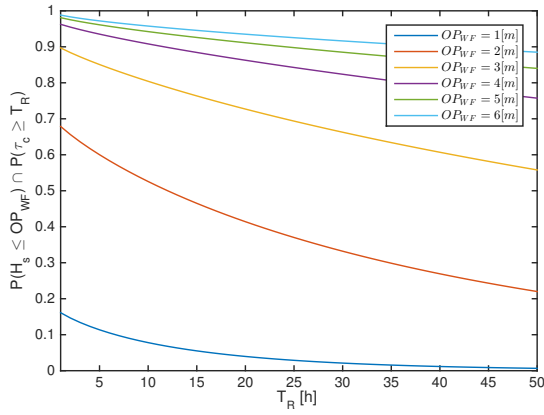
It is clear that increasing OP_{WF} and decreasing T_R will increase the window available for conducting operations. It is therefore of interest to investigate the effect of altering these values with respect to the case at the Heidrun field. The results in Figure 6.2 and 6.3 are calculated based on the provided hindcast data, and illustrate the effect of varying T_R for given values of OP_{WF} for relevant months at Heidrun. Similarly, Figure 6.4 and 6.5 illustrate the effect of varying OP_{WF} for given values of T_R .



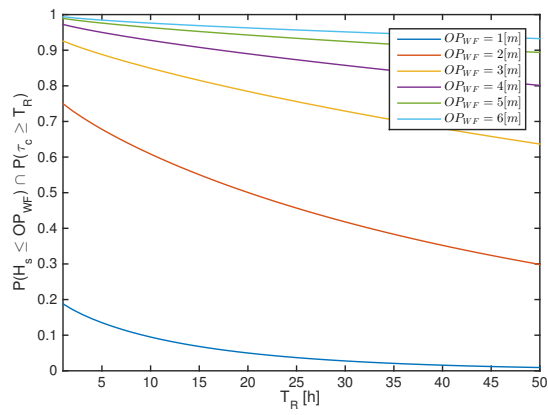
(a) March.



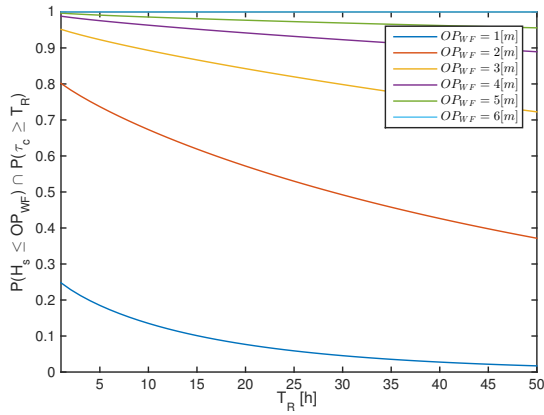
(b) April.



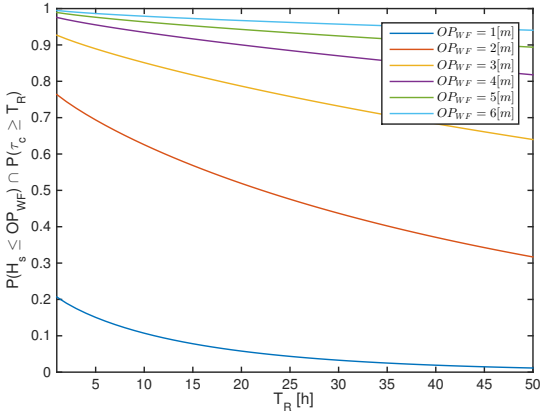
(c) May.



(d) June.

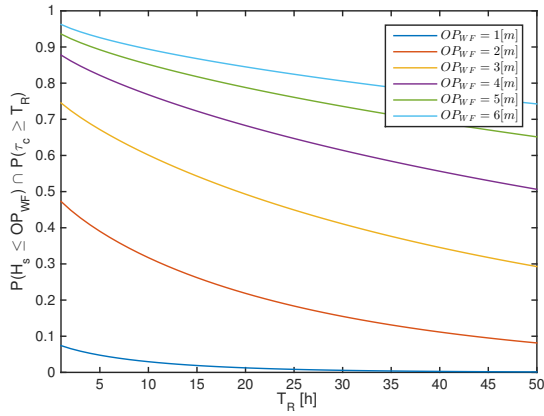


(e) July.

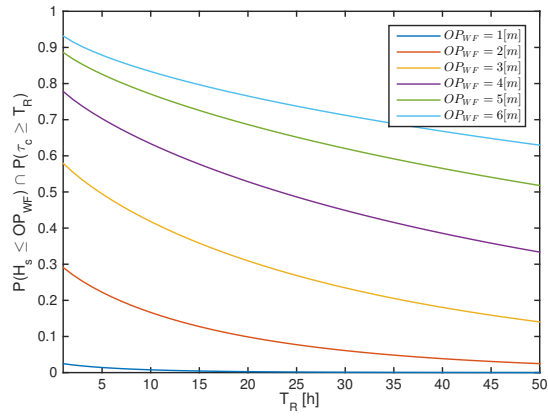


(f) August.

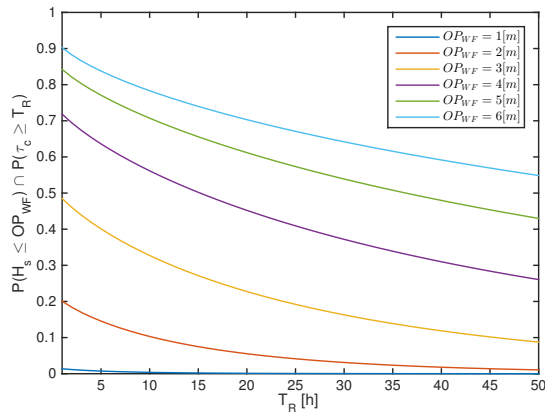
Figure 6.2: Probability of working plotted against T_R for various OP_{WF} given as values of H_s .



(a) September.

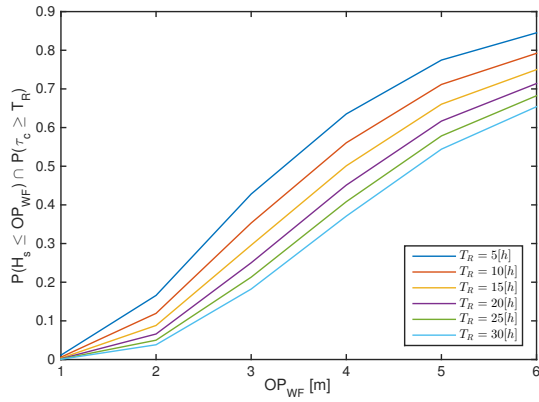


(b) October.

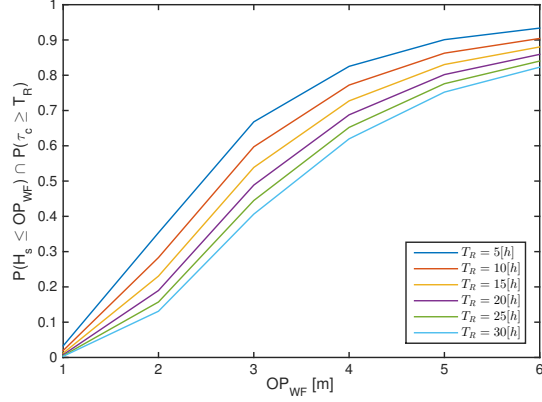


(c) November.

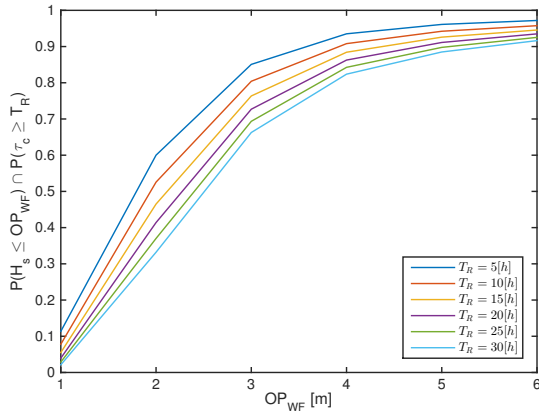
Figure 6.3: Probability of working plotted against T_R for various OP_{WF} given as values of H_s .



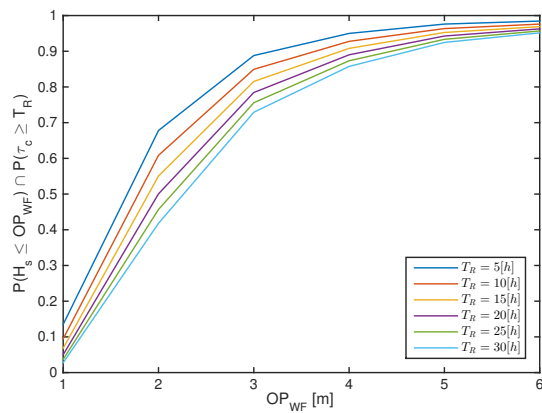
(a) March.



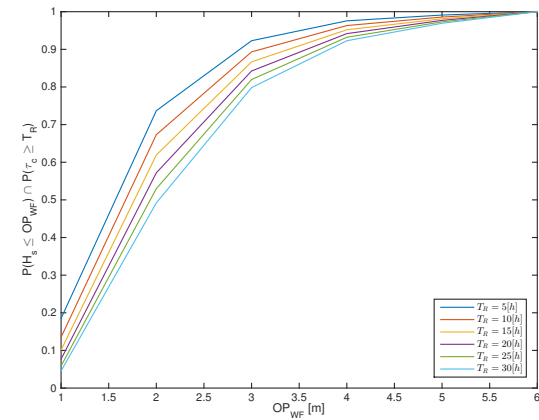
(b) April.



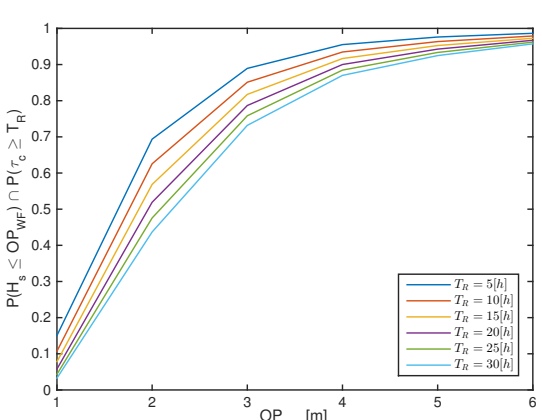
(c) May.



(d) June.



(e) July.



(f) August.

Figure 6.4: Probability of working plotted against OP_{WF} given as values of H_s for various values of T_R .

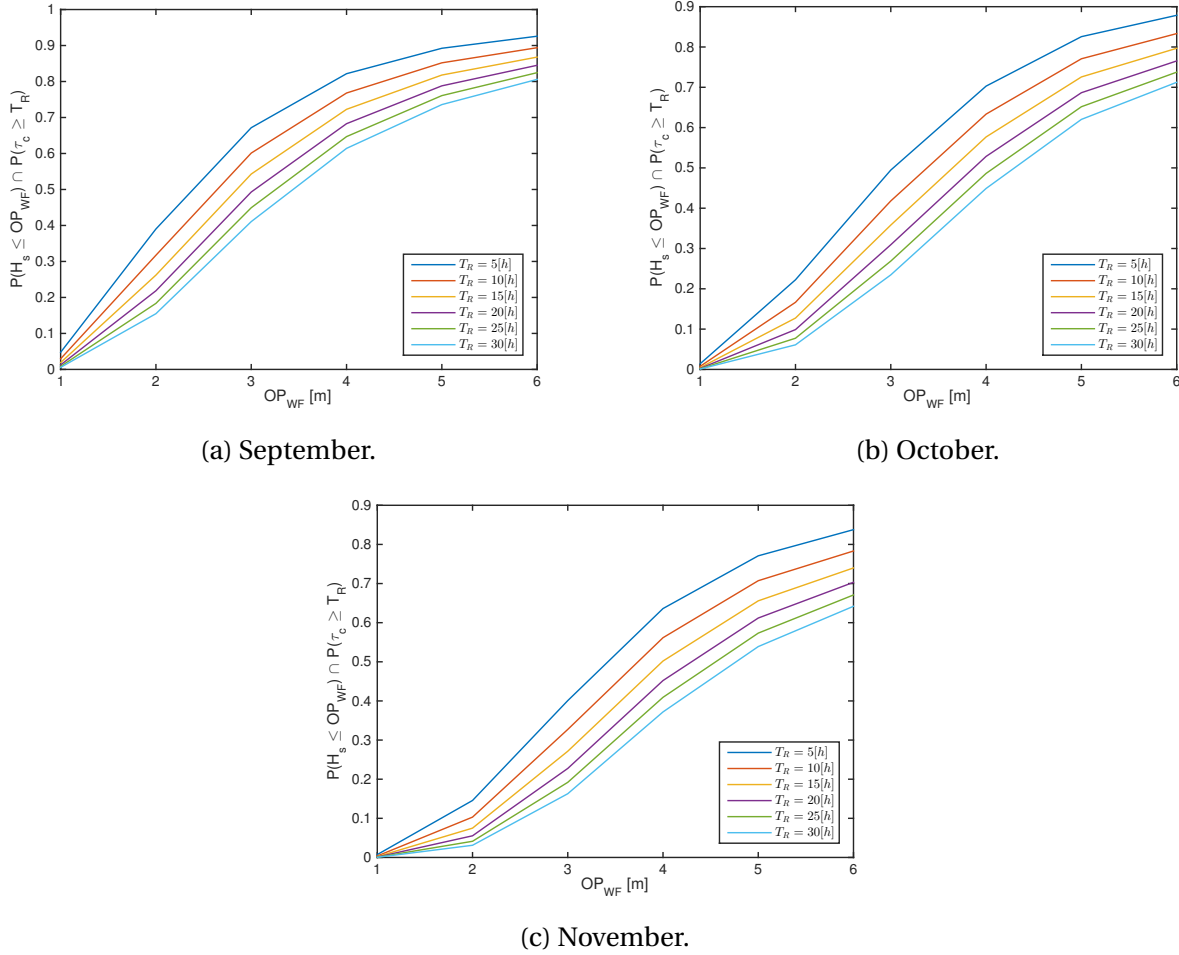


Figure 6.5: Probability of working plotted against OP_{WF} given as values of H_s for various values of T_R .

There is a clear trend in that decreasing T_R results in a higher probability of being able to work. At the same time, one sees that increasing OP_{LIM} has the same effect. The degree to which this is relevant varies from month to month. July clearly has the best operability in general, and decreases towards March and November. Based on the data, one can determine the increase in operability due to a potential decrease T_R or increase in OP_{LIM} .

Factors Affecting the Reference Time

As discussed, the reference time is defined as:

$$T_R = T_{POP} + T_c$$

This means that in order to reduce T_R , one must reduce T_{POP} , T_c , or both. It should be noted that T_c depends on T_{POP} , as mentioned in Section 6.2.3. This means that a reduction in T_{POP} inherently results in a reduction in T_c .

Factors Affecting the Operational Criterion

The operational criterion OP_{WF} depends on the design criterion OP_{LIM} as well as the alpha factor. The alpha factor is again dependent on T_{POP} , so a reduction in T_{POP} will result in an improved OP_{WF} :

$$OP_{WF} = \alpha OP_{LIM}$$

OP_{WF} can therefore be improved by increasing OP_{LIM} , decreasing T_{POP} or improving the accuracy of weather forecasting, thereby increasing the necessary α factor.

6.3.2 Challenging the Safe Condition Criteria

A marine operation shall be designed to bring an object from one safe condition to another as discussed in Chapter 2. A safe condition was defined as a condition where the object is considered exposed to normal risk for damage or loss. The question then becomes, what is a normal degree of risk? Can one consider a subsea installation operation to be in a safe state prior to landing on the seabed? If so, what are the criteria? DNV outlines that a safe condition can also be considered as a condition in which the operation fulfills the requirements relevant for unrestricted environmental loads (DNV GL, 2011a). Table 3-3 in DNV GL (2011a) states that for reference periods less than 3 days, a return period of one month is acceptable, while International Standard Organization (2009) states that those in charge of planning the operation should

define a specific weather window for the same reference period.

Based on this, one can argue that if the sub-operation has a design criterion over the extreme value for a one month return period (see Table 3.5 in Statoil (2004) for monthly marginal extreme values of H_s), it can be considered to be in a "safe condition". As the scope of the analyses performed in this thesis did not include the landing and positioning on seabed sub-operations, specific operational limits are hard to set. However, the results from the final part of the pendulum free-fall phase indicates that relative rough sea states in terms of H_s are acceptable. As such, this suggests that at least the final lowering is relatively robust against realistic conditions. Assuming that this also is the case for the landing on seabed sub-operation, one can detach sub-operations 6-8 from environmental sensitivity. They will then not be considered as a part of the reference time for the operation. The required weather window is defined as the time necessary between two safe conditions. Removing operations 6-8 decreases the necessary size of this window and thereby increases operability. T_R will in this case decrease from 15 hours to 9 hours. This constitutes a 40 % reduction in the reference time.

It can be argued that the state after Vessel B steams into position and prior to cutting of sea-fastening could be a safe condition. If this is to be implemented, a thorough understanding of the risk picture is necessary. At this point in the operation, there will be minimal risk to personnel and equipment due to environmental effects. Relevant equipment will be secured on deck, and personnel secure within the cabin. The characteristic length of the deployment line will also result in a sufficient degree of flexibility such that the two vessels can be considered as separate, decoupled systems. As such, the introduction of a safe condition at this point may be considered reasonable. One can now separate the operation into three operations, where Operation 3 is considered weather unrestricted (see Figure 6.6).

Operation 1			Operation 2				Operation 3		
Sub-Op. 1	Sub-Op. 2	Safe Condition	Sub-Op. 3	Sub-Op. 4	Sub-Op. 5	Safe Condition	Sub-Op. 6	Sub-Op. 7	Sub-Op. 8
Weather Restricted			Weather Restricted				Weather Unrestricted		

Figure 6.6: Safe state partitioning of operation.

By separating into three operations, three different OP_{WF} with their own T_{POP} will be intro-

duced. As T_{POP} is reduced, the α factor will also be increased, increasing OP_{WF} . This allows the requirements for the total operation to be much more flexible.

6.3.3 Challenging the Contingency Time

The contingency time accounts for the uncertainty in T_{POP} . As the PIM is a state-of-the-art method, the relevant failure modes have not yet been sufficiently identified. The contingency time therefore should be twice T_{POP} as outlined by DNV GL (2011a). The second phase of the operation is however a standard subsea lifting operation through the splash zone. As such DNV GL (2011a) cites that it can be taken as 50 % of T_{POP} . Nonetheless, it should not be less than 6 hours. These criteria appear to be unnecessarily conservative. Subsea installation operations through the splash-zone have been thoroughly documented, and the contingency time necessary should be minimal. It can therefore be argued that this time can be minimized even further for this part of the operation. Thorough simulation of the operation through numerical time domain analyses should however be a requirement for reducing contingency times for specific operations.

6.3.4 Challenging the Alfa-Factor

The α factor decreases the value of the design criterion to the operational criteria as a result of uncertainty in the weather forecast. If this uncertainty can be removed, the operational limit can potentially be set to the same value as the design criteria. Innovative forecasting methods may provide measures to achieve this. Real-time wave forecasting is one of the most promising solutions. This allows the installation vessel to receive data related to relevant parameters, such as H_s in real time. Edgar and Horwood (2000) outlines how deterministic sea wave prediction based on live observations can be applied to marine operations. Such observations can be from buoys placed in array around the vessel, or from radar interpretations of the current sea state. Naaijen and Huijsmans (2008) argues also that wave elevation can be estimated based on linear wave modelling. Summing regular wave components at a distance from the vessel and

estimating their future behaviour gives an indication of the future irregular wave picture. The theory indicates that a high level of accuracy might be possible, but technology must improve significantly to achieve this.

In operations with a short sub-operation with a low operational limit, such as lowering through the splash-zone, real time evaluations of the sea state could render the operation feasible in a generally higher forecasted sea state. Once through the splash zone, the operational limits are generally higher. This could increase operability significantly.

6.3.5 Challenging the Design Criteria

When the OP_{LIM} were set for the different sub-operations in Section 6.2.1, only H_s were taken into account. Taking the Splash-Zone phase as an example, it can be observed from the results in Section 5.2.8 that there are some combinations of H_s and T_p that still satisfy the acceptance criteria, even though the H_s is larger than the set OP_{LIM} for the sub-operation. As such, if the process of determining the OP_{LIM} also could take T_p into account, the design criterion could potentially become more flexible since the design criterion would depend on the combination of H_s and T_p . It should be noted that this would require high precision and accuracy when forecasting the weather. Studies have up until now only been conducted on uncertainty in H_s and wind speed. The authors recommend that similar α factors should be developed for T_p forecasts as well.

6.3.6 Implementing Improvements

Implementing the improvements outlined in Section 6.3.2, the improved Dual Cap-X operation using PIM can be separated into three distinct operations with safe states in-between. Each operation will now have their own T_R and OP_{WF} . Operation 1 and 2 as shown in Figure 6.6 will be joined to show the effect of removing operation three from T_R in terms of operability. In addition, the operability of Operation 1 and Operation 2 will be investigated individually given that they can be as viewed separate independent operations. Moreover, the reduced T_c for the

Splash-Zone phase, as discussed in Section 6.3.3, is also enforced.

Detaching Operation 3

By considering Operation 3 (see Section 6.3.2) to be weather unrestricted, it can be removed from T_R for the operation. In addition, the contingency time is now 3.5 hours due to assumed familiarity with splash-zone installation. The new reference period and operational limit will therefore be:

- $T_R = 8$ h
- $OP_{LIM} = 1.6$ m

This gives an indication of the sensitivity of the operability of the operation to a reduction in the reference time. The new monthly operabilities of the installation of the Dual Cap-X using the PIM based on the implemented measures are presented in Table 6.5. The improved operabilities are compared to the results from the base case (second column) presented in Section 6.2.5.

Table 6.5: Improved probability of working.

	Monthly Operability -Base Case [%]	Monthly Operability -Improved Case [%]	Increased Operability [%]
March	4	6	2
April	11	17	6
May	28	36	8
June	36	45	9
July	44	53	9
August	38	47	9
September	14	20	6
October	5	9	4
November	3	5	2

Independent Operations

If the operation is split into 3 separate operations (see Figure 6.6) with safe states in-between, the following operational constraints will apply:

Operation 1:

- $T_R = 5$ h
- $OP_{WF} = 1.6$ m

Operation 2:

- $T_R = 3$ h
- $OP_{WF} = 3.1$ m

Operation 3 will have 100 % operability for all months.

Table 6.6: Improved probability for independent operations.

	Monthly Operability - Operation 1 [%]	Monthly Operability - Operation 2 [%]
March	8	49
April	20	72
May	41	89
June	49	92
July	57	95
August	52	92
September	23	73
October	11	56
November	7	47

It is clear that the operability of the operation increases significantly when separating into independent operations. As seen from Table 6.6, the operability of Operation 2 is much higher than Operation 1, and both have higher values than the base case. This is however not an accurate representation of the operability as a whole as its feasibility depends on the successful implementation of Operation 1 for Operation 2 to be feasible.

It appears that the increase in OP_{WF} has a more significant effect on increasing operability than does a decrease in T_R , but the greatest improvements are achieved through a combination.

6.4 Comparing Traditional 300 m Installation and 3000 m PIM

As has been discussed, Statoil wishes to install subsea infrastructure at 3000 m at the same cost as for 300 m. The PIM may provide the solution.

Traditional deepwater installation of subsea infrastructure requires the use of costly heavy-lift vessels or drilling rigs to render the installation operation feasible. The PIM however requires two small to mid-size vessels (e.g. Anchor Handling Vessels or Subsea Construction Support Vessels). Despite requiring two vessels, the total vessel day rate will be significantly less than that of a heavy lift vessel or drilling rig.

The time required to install subsea hardware at 3000 m depth is also a significant driver. Both the required operation time and the time waiting on weather will define the installation costs. Using smaller, cheaper vessels, the effect of these costs will go down, but simultaneously the operability will go down due to increased environmental sensitivity of smaller vessels. As has been discussed in this chapter, the reference time and operational limits will be decisive for the operability of the operation. The results found in this thesis indicate that the PIM decreases the necessary duration of the operation significantly. The free-fall phase takes approximately 1 hour (depending on current conditions). The decoupling of the free-fall phase from environmental sensitivity also increases operability significantly.

Jacobsen and Næss (2014) studies the typical weather window for the installation of a 300 t tem-

plate in shallow water in the Norwegian Sea using a mid-size vessel by traditional lifting. For the sake of providing a comparison, the values given in Jacobsen and Næss (2014) are used to set the reference time, T_R and the operational limit in terms of significant wave height, OP_{WF} for a traditional installation of a 300 tonne template in 300 m water depth. The operational constraints are:

- $T_R = 12$ h
- $OP_{WF} = 2$ m

It should be noted that these values are typical for a 300 t template while the Dual Cap-X mass is 175 t. Moreover, the geometry of a template is considerably different from that of the Dual Cap-X. Uncertainty in factors such as water filling rates and hoisting speed may also affect the comparison. As such, the comparison should only serve as an indication of how traditional subsea installation in 300 m compares to a installation of the Dual Cap-X in 3000 m using the PIM. In this way, the comparison is not only useful in terms of gaining insight into how the use of the PIM in 3000 m fare against traditional lifting installation in 300 m, but also how the Dual Cap-X as a concept compares to traditional subsea templates with respect to installation.

Table 6.7 presents the resulting operability for the 300 m traditional installation case and compares it with the PIM base case as presented in Section 6.2.5.

Table 6.7: Operability of 300 m traditional subsea installation operation for Heidrun data.

	Monthly Operability -PIM Base Case (3000 m) [%]	Monthly Operability -Traditional lifting (300 m) [%]
March	4	11
April	11	26
May	28	50
June	36	58
July	44	65
August	38	60
September	14	29
October	5	15
November	3	9

When comparing the highly conservative base case operability values to those established for traditional 300 m lifting, it was found that the operability of the PIM lies in some cases 20 % below that of Traditional lifting. This is due to an $OP_{LIM} = 1.6$ m that heavily dominates the operability results. Nonetheless, this is considering an installation at a depth of 3000 m with conservative assumptions and input values. A 20 % difference can as such be viewed as quite low. If one however considers Operation 1 as outlined in Section 6.3.6 to be a separate operation, and assumes that it is completed, one can compare 300 m traditional lifting operability to Operation 2 (solely splash zone lifting) due to the assumption that Operation 3 (free-fall) is unrestricted with respect to environmental sensitivity. The comparable operability is shown in Table 6.8.

Table 6.8: Comparison of improved PIM in 3000 m with 300 m traditional installation for Hei-drun data.

	Monthly Operability -PIM Operation 2 [%]	Monthly Operability -300 m Traditional [%]
March	49	11
April	72	26
May	89	50
June	92	58
July	95	65
August	92	60
September	73	29
October	56	15
November	47	9

The results indicate that the installation of the Dual Cap-X using the PIM at 300 m will have costs comparable to that of a traditional lifting installation in 300 m of a standard subsea template. If the improvements outlined in Section 6.3.6 are implemented the operability of the PIM will increase even more.

Chapter 7

Summary and Recommendations for Further Work

7.1 Summary and Conclusions

This thesis has investigated the installation of the Dual Cap-X using the Pendulous Installation Method. The results are quite promising, and indicate that this method may realize the goal of cost-effectively installing subsea hardware in deepwater conditions.

A thorough understanding of the hydrodynamic forces associated with the installation operation is necessary to identify parameters that will dictate the dynamic response of the system. This dynamic response will be the basis for which the design operational limits are set. As such this thesis shows that relevant theory is central.

During the In-Air phase of the operation, the results from the analysis indicate that pendulous motion of the payload is probable. In order to ensure the safety of personnel and equipment, tugger lines will be necessary.

The numerical analysis of the Splash-Zone phase indicates that slamming is important for the dynamic response of the lifting line. However, the effect of the slamming force on the global

response is highly dependent on the impulse duration. Moreover, the results indicate that wave excitation forces in the form of the combination of Froude–Krylov and diffraction forces may be as dominant as slamming in some sea states. This shows good coherence with the assumption of a small-body structure. As such, in the same way as the accurate estimation of slamming coefficients is important, attention should also be paid in accurately estimating the added mass of the Dual Cap-X. These results are reflected in the trends found for the resultant operational limits. Lower peak periods, and larger significant wave heights yielded lower design limits. Larger wave heights inherently result in larger dynamic forces. Lower peak periods will result in higher wave particle accelerations, enhancing the wave excitation forces found to be dominant. It was also found that lower hoisting speeds yielded lower design limits. This is most likely due to the increased exposure of the payload to wave interaction, and the inherent increased probability of exciting detrimental effects.

Numerical simulations run for the intermediate phase between the Splash-Zone and Free-Fall phases indicate a low level of sensitivity to environmental conditions, with design operational limits assumed above realistic conditions for the installation operation.

The numerical simulations run for the Free-Fall phase investigated the global response of the payload. Sensitivity studies with respect to current, weight and drag coefficients were conducted. The results indicate that the current conditions dominate the global response, and as such the total duration of the free fall. Current profiles both in line and orthogonal to the payload trajectory increase the duration of the Free-Fall phase as the current speed increases. For the maximum current profiles tested, the results indicate that it takes approximately 1 hour for the payload to reach its final position. Increasing the payload weight reduces the duration. Sensitivity to the value of the drag coefficients was also investigated, and found to be less prominent relative to current sensitivity. The results also indicate that the top tension during free-fall is within acceptable ranges in realistic conditions. Once the payload has reached its final position, the results indicate oscillatory behaviour, most likely due to wave induced vessel motion. The results also indicate a stable free-fall of the payload. Nonetheless, detailed local analyses should be conducted to confirm this.

The results from the time domain analyses were utilized to develop a time schedule with rele-

vant operational limits for each sub-operation. Operability was investigated for relevant months from hindcast data for the Heidrun field. It was clear that by challenging existing regulatory practices, the operability could be significantly increased. This could be realized through either reducing the reference period, increasing the operational limit, or both. Improvements to operability can be achieved through challenging the safe condition criteria, contingency time and α - factor. The authors would like to highlight the fact that the potential of such measures should not be underestimated, as the results indicate that significant increases in operability result. The possibility of separating the operation into three independent operations was investigated based on the findings. This significantly increased the operability. It was found that the operability of the installation of the Dual Cap-X using the Pendulous Installation Method at 3000 m water depth has almost equal or higher operability compared to the traditional subsea installation of a template at 300 m depth depending on the improvements made.

The Pendulous Installation Method has the potential to facilitate cost-effective subsea installation in deepwater conditions. It allows for cost reduction with respect to vessel costs, and significantly decreases the required time necessary to install subsea hardware. The installation time, operability and resultant cost of installing the Dual Cap-X at 3000 m water depth appear to be comparable to that of traditional installation of a subsea template at 300 m water depth. As such, it can be concluded that the implementation of the Dual Cap-X design in conjunction with the Pendulous Installation Method has significant potential to render deepwater subsea production fields feasible.

7.2 Recommendations for Further Work

Due to the limited scope of this thesis, there are multiple areas that still require investigation with respect to the feasibility of the Pendulous Installation Method.

The objective of the Free-Fall phase was to evaluate the global behaviour of the system. As a result, local effects were neglected. A variety of hydrodynamic effects may occur during free-fall such as fluttering of the payload. Such instabilities should be investigated. Additionally, the resultant forces that act on the payload due to such phenomena should be evaluated with respect to sensitive components and equipment on the payload.

The seabed positioning and landing phases should also be investigated in depth. The positing of equipment can be extremely time consuming, and in certain cases may result in the operation being infeasible. Sensitivity to relevant parameters such as current profiles and drag coefficients when positioning should be evaluated. Potential improvements to traditional positioning should be investigated and evaluated with respect to the total operability of the Pendulous Installation Method. Limitations related to the velocity of the payload when landing on the seabed should also be evaluated. The potential use of AHC should be investigated, and the impact on operability outlined.

In order to gain a more accurate understanding of the operability of the Pendulous Installation Method, simulations related to weather windows should be conducted. Monte Carlo simulations in which an installation operation is conducted at a random time point in a specific month should be considered. Such simulations would use relevant hindcast data as a future weather forecast, to which a time schedule outlining the reference time and operational limits for each sub-operation will be applied. In this manner the operability of the operation will be much better understood with respect to realistic conditions. SimEvents may be relevant for such an investigation. A detailed cost-analysis based on the operability and necessary vessels and equipment can also be evaluated to gain a more tangible evaluation of the installation costs.

Technical improvements to the Pendulous Installation Method should also be investigated. Such improvements may include improving the hand-off of the deployment line from one vessel to

another, or potentially eliminating the splash-zone lowering phase by dropping the payload directly into the free-fall phase. This might be facilitated by rolling the payload off the end of the vessel via a stinger similar to those used in pipe-laying operations, whilst the vessel steams forward. Potential improvements with respect to operability and cost should also be evaluated.

Appendix A

Acronyms

AHC Active Heave Compensation

DAF Dynamic Amplification Factor

DP Dynamic Positioning

DNV Det Norske Veritas

EVD Extreme Value Distribution

FE Finite Element

FFT Fast Fourier Transform

FK Froude-Krylov

HMPE High-Modulus Polyethylene

JONSWAP Joint North Sea Wave Project

PDF Probability Density Function

PIM Pendulous Installation Method

RAO Response Amplitude Operator

RIFLEX Riser System Analysis Program

ROV Remotely Operated Vehicle

SIMA Simulation Workbench for Marine Applications

SIMO Simulation of Marine Operations

SWL Safe Working Load

USBL Ultra-Short Base Line

Appendix B

Crane Capacity

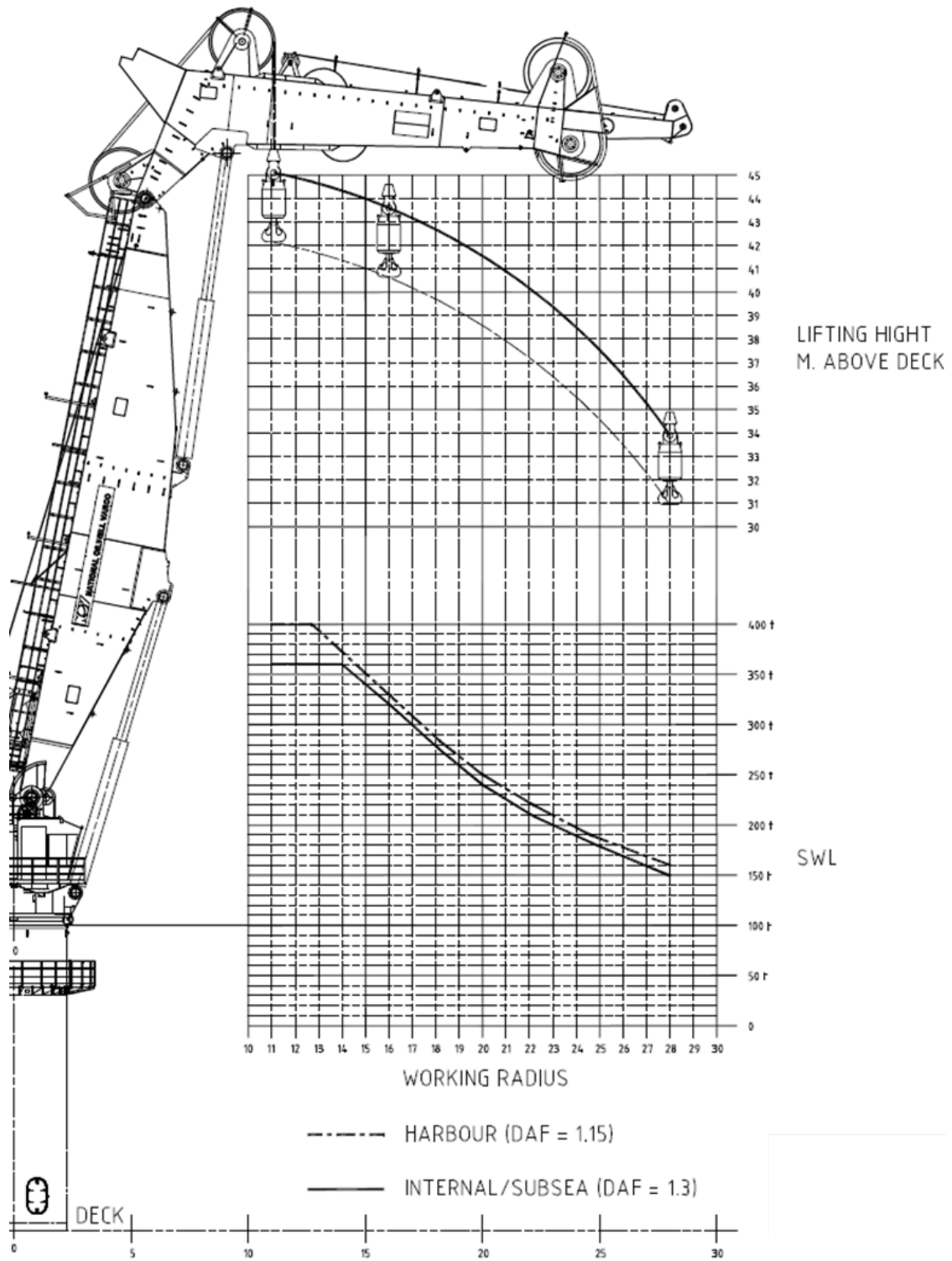
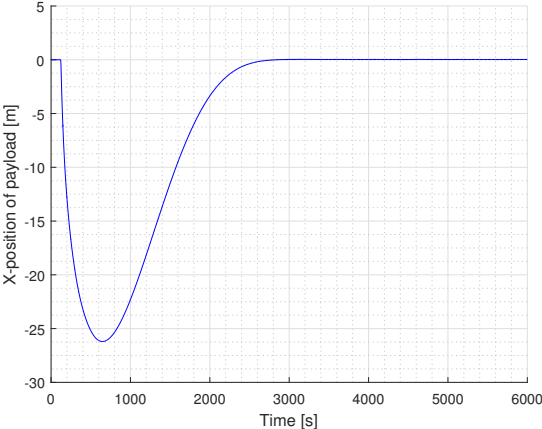


Figure B.1: Capacity of Lifting Crane on Skandi Acergy provided by National Oilwell Varco

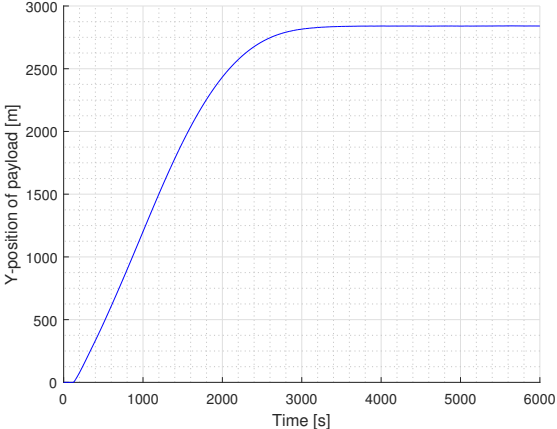
Appendix C

Supporting Free-Fall Results

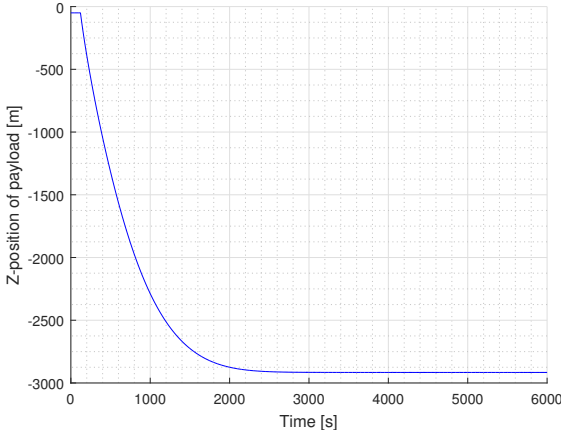
The following results are given for the pendulum free-fall case with the current profile "Maximum current" along negative Y-axis (Section 5.4.4). The results are given in the global coordinate system as defined in Section 4.2.5.



(a) Translation in X-direction.



(b) Translation in Y-direction.



(c) Translation in Z-direction.

Figure C.1: Payload trajectory.

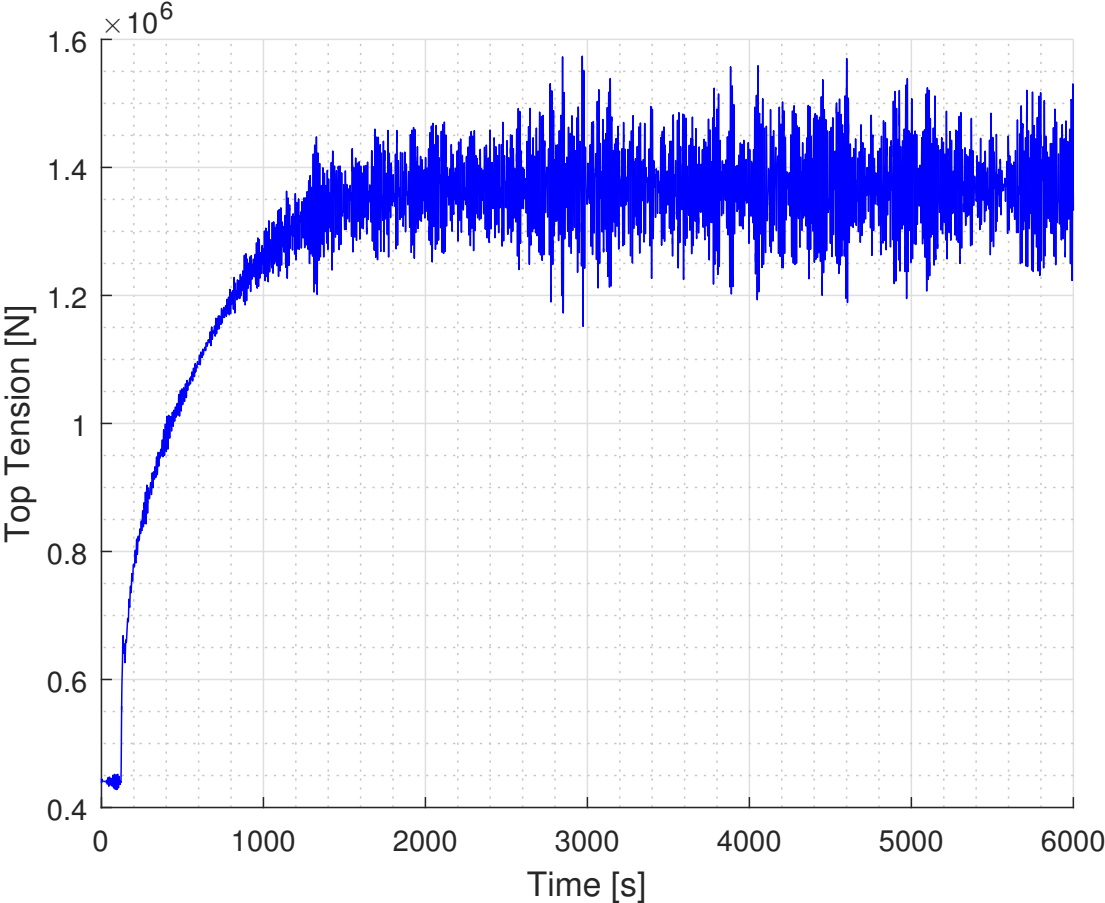
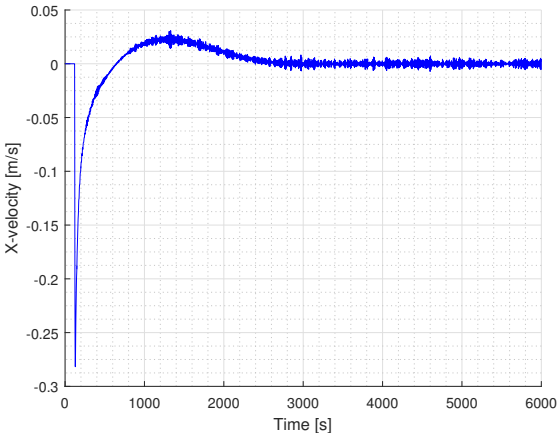
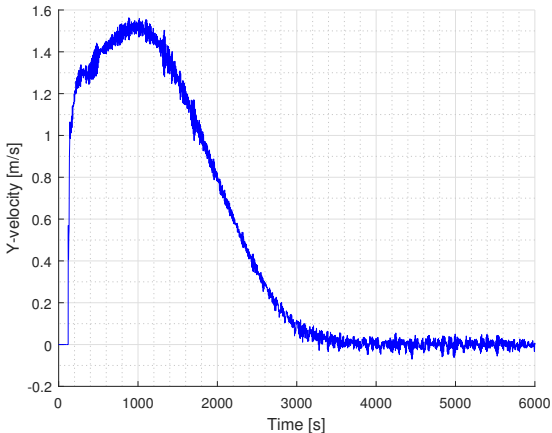


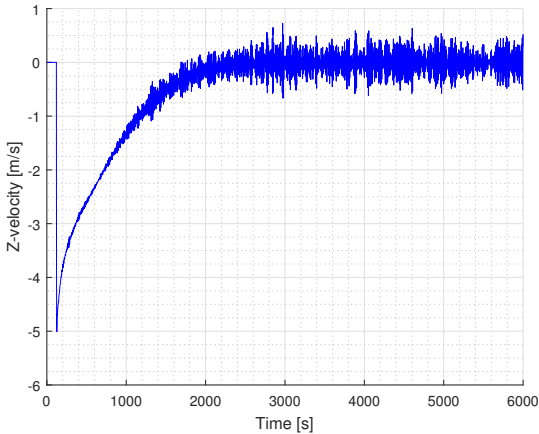
Figure C.2: Top tension.



(a) Velocity in X-direction.

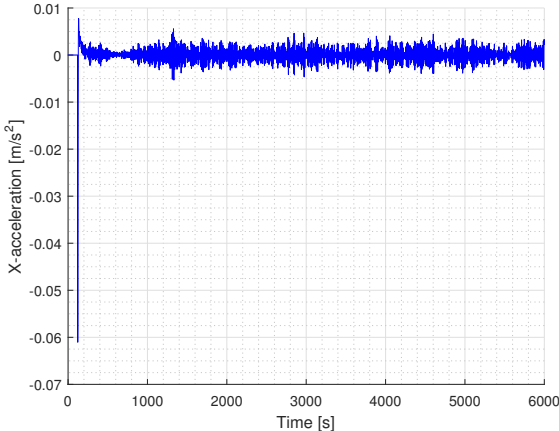


(b) Velocity in Y-direction.

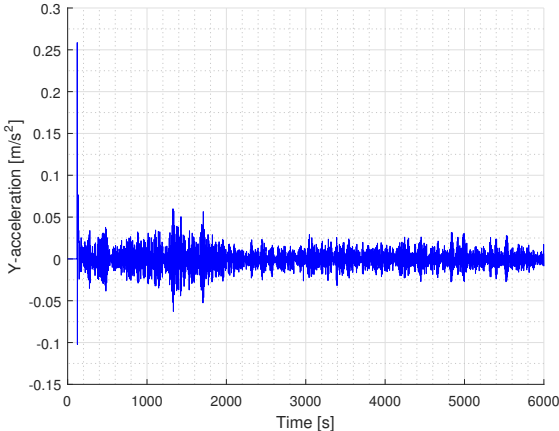


(c) Velocity in Z-direction.

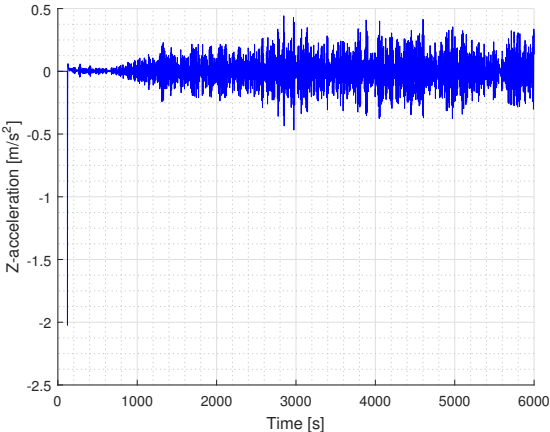
Figure C.3: Payload velocities.



(a) Acceleration in X-direction.



(b) Acceleration in Y-direction.



(c) Acceleration in Z-direction.

Figure C.4: Payload accelerations.

Appendix D

Design Criteria

D.1 Maximum Lifting Wire Tension



Figure D.1: Legend.

Hs/Tp	6	8	10	12	14	16
1						
2						
3						
4						
5						
6	NA					

Figure D.2: Design criteria set by crane capacity for hoisting speed of 0.1 m/s.

Hs/Tp	6	8	10	12	14	16
1						
2						
3						
4						
5						
6	NA					

Figure D.3: Design criteria set by crane capacity for hoisting speed of 0.25 m/s.

Hs/Tp	6	8	10	12	14	16
1						
2						
3						
4						
5						
6	NA					

Figure D.4: Design criteria set by crane capacity for hoisting speed of 0.5 m/s.

D.2 Minimum Lifting Wire Tension



Figure D.5: Legend.

Hs/Tp	6	8	10	12	14	16
1						
2						
3						
4						
5						
6	NA					

Figure D.6: Design criterias for hoisting speed of 0.1 m/s.

Hs/Tp	6	8	10	12	14	16
1						
2						
3						
4						
5						
6	NA					

Figure D.7: Design criteria for hoisting speed of 0.25 m/s.

Hs/Tp	6	8	10	12	14	16
1						
2						
3						
4						
5						
6	NA					

Figure D.8: Design criteria for hoisting speed of 0.5 m/s.

D.3 Minimum Sling Tension

The operational limits presented are representative of all slings. Limits were set with respect to a breached limit in any of the four slings.



Figure D.9: Legend.

Hs/Tp	6	8	10	12	14	16
1						
2						
3						
4						
5						
6	NA					

Figure D.10: Design criteria for hoisting speed of 0.1 m/s.

Hs/Tp	6	8	10	12	14	16
1						
2						
3						
4						
5						
6	NA					

Figure D.11: Design criteria for hoisting speed of 0.25 m/s.

Hs/Tp	6	8	10	12	14	16
1						
2						
3						
4						
5						
6	NA					

Figure D.12: Design criteria for hoisting speed of 0.5 m/s.

Appendix E

Hydrodynamic Coefficients

Overview of Slender Elements in SIMO Body Model

Element	Profile	Length [m]	Width [m]	Height [m]	Aves [m ²]	K1	K2	V1	V2	Z1	Z2	Ca_W	Ca_H	A_X [kg/m]	Ae_Y [m ²]	Ae_V [kg/m]	Ae_Z [m ²]	A_Z [kg/m]	Cdd_Y	Cdd_Z	
OuterFrame_1	HEB200	13.1	0.2	0.2	0.00781	0	0	13.1	0	0	0	0	2.11	1	0	0.03141593	32.2013247	0.03141593	67.9447951	164	194.75
OuterFrame_2	HEB200	13.1	0.2	0.2	0.00781	0	0	13.1	9	9	0	0	2.11	1	0	0.03141593	32.2013247	0.03141593	67.9447951	164	194.75
OuterFrame_3	HEB200	2.4	0.2	0.2	0.00781	0	0	0	0	2.4	0	0	2.11	1	0	0.03141593	32.2013247	0.03141593	67.9447951	164	194.75
OuterFrame_4	HEB200	2.4	0.2	0.2	0.00781	0	0	0	6.6	9	0	0	2.11	1	0	0.03141593	32.2013247	0.03141593	67.9447951	164	194.75
OuterFrame_5	HEB200	2.4	0.2	0.2	0.00781	13.1	13.1	13.1	0	2.4	0	0	2.11	1	0	0.03141593	32.2013247	0.03141593	67.9447951	164	194.75
OuterFrame_6	HEB200	2.4	0.2	0.2	0.00781	13.1	13.1	13.1	6.6	9	0	0	2.11	1	0	0.03141593	32.2013247	0.03141593	67.9447951	164	194.75
Lat_1	HEB500	16.9	0.3	0.5	0.02386	-1.9	15	2.4	2.4	0	0	0	2.11	1	0	0.19634954	201.258279	0.07068583	152.875789	538.125	230.625
Lat_2	HEB500	16.9	0.3	0.5	0.02386	-1.9	15	6.6	6.6	0	0	0	2.11	1	0	0.19634954	201.258279	0.07068583	152.875789	538.125	230.625
Long_1	HEB500	9	0.3	0.5	0.02386	5	5	5	0	9	0	0	2.11	1	0	0.19634954	201.258279	0.07068583	152.875789	538.125	230.625
Long_2	HEB500	9	0.3	0.5	0.02386	7.5	7.5	7.5	0	9	0	0	2.11	1	0	0.19634954	201.258279	0.07068583	152.875789	538.125	230.625
Long_3	HEB500	9	0.3	0.5	0.02386	9	9	9	0	9	0	0	2.11	1	0	0.19634954	201.258279	0.07068583	152.875789	538.125	230.625
Top_long_1	HEB200	5	0.2	0.2	0.00781	0	0	0	2	7	2.4	2.4	2.11	1	0	0.03141593	32.2013247	0.03141593	67.9447951	164	194.75
Top_long_2	HEB200	5	0.2	0.2	0.00781	13.1	13.1	13.1	2	7	2.4	2.4	2.11	1	0	0.03141593	32.2013247	0.03141593	67.9447951	164	194.75
Top_long_angle_1	HEB200	2.4	3.1241	0.2	0.00781	0	0	0	0	2	0	2.4	2.11	1	0	0.03141593	32.2013247	0.03141593	67.9447951	164	194.75
Top_long_angle_2	HEB200	2.4	3.1241	0.2	0.00781	0	0	0	7	9	0	2.4	2.11	1	0	0.03141593	32.2013247	0.03141593	67.9447951	164	194.75
Top_long_angle_3	HEB200	2.4	3.1241	0.2	0.00781	13.1	13.1	13.1	9	7	0	2.4	2.11	1	0	0.03141593	32.2013247	0.03141593	67.9447951	164	194.75
Top_long_angle_4	HEB200	2.4	3.1241	0.2	0.00781	13.1	13.1	13.1	2	0	2.4	2.4	2.11	1	0	0.03141593	32.2013247	0.03141593	67.9447951	164	194.75
Top_lat_angle_1	HEB200	3.061	0.2	0.2	0.00781	-1.9	0	0	2.4	2.4	0	2.4	2.11	1	0	0.03141593	32.2013247	0.03141593	67.9447951	164	194.75
Top_lat_angle_2	HEB200	3.061	0.2	0.2	0.00781	-1.9	0	6.6	6.6	0	2.4	2.4	2.11	1	0	0.03141593	32.2013247	0.03141593	67.9447951	164	194.75
Top_lat_angle_3	HEB200	3.061	0.2	0.2	0.00781	13.1	15	2.4	2.4	2.4	2.4	2.4	2.11	1	0	0.03141593	32.2013247	0.03141593	67.9447951	164	194.75
Top_lat_angle_4	HEB200	3.061	0.2	0.2	0.00781	13.1	15	6.6	6.6	6.6	2.4	2.4	2.11	1	0	0.03141593	32.2013247	0.03141593	67.9447951	164	194.75

Figure E.1: Frame hydrodynamic coefficients.

Fixed Body Element Coefficients (2 suction cans)		
Cds_X [Ns²/m²]	Cds_Y [Ns²/m²]	Cds_Z [Ns²/m²]
9019.00575	29462.08545	20535.72504
A_X [kg]	A_Y [kg]	A_Z [kg]
261069.9118	275140.6864	307946.4335
A_Z		
Rho [kg/m ³]	1025	
H [m]	6.035	
D [m]	4.86	
A_water [kg]	229505.7419	
Ca	0.636619772	
Vr [m ³]	60.10456109	
A_X		
k2	0.83	
A_X [kg]	31564.16997	
A_Y		
k2	1.2	
A_X [kg]	45634.94453	
Cds_X [N/m²]		
Cd	0.3	
A [m ²]	58.6602	
Cds_Y [N/m²]		
Cd	0.98	
A [m ²]	58.6602	
Cds_Z [N/m²]		
Cd	1.08	
A [m ²]	37.10158092	

Figure E.2: Fixed body hydrodynamic coefficients.

Wind Coefficients		
Cds_X [Ns²/m²]	Cds_Y [Ns²/m²]	Cds_Z [Ns²/m²]
10.77881175	35.21078505	24.54269578
Density of air	1.225 [kg/m ³]	

Figure E.3: Quadratic wind coefficients.

Bibliography

- Blevins, R. (1984). Applied Fluid Dynamics Handbook. *Krieger Publishing Company*.
- Cao, S., Yu, J., Zhang, G., and Ma, W. (2012). A Study on the Controllability of Deepwater Manifold during Launch through Pendulous Installation Method. *Advanced Materials Research*.
- Chen, Y. and Mukerji, P. (2008). Weather Window Statistical Analysis for Offshore Marine Operations. *The Eighteenth International Offshore and Polar Engineering Conference*.
- DNV GL (2010). Environmental Conditions and Environmental Loads, Recommended Practice DNV-RP-C205.
- DNV GL (2011a). Marine Operations, General, Offshore Standard DNV-OS-H101.
- DNV GL (2011b). Modelling and Analysis of Marine Operations, Recommended Practice DNV-RP-H103. *Offshore Standard*.
- DNV GL (2014). Loadout, Transport and Installation of Subsea Objects (VMO Standard - Part 2-6) DNV-OS-H206. *Offshore Standard*.
- Edgar, D. and Horwood, J. (2000). The effects of parameters on the maximum prediction time possible in short term forecasting of the sea surface shape. *International Shipbuilding Progress*.
- Ellingsen, K. E. (2015). The "Cap-X" Solution, Statoil Internal Document.
- Faltinsen, O. (1990). *Sea Loads on Ships and Offshore Structures*, volume 1. Cambridge University Press.

- Farrant, T. and Javed, K. (2001). Minimising the effect of deepwater currents on drilling riser operations.
- Fernandes, A. (2010). Investigation of the Flow Induced Small Amplitude Rotation Triggering Flat Plate Fluttering. *IUTAM Symposium on Bluff Body Wakes and Vortex-Induced Vibrations*.
- Fernandes, A. and Rodrigues Neves, C. (2007). The Concomitant Model Testing Approach for the Development of the Pendulous Installation Method of Heavy Devices in Deep Water. *ASME 26th International Conference on Offshore Mechanics and Arctic Engineering*.
- Fernandes, A. C. and Mineiro, F. P. S. (2007). Assessment of hydrodynamic properties of bodies with complex shapes. *Applied Ocean Research*, 29(3):155–166.
- Foo, Y., Gan, K., Giudice, D., and Masi, G. D. (2014). Analysis of Windows of Opportunity for Weather-Sensitive Operations. *Oil and Gas Facilities*.
- Frazer, I., Perinet, D., and Vennemann, O. (2005). Technology required for the installation of production facilities in 10,000 ft of water. Offshore Technology Conference.
- Gordon, R. (2013). Modeling Suction Pile Lowering Through the Splash Zone. *ASME 32nd International Conference on Ocean, Offshore and Arctic Engineering*.
- International Standard Organization (2009). ISO 19901-6:2009: Petroleum and Natural Gas Industries - Specific Requirements for Offshore Structures, Part 6: Marine Operations. Technical report.
- Ireland, J. (2007). Investigation Into the Sensitivity of the Dynamic Hook Load During Subsea Deployment of a Suction Can. *ASME 26th International Conference on Offshore Mechanics and Arctic Engineering*.
- Jacobsen, T. and Næss, T.-b. (2014). Installation of Subsea Structures Using Mid-Size Construction Vessels in Harsh Environments. In *Offshore Technology Conference Asia held in Kuala Lumpur, Malaysia, 25–28 March 2014*.
- Larsen, C. M. (2012). *Marin dynamikk: kompendium for bruk i faget TMR 4182 Marin dynamikk ved Institutt for marin teknikk, Fakultet for ingeniørvitenskap og teknologi, NTNU*, volume

- UK-2012-09 of *TMR4182 Marin dynamikk*. Marinteknisk senter, Institutt for marin teknikk, NTNU, Trondheim.
- Larsen, K. (2015). Lecture notes in tmr4225 marine operations.
- MARINTEK (2011). RIFLEX - Theory Manual Version 3.6.
- Myrhaug, D., Lian, W., and Norges teknisk-naturvitenskapelige universitet Institutt for marin, T. (2014). *Marine dynamics : lecture notes 2009*. Akademika forlag Kompendieforlaget, Trondheim.
- Naaijen, P. and Huijsmans, R. (2008). Real time wave forecasting for real time ship motion predictions. *ASME 27th International Conference on Offshore Mechanics and Arctic Engineering*.
- Næss, T. (2014). Full scale monitoring - closing the design loop.
- Næss, T., Havn, J., and Solaas, F. (2014). On the importance of slamming during installation of structures with large suction anchors. *Ocean Engineering*.
- Newman, J. N. and Landweber, L. (1978). Marine Hydrodynamics. *Journal of Applied Mechanics*, 45(2):457.
- Nielsen, F. G. (2007). *Lecture notes : Marine operasjoner*. Kompendium (Norges teknisk-naturvitenskapelige universitet. Institutt for marin teknikk). Marinteknisk senter, Institutt for marin hydrodynamikk, NTNU, Trondheim.
- Øritsland, O. (1989). *A Summary of Subsea Module Hydrodynamic Data*, volume 511110.05. Norsk marinteknisk forskningsinstitutt, Trondheim.
- Øritsland, O. and Lehn, E. (1987). Hydrodynamic forces on subsea modules during lifting operations. *3rd International Symposium on Practical Design of Ships and Mobile Units*.
- Plummer, C., Macfarlane, G., and Drobyshevski, Y. (2009). Hydrodynamic Properties of a Suction Can Oscillating Near the Free Surface. *ASME 28th International Conference on Ocean, Offshore and Arctic Engineering*.

- Sarkar, A. and Gudmestad, O. T. (2010). Splash Zone Lifting Analysis of Subsea Structures. *29th International Conference on Ocean, Offshore and Arctic Engineering: Volume 1*, pages 303–312.
- Sarpkaya, T. (2010). *Wave Forces on Offshore Structures*. Cambridge University Press.
- SIMO Project Team (2015). SIMO - Theory Manual Version 4.6 rev 0.
- Søfteland, T., Skrunes, O., and Karunakaran, D. (2014). Lifting Analysis of Subsea Framework Structures. *ASME 2014 33rd International Conference on Ocean, Offshore and Arctic Engineering*.
- Standing, R. G., Mackenzie, B. G., and Snell, R. O. (2002). Enhancing the technology for deepwater installation of subsea hardware. Offshore Technology Conference.
- Statoil (2004). Metocean Design Basis for Heidrun Area.
- Statoil (2010). Metocean Design Basis for Area Outside Coast of Tanzania.
- Statoil (2016). CAD drawings of the Dual Cap-X.
- Thurston, K., Swanson, R., and Kopp, F. (2011). Statistical characterization of slacking and snap loading during offshore lifting and lowering in a wave environment. *ASME 30th International Conference on Ocean, Offshore and Arctic Engineering*.
- Walker, R. T., Van Nieuwkoop-Mccall, J., Johanning, L., and Parkinson, R. J. (2013). Calculating weather windows: Application to transit, installation and the implications on deployment success. *Ocean Engineering*, 68:88–101.
- Wang, A., Yang, Y., Zhu, S., Li, H., Xu, J., and He, M. (2012). Latest progress in deepwater installation technologies.
- Wang, A., Zhu, S., Zhu, X., and Xu, J. (2013). Pendulous Installation Method and its Installation Analysis for a Deepwater Manifold in South China Sea. *The Twenty-third International Offshore and Polar Engineering Conference*.